IPP-Report

Max-Planck-Institut für Plasmaphysik

Thomas Pütterich

Investigations on Spectroscopic Diagnostic of High-Z Elements in Fusion Plasmas

IPP 10/29
April 2006

Abstract

Nuclear fusion of deuterium and tritium relies on the accomplishment of plasma temperatures in the range of 20 keV. In magnetic confinement fusion, the heat transport and radiation losses are compensated by plasma heating. This scheme relies on the control of the loss mechanisms and in particular the plasma radiation. Tungsten (W) is the main candidate for the first wall of a reactor due to its robustness against physical sputtering by the plasma ions, however, when W reaches concentrations of 10^{-4} in the plasma, it causes unduly large plasma cooling by radiation. This implies restrictive impurity control for W, which needs reliable diagnostic by plasma spectroscopy. A pre-requisite for interpretation of the W-spectra is the availability of atomic data for W. The most intense spectral lines of highly ionized W are emitted in the VUV and soft X-ray range. To perform calculations on atomic data the code packages incorporated in the ADAS project are used. The electronic structure of nearly all W-ions is calculated by the Cowan-code (Hartree-Fock algorithm). In a second step, the cross sections for electron impact excitation are evaluated via the Cowan-code using the plane wave Born-approximation. A detailed collisional-radiative model is employed to calculate the model-spectra for each ion in equilibrium. Finally, ionization and recombination rates of W are evaluated by semi-empirical formulae, which make use of the electronic structure calculations of the Cowan-code. All atomic data are confronted with experimental measurements from the Garching tokamak ASDEX Upgrade and the Berlin electron-beam ion trap (EBIT). The experimental investigations extend up to 5 keV electron temperatures, which is the maximum of the routine operation at ASDEX Upgrade. 'Impurity accumulation', which is characterized by a strong peaking of the impurity density profile, enables unique investigations on the fractional abundance of Ag-like W^{27+} up to Co-like W^{47+}. According to this findings different sets of ionization and recombination data (originating from independent sources) are evaluated. The recombination rates for few states are corrected empirically satifying boundary conditions which arise from experimental evidence. Focus was put on the two most intense spectral features at 4-6nm (VUV) and at 0.4-0.8nm (soft X-ray). At 5nm the spectral emissions of Ag-like W^{27+} to Cu-like W^{45+} are superimposed and the EBIT-data is used to disentangle the emissions of each ionization state. Very rough agreement is found for the emissions below Kr-like W^{38+} at electron temperatures below 2 keV, while the level of agreement improves for the spectral lines emitted by Se-like W^{40+} to Cu-like W^{45+} at electron temperatures above 2 keV. At these temperatures Kr-like W^{38+} to about Mn-like W^{49+} show emissions in the soft X-ray, for which the modelled spectra give good agreement. Both spectral features have been studied also for isoelectronic sequences by injecting the impurities hafnium, tantalum, rhenium, gold, lead and bismuth. Additionally, xenon is targeted by the same code packages, as xenon might be injected in future experiments or a reactor for intentional plasma cooling. The systematical trend for these elements is the same as indicated for W, as the agreement improves for higher charged ionization states and higher electron temperatures. Predictions on radiative plasma cooling (cooling factor CF) have been based up to now on the rough 'Average Ion Model' (AIM) and a further result of the work is the analysis of plasma cooling with the outlined, superior model. All data, which are benchmarked by experimental spectra, are used to calculate the CF of the high-Z elements. The resulting CF does not exhibit large differences to that from the AIM, in particular the new data predicts about factor 2 less radiation in the range 2-5 keV while for higher electron temperatures the difference is decreasing to negligible values at about 15 keV. This imposes no change on the predictions of the maximum tolerable W concentration in the core plasma of a reactor. Finally, the new atomic data is used to predict spectral lines at higher electron temperatures, which will be important to diagnose the W concentration in the central part of the reactor plasma.

Investigations on Spectroscopic Diagnostic of High-Z Elements in Fusion Plasmas

Dissertation zur Erlangung des Doktorgrades
an der Mathematisch-Naturwissenschaftlichen Fakultät
der Universität Augsburg

Thomas Pütterich

25. Juli 2005

Mündliche Prüfung:
25. November 2005

Erstgutachter: Prof. Dr. Kurt Behringer
(Universität Augsburg)
Zweitgutachter: Prof. Dr. Achim Wixforth
(Universität Augsburg)
Drittgutachter: Prof. Dr. Hugh P. Summers
(University of Strathclyde, Glasgow)

Contents

Chapter 1

Introduction

1.1 Overview of Present and Future Energy Supply

At the beginning of the 21st century it is clear that the supply of energy in the next 100 years will be a serious issue for the world. Today, most of the world's energy needs are covered by burning fossil fuels like coal, oil or natural gas, while nuclear fission is playing a recognizable role for the production of electricity. Renewable energy sources are still playing only a minor role. A large energy request per person persists in the industrial nations of north America, Europe and Japan as energy consumption is correlated with living standard. Countries like China and India, which are stepping up their living standard, will catch up with their energy consumption per person in the first half of this century. This means that these countries will increase their energy consumption by about a factor of 3 –10. According to this projection, China will overtake the energy needs of the United States of America, the country with the largest consumption of energy, today. Even though energy saving strategies are discussed, the developments sketched above will dominate the world's energy market in this century. In parallel, the resources of fossil fuels will get scarce and it is recognized world wide that the production of CO_2, is causing the 'green house' effect, which has implications on earth's climate that make an negative impact on humans in many regions of the world. In any way, new sources of energy need to be tapped to replace the huge fraction of primary energy that is produced from fossil fuels. Today three possible candidates seem feasible, while probably a single of them is not enough.

Nuclear fission is one candidate as long lasting resources exist, when using the technically challenging fast breeding technology. However, this option seems not practicable on a global scale because safety concerns have led to low acceptance among the population. If other options are available, most likely these will be preferred.

Renewable energy sources are another candidate, which, however, lacks a straight-

forward implementation on large scale. The extension of this sector seems to have far-reaching implications on energy distribution and prices. For instance, the largest wind power potentials in Germany lie off-shore, i.e. at sea, tens of kilometers in front of the shore. A major production of electricity using off-shore wind parks (a group of wind mills), needs appropriate transport capacities for electricity from the north and Baltic Sea to the locations of electricity consumption, i.e. cities or region with dense population. Additionally, power plants need to reserve capacity in case of a wind park being switched off due to unsuitable wind conditions or due to no wind. These backup systems need fast reaction times, because wind parks may be switched off within seconds. Same or similar problems need to be overcome for a world wide implementation of renewables. Still it is worth to pursue energy production from renewable sources, as considerable potentials exist and the development of new technologies like the hydrogen technology may mitigate some of the mentioned problems.

The third option is fusion, which is technically the least developed possibility, but could produce power commercially before 2050. The raw materials deuterium and lithium are largely available all over the world for millions of years, given today's energy consumption. There are some safety issues that have to be dealt with, but in contrast to the dangers of nuclear fission these are well confined and controllable. Therefore, fusion is a valuable option for replacing fossil fuels and reducing CO_2 emissions. Additionally, the world wide availability of the fuel yields a low potential for political conflicts, an issue that could arise for renewable energy sources. More details are available in [1].

1.2 Fusion in General

Fusion power plants are planned to make use of the fact that fusing deuterium (D) and tritium (T) produces large amounts of energy, that is available as kinetic energy (17.6 MeV) in the reaction products He and neutrons (n) (equation 1.1).

$$\mathrm{D} + \mathrm{T} \rightarrow {}^{4}_{2}\mathrm{He}\,(3.5\,\mathrm{MeV}) + \mathrm{n}\,(14.1\,\mathrm{MeV}) \tag{1.1}$$

For the nuclear reaction to take place, it is necessary that the nuclei overcome the repelling Coloumb force acting between the two protons. Therefore, the reaction rate $< \sigma v >$, which is the Maxwellian average over the cross section σ and the velocity v between the reaction partners D and T exhibits a broad maximum at temperatures between 20 keV and 100 keV (figure 1.1). This corresponds to the maximum of the cross section at 64 keV in the center-of-mass frame, which exists due to the resonance with an exited nuclear state of ${}^{5}_{2}\mathrm{He}$ at this energy. Below temperatures of 10 keV the reaction rate is strongly decreasing. In principle, other fusion reactions (equation

1.2, 1.3, 1.4) are also possible, however, these show a reaction rate that is suitable for the construction of a power plant only at temperatures well above 100 keV (figure 1.1). At these high plasma temperatures, Bremsstrahlung is an important power loss mechanism of the plasma and it is difficult to maintain the high temperatures for a steady state reactor.

$$\mathrm{D} + \mathrm{D} \rightarrow {}^{3}_{2}\mathrm{He} + \mathrm{n} + 3.3\,\mathrm{MeV} \tag{1.2}$$

$$\mathrm{D} + {}^{3}_{2}\mathrm{He} \rightarrow {}^{4}_{2}\mathrm{He} + \mathrm{p} + 18.4\,\mathrm{MeV} \tag{1.3}$$

$$\mathrm{T} + \mathrm{T} \rightarrow {}^{4}_{2}\mathrm{He} + 2\mathrm{n} + 11.3\,\mathrm{MeV} \tag{1.4}$$

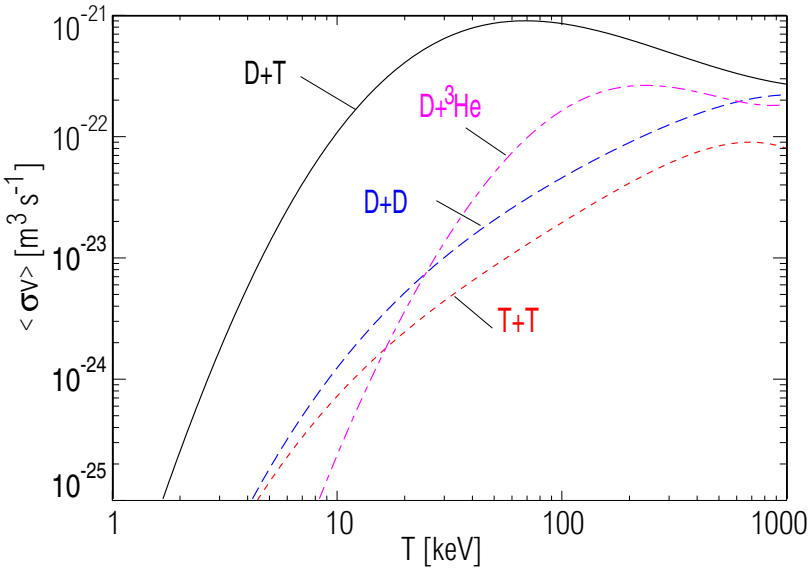

Figure 1.1: Reaction rate $< \sigma v >$ of some fusion reactions

As tritium needs to be produced artificially, the breeding processes that are shown in equation 1.5, 1.6 are foreseen in a fusion power plant. The used neutron is the same neutron that also carries 14.1 MeV kinetic energy from the fusion process. The breeding will take place in a lithium blanket, which surrounds the reaction chamber. Its temperature will be kept constant by a coolant that transports the original fusion energy to a power generating turbine.

$$\mathrm{n} + {}^{7}_{3}\mathrm{Li} \rightarrow \mathrm{T} + {}^{4}_{2}\mathrm{He} + \mathrm{n} - 2.47\,\mathrm{MeV} \tag{1.5}$$

$$\mathrm{n} + {}^{6}_{3}\mathrm{Li} \rightarrow \mathrm{T} + {}^{4}_{2}\mathrm{He} + 4.78\,\mathrm{MeV} \tag{1.6}$$

There are two branches of fusion research, namely inertia confinement fusion (ICF) and magnetic confinement fusion (MCF). Both concepts plan to use a hot plasma to fuse the nuclei of D and T.

In the concept of ICF a small fuel pellet with the size of $\approx 1\,\mathrm{mm}$ is irradiated with an intense laser (0.1–1 MJ) or heavy ion beam. The recoil due to ablation of outer layers of the pellet compresses the core by a factor larger than 1500 (electron density $n_e \approx 7 \cdot 10^{31}\,\mathrm{m}^{-3}$) giving rise to an increase in core temperature up to T≈10 keV. Inertia is confining this very dense and hot plasma for about 1 ns, which is enough to fuse a considerable amount of the fuel. One problem which needs to be overcome is that the irradiated pellets exhibit dynamical Rayleigh-Taylor instabilities, which limit the compression of the pellet core. A technical realization of a ICF power plant, is possible if several pellets per second are ignited, while the plant should be designed to withstand these frequent, powerful explosions. However, large funding for this branch of fusion research exists in USA, France and Japan.

The scheme of MCF is using a strong magnetic field to confine the charged particles of the hot ($\approx 20\,\mathrm{keV}$), steady-state plasma via the Lorentz force. In a reactor, when a deuterium-tritium mixture is used this leads to a certain rate of fusion reactions that produce fast neutrons, which leave the plasma, and energetic helium nuclei, which supply their kinetic energy to the plasma. The magnetic field, which is of the order of few Teslas leads to the confinement of all charged particles including the helium nuclei. Following this argument a plasma of certain size produces a fixed amount of intrinsic plasma heating corresponding to the reaction rate shown in figure 1.1. If external heating is switched off, the energy losses at 20 keV plasma temperature must not be larger than the intrinsic heating in order to maintain the necessary temperature. 'Ignition' of the plasma is the technical term for reaching this self-sustaining state. This has been one challenge for MCF research, as radiation losses, heat conduction and convection are transporting energy out of the plasma very efficiently. Possibilities have been explored and developed to minimize these losses. As a number of merit the triple product of plasma density n , plasma temperature T and the energy confinement time τ_E can be used. τ_E is the stored energy of the plasma divided by the total heating power and a high value of τ_E indicates that high temperatures can be reached for a fixed amount of heating. Even though it took about 50 years, the progress of MCF research presented in figure 1.2 is remarkable. MCF provides a continuous production of energy, which makes it compatible to the infrastructure of a conventional power plant. Many results of this thesis aim for application in the field of MCF to which a more detailed introduction can be found in the appendix A. The Garching tokamak (s. appendix A) ASDEX Upgrade (s. appendix B.1), is an experiment, which investigates physics issues relevant to a future reactor. Plasmas with electron densities of about $1 \cdot 10^{20} m^{-3}$ and temperatures of the order of 10 keV are analyzed and one focus of the research are the wall materials which face the edge of the hot plasmas. Plasma pulses at ASDEX Upgrade last for about 10 s, which is sufficient to investigate nearly

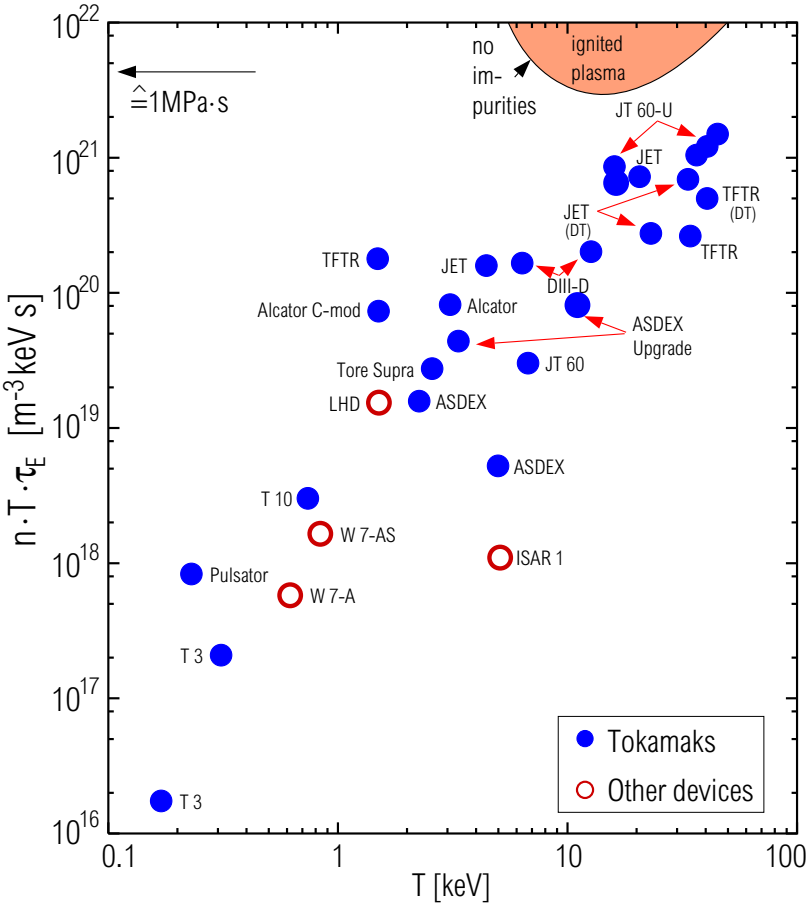

Figure 1.2: Triple product for several experiments versus plasma temperature indicating the progress of MCF research; a reactor will operate inside the region labeled with 'ignited plasma'; a tokamak is a certain experiment type, which is explained in appendix A

all relevant physics issues. It may be noted, that only a small fraction of terms, effects and phenomena connected to a fusion plasmas are encountered in this thesis and only these are explained, which are connected to presented analyses. The main focus of this work is put on atomic physics issues, while the plasma is only used as a tool, although the results of this thesis have implications on fusion plasmas.

1.3 Impurities and First-Wall Materials in MCF

For a fusion plasma operation is limited by the plasma pressure. This imposes restrictions on the particle densities that can be obtained in a plasma at a given plasma temperature. Therefore, the presence of impurities is unwanted in the central, hot region of a fusion plasma, as the they dilute the deuterium-tritium fuel and they decrease the energy confinement by increasing the radiative losses of the plasma. Both is deteriorating the performance of a fusion reactor. Despite of the various efforts to minimize

the amount of impurities that are entering the main plasma (e.g. the divertor concept featured in appendix A) a contamination of it is inevitable. For impurities with a nuclear charge Z below ≈ 30 the nucleus is completely stripped in the hot center of the reactor plasma and radiative losses are mainly caused by Bremsstrahlung. If electrons remain bound to the nucleus, line radiation occurs which is for the plasma regimes of MCF the most efficient mechanism for radiative losses. Thus, impurity concentrations of 1 % carbon are easily tolerable, while a tungsten concentration above $2\text{-}3{\cdot}10^{-4}$ is inhibiting self-sustained fusion at all. This is featured in figure 1.3, which shows the operational window of a fusion power plant for different impurity concentrations. Helium complicates the situation and needs to be considered separately, because it is a product of the fusion process. In figure 1.3 the operational window of a power plant is presented for the assumption that the confinement time of the α-particles $\tau_\alpha = 5\tau_E$. τ_α is the particle content of the plasma divided by the source and accordingly gives the typical time for an α-particle to stay in the plasma, so for high enough particle confinement the fusion reaction is extinguished by its own ash. This explains, why the consideration of helium leads to a closed curve indicating the operational space of an ignited fusion reactor in figure 1.3. The other impurities are considered on top of the helium ash. Carbon seems to be the ideal element for the first-wall, because as a plasma impurity it reduces the energy flow to the wall very efficiently, by radiating at the edge of the fusion plasma (electron temperature $T_e \leq 500\,\text{eV}$), where electrons still remain bound to the nucleus. Despite this advantages of carbon and its high sublimation point of 3800 K it is probably not used in a future reactor, as it is eroded too fast under reactor conditions [2, 3]. This applies to all materials with a nuclear charge of less than about $20-30$, especially to beryllium which is planned to be used on a large scale in the next step fusion experiment ITER (cf. appendix B.3). Beryllium is considered to be a temporary solution, for an additional problem that is caused by carbon. Namely, it has been found in today's fusion devices [4–7], which operate with first-walls largely made from graphite of carbon fiber composites (CFC), that amorphous carbon-hydrate layers form during plasma operation inside the vacuum chamber. If similar layers formed in ITER, tritium would be co-deposited. Within less then 100 plasma discharges (a tenth of its design value) ITER's inventory of tritium could be at the safety limit of 350 g, which would delay further operation [8–10]. Therefore, the use of CFC is foreseen in ITER only on a well confined area in the divertor, to minimize the amount of mobilized carbon.

For a reactor, alternative wall materials are discussed, which need to be robust against sputtering by plasma particles. Although high-Z materials, i.e. materials with a nuclear charge well above 40, exhibit the unfavorably pronounced capability to cause radiative losses, their use is rediscussed as they can be a possible remedy

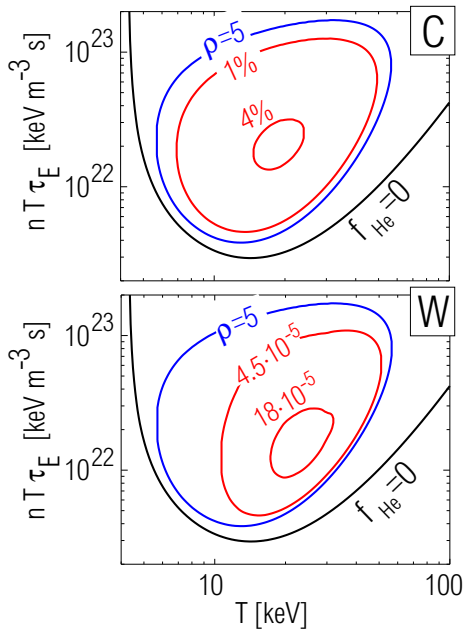

Figure 1.3: Operational window of a fusion plasma for different impurity concentrations. The black line indicates the burn region without impurities and without helium, the blue line considers the contamination of the plasma by the He ash assuming a He-confinement time of $\tau_\alpha = 5\tau_E$ ($\hat{=}\rho = 5$). The red lines indicate the burn region for an additional impurity content of the plasma for the impurities carbon (C) and tungsten (W).

against the strong erosion potential of the plasma in a future reactor. Tungsten is such a material and the element with the highest melting point and acceptable nuclear properties. Therefore, it is the top choice of all high-Z materials. In the 1970's first experiences with tungsten as a first-wall material ended disapointingly [11], as the huge radiative losses in the plasma center due to tungsten led to hollow temperature profiles. Today, these problems are reliably suppressed by the superior divertor (s. appendix A) concept [12] and operational measures, which meanwhile have been developed. ASDEX Upgrade is world-wide the first, large fusion experiment, which reconsidered tungsten as a plasma facing material on a large scale and did this with great success increasing the surface coverage of tungsten from year to year. An extensive work on these activities and its meaning for future fusion devices can be found in [13]. The tungsten experiments since 1996 supported the actual ITER and DEMO (cf. appendix B.3 and B.4) designs, which use tungsten at least in the divertor and possibly also at other plasma facing surfaces.

However, still a cautious plasma operation is necessary to avoid situations of unduly large impurity concentrations. A basic pre-requisite for investigations on and operation with tungsten is the ability to diagnose the impurity concentrations, if possible spatially resolved. This can be done best by passive spectroscopy and bolometry. To link the measured spectra or detected radiation power to the abundance of an im-

purity it is necessary to know the atomic properties of the impurity. Therefore, the calculation and verification of atomic data describing these properties are important necessities.

1.4 Outline

This work investigates the atomic properties of tungsten, in hot fusion plasmas like that of ASDEX Upgrade. For this purpose, the atomic physics code package (Cowan code [14] implemented in the Atomic Data Analysis Structure (ADAS) [15, 16]) is used to calculate the atomic properties of high-Z elements in a plasma surrounding. This means, that on the one hand the wavefunctions and energy levels for the most important levels are evaluated for all tungsten ions. Giving rise to the transition probabilities and wavelengths for certain transitions. On the other hand also the much more elaborate calculations on electron impact cross sections are performed using the plane wave Born-approximation, which are then used to evaluate the intensities of the spectral lines via a collisional radiative model. A main goal of the thesis is the verification of the results by comparing them to experimentally obtained spectra and total radiation measurements at ASDEX Upgrade (appendix B.1) and the electron beam ion trap in Berlin [17]. Not only the spectral emissions are documented, but also the efficiency of tungsten to cause radiative losses, the so called 'cooling factor', is subject of the present investigations. In this context it is interesting, if the tolerable tungsten concentration in a plasma of a fusion reactor is supported by the present evaluation of atomic data. Furthermore, the question of how to diagnose tungsten in future devices will be addressed. The focus is put on tungsten, because of its relevance for future fusion devices. However, investigations on xenon (Z=54), hafnium (Z=72), tantalum (Z=73), rhenium (Z=75), gold (Z=79), lead (Z=82) and bismuth (Z=83) were also performed. While xenon might be relevant as diagnostic gas in future devices the other elements are investigated here to benchmark the comparison of spectra and code calculations also for the neighboring elements of tungsten. It may be noted that elements like hafnium, tantalum and rhenium are discussed (e.g. [18]) as erosion markers, which are buried under a layer of the first wall material at locations of strong plasma erosion. When the marker depth is reached after some months of operation the marker material is thought to be detectable in the spectra of plasma diagnostics, an assumption which my be doubted due to the unclear impact of small localized impurity sources onto the impurity concentration of the main plasma.

In chapter 2 an overview of the atomic physics involved is given, ranging from very basic considerations to the description of the data which finally were obtained in the course of this work. In chapter 3 the spectrometer and radiation diagnostics at ASDEX

Upgrade are introduced along with the absolute calibration that has been performed for the most important spectrometers. The calculated atomic data are then compared to the experimental findings in chapter 5, 6, 7 and 8. For these investigations, the atomic data need to be interpreted in the context of the experiment, which means that they are used to simulate the view of the spectrometers across the plasma. The modeling procedure is described in the preceding chapter 4, which also deals with transport effects inside the plasma. An important ingredient of the modeling is the radial distribution of the ion states of the high-Z impurity. The ionization balance, i.e. the fractional abundance of each ion state versus electron temperature, is investigated in chapter 5 for tungsten, neighboring elements and xenon. The details of the tungsten spectra are compared to the code calculations in chapter 6, while also spectral features are presented which could not be reproduced by the modeling. In chapter 7, the spectral features of neighboring elements are investigated in the isoelectronic context. Additionally, investigations on xenon spectra are presented. In chapter 8, the cooling factor, i.e. the efficiency of an element to cause radiative losses in a plasma which is of central importance for a fusion reactor, is presented for the high-Z elements and partially compared to direct measurements. In chapter 9 the implications of the present findings on future experiments and a reactor are investigated. Namely, predictions for the spectra at JET, where a tungsten experiment is planned for 2009, and ITER are presented which enable for deriving the diagnostic requirements for ITER. Finally, the work is summarized in chapter 10.

Chapter 2

Calculation of Atomic Data

Radiation of atoms and ions is one of the most famous examples where macroscopic effects like the emission of spectral lines can be only understood by a quantum mechanical model. For the hydrogen atom, calculations can be performed using the most advanced models up to a very detailed level. Peculiarities for instance like the Lamb-shift are well understood by quantum electrodynamics. In turn this means that a spectroscopic observation can be interpreted very well. For interpretation, data like cross sections of atom-electron collisions or transition probabilities between certain levels are needed. These data are called 'atomic data', a term which is used quite generally for any data concerning the basic properties of atoms and ions. Unfortunately, an exact quantum mechanical treatment is not possible for species with more than one electron. Therefore, numerical approximations are used to obtain atomic data for these species. This introduces an additional uncertainty to the interpretation of a measurement. Depending on how accurately the important features of a atomic process are considered, the quality of atomic data may vary from method to method. The data concerning an isolated atom or ion are describing only the structure of it. The wavefunctions allow to determine the energies, i.e. wavelengths, of transitions and their probability. This structure can be evaluated within short time scales by various atomic codes. For determining the line intensities of these transitions emitted in a plasma the interaction of the ions with electrons need to be addressed. In a fusion plasma the electron impact excitation plays the most important role, and the quantum mechanical determination of cross sections for this process involves calculations that consider the interaction of the scattered free electron with the structure of the ion. Large and time-consuming calculations are necessary to do so. In section 2.1, a brief overview will give some insight into the atomic physics of one and many electron systems in a plasma surrounding. Detailed additional information is available in [14]. In section 2.2 various atomic calculations methods for determining line intensities or

cross sections of electron impact excitation, which differ by quality and complexity, will be introduced. In section 2.3 the data which were produced or are used in the course of this thesis is described.

2.1 Brief Overview of Atomic Physics

2.1.1 Structure of Atoms/Ions

Quantum Mechanical Principles

Some facts that arise from quantum mechanics are summarized here, but can be found in quantum mechanics text books like [19]. In quantum mechanics a complex wave function Ψ contains all the information, which is needed to describe physical quantities. Ψ depends on the physical problem and is found by solving the Schrödinger equation (if relativistic effects are neglected):

$$H\Psi = i\hbar\frac{\partial\Psi}{\partial t} \tag{2.1}$$

H, the Hamiltonian, is the energy operator and consists of one part representing the kinetic energy and one representing the potential. For a spherically symmetric potential $V(r)$ the Hamiltonian $H = -\frac{\hbar^2}{2m}\Delta + V(r)$. $\hbar$ is the Planck constant over 2π and Δ is the Laplace-operator. The Schrödinger equation is the quantum mechanical equivalent to the equation of motion for the Hamilton formalism in classical mechanics. Ψ is an element of the complex vector space of quadratically integrable functions, which are defined on $\mathbb{R}^n$ in general. In the following the focus lies on $\mathbb{R}^3$. A scalar product of Ψ_1 and Ψ_2 is defined by:

$$\int_{\mathbb{R}^3} \Psi_1^* \Psi_2 dV =: \langle\Psi_1|\Psi_2\rangle \tag{2.2}$$

dV is a differential volume of $\mathbb{R}^3$. On the right hand side the Dirac notation for the scalar product was chosen. It may be noted here that many considerations in physics are done on separable Hilbert spaces, i.e. spaces with finite or countable dimensions.

Physical quantities, 'observables', are represented in quantum mechanics by hermitian operators. In the following the same symbols are used for an observable and for the corresponding operator. 'Hermitian' implies, that any wave function Ψ can be written in an expansion of normalized, orthogonal basis functions ψ_i, that are eigenfunctions of O with real eigenvalues o_i: $\Psi = \sum_{i=0}^{n} \psi_i c_i$ with c_i being complex constants. The

expectation value for such an observable is, using the definition and orthonormality:

$$\begin{aligned}\langle O\rangle = \langle\Psi|O|\Psi\rangle &= \int_{\mathbb{R}^3} \Psi^* O \Psi d^3r = \int_{\mathbb{R}^3} (\sum_{i=0}^{n} \psi_i c_i)^* \sum_{j=0}^{n} \psi_j c_j o_j d^3r \\ &= \sum_{i=0}^{n}\sum_{j=0}^{n} c_i c_j o_j \int_{\mathbb{R}^3} \psi_i^* \psi_j d^3r = \sum_{i=0}^{n} |c_i|^2 o_i \end{aligned} \tag{2.3}$$

The result of a measurement of a physical quantity corresponding to the operator O is always an eigenvalue of O. For a wave function which is not an eigenfunction of an operator there are several measurements possible. The probability of measuring one special o_i is given by the coefficient $|c_i|^2$ and therefore the expectation value for an measurement is given by the above sum (right hand side of 2.3).

The properties of the operators define the nature of observables. A basic property of two operators A and B is their commutator $[A, B] = AB - BA$. If they commute, i.e. $[A, B] = 0$, the eigenfunctions of A are also eigenfunctions of B and vice versa. On the other hand, if all commuting operators are found for a problem, the physical properties of eigenfunctions can be completely characterized by the eigenvalues, which in the case of countable eigenvalues are represented by so called quantum numbers. A special case occurs, if a operator A commutes with the Hamiltonian H.

$$\begin{aligned} i\hbar\frac{d\langle A\rangle}{dt} &= i\hbar \int \Psi^* A \frac{\partial\Psi}{\partial t} d^3r + i\hbar \int \frac{\partial\Psi^*}{\partial t} A\Psi d^3r + i\hbar\langle\frac{\partial A}{\partial t}\rangle \\ &= \int \Psi^* AH\Psi d^3r - \int \Psi^* HA\Psi + i\hbar\langle\frac{\partial A}{\partial t}\rangle \\ &= \langle[A, H]\rangle + i\hbar\langle\frac{\partial A}{\partial t}\rangle \end{aligned} \tag{2.4}$$

If A is not explicitly dependent on time equation 2.4 means that the commutator $[A, H] = 0$ if and only if A corresponds to a constant of motion. If $[A, B] = C \neq 0$ then A and B don't have a common set of eigenfunctions and a simultaneous measurement of both quantities is producing an intrinsical scatter of the measured values according to Heisenberg's uncertainty relation. It (equation 2.5) relates the square root of the variance of the observables A and B, i.e. ΔA and ΔB, to the modulus of the expectation value of C:

$$\Delta A \Delta B \geq \frac{1}{2}|\langle C\rangle| \tag{2.5}$$

Only for a vanishing C an exact measurement of A and B is possible.

Angular Momentum

A constant of motion in an spherically symmetric potential is angular momentum. Therefore, it plays a very important role for all considerations in an atom, where

the nucleus generates such a potential. The operator J is formed accordingly to its definition in classical mechanics: $J = r \times p$ with the position r and the momentum operator p. If J is a constant of motion, it commutes with the Hamiltonian, however its components do not commute with each other:

$$J_x J_y - J_y J_x = i\hbar J_z \tag{2.6}$$

$$J_y J_z - J_z J_y = i\hbar J_x \tag{2.7}$$

$$J_z J_x - J_x J_z = i\hbar J_y \tag{2.8}$$

A commuting set of operators is found in J_z and $J^2 = J_x^2 + J_y^2 + J_z^2$. By simple considerations, it is found that the possible eigenvalues of the J^2-operator are $\tilde{j}(\tilde{j}+1)\hbar$ for $\tilde{j} = 0, \frac{1}{2}, 1, \frac{3}{2}, \ldots$. For a certain j the eigenvalues of the J_z-operator are $m_{\tilde{j}}\hbar$ with $m_{\tilde{j}} = -\tilde{j}, -\tilde{j}+1, -\tilde{j}+2, \ldots, \tilde{j}-1, \tilde{j}$.

If two subsystems exist with angular momenta J_1 and J_2 it is possible to couple both momenta to a single momentum J of the total system. The corresponding possibilities for $\tilde{j}$ can be derived from actual values $\tilde{j}_1$ and $\tilde{j}_2$: $\tilde{j} = \tilde{j}_1 + \tilde{j}_2, \tilde{j}_1 + \tilde{j}_2 - 1, \tilde{j}_1 + \tilde{j}_2 - 2, \ldots, |\tilde{j}_1 - \tilde{j}_2|$.

Hydrogen-like Atoms and low-Z Elements

A Hydrogen-like atom is the simplest case for an electron nucleus system. This example will be used here to explain certain principles and terms. The time-independent Schrödinger $H\Psi = E\Psi$ equation needs to be solved with a Hamilton-operator for an electron inside the electric potential of a proton, i.e.:

$$H = -\frac{\hbar^2}{2\mu}\Delta - \frac{e^2 Z}{4\pi\epsilon_0 r} \tag{2.9}$$

$\mu = m_e m_n/(m_e + m_n)$ is the reduced mass (m_e electron mass, m_n mass of nucleus), e the elementary charge, Z the number of protons in the nucleus, ϵ_0 the electric constant, r the radial distance from the proton and Δ, the Laplace-operator. The separation ansatz $\Psi = R(r)Y(\phi,\theta)$ with ϕ and θ being the azimuth and elevation angle in spherical coordinates is used to solve the equation. The spherical harmonics Y_{ℓ,m_ℓ} solve the pure angular part of the equation, while the solutions for the radial part $\mathrm{R}_{n,\ell}$ can be also obtained, but are not specified here, because the details are not important for the general considerations and can be reviewed in many quantum mechanics text book like [20]. Solving the Schrödinger equation this explicit way, it is derived that for a so called principal quantum number n the angular momentum l of the electron has the eigenvalues $\ell(\ell+1)\hbar$ with $\ell = 0, 1, 2, 3, 4, 5, \ldots, n-1$ denoted as s,p,d,f,g,h,..., which is of course in agreement of the general findings about angular momentum. Accordingly, l_z has the eigenvalues $m_\ell\hbar$ for each ℓ with $|m_\ell| \leq \ell$. The

combination of n and and ℓ is called an orbital. The problem is complicated by the fact, that the electron itself is carrying an intrinsic angular momentum s, called spin, with only one eigenvalue $\sigma(\sigma+1)\hbar$ ($\sigma = \frac{1}{2}$) and correspondingly two eigenvalues $m_\sigma\hbar$ ($\sigma = -\frac{1}{2}, \frac{1}{2}$) for s_z. Coupling of the orbital angular momentum l and the spin s results in a total angular momentum j for one electron.

The Hamiltonian needs to consider the interaction energy of the magnetic moments corresponding to l and s. This leads to an additional term $\propto l \cdot s$ in the Hamiltonian, which makes the commutators $[l, H]$ and $[s, H]$ non-zero. Hence, the observables l and s are, strictly speaking, not anymore constants of motion. However, as the interaction energy between l and s is relatively small compared to the electrostatic interactions, l and s are meaningful for the hydrogen atom. Even for elements with low nuclear charge and few electrons the coupling of L and S remains a sensible concept, when first the orbital angular momenta l of all electrons are coupled to L and the spins s of all electrons are coupled to S. This coupling scheme is therefore called LS-coupling. J denotes the total angular momentum of the multi-electron system and the quantum numbers of L,S and J are denoted as $\tilde{\ell}, \tilde{\sigma}$ and $\tilde{j}$.

Considering elements with several electrons the Hamiltonian may be approximated by summing up Hamiltonians for single electrons $H_{kin} + H_{e-n} + H_{s-o}$ and adding an additional term H_{e-e} that accounts for the interaction between the electrons (s. equation 2.10). r_i denotes positional-coordinate vector of the i^{th} electron with respect to the nucleus, $r_{i,j} = |r_i - r_j|$ and $\xi_i(r_i)$ is a proportionality factor that has to be specified.

$$\begin{aligned} H = \quad & H_{kin} + H_{e-n} + H_{e-e} + H_{s-o} = \\ = & -\sum_i \frac{\hbar^2}{2\mu}\Delta_i - \sum_i \frac{e^2 Z}{4\pi\epsilon_0 |r_i|} - \sum_i \sum_{j>i} \frac{e^2}{4\pi\epsilon_0 r_{i,j}} + \sum_i \xi_i(|r_i|)(\mathbf{l}_i \cdot \mathbf{s}_i) \end{aligned} \tag{2.10}$$

For elements with several electrons, the individual spin and orbital angular momentum are sensible values and LS-coupling applies. The distribution of electrons into the hydrogen-like orbitals is the underlying ansatz for the wavefunctions according to equation 2.11, where $\hat{\sigma}_{m_{\sigma_i}}(s_{i,z})$ was introduced to characterize the spin state of the ith electron.

$$\psi = \prod_{i=1}^{n} \varphi_i \tag{2.11}$$

$$\varphi_i = \frac{1}{|r_i|} P_{n_i,\ell_i}(|r_i|) Y_{\ell_i,m_{\ell_i}}(\theta_i, \phi_i) \hat{\sigma}_{m_{\sigma_i}}(s_{i,z}) \tag{2.12}$$

The population of orbitals is restricted by the Pauli-principle that prevents two electrons from agreeing in all quantum numbers $n, \ell, m_\ell, m_\sigma$. The number of electrons with a certain principal quantum number n is fixed as well as the number of electrons

in a certain orbital, i.e. combination of n and ℓ. For example, the maximum number of electrons that can be attributed to the principal quantum number 2 is 8, while in the 2p-orbital a maximum of 6 electrons fit in. A so called configuration, denotes all states with a identical distribution of electrons into orbitals. The ground state of neutral carbon is contained in the configuration $1s^2\,2s^2\,2p^2$, along with 3 more levels. These are formed by different coupling of the two 2p-electrons. The lower-lying electrons, i.e. $1s^2$ and $2s^2$, are in closed sub-shells and couple to a state with neither orbital angular momentum nor spin. However, when considering the radial part P_{n_i,ℓ_i} of the solution to the multi-electron Schrödinger-equation the electrons need to be considered. P_{n_i,ℓ_i} needs to be determined numerically.

The Hamiltonians 2.9 and 2.10 are neglecting relativistic effects. These can be considered by solving the more complicated Dirac-equation [21–23]. For the approximation that the velocity of the considered electrons is small compared to the speed of light, correction terms can be determined as an addition to the Schrödinger equation. One term , which is $\propto\ l \cdot s$, can be identified with the energy of the spin-orbit coupling. The other two terms, are the so called Darwin- and mass-velocity-term. The first is connected to the non-localizability of the electron while the mass-velocity term accounts for the change of electron mass due to its velocity. For the hydrogen atom, but also when considering outer electrons of more complicated atoms and ions, these approximations give satisfying agreement.

2.1.2 Complex Atoms

If the electrostatic energies (3rd term in equation 2.10) are negligible compared to the spin-orbit interactions (4th term in equation 2.10), pure jj-coupling applies. In this coupling scheme first the orbital angular momentum and the spin is coupled to a total angular momentum j for each electron. These angular momenta couple to the total angular momentum J of the ion or atom. For elements with large nuclear charge, this coupling scheme may apply. However, it is often not beforehand obvious how the angular momenta and spins of all electrons are coupled. Several additional coupling schemes exist that differ in the order in which the different orbital angular momenta and spins are coupled. In many cases the real coupling conditions are not described by any pure coupling scheme, such that the only meaningful observables concerning angular momentum are J and J_z. This regime is called intermediate coupling.

As a consequence a single electron in a multi-electron system cannot be attributed to a certain hydrogen-like orbital. Nevertheless, the hydrogen-orbitals are a complete set of basis functions and it is therefore possible to describe an arbitrary wavefunction Ψ_N for N-electrons by a linear combination of wavefunctions, each of which is a product

of N hydrogen orbitals $\varphi_{i,k}$, where k has no physical meaning and just numbers the basis functions.

$$\Psi_N = \sum_{k=1}^{\infty} C_k \psi_{N,k} \tag{2.13}$$

$$\psi_{N,k} = \prod_{i=1}^{N} \varphi_{i,k} \tag{2.14}$$

This is a infinite series in general, but often a state is described with high precision by a linear combination of finite number of states that belong to few configurations. Hence, the series 2.13 can be truncated. The fact, that more than one configuration is used to construct the actual wavefunction Ψ_N is called configuration mixing. The participating configurations are restricted to one parity, which is the parity of the state Ψ_N. Parity is a basic property of a wavefunction in a spherical symmetric field. It arises, as for a solution $\Psi_N(|r|, \theta, \phi)$ of a central field problem the function $\Psi_N(|r|, -\theta, -\phi)$ also is a solution to the problem, which means $\Psi_N(|r|, \theta, \phi) = \Psi_N(|r|, -\theta, -\phi)$ or $\Psi_N(|r|, \theta, \phi) = -\Psi_N(|r|, -\theta, -\phi)$. Respectively, $\Psi_N(|r|, -\theta, -\phi)$ is said to have even or odd parity and at the same time all basis functions of the series 2.13 need to belong to the same parity. The parity for a configuration $n_1 l_1^{x_1} .....n_N l_N^{x_N}$ is odd or even if $\prod_{i=1}^{N} l_i^{x_i}$ is -1 or 1, respectively. Typically, every operator O has a definite parity p_O. If one assumes that two wavefunction Ψ and Ψ' have parities p and p'. Then, using Cartesian coordinates

$$\begin{aligned}
\langle \Psi | O | \Psi' \rangle = & \int\int \int_{\infty}^{-\infty} \Psi^*(-x,-y,-z) O \Psi'(-x,-y,-z)(-dx)(-dy)(-dz) = \\
= & \quad (-1)^{p+p'+p_O} \int\int \int_{-\infty}^{\infty} \Psi^*(x,y,z) O \Psi'(x,y,z)(dx)(dy)(dz) = \\
= & \quad (-1)^{p+p'+p_O} \langle \Psi | O | \Psi' \rangle
\end{aligned} \tag{2.15}$$

implies that $\langle \Psi | O | \Psi' \rangle$ is zero unless $p + p' + p_O$ is even.

2.1.3 Energies and Transitions in Atoms/Ions

Of immediate interest are the energies of the states and the Einstein-coefficients that give the probability of a radiative decay of a state by spontaneous emission. The energy eigenvalues of the Schrödinger equations can be found by diagonalizing the the matrix $H_{i,k} = \langle \psi_{n,k} | H | \psi_{n,i} \rangle$. The off-diagonal elements in $H_{i,k}$ demonstrate the effect of so called configuration interaction, which is a consequence of the configuration mixing. When limiting the number of basis functions for a detailed calculation, care has to be taken to include all basis functions with major contributions to the states of

interest. Every observable that is determined relies on the good representation of the actual state by the linear combination of basis functions.

The Einstein-coefficients A_{ik} for electric dipole radiation between the two states Ψ_i and Ψ_k of an N-electron system can be evaluated with the dipole operator $D = \Sigma_{i=1}^{N}(-e)r_i$ via the expression 2.16.

$$\langle\Psi_i|D|\Psi_k\rangle \tag{2.16}$$

The operator D itself has odd parity. According to equation 2.15 the transition probability is non-zero only if $|\Psi_k\rangle$ has a different parity than $\langle\Psi_i|$. By expressing D with the solutions of angular part $Y_{1,-1/0/1}$ it is possible to derive from the orthogonality of $Y_{\tilde{j},m_{\tilde{j}}}$, that certain selection rules apply for a dipole transition. J_k and J_i are the total angular momenta of Ψ_k and Ψ_i, respectively. The expression 2.16 is non-zero only if $\tilde{j}_i - \tilde{j}_k = \pm 1$ or 0, and not $\tilde{j}_i = 0$ and $\tilde{j}_k = 0$. Similarly, for $m_{\tilde{j}_i}$ and $m_{\tilde{j}_k}$ the selection rule $m_{\tilde{j}_i} - m_{\tilde{j}_k} = \pm 1$ or 0 applies.

Radiative transitions are also possible as magnetic transitions, and additionally higher multipoles are possible. These transitions may be of considerable importance for highly charged ions. For multiply ionized tungsten which is investigated in this work, the strongest spectral line in the soft X-ray spectrum is an electric quadrupole line. In this work, spectral lines are considered that are magnetic dipole (M1), electric dipole (E1) and electric quadrupole (E2) transitions. The operators for M1 and E2 have even parity and therefore, no parity change takes place. The selection rules for M1-transitions are identical to the E1-transitions while for E2-transitions $\tilde{j}_i - \tilde{j}_k = \pm 2, \pm 1$ or 0 and $\tilde{j}_i + \tilde{j}_k \geq 2$ and $m_{\tilde{j}_i} - m_{\tilde{j}_k} = \pm 2, \pm 1$ or 0.

2.1.4 Processes in Plasmas and Population Equilibria

When an atom or ion is in a plasma several processes occur. Table 2.1 features some of these processes. The electron density is of large importance, when considering the relative frequency of occurrence for each reaction. Both the ionization-recombination equilibrium and the population of the states within the atoms and ions are influenced by the processes.

For a certain atom or ion state, models for emission of photons are explained in the following. The emission of photons can be quantified by the emissivity $\epsilon_{i,k}$ for a transition between the state i with density n_i and state k. Simply, $\epsilon_{i,k} = n_i A_{i,k}$. As $A_{i,k}$ is constant, n_i is of interest. n_i can be calculated by consideration of the most important processes that influence the population equilibrium. Three regimes for population equilibria, which are related to different electron densities, can be identified. For small electron densities, i.e. about $n_e \leq 1 \cdot 10^{18}\,\mathrm{m}^{-3}$, electron collisions with

electron impact excitation	$\longleftrightarrow$	collisional deexcitation
$A+e$	$\longleftrightarrow$	$A^{\star}+e'$
photo absorption	$\longleftrightarrow$	spontaneous emission
$A+h\nu$	$\longleftrightarrow$	$A^{\star}$
electron impact ionization	$\longleftrightarrow$	three body recombination
$A^{z}+e$	$\longleftrightarrow$	$A^{z+1}+e'+e''$
photo ionization	$\longleftrightarrow$	radiative recombination
$A^{z}+h\nu$	$\longleftrightarrow$	$A^{z+1}+e$
excitation autoionization	$\longrightarrow$	
$A^{z}+e$	$\leftrightarrow A^{z\star\star}+e' \rightarrow$	$A^{z+1}+e'+e''$
dielectronic recombination	$\longrightarrow$	
$A^{z+1}+e'$	$\leftrightarrow A^{z\star\star} \rightarrow$	$A^{z}+h\nu$

Table 2.1: Processes that occur in a plasma. A is an atom or ion, which may be excited ($A^{\star}$) or doubly excited ($A^{\star\star}$). A^{z} is an atom or ion with charge z. e, e′ and e″ denote electrons with different energies, while $h\nu$ represents a photon. The lowest two processes happen in two steps and are important for the balance of ionization and recombination rates.

ions and atoms happen rarely and are followed by (a) radiative decay(s) to their ground state before a further collision takes place. This rule of thumb applies for low-Z impurities, but as the transition probabilities are proportional to Z^4 (Z being the charge of the ion), the following considerations are also good approximations for high-Z elements in most plasmas of magnetic confinement fusion. For this so called 'corona population equilibrium' equation 2.17 applies, where $X_{1,i}$ is the excitation rate coefficient for excitation from the ground state with density n_1 into state i and $\sum_{m<i} A_{i,m}$ is the sum of all transition probabilities that are non-zero for a decay of state i. $b_{i,k}$ is called the branching ratio, as it is the relative probability for state i to decay via the transition of interest into state k.

$$\epsilon_{i,k} = n_1 n_e X_{1,i} \frac{A_{i,k}}{\sum_{m<i} A_{i,m}} = n_1 n_e X_{1,i} b_{i,k} \tag{2.17}$$

The emissivity $\epsilon_{i,k}$ is proportional to the electron density as the emissivity is directly connected to the excitation processes. For electron densities $n_e \geq 1 \cdot 10^{23}\,\mathrm{m}^{-3}$ (for high-Z elements this limit might be at much higher densities as the transition probabilities scale with Z^4), all processes which involve electron collisions happen more frequently than radiative processes. The dominant populating processes and depopulating processes are proportional to the electron density and therefore $\epsilon_{i,k}$ is approximately independent of electron density. The plasma discharges in tokamaks exhibit electron densities in the domain in between the above considered regions up to few $1 \cdot 10^{20}\,\mathrm{m}^{-3}$. In the range $1 \cdot 10^{18}\,\mathrm{m}^{-3} \leq n_e \leq 1 \cdot 10^{23}\,\mathrm{m}^{-3}$ all important populating processes need to

be considered in a system of differential equations, which also contains all states of an ion or atom that influence the population of the considered state. The results of such a collisional-radiative model are represented by a photon emissivity coefficient (PEC) as shown in equation 2.18,

$$PEC(T_e, n_e) = \frac{\epsilon}{n_e n_z} \tag{2.18}$$

where n_z equals the density of the considered charge state. More details on the calculation of PECs are given in section 2.3.2. For many applications in a tokamak when just coarse evaluations are needed, the corona equilibrium is sufficient and the large effort of the collisional-radiative modeling may be omitted.

In table 2.1 some processes are presented which are responsible for ionization and recombination. Similar to the population equilibrium within a certain charge state the electron density also influences the relative importance of these processes. The equilibrium for low electron density is called 'corona equilibrium' and considers electron impact ionization and radiative recombination. For high densities the Saha-equation describes the equilibrium, which is governed by electron impact ionization and three body recombination. For the electron density regime, which applies for tokamaks a detailed consideration of all processes in a collisional-radiative model is necessary to obtain the ionization and recombination rates. Crucial roles are played by the two processes of excitation-autoionization and dielectric recombination. Here resonances occur, which makes their evaluation more challenging. Additionally, the processes happen in two steps which complicates the situation. More details on ionization and recombination is given in sections 2.3.3, 2.3.4 and 4.2.

2.2 Electron Impact Calculation Methods

In section 2.1.4 it is stated that the knowledge of all important processes is necessary to make predictions on spectral lines emitted in a tokamak. While the Einstein coefficients $A_{i,k}$ for high-Z elements are obtainable by various atomic codes, even by full relativistic codes like GRASP [24], a major limitation has been the calculation of cross sections of electron impact excitation and ionization. In this chapter four methods are introduced that span from low to high quality and from high to low availability due to the increasing complexity of the calculations. The main focus of the present work lies on the multi-configuration method with plane wave Born-approximation, as this method is a large improvement in comparison to the average ion model, and allows for automated calculations of nearly all states of tungsten and other high-Z elements. Additionally, some other calculation methods for electron impact cross section are introduced in this section. It may be noted that apart from the described method other

methods exist, like convergent close coupling or time dependent Schrödinger equation calculations, that produce data of highest quality but are even less applicable to high-Z elements on a large scale due to their excessive computing requirements.

2.2.1 Average Ion Model

The average ion model [25] does not calculate any cross sections, however, it is able to predict the total radiated power of an impurity. The model introduced in [25] makes use of scaling laws and formulas which are applied for an averaged ion. The distribution of electrons into the shells and their energies are constructed according to general quantum mechanical findings. However, no quantum mechanical calculations on the actual ion are performed. Therefore, the data could easily be obtained for arbitrary elements, but spectral information is missing. Especially, processes which involve resonances are expected to exhibit low quality, but on average the discrepancies can cancel and bulk parameters like the cooling factor may exhibit deviations of factor 2 –3 only. The cooling factor of [25] was updated in 1995 [26, 27] for electron temperatures below 5 keV. The data set, which is used in this work is a combination of both data sets using the new data below 5 keV and the data of [25] above.

2.2.2 Plane Wave Born-Approximation

The ADAS project [15, 16] has recently incorporated the Cowan code [14] to evaluate cross sections of electron collisions with atoms and ions. The emphasis is put on highly charged species, as the calculation of near neutral ions needs adjustments, which are difficult to perform in an automated manner. The automation is necessary to cope with the large number of ion states, which sometimes contain thousands of important electronic states. For each ion, first the electronic structure is evaluated using the multiconfigurational Hartree-Fock code with relativistic corrections, i.e. the the Cowan code. The structure information is further used in the calculations for cross sections of electron collisions. In detail, the scattered electrons are modeled as plane-waves that are scattered by the bound electrons. An incoming electron with a wavefunction $e^{ik\cdot r}$ transfers momentum and energy by a inelastic scattering process onto the atom or ion and is leaving the scattering region being described by a wavefunction $e^{ik'\cdot r}$. The negative transferred momentum is obtained from K= k′-k and the transferred energy equals $\Delta E = \frac{\hbar}{2m_e}(\mathrm{k}^2\text{-}\mathrm{k}'^2)$. The detailed evaluation of the cross sections is described in [14] and references therein. It may be noted that spin transitions during electron collisions are not possible in this model as the scattered electron is always separately treated and an exchange with bound electrons is not possible. However, for high-Z elements, where the quantum number spin is not preserved anyhow this insufficiency

may be noticeable only for special cases. Best accuracy is attributed to the plane-wave Born method for high electron energies compared to ΔE, where resonant processes and large scattering angles are less important.

2.2.3 Distorted Wave Approximation

In this thesis comparisons with calculations of the HULLAC [28–31] and RATIP [32, 33] code packages are presented. Along with codes that calculate the atomic structure in fully relativistic manner HULLAC and RATIP contain distorted wave codes that evaluate the cross sections for electron excitation. The distorted wave approximation allows for the scattered electron being perturbed by the potential and to interact with the bound states such that spin transitions are possible. The results for cross sections are more accurate than those resulting from plane-wave Born approach due to the more realistic model. The scattered electron is described by an expansion of numerous partial waves, which is one reason why this approach is more intense in computing time. HULLAC is developed for obtaining numerous excitation rates of many spectral lines belonging to an ionization state. However, the calculations are more time consuming and hence less flexible compared the plane-wave Born approach. Additionally, as the HULLAC code is not freely available the flexibility is further restricted.

2.2.4 R-Matrix Calculation

Even higher quality is possible for low energies, when the resonances of the N+1 electron system, i.e. the N-electron target plus the scattered electron are considered properly. This is not possible with all of the above codes, but the R-matrix [34] with pseudo states approach (RMPS) can handle this. In this scheme the configuration space is partitioned into two regions by a sphere of radius r=a. a is chosen such that all bound states and pseudo states, i.e. continuum states that are treated similar to bound states, of the target are contained in the sphere. Outside the sphere the behavior of the scattered electron can easily be treated. Inside the sphere a N+1 electron system is considered and the energies of this system allow to find all resonances in the scattering process. These are of importance for electrons with energies comparable to the excitation or ionization energy. In a plasma the resonances are not always of large importance, when the population of excited states are investigated, because a large contribution of the excitation processes is caused by scattering processes with small scattering angles, which are described reasonable well also by the plane-wave Born approach. The RMPS method is very intense in computing time and therefore, it is feasible for certain ion states of high-Z elements only.

2.3 Calculation of Data within this Work

The main focus of this thesis lies on the data which are calculated by the Cowan code. These contain structure information of ions and electron impact rates. Other codes in ADAS utilize this information on various quality levels. The detailed interpretation of the Cowan code data is obtained by the ADAS code '208', which results in PECs for spectral lines. A bulk interpretation (ADAS codes '407/408') of the Cowan code data enables the derivation of ionization and recombination rates, data on continuum radiation and data on total radiation of an ion state. The procedures are described in this chapter, more details are available in the ADAS documentation [15, 16] and in [35]. In this work the superior 'Case B' implementation of the codes '407/408' is used.

2.3.1 Ionization Potentials

The ionization potentials are needed for the parameterization of ionization and recombination data. A set of ionization potentials from [36] is used by default. Nevertheless, a better accuracy of data could be achieved by employing the fully relativistic code GRASP [24]. A comparison of the two data sets along with the data from the HULLAC code is featured in figure 2.1. Due to the GRASP code restricting the maximum number of electrons in orbitals with $l \geq 2$ the GRASP calculations could be performed only down to Cd-like W^{26+}. The deviations between HULLAC, GRASP and [36] are negligible for the baseline quality calculations of high-Z elements, however, for the high precision investigations performed at the EBIT (cf. section 5.1, 6.2.1 and 6.3.1) the differences between the HULLAC/GRASP data and data of [36] do matter as they approach 10 % for the Ni-like W^{46+} and the states above.

2.3.2 Structure, Collision Strengths and Line Intensities

The main focus of this work lies on the characterization and validation of the ADAS data, which are obtained via the Cowan code. The code is used to obtain the energy levels and transition probabilities for electric dipole, electric quadrupole and magnetic dipole transitions, because these transitions are responsible for the main contributions of the radiative losses in a plasma. In certain cases the wavelengths of single transitions have been evaluated independently by the fully relativistic code GRASP [24]. The collision strengths (s. [15, 16]) are further evaluated with the Cowan code by realization of the plane-wave Born approximation. By performing a Maxwell-average the effective collision strengths are obtained (s. [15, 16]). A collisional-radiative model is then used to obtain the population of the states for a mesh of electron temperatures and densities. This results in a photon emissivity coefficient for each spectral line as a function of n_e

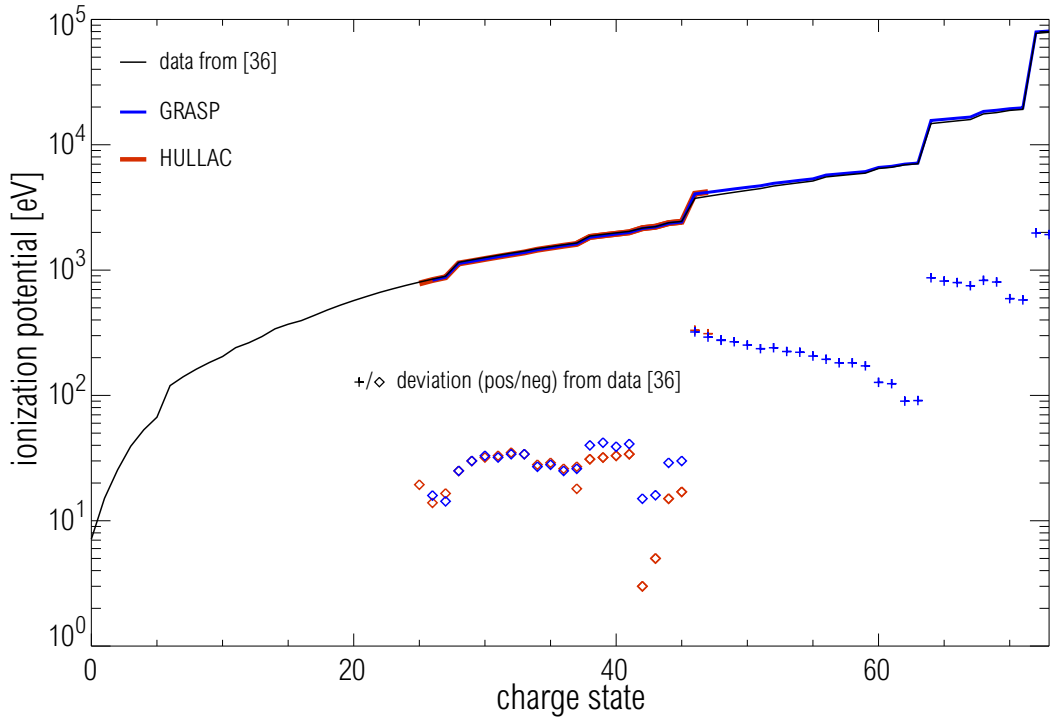

Figure 2.1: Ionization potentials of all tungsten ions from [36], values for In-like W^{25+} to Co-like W^{47+} from HULLAC and values for Cd-like W^{26+} to H-like W^{73+} from GRASP. Symbols indicate the difference between the values from [36] and GRASP/HULLAC.

and T_e.

A peculiarity of high-Z elements is the vast number of spectral lines that some of the ionization states emit. To handle the lines efficiently the feature photon emissivity coefficient (FPEC) was introduced within the ADAS environment, which allows to sum the PECs of many lines in a small wavelength region. A whole wavelength range can be covered by these small bins emulating the finite resolution of a spectrometer system. In Figure 2.2 the FPEC for Ni-like W^{46+} in the soft X-ray range is presented for the electron density $6 \cdot 10^{19}\,\mathrm{m}^{-3}$. When investigating the detailed spectra of tungsten this simplification is not necessary, however, it is a powerful tool to reduce the data detail for real time analysis.

It turns out (cf. chapter 8) that the total line radiation is dominating the total radiative losses caused by tungsten in a fusion plasma. In contrast to the average ion model the detailed information of quantum states, cross sections for excitation and the distribution versus wavelength is known for the emissions. This higher quality data can be tested in well diagnosed fusion plasmas by comparing the absolute power of spectral emissions to spectrometer measurements. Additionally, the measurement of the soft X-ray cameras (s. section 3.1.2) can be interpreted as it is known which part of the total radiated power is shielded by the Be filters (cf. figure 3.2).

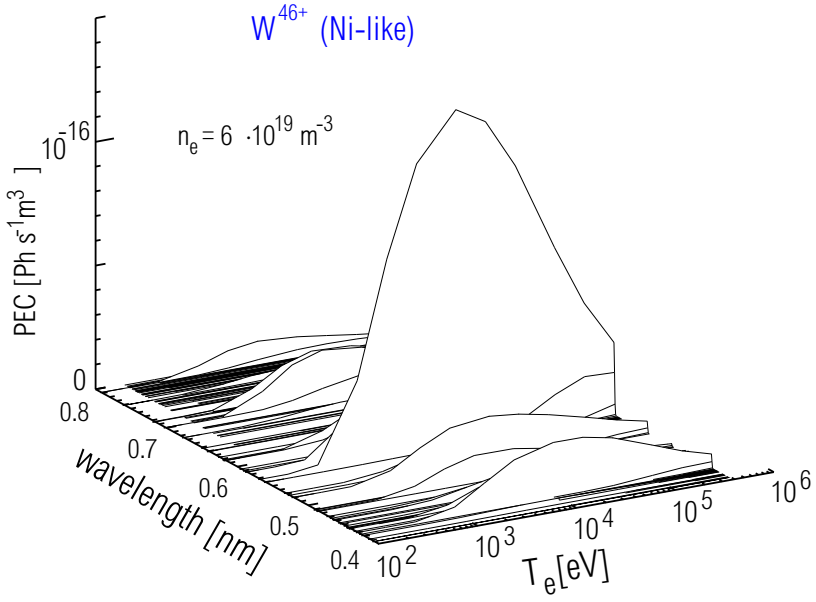

Figure 2.2: FPEC of Ni-like W^{46+} in the soft X-ray range for a electron density $6 \cdot 10^{19}\,\mathrm{m}^{-3}$. Featured is the FPEC with 1024 bins, but in principle also much fewer bins are possible to overview the emissivity distribution.

2.3.3 Ionization Rate Coefficients

The ionization rate coefficients are obtained by different methods. The ADAS codes '407/408' implement two semi-empirical methods. 'Case A' implements the semi-empirical parameter form of [37], which neglects excitation-autoionization. Its quality is better than the unmodified ADPAK data [25], which rely on the average ion model, because a more detailed ion structure, i.e. the results of the Cowan code, is entering the parameter form. However, as excitation-autoionization is of importance the 'Case B' implementation of ADAS is considered for comparisons to experimental data. Here the semi-empirical expression of [38] is implemented considering direct ionization and excitation-autoionization. The parameter form uses the results of ion structure calculations from the Cowan code. The data offers baseline quality, as the model is semi-empirical considering few details of the ion structure only. The details of the implementation can be reviewed in [15, 16, 35]. In the following chapters these data are referred to as '408' data. In the case of tungsten, a third set of ionization data originate from [39], where corrections, which emulate excitation-autoionization, were applied to the ADPAK data. Recently, an additional set of data became available [40] for tungsten, which determines the ionization coefficient by calculations of cross sections in a configuration average manner using a distorted wave method (CADW). The method is described in [41] for krypton. The quality of this calculation is clearly superior to the baseline data.

2.3.4 Recombination Rate Coefficients

Quantum mechanical calculations on recombination are not possible without knowledge of the important recombination channels. These are difficult to predict and a large range of principal quantum numbers and angular momenta may be of importance. Especially for high-Z elements this means that semi-empirical formulae are necessary to evaluate the recombination rates. This is done independently for radiative and dielectronic recombination, as for the latter the branching ratios between autoionization and radiative stabilization need to be considered. Due to the effect of finite electron density an upper limit on the principal quantum number exists, which needs to be considered for the recombination processes. The radiative recombinations are calculated by generalizing data of hydrogen, while rates for dielectronic recombination are obtained by the general formula of Burgess [42] ('Case A') or by using the Burgess-Bethe general program (BBGP) (cf. [43]) employing the dipole resonances of the receiving ion ('Case B'). The details of the formulas used can be reviewed in [15, 16, 35]. The ion structure information entering into these formulas are obtained via the Cowan code.

2.3.5 Continuum Radiation

Three contributions are considered, i.e. radiative and dielectronic recombination and Bremsstrahlung. For each radiative recombination event it is assumed that the ionization energy of the recombined ion is emitted. For dielectronic recombination the dipole transition energies of the receiving ion that were used for estimating the resonances in section 2.3.4 and the ionization energy of the recombined ion is emitted. For Bremsstrahlung the hydrogenic free-free formula with unity gaunt factor is used. Again, the details of the formulas used can be reviewed in [15, 16, 35].

2.3.6 Parameterisation of Total Line Radiation

Unlike the detailed collisional-radiative modeling which is performed to obtain emissivities of single spectral lines, it is possible to estimate the total radiation by a zero-density estimation. In this approximation, any excitation from the ground state will result in emission of photons accounting for the excitation energy. The results of the Cowan code calculations are used to obtain the rates for excitation into the considered states. Multiplied with the excitation energy this equals directly the radiated power for this simple model.

Chapter 3

Diagnostics and Experiments at ASDEX Upgrade

At ASDEX Upgrade several spectrometers and radiation diagnostics are available. In the following, the term 'diagnostic' is used also for spectrometers. The wavelength region from 0.1 –100 nm is of special interest for this work, as in this wavelength region the most intense emissions of the hot main plasma originate. Each diagnostic is monitoring a certain wavelength interval as indicated in figure 3.1. In this chapter, the diagnostics which are used for the analyses are introduced.

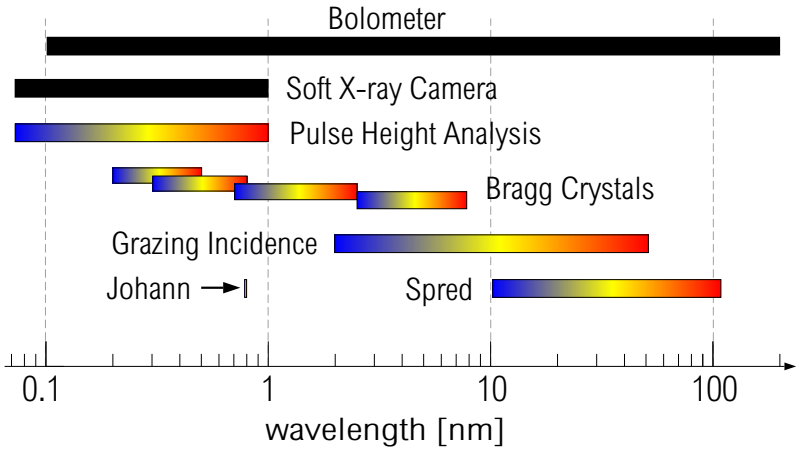

Figure 3.1: Overview of wavelength regions that can be monitored by spectrometers and radiation detectors. The black bars denote the detection range for diagnostics without energy resolution, while the color-shaded bars represent the wavelength range of diagnostics with energy resolution.

3.1 Diagnostics for Integrated Radiation

3.1.1 Bolometer

The bolometer is detecting the radiated power along about 100 lines of sight (LOS). The detector itself consists of a thin metal foil that is heated up by the absorbed radiation. The temperature rise measured by the change in resistance is divided by the thermal capacity to derive the total radiated power. The response of this detector is flat over a large wavelength range. The large number of LOSs is necessary for obtaining spatially resolved information by tomography. However, the detection principle limits the time resolution to ms due to the finite heat capacity of the metal film.

3.1.2 Soft X-ray Cameras

Soft X-ray cameras (SXR-diagnostic, s. [44]) are semiconductor detectors that equipped by Be-filters with a certain thickness d_f. At each photon energy the transmittance of the Beryllium (Be) is $\propto e^{\frac{-d_f}{\kappa_{Be}(h\nu)}}$, where $\kappa_{Be}(h\nu)$ is characteristic for Be and varies for different photon energy $h\nu$. Similarly the absorption of photons in the active layer of the silicon detector increases with its thickness d_d being $\propto 1 - e^{\frac{-d_d}{\kappa_{Si}(h\nu)}}$. In figure 3.2 resulting detection efficiencies for combinations of Be-filters and Si detectors are presented. The measured signal is proportional to the energy of the detected photons. However, an absolute calibration is not easily obtained, because for this the distribution of power in front of the Be-filter needs to be known. Spatially resolved information is obtained by SXR-diagnostic due to the about 60 LOSs. It is well suited to investigate dynamical processes on a timescale of μs.

3.2 Spectrometers

In the present work the details of the energy distribution of emitted photons are investigated. In this section the available spectrometers are introduced and grouped according to their observed wavelength range.

3.2.1 Vacuum Ultra Violet (VUV)

The VUV range owes its name from the fact that the radiation is easily absorbed by the atmosphere, which is avoided by evacuating the spectrometer and connecting it directly to the plasma vacuum. Furthermore, the detectors used at ASDEX Upgrade rely on open microchannel-plates (MCPs), which require low pressure of less than

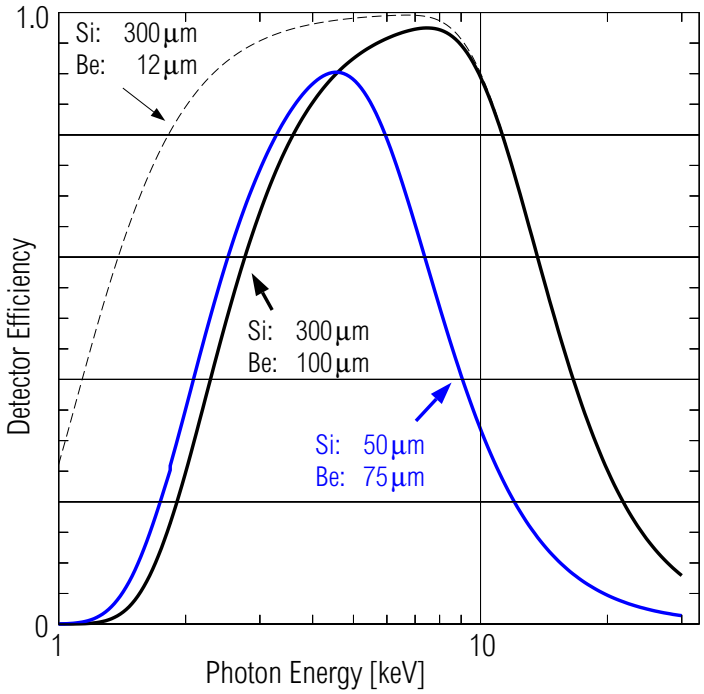

Figure 3.2: Detector efficiencies for 3 configurations of SXR-cameras at ASDEX Upgrade

$1{\cdot}10^{-6}$mbar for protection.

SPRED

The so called SPRED spectrometer (survey, poor resolution, extended domain) [45] was used as a monitor for the wavelength region 10 –105 nm with a relatively low resolution of $\Delta\lambda \approx 0.3$ nm. The detection is accomplished by an open microchannel-plate MCP, which converts the photons into electrons which are multiplied in the microchannels. A phosphor screen converts the electrons into fluorescence photons which are detected by a programmable CCD camera of the company PROSCAN [46]. Time resolutions of about 10 ms are typical. An absolute calibration has been performed earlier [47] via the branching ratio of spectral lines, which are emitted in the visible spectral range and in the VUV.

Grazing Incidence

A major experimental tool for this work is the 2.2 m grazing incidence spectrometer manufactured by McPherson [48]. A detailed description of it is available in [49]. Measurements were obtained in the VUV-region from 2 –50 nm. The detection principle works similar to the SPRED spectrometer, while instead of a CCD camera a diode array is used. The wavelength calibration was refined several times so that from 4 –14 nm

an uncertainty of only 0.005 nm could be achieved. This was obtained by frequent *in situ* calibrations using the H-like and He-like spectral lines of boron, carbon and oxygen that are visible at the beginning of nearly every plasma discharge. An absolute calibration in this wavelength range was performed which is described in section 3.5.2. As featured in figure 3.3, the grazing incidence spectrometer has a variable LOS that

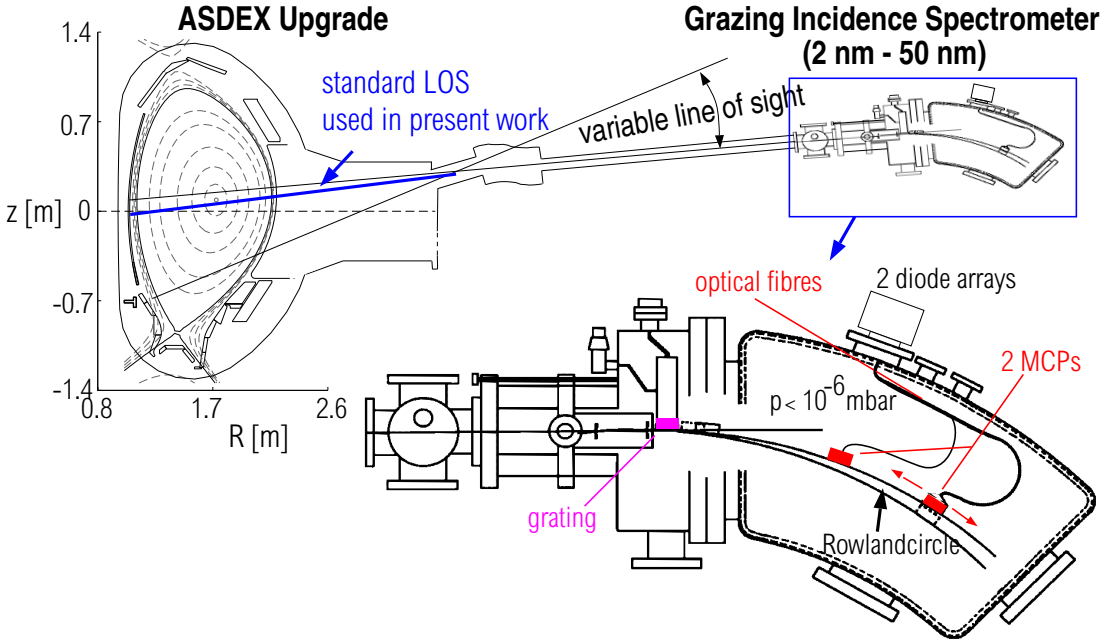

Figure 3.3: Setup of the grazing incidence spectrometer at ASDEX Upgrade. The upper and lower limit of the variable line of sight is indicated. The default setting, which is used in this work, is indicated with the blue line. In the grazing incidence spectrometer, 2 MCPs are located at different positions of the same optical axis. The fluorescence light of the phosphor layer attached to the MCPs is transported to the diode arrays via optical fibres.

can be changed in between plasma discharges.

3.2.2 Soft X-ray spectral range

The photons in this wavelength range (0.1 –2 nm) allow to use thin filters and window foils that absorb only a small fraction of the photons. This fact gives the possibility to separate the vacuum of the plasma discharge from the detector or from the whole spectrometer, which is desired for devices in which tritium is part of the plasma. The spectrometers at ASDEX Upgrade use crystals as dispersive elements in reflective geometry. Reflexion occurs only if the incident angle ϑ measured towards the crystal surface equals the reflecting angle and if the wavelength of the incident radiation fulfills the Bragg-equation (3.1) for a k called the 'order' of reflexion. d denotes the lattice

spacing of the crystal. ϑ is called 'Bragg angle'.

$$k\lambda = 2d\sin\vartheta \tag{3.1}$$

For the spectrometers in this spectral range a central LOS was chosen, as the most intense emissions in this spectral range emerge from the hot plasma center.

Bragg Scanning Crystal Spectrometer

2 Bragg-crystal spectrometer (cf. figure 3.4) sharing a single spectrometer housing are available at ASDEX Upgrade. They are using a flat crystal which is rotated during a plasma discharge for monitoring a wavelength interval. Before the incident light can be

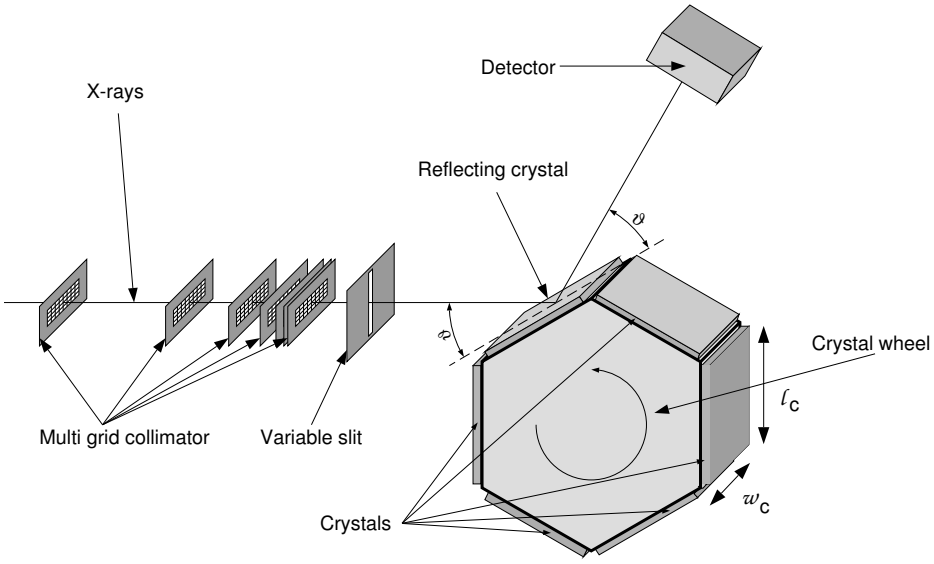

Figure 3.4: Scheme of the Bragg-crystal spectrometer. The multi grid collimator is providing collimated light, that is analyzed with a flat crystal. The angle ϑ is scanned several times during a plasma discharge between certain limits, while the detector is moving such that the incident and reflecting angle of the light are equal. The variable slit is used to attenuate the incident light. The reflecting crystal can be exchanged in between plasma discharges by rotating the crystal wheel which provides six crystals with different lattice spacings d.

analyzed by the Bragg-crystal spectrometer the light needs to be collimated to obtain wavelength resolution. This achieved by a multi grid collimator [50] installed in the spectrometer's LOS. A slit with a height of 50 mm and a variable width of $0-40$ mm is installed directly behind the collimator allowing for an adjustable attenuation. The direction of the incident light is fixed by the LOS of the spectrometer. The rotation of the crystal is constantly changing the incident angle ϑ, while the detector has to be moved simultaneously by the doubled angular velocity such that the reflected angle which needs to equal the incident angle is aligned with the detector. Its sensitive area is $30 \times 40\,\mathrm{mm}^2$ and is optimized to detect all the reflected photons also in the case of

Nr.	System A, α_{div}= ±0.55 mrad			System B, α_{div}= ±1.11 mrad		
	Crystal	2d (nm)	measurement range (nm)	Crystal	2d (nm)	measurement range (nm)
1	Topaz (303)	0.2712	0.047 - 0.270	Topaz (303)	0.2712	0.047 - 0.270
2	Silicon (111)	0.6271	0.109 - 0.625	Silicon (111)	0.6271	0.109 - 0.625
3	ADP (101)	1.0640	0.185 - 1.061	ADP (101)	1.0640	0.185 - 1.061
4	KAP (100)	2.6579	0.460 - 2.647	KAP (100)	26.579	4.60 - 26.47
5	Lead stearate	10.04	1.70 - 10.00	Lead stearate	10.04	1.70 - 10.00
6	Multilayer	9.65	1.68 - 9.61	LiF (220)	0.2848	0.047 - 0.280

Table 3.1: Available crystals for both Bragg crystal spectrometers at ASDEX Upgrade. The wavelength range for all crystals is given for Bragg angles ϑ between 9° and 80°. α_{div} denotes the vertical divergence angle of the incident photons, which is achieved by a separate collimator for each system.

small excursions of the detector from the optimal position. An important property of the crystal is the lattice spacing d which determines the wavelength interval that can be analyzed. To maximize the flexibility of the spectrometers 6 crystals (cf. table 3.1) are provided with different d that can be interchanged in between plasma discharges by rotating the crystal wheel (cf. figure 3.4). The dimensions of the crystals are 100 $\times$ 50 mm^2.

The detector is a multi strip gaseous chamber (MSGC) [51] which allows single photon counting at count rates of up to 1 – 2 MHz. Photons from the spectrometer volume enter the detector through a ≈2 μm thick Mylar foil covered by a 80 nm thick aluminum layer that shields the detector from low energy stray light and acts as a cathode. The foil also seals the detector volume with atmospheric pressure from the vacuum of the spectrometer. To ensure a constant detector performance the detector gas (83.25 % Ar, 9.25 % methane and 7.5 % butane) is kept continously flowing through the counter. The detection volume is ≈ 9 mm thick allowing for detection of photons up to 15 keV photon energy. To correct for background signals due to neutron irradiation a second MSGC shielded from the incident photons is available in each detector. A calibration of this background correction is performed with closed spectrometer slit during plasma discharges with high neutron rates.

This setup gives spectral resolutions of $\Delta\lambda/\lambda$ = 100 – 2000 depending on the used crystal. The wavelength calibration can be performed *in situ* for almost every discharge, as well-known H-like or He-like emission lines of intrinsic impurities are visible. Although photons are counted, an absolute calibration is necessary, as the reflection efficiency of the crystals, the transmittance of the aluminum coated mylar foil and

the counter efficiency need to be determined for the actual system. A calibration was performed already earlier [52] which was refined in the course of this work (cf. section 3.5.1). More details on the spectrometers are available in [52].

Johann-Spectrometer

The principle of the Johann-spectrometer [53] uses a bent crystal where the curvature radius R is defining the Rowland circle with radius R/2 (cf. figure 3.5). This setup allows to collect light from a homogeneous light source like the tokamak discharges at ASDEX Upgrade and record high resolution spectra. However, this is limited by the fact, that the arrangement does not offer a perfect focus due to the same curvature of the crystal lattice, which fixes the Rowland circle, and the crystal surface, which determines the focus. For small crystals, i.e. small apertures of the optical system, the approximation that A≈A′ and C≈C′ is good enough, however, the systematical shift at the detector to lower wavelengths gets apparent at a certain crystal size. This is suppressed by the Johansson-setup (cf. [54]), where the bent crystal is ground until its curvature is identical to that of the Rowland circle, while the crystal's lattice is still curved with radius R.

With the Johann-setup the maximum achievable resolution is given by

$$\frac{\lambda}{\Delta\lambda} = 32(\frac{R}{s})^2 tan^2\vartheta \tag{3.2}$$

with the crystal length s and Bragg angle ϑ.

For the Johann-spectrometer at ASDEX Upgrade R = 1.5 m. The resolution $\lambda/\Delta\lambda$ varies between 1000-4000 depending on the geometry (cf. equation 3.2), the properties of crystal and detector.

For this work the spectrometer was used as a monitor for the spectral line of Ni-like tungsten at 0.793 nm. An EDDT crystal was used with 2d = 0.8808 nm. The resolution $\lambda/\Delta\lambda$ is about 1000 and is not limited by the effects that enter in equation 3.2, but by imperfections of the layer structure of the crystal. The detector is using a closed MCP: The soft x-ray photons cause fluorescence of a phosphor layer which is in the vacuum. The visible photons are transmitted through a vacuum window and then detected by an intensified programmable CCD camera manufactured by the company PROSCAN [46]. The intensifier uses a closed MCP for multiplying single photo-electrons that emerge from the coating at the front of the MCP. The multiplied electrons are then made visible by another phosphor layer directly in front of the CCD chip.

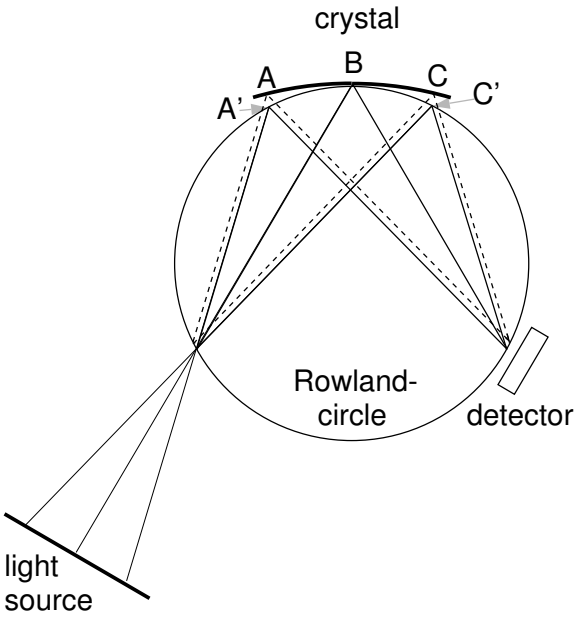

Figure 3.5: Scheme of a Johann-spectrometer and its Rowland circle. Also featured are the deviations of the focus that arise due to the fact that the curvature of the Rowland circle is not equal to the curvature of the crystal surface.

3.2.3 Pulse Height Analysis

The heart of the diagnostic called 'pulse height analysis' is a semiconductor detector that is shielded from low-energy photons by a beryllium foil of adjustable thickness. A variable blind attenuates the X-ray intensity from the plasma discharge. Each individual photon creates a number of electron-hole pairs in the detector, which is proportional to the photon's energy. The number of electron-hole pairs determines the size of the current pulse, which is read out from the detector. As the size of the pulses is recorded a spectrum is obtained from about 1 keV to 15 keV photon energy with moderate resolution of about 300 eV. The line of sight is identical to that of the Bragg-crystal spectrometer . A detailed description is available in [55].

3.3 Impurity Injection

Impurities are usually unwanted in a fusion plasma, but a contamination of the plasmas is unavoidable. For this reason, the emissions, the transport and the effects of impurities need to be studied in today's experiments. To do this, impurities are injected on purpose via various systems namely pellet injection, laser ablation, probe erosion and gas puffing. For this work, gas puffing and laser ablation are used.

For gaseous impurities, i.e. xenon in this work, it is easiest to just puff the gas into

the plasma chamber. The gas is ionized at the edge of the plasma by collisions with hot electrons. Some of the impurity ions then enter the main plasma due to the transport effects in the plasma. The various transport effects can be modeled by diffusion and drifts. Even though the injection is fairly simple it is complicated to obtain a constant impurity level in the plasma, as the impurity may recycle differently than the majority of the plasma ions. For xenon a nearly constant concentration could be achieved by a specially designed puffing trajectory that is decreasing in time.

Solid impurities may be injected at ASDEX Upgrade by laser-ablation (cf. [56–58] for further reference on laser-ablation in general) via the laser blow-off system. It consists of a 0.6 J Nd-YAG laser with pulse length 8 ns and wavelength 1064 nm. The infrared light exhibits a lower ablation efficiency than light in the visible or UV, but a smaller fraction of the ablated particles is charged [58]. Charged ions penetrate into the plasma with low efficiency, as the strong magnetic field that confines the plasma prevents that. The used laser features a maximum repetition rate of 20 Hz. The laser pulse is defocused before it is transmitted through a vacuum window and then focused on the targets which are placed at a distance of about 50 cm from the plasma edge. By moving the focusing lens, which is situated just outside the vacuum, it is possible to adjust the focus in the plane of the target, while the laser is simultaneously fired with a certain repetition rate. This procedure permits that throughout a discharge impurities can be constantly injected. In the case of 20 Hz laser-ablation rate the impurities are fueling the plasma center quasi-continuously as the typical particle transport time there is of the order of 100 ms.

Four targets are clamped onto the target holder at the same time. The targets are mostly made from thin metal films that are evaporated onto thin glass plates of size 50×50 mm^2. During ablation, the laser is transmitted through the glass and then absorbed by the impurities, which are situated on the plasma-facing side of the glass. Impurities for which the evaporation process does not produce ablatable targets need to be specially processed. For instance, the gold films that are produced via evaporation are reflecting the laser power very efficiently, such that ablation is not possible. However, when gold is precipitated from a solution it forms small unevenly structures that appear black. After grinding, the resulting black powder is glued onto the glass target and can easily be ablated. The magnitude of the impurity injection needs to be carefully adjusted. On the one hand a higher impurity concentration produces more signal, but on the other hand a too large impurity concentration disturbs the plasma leading to a change in plasma parameters.

3.4 Intrinsic Impurities

Since 1993, the W-experiment is pursued at ASDEX Upgrade (s. appendix B.1). In the course of this activity the graphite first wall of the tokamak is stepwise exchanged for tungsten coated surfaces. An extensive overview of the W-programme at ASDEX Upgrade can be found in [13]. 1993 –1996 the W-divertor experiment was performed, which lead to operation with a full tungsten divertor in the campaign 1995/1996 [59–62]. After successful demonstration of the low impact of tungsten divertor sources on the tungsten concentration of the main plasma, the divertor was replaced by a carbon divertor. In 1999, the tungsten programme for the main chamber was initiated, which aims for eliminating all carbon by coating the plasma facing components with tungsten. The graphite tiles of the heatshield have been replaced stepwise by tungsten coated tiles [63]. In the recent campaign, i.e. 2004/2005, about 70 % of the total plasma facing surfaces are coated with tungsten [12]. In the next two years a completion up to 100 % is planned. The tungsten concentration has been growing steadily corresponding to the increasing area of tungsten surfaces, but is usually below the range of few 10^{-5}. The spectrum of tungsten could be studied in numerous discharges.

Even though the area of carbon surfaces was decreased, the carbon concentration is nearly unchanged of the order of 1 %. This is in agreement with investigations on carbon sources [64–66] which demonstrate that only a small part of carbon that is found in the plasma originates directly from a carbon surface. A large part of the carbon atoms/ions seem to recycle at the walls regardless what material the wall is made of [64, 66].

Boron is used for conditioning the wall of ASDEX Upgrade. At the plasma startup, the strong resonance spectral lines of H-like and He-like boron can be observed with the grazing incidence spectrometer, which made frequent in-situ wavelength calibrations possible. The spectral lines are emitted at electron temperatures below 500 eV.

Spurious amounts of fluorine, neon, silicon, sulfur, chlorine and argon can be detected frequently via the H-like and He-like resonance lines in the soft X-ray range. The occurrence of these spectral lines allows to perform a wavelength calibration of the Bragg scanning crystal spectrometer.

3.5 Intensity Calibration

3.5.1 Bragg Scanning Crystal Spectrometer

The MSGC counter is detecting single photons. Therefore, it is possible to calculate the radiance of spectral lines by considering the reflectivity of the crystal, the geometry

of the setup, the transmission of the detector window and the absorption within the detector gas. Figure 3.6 gives the sensitivity curve of the system A for the the three considered crystals and a slit width of 20 mm. The calibration factors, which are resulting from the following investigations are already applied. Deviations from the

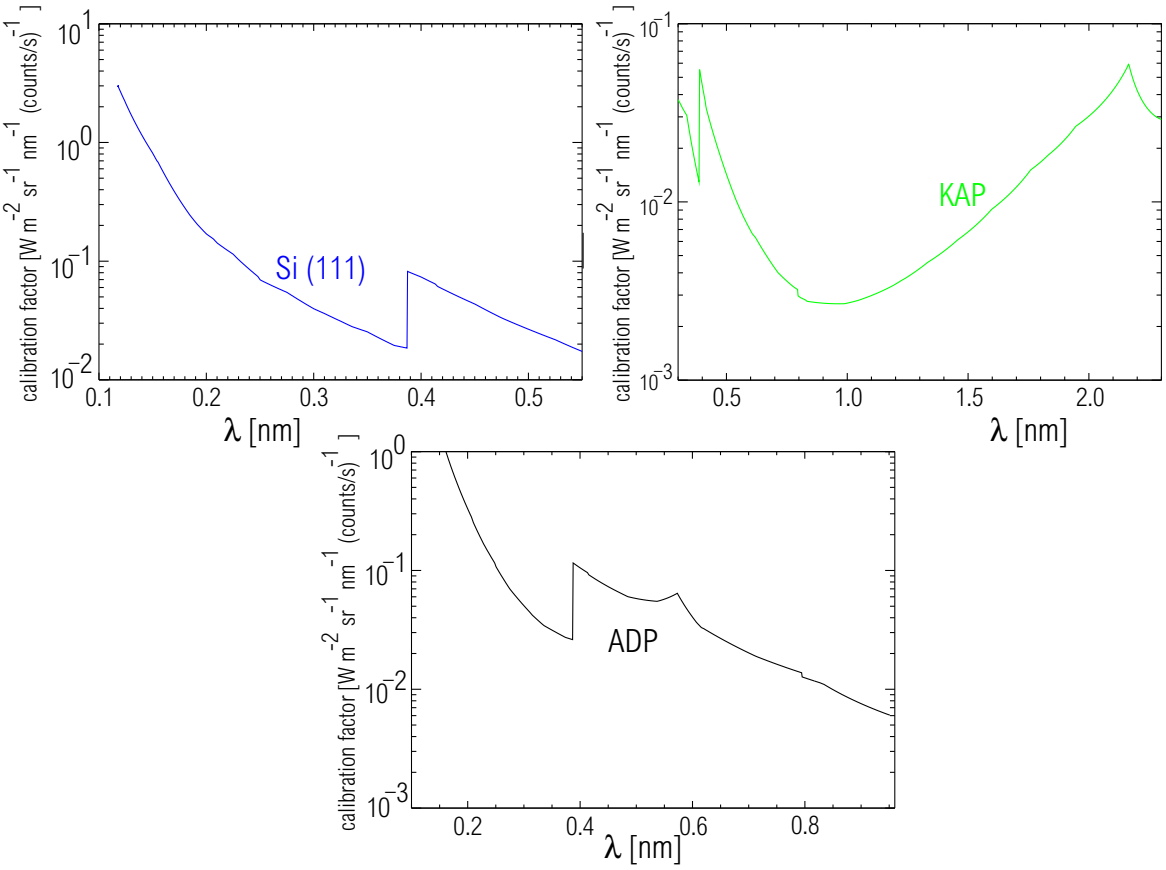

Figure 3.6: Total sensitivity of the system A using 20 mm slit width for the crystals Si(111), ADP and KAP. The geometry of collimator and spectrometer, the reflectivity of the KAP crystal at the Bragg angle, the transmission of the detector window and the absorption within the detector gas are taken into account. Additionally, a calibration factor was applied, which is constant for each crystal and results from the recent calibration.

ideal setup might influence the accuracy of such an calculation. For instance, the crystal reflectivity is given or calculated for ideal crystals and defects in the real crystal will generally lead to a deterioration of the reflectivity at the Bragg angle. However, an accuracy better than a factor of 3 is expected for the KAP and ADP crystals, as here cross calibrations with other diagnostics have been performed earlier to verify the predictions [52]. In the course of the present work two independent procedures where applied to update the calibration. These are elucidated in the following.

Calibration with Well Characterized X-ray Source

The main focus was put on the wavelength region 0.3 – 0.9 nm where the most prominent X-ray emissions of tungsten are observed. An X-ray tube with an homogeneous emission characteristics [55] was equipped stepwise with yttrium (Y), tin (Sn) and aluminum (Al) anodes, which were characterized with a pulse height analysis using a silicon-lithium drift detector in the laboratory. These spectra are dominated by lines of Y (L_α), Sn (L_α) and Al (K_α) at ≈ 0.64 nm, ≈ 0.36 nm and ≈ 0.83 nm, respectively. The well-known geometry and efficiencies of the laboratory setup allow for an absolute measurement of the emitted radiance analog to the investigations in [55].

The X-ray tube was then introduced into the LOS of the Bragg crystal spectrometer. Due to the low intensity of this source compared to typical plasma emissions the signal to noise ratio is critical for the accuracy of the calibration. Focus was put on the calibration of System B, which due to the larger collimator opening achieves more than a factor of 2 larger signals at the same source intensity. Relative calibration factors have been calculated that relate the calibration factors of new and old calibration. The relative calibration factors which were obtained by this direct method are shown in figure 3.7 as diamonds. The featured uncertainties are mainly caused by the spectrometer measurements due to the low signal to noise ratio and uncertainties of the X-ray source alignment and sum up to 40%, which is obtained by the uncertainties of the integration of the spectral line envelope and by variations of the spectrometer slit to check the X-ray source alignment. For the Al anode a systematic decrease of signal was observed during the spectrometer measurements. After venting the X-ray tube, the anode was covered by a thin layer which had formed during calibration possibly being the cause for the signal deterioration. An analysis of this measurement led to a systematical increase of the uncertainties towards lower ratios of calibration factors down to the 0.3-fold value of the measurement. This increase of uncertainty is estimated by an extrapolation of several consecutive measurements towards a virgin Al anode. For the ADP crystal, the actual results are nearly in agreement to the calibration presented in [52]. For the KAP crystal, the deviation of factor 7 is surprisingly large, however, the only available data point relies on the hampered measurements with the Al anode. The deviations for the Si crystal are even larger, while the experimental experience also suggests the validity of this data point. The theoretical predictions seem to be flawed. This is the case for both available data sets for the crystal reflectivity, i.e. the one from the computer code GID [67] used in [52] and the other from [68]). Further evidence for the shown discrepancies, which probably arises from a non-ideal crystal, is presented in the following. In a second step, comparisons between measurements during plasma operation are used to obtain information about the calibration factors.

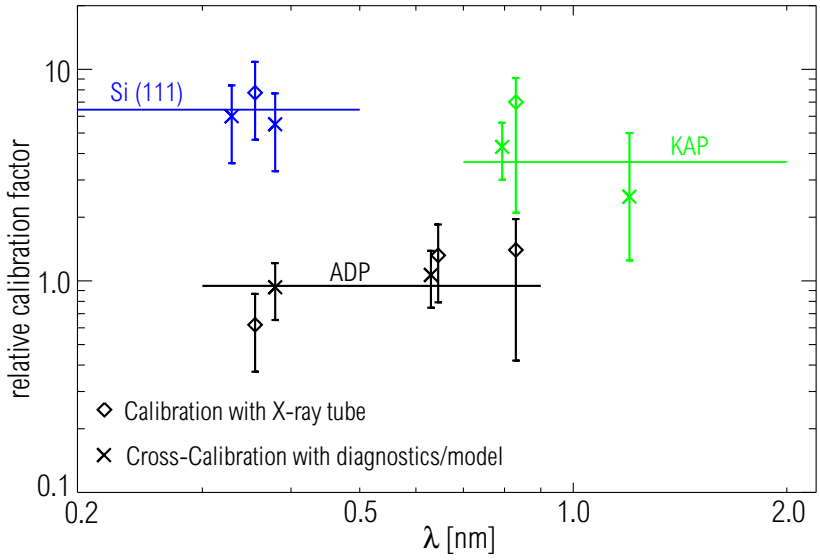

Figure 3.7: Relative calibration factors which relate the present calibration to that presented in [52]. Diamonds originated from the calibration with a characterized X-ray source, while crosses originate from comparisons to other diagnostics implementing model predictions. Horizontal lines indicate the finally used calibration factors which result as weighted mean of the data points.

Cross-Calibration with Other Diagnostics

System A and System B were compared in hundreds of discharges and the calibrations of both channels agree with each other for the ADP, KAP and the SI(111) crystal. Therefore, a relative factor between the ADP and the Si(111) crystal can be obtained from a discharge which exhibits spectral line at overlapping wavelengths. This is the case for discharges with argon injection. The H-like and He-like argon lines between 0.3 nm and 0.4 nm were recorded in the discharges #19197-19201 using ADP and Si (111) crystals on system A and B, respectively. A monitor of the He-like argon lines is available, since the Johann spectrometer is detecting routinely the second order reflection of the He-like argon lines. The relative comparison of both crystals gave two additional data points (crosses) in figure 3.7 for the Si (111) crystal. These underline the large factor in between the new calibration and the theoretical predictions, which was already diagnosed by the measurements with the X-ray tube.

The absolute emissivity of the spectral lines relates to the concentration of argon, which can be measured by the increase of total radiation caused by argon injection. The total radiation measurement is taken from the deconvolution of the bolometer signals (s. figure 3.8(a)) and the increase due to argon is diagnosed within 10 –20 % uncertainty. For comparison, the transport model STRAHL (s. chapter 4) was used to obtain a relation between total radiation (s. figure 3.8(b)) and the emissivities of H-like (0.374 nm) and He-like (around 0.397 nm) lines (s. figure 3.8(c)) which are integrated along the spectrometers LOS. STRAHL calculates the fractional abundance

of each impurity ionization state along the plasma radius and takes transport into account. The assumed transport coefficients are nearly without effect (less than 10 %) on the relation between radiation and argon density. The atomic data were taken from ADAS [16]. The predictions then were compared to the measured signal (s. figure 3.8(d)). The analysis of #17833 allowed for obtaining one calibration point for the ADP crystal around 0.385 nm to which an uncertainty of 30 % was attributed. The uncertainties of the theoretical data were assumed to be of the order of 10 %, as recent high accuracy data in ADAS were available from [35], and are included in the 30 % error bars presented in figure 3.7. Discharge #17833 was also used to recalibrate the SXR camera A (s. section 3.1.2), which had been calibrated in 1995 [69] and lost sensitivity due to neutron irradiation [70]. In discharges #17833 the SXR signal is dominated by the line radiation of H-like and He-like argon as is known from the atomic data interpreted with the sensitivity of the SXR cameras. To relate the spectrometer signal to the signal of the SXR camera the transmission of the Be filter incorporated in the SXR diagnostic has to be taken into account. The signal of the SXR system was found to be too low by a factor of 2.6, while the detector diodes have been renewed before the discharge #14049. This deterioration is plausible, as earlier investigations at ASDEX Upgrade [71] point towards similar deterioration after about 2000-3000 plasma discharges. Using the degradation factor of 2.6, a further cross calibration was performed in discharge #18060. Here the radiation in the soft X-ray range is dominated by the H-like and He-like lines of silicon as the tokamak walls had been conditioned by coating with silicon at that time. The recalibrated soft X-ray camera was now used and compared to the signal of the spectrometer, which resulted in an additional calibration data point at ≈ 0.63 nm (s. section 3.7) for the ADP crystal.

The tungsten line at 0.794 nm is routinely measured during the scans of both spectrometer channels A and B using the KAP and ADP crystals, respectively. The Johann spectrometer monitors the tungsten line. The calibration data point at 0.794 nm for the KAP crystal (s. figure 3.7) was obtained by comparing the signal of the Bragg spectrometer for ADP and KAP crystals to the signal of the Johann spectrometer the calibration data point at 0.794 nm (s. figure 3.7) The uncertainty reflects the scatter in the ratios between the the Bragg signals and the Johann signals.

To add another calibration point for the KAP crystal the H-like Ne line at 1.2 nm was analyzed for discharges #19313 and #19404 and related to the Ne concentrations derived from charge exchange measurements. This analysis introduces larger uncertainties than the above presented analysis on the H-like and He-like emissions of argon, since the H-like Ne exist at the edge region of the plasma which is also the location of a strong inward drift for plasma ions (s. [72]). Depending on the magnitude and radial profile of the drift velocity, which are difficult to diagnose, the Ne concentration in the

bulk plasma might be influenced by up to a factor of 5 (compared to a situation with no inward drift) while the radiance of the H-like spectral lines is nearly unchanged (s. [72, 73]). For the modeling a reasonable guess of this drift velocity was used, which is based on the investigations [72] and a factor of 2 was assumed as uncertainty of the modeling. The atomic data were taken from the ADAS database [16]. The resulting data point at 12 nm is shown in figure 3.7.

In general, the results of the cross-calibrations agree with the findings which originate from the calibration with the X-ray tube. The relative calibration factors are chosen to be a single factor for each crystal and are indicated in figure 3.7 as horizontal lines referring to the weighted mean of the data points for each crystal.

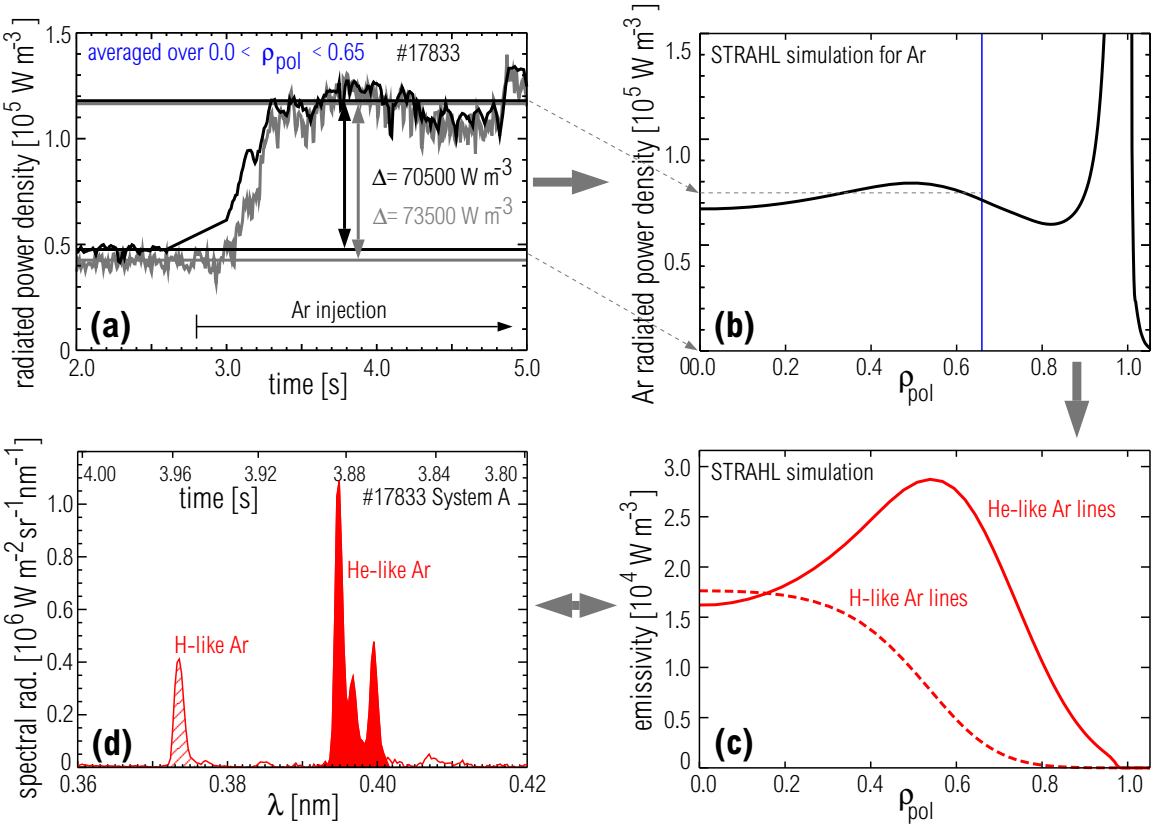

Figure 3.8: *(a)* Measured radiated power density averaged over radius $0 \leq \rho_{pol} \leq 0.65$ obtained by deconvolution of bolometer signals. The black line refers to a 2D-tomographic deconvolution, while the gray line was obtained by an alternative algorithm which assumes constant power density on a flux surface. Argon injection starts at 2.8 s. *(b)* Simulated total radiation caused by argon for an adjusted STRAHL simulation run (s. chapter 4); *(c)* Predicted emissivities for the H-like (at 0.374 nm) and He-like (around 0.397 nm) lines (both s. figure 3.8(d)) for the identical STRAHL simulation run using atomic data from ADAS; *(d)* Measured spectra of the Bragg spectrometer for the analyzed discharge.

3.5.2 Grazing Incidence

Similar to the latter calibration method which used the H-like Ne line, the H-like and He-like lines of boron and the He-like lines of carbon were compared to the central charge exchange measurements to obtain a calibration for the grazing incidence spectrometer. For discharge #19172 the modeling of carbon and boron was performed which employed the transport coefficients taken from [72] and atomic data from ADAS. The resulting calibration points are featured in figure 3.9 as diamonds and the presented uncertainties relate to the difficulty to model the relation of transport at the edge region to the central part of the plasma. A further calibration data point was obtained for a certain discharge type with so called impurity accumulation (s. description in chapter 5), where a small region with a narrow range of electron temperatures is emitting most of the radiation. A large fraction of this radiation is caused by tungsten as the transport effect that is responsible for the impurity accumulation increases with Z. About 90 % of the radiation caused by tungsten is emitted in the spectral feature at 5 nm called 'tungsten quasicontinuum'. It was assumed that 75 % of the radiation in the accumulation region, which is diagnosed well by the bolometer, is found in the quasicontinuum, which is monitored by the grazing incidence spectrometer. This dominance of tungsten for the central impurity radiation is based on the measurements on iron and copper densities, which are responsible for about 10% of the impurity radiation, and the general observation that light elements are only weakly influenced by impurity accumulation. The analysis for discharge #19436 leads to the data point for the calibration that is featured in figure 3.9 which agrees with the above calibration results. The corresponding error bars are estimated, including the uncertainties for the atomic data and the contributions of other spurious impurities in the accumulation region, which are not quantified. At 23.7 nm a comparison to the SPRED spectrometer is indicated in figure 3.9 with a square. The wavelength was chosen because the SPRED spectrometer was calibrated using the branching ratio between the Paschen-α line at 468.57 nm and the Lymann-γ line at 24.3 nm of He^+.

Along with the calibration points a relative sensitivity curve (solid line) for a channel electron multiplier (taken from [74]) is shown in figure 3.9. As an uncoated MCP consists of many of these channel electron multiplier the relative behaviour of the calibration curve versus wavelength applies here. The reflectance of the grating varies only slightly for different wavelengths because the angle of incidence equals only 2 ° (s. [75]). The reflectance into the first order is unknown for the considered grating, and it is assumed to be constant for the wavelength range of interest. This assumption is of low importance for the further investigations, because the absolute calibration is of importance only at 5 nm, where the calibration data points are available. The calibration curve of the detector is used to interpolate the calibration. In [74] it is stated

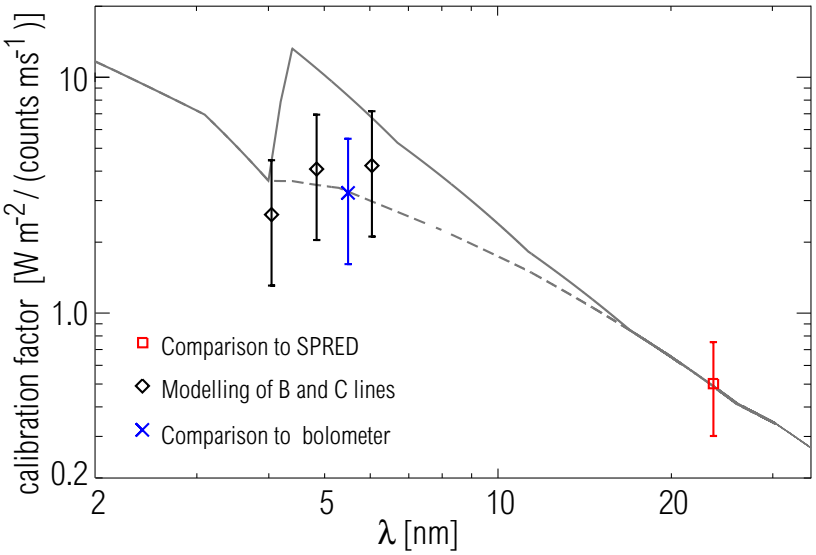

Figure 3.9: Absolute calibration factors for the grazing incidence spectrometer. Diamonds denote the calibration results from the STRAHL modeling of H-like and He-like lines emitted by boron and carbon. The cross denotes the calibration point that results from comparing the emission of the tungsten quasicontinuum to the bolometer signal. The square shows the comparison of the grazing incidence to the SPRED calibration for the HeII line at 23.7 nm. The solid line is the relative dependence of the calibration factor of a channel electron multiplier with carbon contamination [74] normalized to the calibration results. The dashed line is the tentative relative dependence for a contamination-free detector, which was used to interpret the spectra.

that the increase of the calibration factor at 0.4 nm is caused by the contamination of the channel electron multiplier by carbon (pump oil) and will be less pronounced for carbon-free surfaces. As the grazing incidence spectrometer at ASDEX Upgrade is well protected against the leakage of pump oil the calibration curve was corrected for the K_α absorption edge (at 4 nm) of carbon and the dashed line denotes the used calibration curve. The values that result from the different calibration methods agree within the uncertainties. However, as only indirect methods were used, larger uncertainties than for the Bragg calibration remain.

Chapter 4

Modeling of Spectra

4.1 General Parameters Influencing Spectroscopic Measurement in a Fusion Plasma

The spectroscopic interpretation of measurements taken from a tokamak plasma is not straight-forward due to the properties of the plasma and the viewing geometry. Basic discharge properties that are important for the measurements are the spatial temperature and density profiles of the plasma, the plasma shape and position that may be altered within certain limits and the impurity density profile which may be different for each impurity of the plasma. There are other parameters, that could be considered additionally, depending on the detail in which the spectra are analyzed. For high-Z elements, an interpretation on the most basic level is necessary first, i.e. to understand which spectral lines are emitted by which ion states and what is the line strength of the spectral line. Closely connected is also the question for the fraction of the impurity that resides in a certain ion state as a function of electron temperature. The atomic data on ionization and recombination (cf. section 2.3) give information about the fractional abundance of each ion state versus electron temperature in equilibrium for a plasma without transport. Transport effects may be introduced numerically as is featured in the next section. To obtain a modeled spectrum that is equivalent to the measured one it is necessary to trace the LOS of the diagnostic through the plasma such that the radiation from different plasma regions is weighted in the correct way. This is a numerical integration along the LOS. The integrand is not known in experiment, therefore, it is not sufficient to only test the model by comparing the integral along a LOS of model and experiment, but also the integrand itself is of interest. Information on it can be obtained by varying the experimental conditions, like changing the electron temperature, density or impurity profiles. Finally the total integral of the model can be compared to the measurement. The details of the modeling are

described in the following.

4.2 Modeling the Ion Balance

As described in section 2.3 the atomic calculations provide ionization and recombination rate coefficients S and α, respectively. In equilibrium the ionization rate $\dot{N}_{z,z+1} = n_e n_z S_z$ equals the recombination rate $\dot{N}_{z+1,z} = n_e n_{z+1} \alpha_{z+1}$. This gives for the two charge states z and z+1:

$$\frac{n_{z+1}}{n_z} = \frac{S_z}{\alpha_{z+1}} \tag{4.1}$$

In the corona population equilibrium (cf. section 2.1.4), S and α are a function of T_e only and the above formula can only be used for a low electron density approximation. However, it is possible to put corrections, which are calculated by collisional-radiative models, due to electron densities into the rate coefficients, which makes both S and α a 2-dimensional function of T_e and n_e. The fractional abundance for all ion states can be evaluated by a set of equations like 4.1 for each z and the additional condition that sum of all charge state densities $\Sigma_{z=0}^{Z} n_z$ is the density of the impurity $n_{impurity}$ with the nuclear charge Z. Figure 4.1 features the fractional abundances, i.e. densities normalized to n_W, of the charge states of tungsten versus T_e for $n_e = 1 \cdot 10^{20}\,\mathrm{m}^{-3}$.

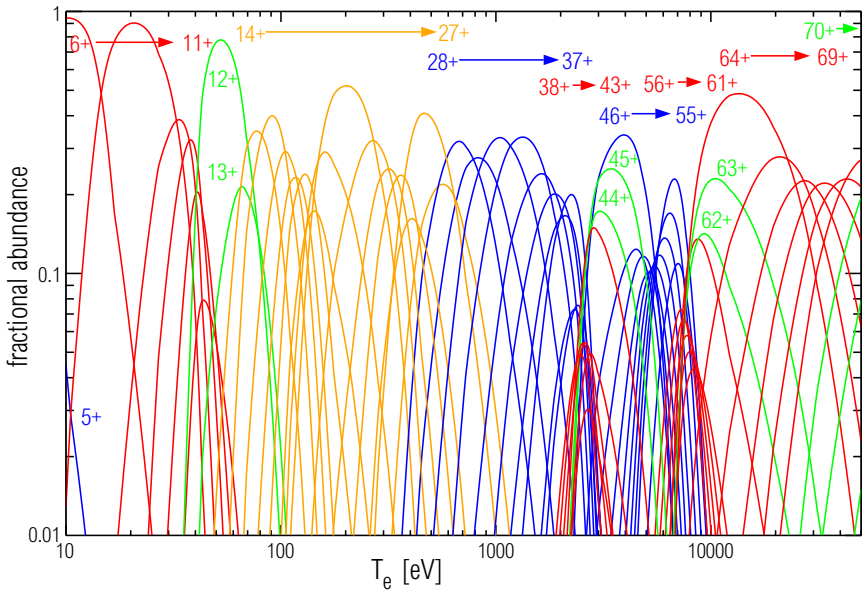

Figure 4.1: Transportless ionization balance for tungsten at an electron density of $1 \cdot 10^{20}\,\mathrm{m}^{-3}$. This balance is identical to the one labeled 'modified CADW+408' in figure 5.9(d), but here a larger electron temperature interval is featured. Colors denote the angular momentum of the 'outer most' electron(s) of the ground state configuration: orange – f, blue – d, red – p, green – s;

In a tokamak plasma the equilibrium is altered by transport. Different transport phenomena can be modeled by particle diffusion and drift, both may vary along the plasma radius. In this work transport effects are considered via the transport code STRAHL [76, 77]. It numerically solves the radial transport equation 4.2 for a circular model plasma. The model plasma corresponds to the plasma from experiment, as the magnetic structure and profiles of electron densities and temperatures of the experimental plasma are mapped onto the circular plasma, such that equal plasma volumes for model and experiment are contained within corresponding flux tubes, i.e. the surfaces with constant magnetic flux. Equation 4.2 is solved at every numerical grid point on the radius of the plasma, where $-\nabla\Gamma_z$ is the transport term and Q_z the source term of the ion density n_z.

$$\frac{\partial n_z}{\partial t} = -\nabla\Gamma_z + Q_z \tag{4.2}$$

The source term connects the ion state z to the neighboring ion states z-1 and z+1 via ionization and recombination, as can be seen in equation 4.3. In principle, the consideration of charge exchange is also possible but is not considered any further here.

$$\begin{aligned} Q_z = \quad & - \quad (n_e S_z + n_e \alpha_z) \quad \cdot n_z \\ & + \quad n_e S_{z-1} \quad \cdot n_{z-1} \\ & + \quad n_e \alpha_{z+1} \quad \cdot n_{z+1} \end{aligned} \tag{4.3}$$

$$-\nabla\Gamma_z = \frac{1}{r}\frac{\partial}{\partial r} r \left(D_\perp \cdot \frac{\partial n_z}{\partial r} - v \cdot n_z \right) \tag{4.4}$$

Equation 4.4 details the transport term in equation 4.2 including flux surface (s. appendix A) averaged diffusion coefficient D and drift velocity v. These coefficients are subject to experimental investigations. Analyses are performed on plasmas in which impurities are injected and the radial evolution of the impurity densities allows to backtrack the transport coefficients. Typically, anomalous transport, i.e. turbulence, dominates the coefficients. D and v have been measured in ASDEX Upgrade [72, 73, 78–80]. Typical results are featured in figure 4.2 for different plasma regimes. As all of the investigations are performed in H-mode plasmas, which is a mode of plasma operation giving rise of high confinement and which is accessible only with a divertor (s. appendix A), focus is put on the transport coefficients in that regime. In figure 4.3 the parameters for the edge of the plasma are featured for the H-mode regime. At the plasma edge the so called edge localized mode (ELM) frequently occurs and expels particle and energy ('ELM on'), while in between such events ('ELM off') a transport barrier persists and an inward drift is observed. On average the ELMs

reduce the large inward drift and increase the diffusion coefficient locally. When modeling the transport of impurities, this edge region between $0.9 \leq \rho_{pol} \leq 1.0$ is critical for relating the edge to the central impurity densities. For the modeling of the bulk plasma this is of low importance. Still, when comparing the emissions of cold regions at $\rho_{pol} \geq 0.9$ with the central emissions uncertainties may arise due to this delicate interplay of diffusion and drift in the edge region. However, it is found for the impurities Ne, B and C that the use of the presented transport parameters agree within a factor of 2-3 with the conditions found in experiment. This finding suggests that the summed effect of diffusion and drift at the plasma edge varies within moderate boundaries. For most investigations of this thesis, the impurity concentrations of the bulk plasma are of interest and the effects at edge plasma are of secondary importance. In the anomalous transport regime the charge of the impurity is of low importance, which makes the use of typical transport parameters for tungsten reasonable.

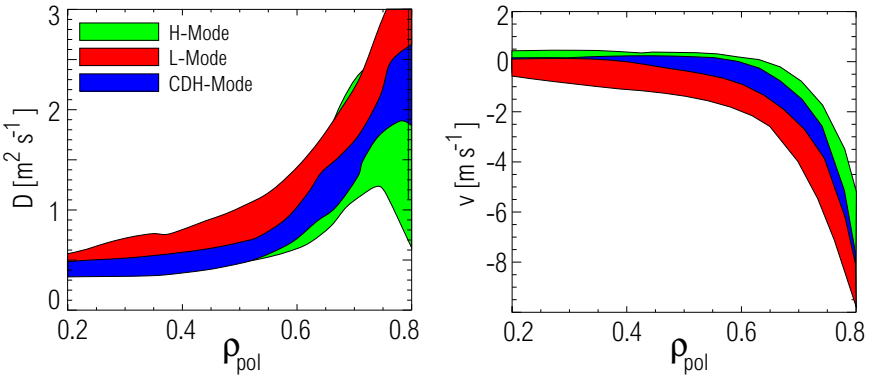

Figure 4.2: Transport parameters (temporally average over the so called sawteeth, which is a plasma instability, which occurs frequently and redistributes particles and energy in the central region of the plasma) of the central plasma for the L-mode, CDH-mode and H-mode regime measured at ASDEX Upgrade. The data are taken from [78, 79]. In the present work the coefficients for the H-mode regime apply.

In [39] it has been demonstrated that for the interpretation of equilibrium line intensities (s. above's transport coefficients in figure 4.2) transport can be neglected in the core of the plasma. To underline this fact the ionization balance after reaching the equilibrium state at a constant source rate of tungsten corresponding to discharge #16778 (s. figure 4.4(a)) is shown in figure 4.4(b) with typical transport switched on (black lines) and off (colored lines). At the edge of the plasma, i.e. outside the magnetic coordinate $\rho_{pol} = 0.9$ a difference between the colored and black lines exists, which is influencing the integrals of a LOS running through the center of the plasma by much more than 20 %. For $\rho_{pol} \leq 0.9$ only small deviations show up which for a LOS integrated measurement are hard to notice at all.

A special case applies, when the central anomalous transport in ASDEX Upgrade

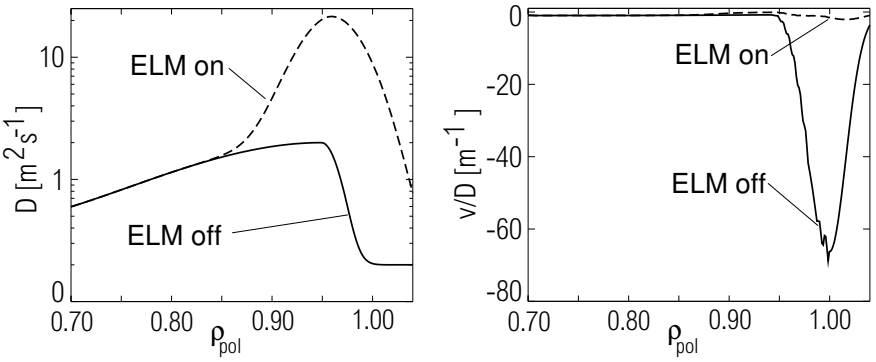

Figure 4.3: Transport parameters at the plasma edge of a H-mode discharge measured at ASDEX Upgrade. The data are taken from [72, 73, 80]

is in the range or below $\approx 0.1\mathrm{m}^2/\mathrm{s}$ which is approximately an upper border for the diffusion coefficient obtained from neoclassical theory. At this point, the neoclassical theory predicts a radial inward drift for impurities, if a gradient of the background ions exist. The drift is observed and leads to a gradient of the impurity concentrations. This effect is mitigated by diffusion, but as the ratio of drift over diffusion coefficient is approximately proportional to the charge of the impurity, the central peaking of impurity concentration is more enhanced for higher charged impurities like tungsten. So called impurity accumulation is observed, which is a well characterized phenomenon [81, 82]. This distinctive feature is unwanted for plasma operation, but yields a powerful potential for analysis. It is exploited for the investigations in chapter 5. For more details on the interplay of turbulent and neoclassical transport, confer [83].

4.3 Performing the Integration along a Line of Sight

For a spectrometer, the spectrum is modeled by numerically performing the integration in equation 4.5 of the plasma emissions along the LOS.

$$I = \int_{LOS} \varepsilon(r) dl \quad , \quad \text{where} \qquad \varepsilon(r) = \sum_{z=0}^{Z} \mathrm{FPEC}_z(r) f_z(r) c(r) n_e(r) \tag{4.5}$$

and r is the plasma radius, while $\mathrm{FPEC}_z(r)$ is the feature photon emissivity coefficient (cf. section 2.3.2) of the ionization state z, $f_z(r)$ its fractional abundance, $c(r)$ the impurity concentration and $n_e(r)$ the electron density at a plasma radius r. It is straight-forward to evaluate the integral by using the theoretical information for $\mathrm{FPEC}_z(r)$, $f_z(r)$ and measurements for $c(r)$, $n_e(r)$ and $T_e(r)$, which enter into the evaluation of $\mathrm{FPEC}_z(r)$ and $f_z(r)$. However, when comparing the modeled spectrum

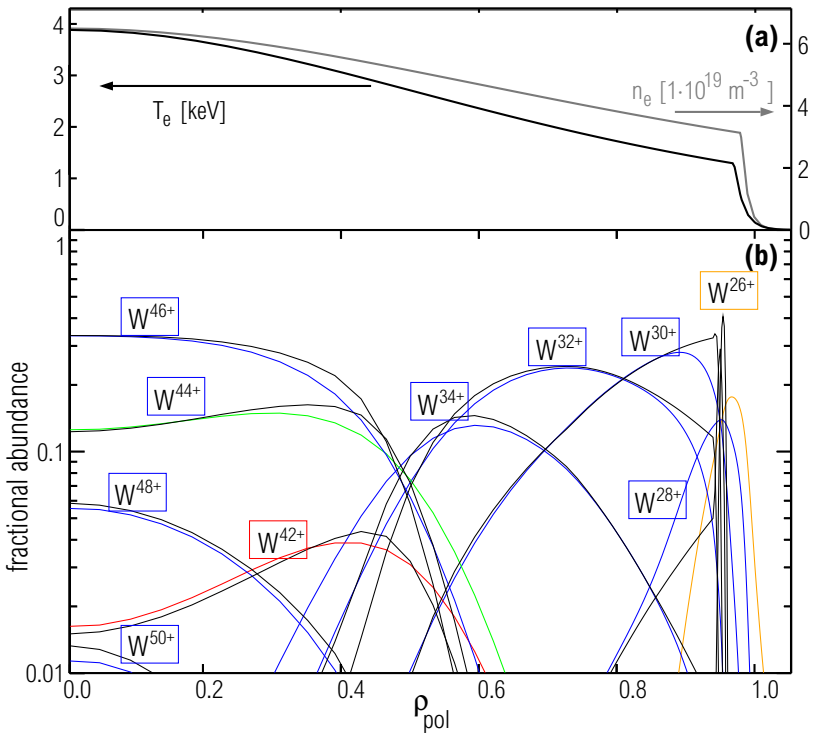

Figure 4.4: *(a)* Electron temperature and density profiles from discharge #16778 at 3 s. The profiles have been used to obtain the ionization balance featured in part (b) of the figure. *(b)* Fractional abundance for several ionization states between Cd-like W^{26+} and Cr-like W^{50+}. Black lines correspond to the ionization balance in a transportless plasma, while the colored lines denote the fractional abundances in a plasma with typical transport coefficients. Colors denote the angular momentum of the 'outer most' electron(s) of the ground state configuration: orange – f, blue – d, red – p, green – s;

to the measurements the influence of all these parameters needs to be considered. As will be explained in the following chapters, impurity accumulation, which is a special feature of impurity transport, can be used to simplify the integral to a quasi-local measurement.

Chapter 5

Ionization Balance of Tungsten

The main focus of this chapter is the ionization balance of tungsten in a fusion plasma. In the course of these investigations, the behavior of spectral lines versus electron temperatures is examined. The assignment of spectral lines to an ion state is a necessity for the following analysis. Therefore, an overview on the identification methods of spectral lines is given in section 5.1, while results of the identification are presented in chapter 6. Investigations on the ion balance are then presented in section 5.2. In section 5.3 the results for other high-Z elements on which focus is put in the present work are summarized.

5.1 Methods for Identification of Spectral Lines

Spectral lines of tungsten can be identified by comparing measured spectra to the theoretical predictions. For this, it is necessary to predict the wavelengths and the line intensity accurately, because often many spectral lines of different tungsten ion states are observed in the same spectral region. Thus, it is important and non-trivial to identify the ion state which is emitting a spectral line or feature. In principle, lines of highly charged tungsten can be investigated in the spectra of beam foil experiments and laser produced plasmas. However, the corresponding spectra are known to be very line-rich, owing to the fact that in these plasmas recombination is an important process for the population of upper levels. This increases the difficulty to interpret and identify single spectral lines. The best experimental tool to accomplish the assignment of spectral lines to ionization states is an electron-beam ion trap (EBIT) [17]. This device ionizes and excites the ions of a certain element with a nearly monoenergetic (ΔE=50 eV) electron beam. Therefore, the maximum ionization state in the device is known by comparison to the ionization potentials, which can be calculated to high accuracy. Results of this method are shown in sections 6.2.1 and 6.3.1. In figure 2.1,

ionizations potentials of tungsten are shown from [36], from HULLAC [28–31] and GRASP [24]. The differences are important for high accuracy experiments like the EBIT investigations and therefore only the high quality data of HULLAC and GRASP are considered for them. As the recombination processes are of low importance the ion state distribution is peaked at the maximum possible ion charge or at the lower charged neighbors. Another experimental tool that provides highly charged tungsten for detailed investigations is a tokamak. Here ionization and recombination are close to equilibrium for most of the plasma and the spectra are typically dominated by electron impact excitation, while recombination processes only play a considerable role for special spectral lines. For the analysis of the spectra from ASDEX Upgrade the electron temperatures are available along the plasma radius, which narrows the range of candidate ion states. Still, a wide range of ion states exist in abundances relevant to spectroscopic measurements. Spectrometers monitor the plasma along a line of sight (LOS), which results in a superposition of emissions from different locations in a spectrum. A limited radial resolution is possible by the analysis of correlations between the spectrum and a change of electron temperatures in the plasma. Still, if no further information than such a spectrum is available detailed predictions need to be involved. The theoretical data rely on the ion structure calculation, but also on calculations of cross sections for electron impact and a collisional-radiative model. All these steps include considerable uncertainties for high-Z elements such that the assignment of spectral lines holds uncertainties which are difficult to quantify. In the course of this work a special discharge type was used to largely overcome these difficulties for the VUV wavelength region. These discharges exhibit impurity accumulation in a very narrow radial region (diameter of about 20 cm) of the core plasma. The impurity accumulation is monitored by comparing the measurements of the bolometer on two LOS, as featured in figure 5.1. The accumulation starts at about 6.2 s after start of the plasma discharge. At t=6.8 s, the central bolometer channel measures about a factor of 5 larger radiation intensity than the channel that is monitoring the plasma slightly off-central. As the transport along magnetic field lines is dominant the plasma parameters and impurity concentrations can be considered constant on a flux surface. Therefore, the region responsible for the increase in the radiation signal is well defined. Even though the accumulation region exist only on a small fraction of the total LOS of the central bolometer channel this region dominates the radiation signal. Measurements of the electron temperature along the plasma radius exhibit that in the monitored part of the accumulation region the electron temperature profile is nearly flat and a electron temperature can be attributed to the central region with an uncertainty of $\Delta T_e = 200\,eV$. The evolution of this central temperature, which is also presented in figure 5.1, is influenced by a complex interplay of radiative losses, heating processes

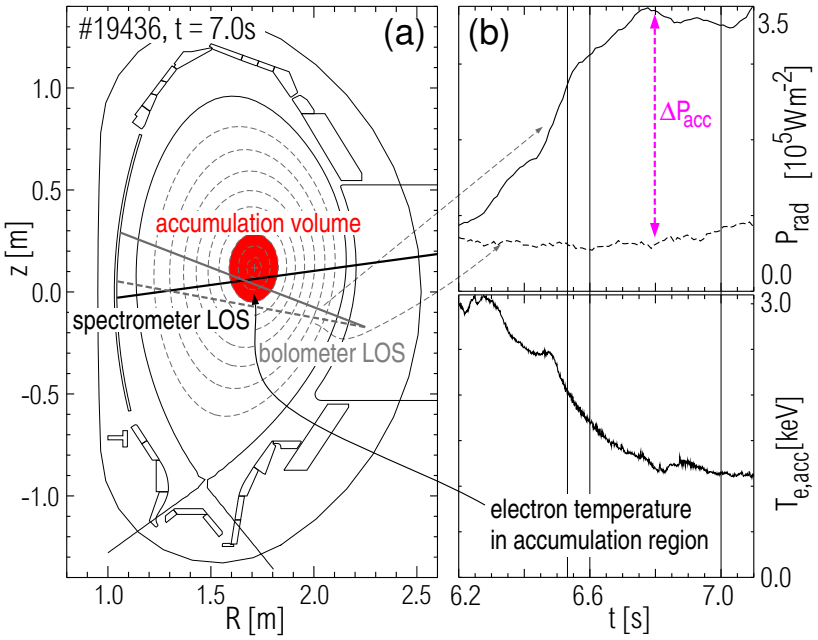

Figure 5.1: *(a)* Magnetic Equilibrium and experimental setup for the measurement of the VUV spectra at ASDEX Upgrade showing the spectrometer's and bolometer's lines of sight; *(b)* Time traces for line integrals of radiation intensity P_{rad} and temperature at $\rho_{pol} = 0.2$. ΔP_{acc} indicates the radiation emitted in the accumulation region. The vertical lines mark the time points of the spectra shown in figure 6.2.

and energy transport. This setup allows for spectroscopic measurements that are dominated by a region with a well-known narrow electron temperature interval. A temporal variation of the electron temperature is naturally provided. The intensity dependence of spectral lines can be correlated to the change of plasma parameters in the accumulation region and it is mainly influenced by the abundance of the emitting ion as is discussed in the following. The emissivity of a spectral line in a homogeneous plasma with T_e depends on the density of the upper state of the considered transition and the corresponding Einstein coefficient. The results of a collisional-radiative model, which considers the populating processes of this upper level, can be expressed by a photon emissivity coefficient (PEC), such that the emissivity $\epsilon_{i,j}$ of a transition from level i to j is given by equation 5.1 (cf. section 2.1.4),

$$\epsilon_{i,j} = PEC_{i,j}(T_e, n_e)\, n_e\, n_W\, f_z \tag{5.1}$$

where n_W is the total tungsten density and f_z equals the fractional abundance of the emitting tungsten ion. The T_e dependence of the PEC is negligible compared to that of the fractional abundance of the emitting charge state. Therefore, the emissivity of a line varies mostly with the fractional abundance of the ion state. This fact is highlighted for Cu-like W^{45+} in figure 5.2. Typically, the emissivities of spectral lines show strong variations only for electron temperatures in the range of the excitation

threshold ΔE, which is much smaller for the investigated VUV lines than the ionization potential. The soft X-ray spectral line at 0.57 nm with $\Delta E = 2.2\,\mathrm{keV}$ is plotted as an example of larger variations in the emissivity. Still, in the electron temperature range, where Cu-like W^{45+} exhibits considerable abundances the variations are only about 20 %. The fractional abundance indicated in figure 5.2 may be weakly shifted or broadened by the transport in a tokamak discharge. However, the central part of the plasma is characterized by weak transport, especially when impurity accumulation occurs, causing unimportant deviations from the featured curve (cf. figure 4.4). Therefore, the variation in the line intensities measured for different plasma temperatures T_e resembles the density evolution of the emitting ion charge. Consequently, the intensity of spectral lines emitted by an ion state show nearly the same T_e-dependence if the change in temperature is slow compared with the typical time constants of the collisional-radiative processes which populate the levels of the ion.

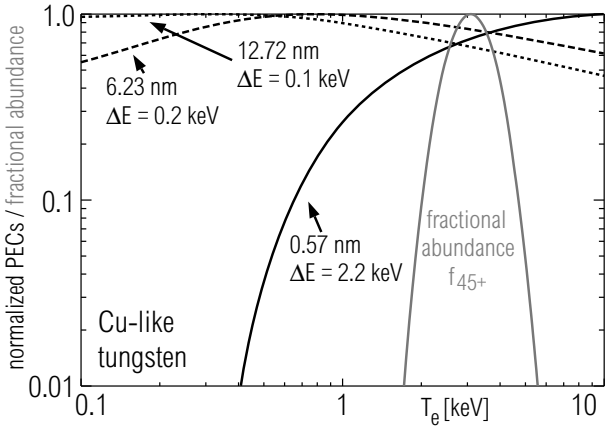

Figure 5.2: Normalized PECs (ADAS) of spectral lines emitted by Cu-like W^{45+} and the normalized fractional abundance [39] of Cu-like W^{45+} versus electron temperature T_e for a homogeneous plasma. ΔE denotes the energy required for excitation from the ground state.

5.2 Ionization Balance and Comparison to Predictions

With the knowledge of the emitting ionization state of spectral lines and features it is possible to analyze the ionization balance in detail. While in section 5.1 just the evolution characteristics of the line intensities is of interest, it is also possible to renormalize the line intensity by the total radiation that originates from the accumulation region. This removes the impact of a varying total tungsten concentration on the

individual spectral lines. As a result, this normalized line intensity is proportional to the fractional abundance of the ion state, as explained in section 5.1.

5.2.1 Relative Fractional Abundances versus T_e

For several discharge phases with impurity accumulation, spectral line intensities I_l, which were measured by the grazing incidence and Johann spectrometer, were divided by the total radiation ΔP_{acc} (e.g. figure 5.1) originating from the accumulation region, which is derived from a comparison of two LOS of the bolometer. Following equation 5.2, these ratios F_l are proportional to the fractional abundance, if the cooling factor L_z (s. chapter 8) and the PEC_l of the spectral line are varying weakly with electron temperature. The weak dependence of the PEC_l was explained in section 5.1, while the assumption of weak variations in the cooling factor L_z at electron temperatures between 1 keV and 5 keV is supported by the findings in chapter 8.

$$F_l = \frac{I_l}{\Delta P_{acc}} \propto \frac{PEC_l n_e n_W f_z}{L_z n_e n_W} \propto \frac{PEC_l f_z}{L_z} \tag{5.2}$$

The ratios F_l from all considered discharge phases were multiplied by a single normalization factor for each spectral line, such that the maximum of the ratio approaches 1. The relative behavior of the fractional abundance f_z for the ion states Se-like W^{40+} to Ni-like W^{+46} versus electron temperature have been obtained by this procedure. In figure 5.3 and 5.4 the experimental data are compared to theoretical predictions which were also normalized to 1. The predicted fractional abundances are derived for a transportless plasma using different sets of ionization and recombination rate coefficients that result from the calculations introduced in chapter 2.3. As impurity accumulation takes place the assumption of no transport in the plasma causes negligible deviations (s. section 4.2). The green curve in figures 5.3 and 5.4 corresponds to an empirically adjusted set of coefficients which are explained in section 5.2.2. Comparing first the black curves with the measured data points, the predicted curves 'CADW+408' offers the best agreement to the fractional abundances of Se-like W^{40+} to Ni-like W^{46+} tungsten. As this curve corresponds to the combination of ionization coefficients from CADW calculations with the recombination coefficients from the level-resolved baseline calculations from ADAS, the best available data are entering here. The deviations of the other calculations are large and are not understood in detail. Although the data 'CADW+408' describe well the relative abundances of the ion states Se-like W^{40+} to Ni-like W^{46+}, deviations get apparent for the ion states Ag-like W^{27+} to Y-like W^{35+}. As the individual emissions of each ion state in the quasicontinuum is difficult to track the integrated intensity of the quasicontinuum and the intensity of the short wavelength edge of the quasicontinuum are tracked for different

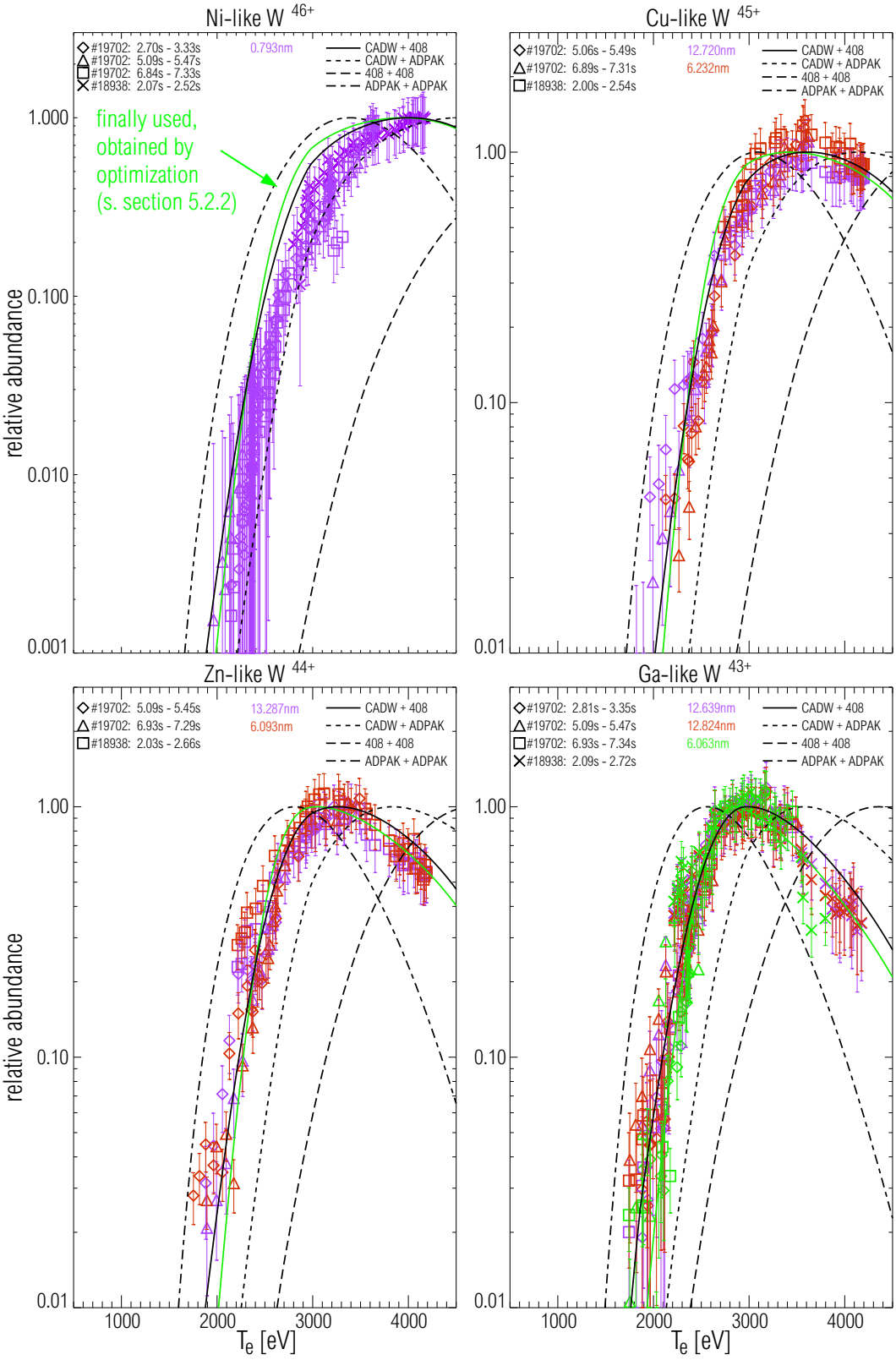

Figure 5.3: The relative abundances of Ni-like W^{46+} to Ga-like W^{43+} derived from theoretical data (lines) and from measurement (symbols). Measurements originate from impurity accumulation phases. The data are color coded indicating the analyzed spectral lines. The uncertainty in electron temperature is ± 200 eV. The legend is featuring the underlying ionization and recombination data by abbreviations on the left and on the right of the '+', respectively. 'CADW' = configuration average distorted wave data (s. section 2.3.3), '408' = ADAS baseline data using level-resolved calculations from the Cowan code, 'ADPAK' = data from the average ion model [25], which were modified in [39] according to experimental findings. The green line is the result of a modification of the 'CADW + 408' data, which will be explained in section 5.2.2

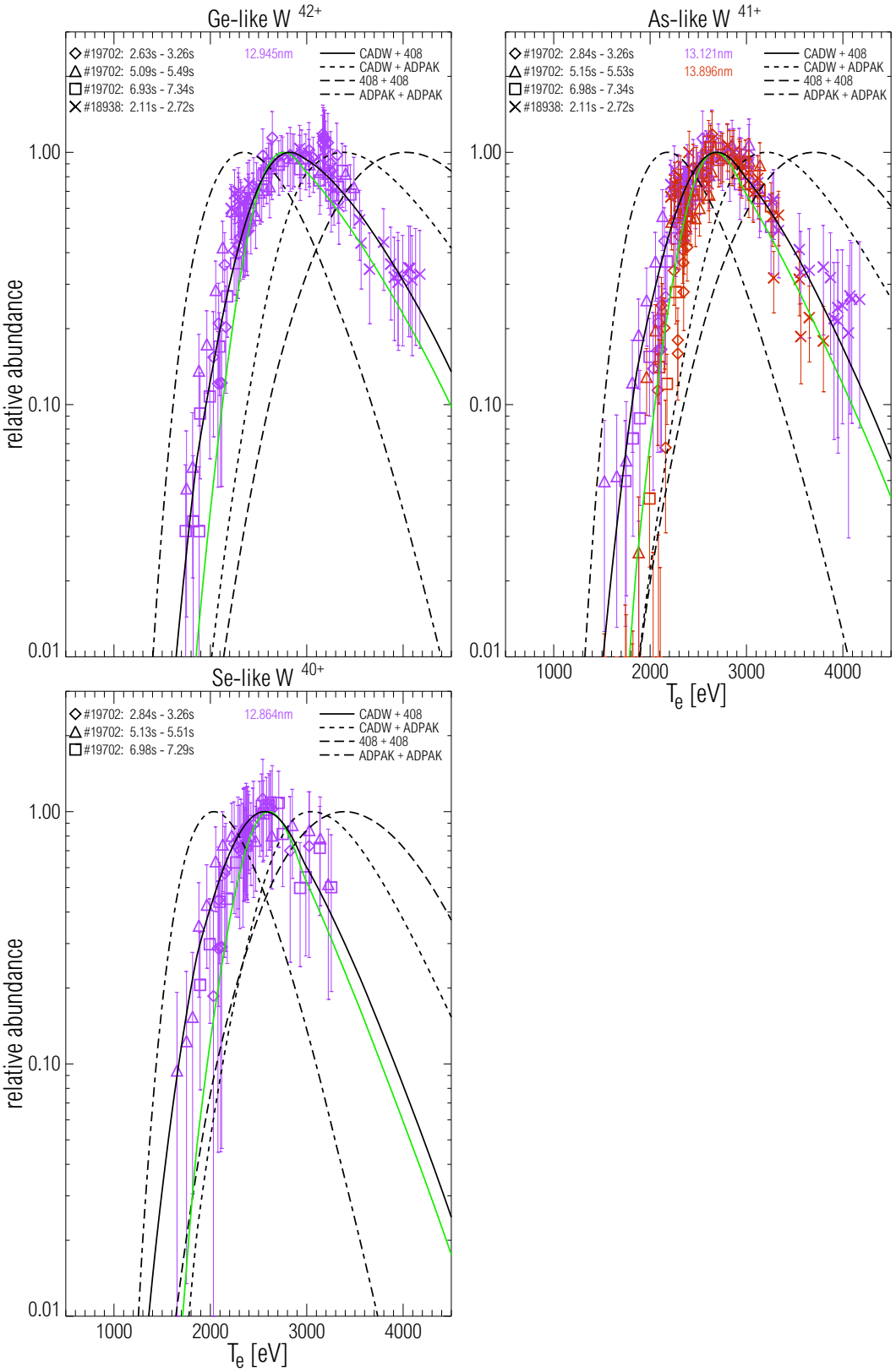

Figure 5.4: The relative abundances of Ge-like W^{42+} to Se-like W^{40+} derived from theoretical data (lines) and from measurement (symbols). Measurements originate from impurity accumulation phases. The data are color coded indicating the analyzed spectral lines. The uncertainty in electron temperature is ± 200 eV. The legend is featuring the underlying ionization and recombination data by abbreviations on the left and on the right of the '+', respectively. 'CADW' = configuration average distorted wave data (s. section 2.3.3), '408' = ADAS baseline data using level-resolved calculations from the Cowan code, 'ADPAK' = data from the average ion model [25], which were modified in [39] according to experimental findings. The green line is the result of a modification of the 'CADW + 408' data, which will be explained in section 5.2.2

electron temperatures. Both are presented in figure 5.5 and compared to the theoretical predictions, which are obtained from summing up the fractional abundances of Ag-like W^{27+} to Y-like W^{35+}. In this sum each ion state is weighted by the predicted

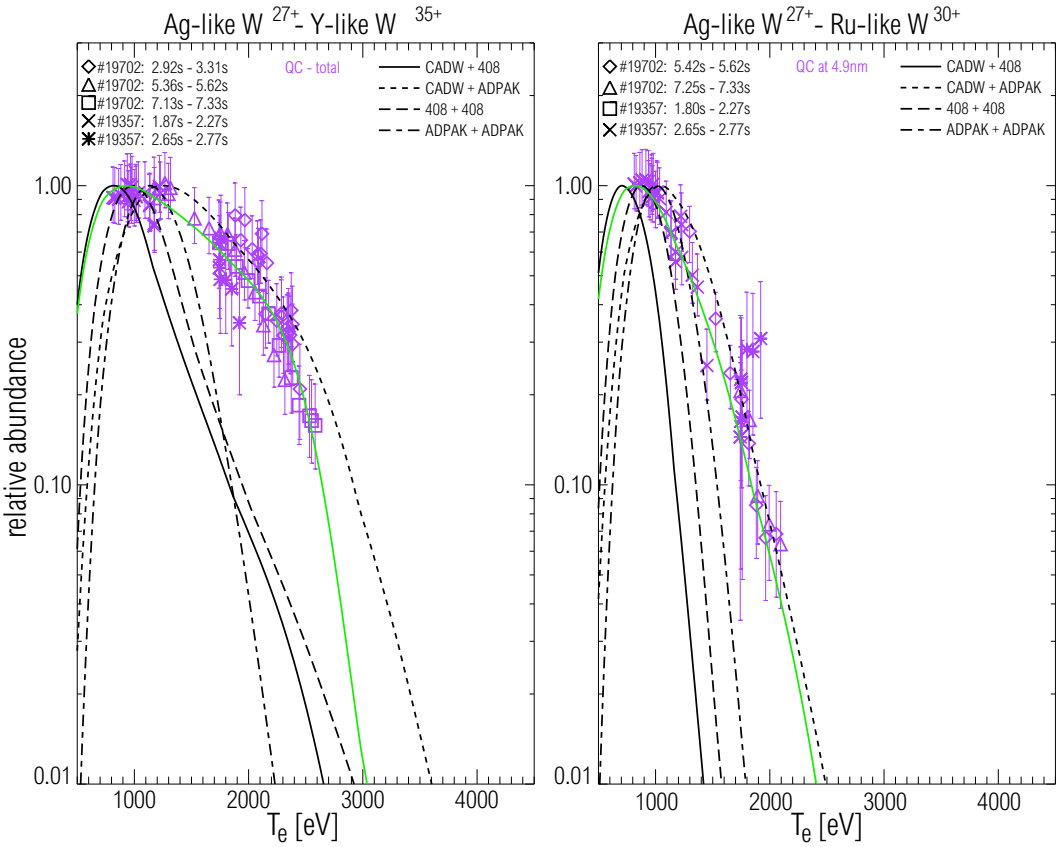

Figure 5.5: The relative abundances of the weighted sum (see text) over Ag-like W^{27+} to Y-like W^{35+} and W^{27+} to Ru-like W^{30+} derived from theoretical data (lines) and from measurement (symbols). Measurements originate from impurity accumulation phases. The uncertainty in electron temperature is ± 200 eV. The legend is featuring the underlying ionization and recombination data by abbreviations on the left and on the right of the '+', respectively. 'CADW' = configuration average distorted wave data (s. section 2.3.3), '408' = ADAS baseline data using level-resolved calculations from the Cowan code, 'ADPAK' = data from the average ion model [25], which were modified in [39] according to experimental findings. The green line is the result of a modification of the 'CADW + 408' data, which will be explained in section 5.2.2

emissivity contributing to the quasicontinuum (s. section 6.2), which has some impact (factor of ≈3 between Rh-like W^{29+} and Y-like W^{35+}) on the shape of the curves. For comparison to the emissivity at the short wavelength edge of the quasicontinuum the predicted fractional abundances of W^{27+} to Ru-like W^{30+} were summed up.

The fractional abundances do not exhibit information on the ionization or recombination coefficients separately and therefore, no experimental information on the separate rates have been obtained. Nevertheless, some of the used ionization and recombination rate coefficients are briefly presented in the following. In figure 5.6 a comparison

between the '408' and CADW ionization rate coefficients is presented. Both sets of

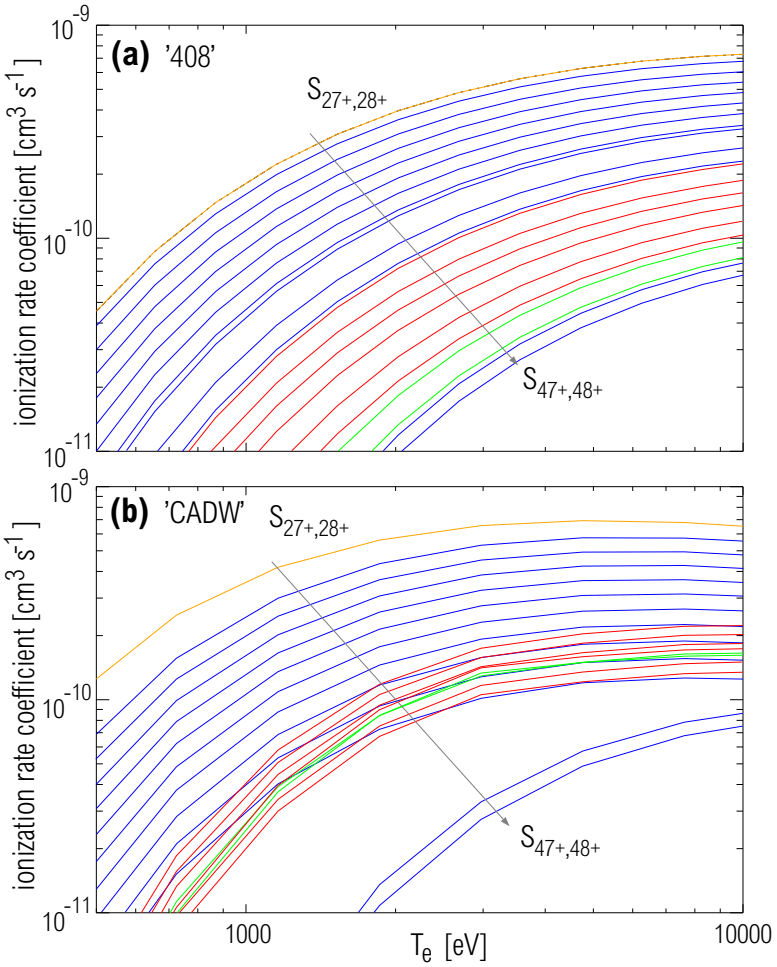

Figure 5.6: *(a)* Ionization rate coefficients S calculated by the '407/408' ADAS codes labeled with '408' for ionization of Ag-like W^{27+} to Co-like W^{47+}. Colors correspond to the scheme used throughout this thesis: Color code corresponds to the angular momentum of the 'outermost' electron in the ground state configuration of the ionized ion: orange – f, blue – d, red – p, green – s. For increasing charge state the ionization rate is decreasing monotonically; *(b)* CADW ionization rate coefficients from [41] for ionization of Ag-like W^{27+} to Co-like W^{47+}. For increasing charge state the ionization rate is decreasing monotonically within each 'shell';

data exhibit a regular development of the rate coefficients for increasing charge states. The '408' data are decreasing monotonically for all ionization states between Ag-like W^{27+} and Co-like W^{47+}, while for the CADW data the rates jump to higher values for the 4p and 4s shells, but exhibit the monotonic behavior within each shell. The CADW ionization rates are growing faster for increasing electron temperatures, but reach about the same maximum as the rates from '408'. When considering the recombination coefficients calculated by '408' a less structured picture occurs (s. figure 5.7).

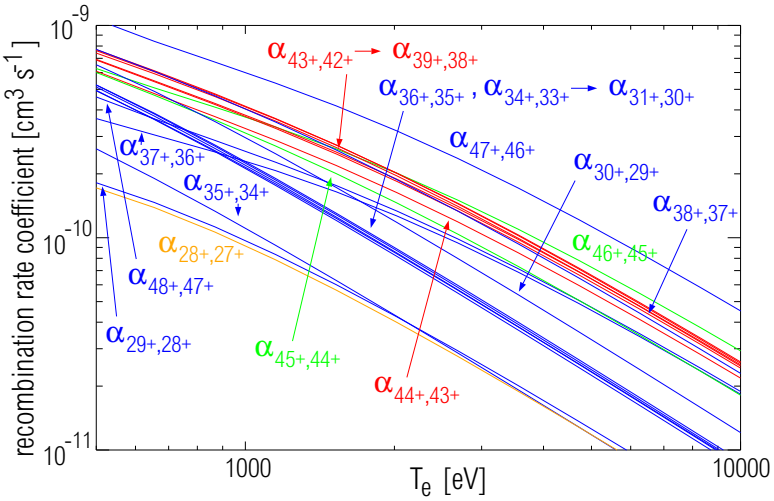

Figure 5.7: Recombination rate coefficients α calculated by the ADAS codes labeled with '408' (s. section 2.3.4). Color code corresponds to the angular momentum of the 'outermost' electron in the ground state configuration of the recombined ion: orange – f, blue – d, red – p, green – s.

5.2.2 Relative weight of fractional abundances

In the above section the relative behavior of the fractional abundances of ion states have been investigated independently of each other. When comparing the line intensities of different ion states these contain information about the ratio of their fractional abundances integrated along the spectrometer's LOS. To obtain this information the line strengths of the considered lines need to be known. For the discharges #16778 and discharge #19115 a comparison between modeled and measured spectra is performed with the aim to investigate the relative ion abundances. In the spectral ranges 0.4 –0.8 nm (soft X-ray), 4 –7 nm (VUV) and 12 –14 nm (VUV) the spectral lines which are emitted by a single ion state are summed up and compared to the sum of corresponding lines in the model. The sums, but not single spectral lines, are compared to decrease the uncertainties that arise in the prediction of single line strengths. The obtained ratios are then normalized by the ratio for Zn-like W^{44+}, which is an arbitrary choice. In figure 5.8, the comparisons of spectral lines in discharge #16778 and discharge #19115 to modeling results are featured for the ionization and recombination data 'CADW+408' (figure 5.8(a)) and adjusted modified 'CADW+408' data (figure 5.8(b)). The modification was done in agreement with the experimental findings and the adjustment was performed on the recombination data only, because the available CADW ionization data are considered to be of higher accuracy, while in principle the lowering of ionization rate coefficients would have a similar effect as the increasing of recombination rate coefficients and vice versa. Additionally, it may be noted that the application of one factor to a recombination rate for all electron temperatures may

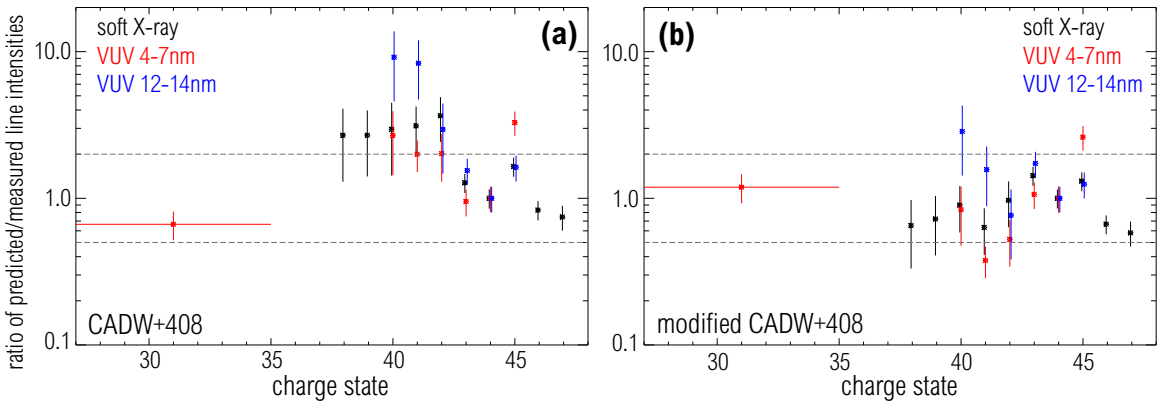

Figure 5.8: *(a)* Ratios of predicted over measured line intensities for different wavelength ranges versus ionization state using the 'CADW+408' ion balance (s. figure 5.3, 5.4, 5.5 and 5.9). All lines of an ionization state are summed in the model and in the spectrum to mitigate the uncertainties that would occur for a single spectral line.*(b)* Similar data to part (a) of the figure, but using modified 'CADW+408' data. The modifications are described in the text.

not be a realistic correction as also the shape of a recombination rate holds uncertainties, which might translate more efficiently to a different fractional abundance of an ionization state.

Three experimental boundary conditions were met by the adjustments and all three are in disagreement with the unmodified 'CADW+408' data: The first evidence which is in contradiction to the original 'CADW+408' data is featured in figure 5.5. Here the emission of the quasicontinuum and therefore the abundance of states up to Y-like W^{35+} is seen at larger electron temperatures than predicted. Secondly, no experimental evidence of the charge states Sr-like W^{36+} and Rb-like W^{37+} is seen in experiment, but the model predicts large isolated spectral lines in the spectrum around 5.5 nm due to the relatively large fractional abundances of the 'CADW+408' ionization balance (cf. figure 5.9). Both is suggesting that these latter ionization states are suppressed in experiment by a shift of the lower lying ionization states towards higher electron temperatures. This was achieved by increasing the recombination coefficients of Sr-like W^{36+} by a factor of 7. The recombination coefficients of the lower charged neighbors were also increased to give a continuous behavior for the ion states Ag-like W^{27+} to Y-like W^{35+} (s. table 5.1). These adjustments result in the green curves in figure 5.5, which resemble the experimental data. The third deviation of the theoretical data from experimental findings is featured in figure 5.8. The fractional abundances of Kr-like W^{38+} to Ge-like W^{42+} are predicted too large, as can be judged from the two VUV and the soft X-ray spectra. In the spectra the lines of these ion states are overestimated by a factor 2 –10. Therefore, the rate of recombination into Ge-like W^{42+} was adjusted by lowering it to the 0.3-fold value, which offered better agreement between model

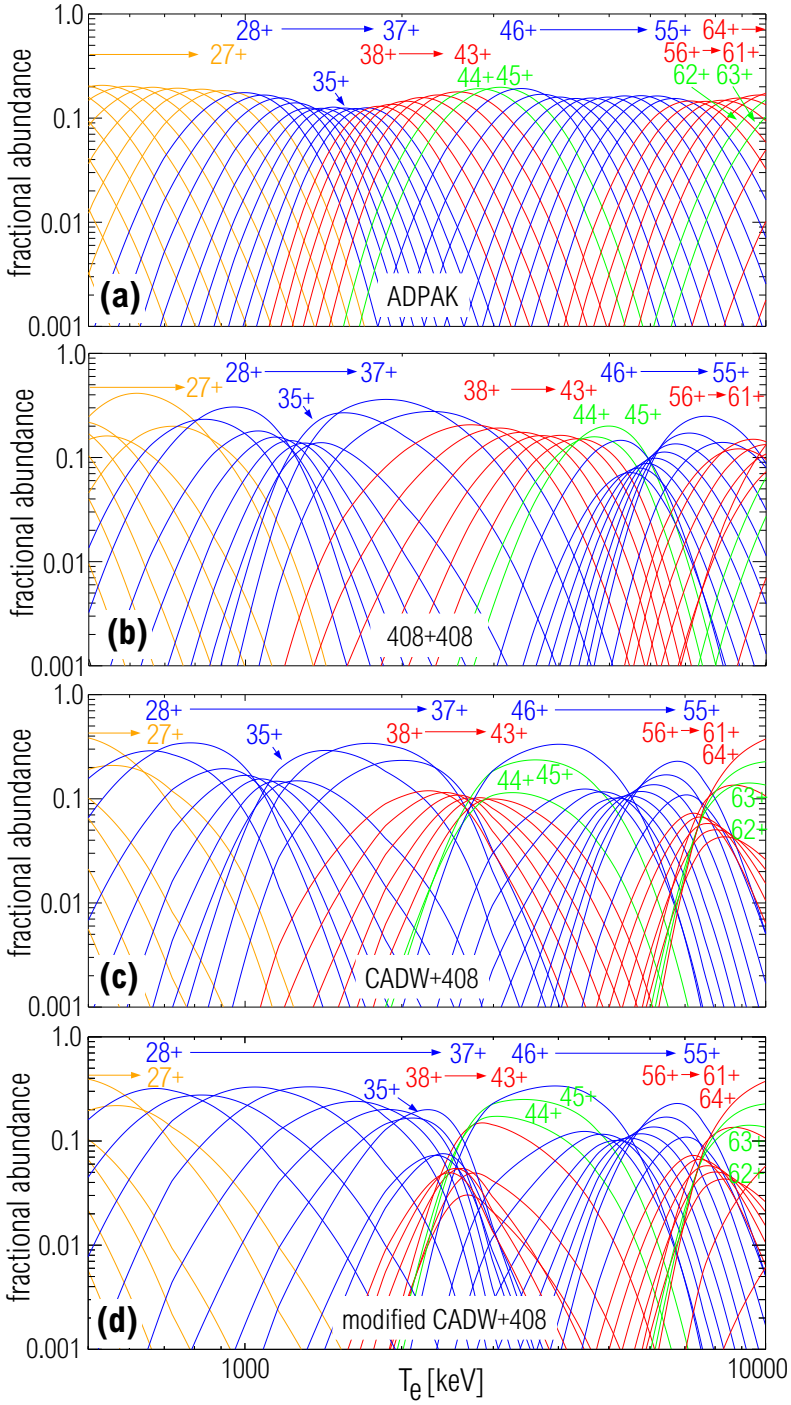

Figure 5.9: *(a)* Transportless fractional abundances of tungsten ionization states using ADPAK ionization and recombination data from [25], which were modified according to [39]. Numbers denote the charge state. Colors denote the angular momentum of the 'outer most' electron(s) of the ground state configuration: orange – f, blue – d, red – p, green – s; *(b)* Transportless fractional abundances of tungsten ionization states using 'ADAS 408' ionization and recombination data.; *(c)* Transportless fractional abundances of tungsten ionization states using CADW ionization and 'ADAS 408' recombination data.; *(d)* Transportless fractional abundances of tungsten ionization states using CADW ionization and modified 'ADAS 408' recombination data. Modifications are described in the text.

Recombined Ion	F_{corr}
Co-like W^{47+}	1.0
Ni-like W^{46+}	1.0
Cu-like W^{45+}	1.0
Zn-like W^{44+}	1.3
Ga-like W^{43+}	0.9
Ge-like W^{42+}	0.3
As-like W^{41+}	0.6
Se-like W^{40+}	1.7
Br-like W^{39+}	1.0
Kr-like W^{38+}	1.0
Rb-like W^{37+}	1.0
Sr-like W^{36+}	1.0
Y-like W^{35+}	7.0
Zr-like W^{34+}	5.0
Nb-like W^{33+}	4.0
Mo-like W^{32+}	3.4
Tc-like W^{31+}	3.1
Ru-like W^{30+}	1.5
Rh-like W^{29+}	0.6
Pd-like W^{28+}	1.5
Ag-like W^{27+}	1.0

Table 5.1: Correction factor F_{corr} of the recombination rate coefficients that are introduced for improved agreement with the experimental findings.

and experimental data. Such change of coefficients is delicate for the ionization states Se-like W^{40+} to Ni-like W^{46+} as the relative shape of the abundance curves is also given by experimental evidence (s. figures 5.3 and 5.4). By the adjusting factors featured in table 5.1 these boundary conditions are met (s. green curve in figures 5.3 and 5.4) and the relative line strengths of the considered ionization states are modeled within an uncertainty of factor 2-3 (s. figure 5.8(b)). It may be noted, that the adjustment of the recombination data described above, which had impact on the ionization states below Kr-like W^{38+}, also leads to better agreement in figure 5.8 for the ionization states emitting the quasicontinuum, i.e. Ag-like W^{27+} to Y-like W^{35+}.

5.3 Investigations on Other High-Z Elements

In this thesis, xenon (Z=54), hafnium (Z=72), tantalum (Z=73), rhenium (Z=75), gold (Z=79), lead (Z=82) and bismuth (Z=83) were also investigated at electron temperatures up to 4 keV. As the impurities were injected in dedicated discharges, fewer

experimental data than for tungsten is available and the investigations could be performed to a lesser detail. For these elements no CADW ionization data were available. While xenon might be relevant as diagnostic gas in future devices the other elements are investigated here to benchmark the comparison of spectra and code calculations also for the neighboring elements of tungsten. The ionization balance of xenon has been available in ADAS, but was reevaluated in the course of this work. The data, which were obtained now results from the 'case B' implementation of the '407/408' ADAS codes and are compared in the following. In figure 5.10 the two ionization balances are presented. It may be noted that not only the evaluation of ionization and recombination data is based on the two different cases A and B, but also the ion structure data, which enter into the code, are more elaborate for the present work. The ionization balance for xenon is compared in the following for two discharges. The first discharge #17138 exhibits impurity accumulation with an electron temperature in the accumulation region of $\approx 1.3 \pm 0.2$keV. The discharge #17344 exhibits an approximately flat xenon concentration profile at the radial region $0 < \rho_{pol} < 0.9$ as can be derived from the bolometer measurements. In figure 5.11 the spectra dominated by the impurity accumulation is presented along with the xenon spectra obtained via the two available ionization and recombination data sets. Good agreement is not found for any modeled spectrum. For the 'Case A' spectrum too strong emphasis is put on the ionization states above V-like Xe^{31+}, which is corresponding to the ionization states inside the accumulation region for the modeled ionization balance. Nevertheless, the ionization states below Ni-like Xe^{26+} are still pronounced in the spectrum as the impurity accumulation is moderately strong with a peaking factor of about 6. In comparison to Ni-like Xe^{26+} these lower ionization states are too strong. The situation for the 'Case B' data is better, as the ionization states of Ni-like Xe^{26+} to V-like Xe^{31+} are well visible in the spectrum, while the relative decrease in intensities, when considering increasing charge states, is more pronounced than in the measured spectrum. The ionization states below Ni-like Xe^{26+} are like for the 'Case A' data modeled too strong by far. The overestimation of these ionization states corresponds to the fractional abundances of the ionization states below Ni-like Xe^{26+}, which exceed that of Ni-like Xe^{26+} by far. Apart from these ionization states the 'Case B' offers a better description of the ionization balance at 1.3 keV. The analysis of discharge #17344, where a approximately flat xenon concentration profile exists, underlines these results, as again the xenon ionization states below Ni-like Xe^{26+} appear too strong in the spectra. The more evenly distributed fractional abundances of the ionization states Xe^{26+} to K-like Xe^{35+} of the 'Case B' data (cf. figure 5.10) also gives better agreement with the measurement in #17344, while the 'Case A' data overestimate the ionization states above V-like Xe^{31+} and underestimate the ionization states Ni-like

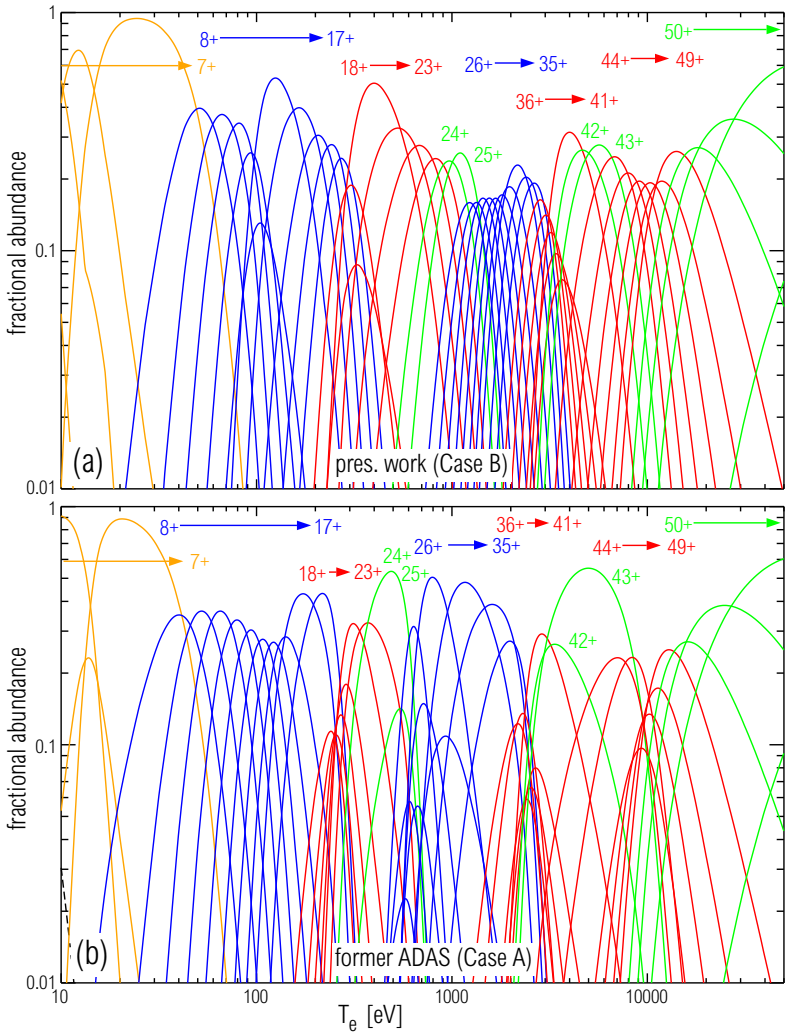

Figure 5.10: *(a)* Fractional abundances of xenon charge states for a transportless plasma. Ionization and recombination data are produced by the ADAS codes '407/408' using 'Case B'. Color code corresponds to the angular momentum of the 'outermost' electron in the ground state configuration: orange – f, blue – d, red – p, green – s; *(b)* Same as (a) but using the previous 'Case A' and less detailed ion structure information and electron impact cross sections..

Xe^{26+}, Co-like Xe^{27+}, Mn-like Xe^{29+}, Cr-like Xe^{30+} and Ti-like Xe^{32+} in comparison to the other emissions. In principle, the observed discrepancies could also originate from errors in the calculated PECs, but the systematic correlation of discrepancies for ionization states with their fractional abundances hints towards a strong influence of the ionization balance. In section 7.2 an additional comparison to the 'Case B' data is presented for discharge #19998, which exhibits also a flat xenon concentration profile. In line with the results of section 5.2.1 which documented that the ionization balance '408+408' exhibits considerable deviations to the measurements for tungsten, also for xenon discrepancies were found. Therefore, the '408+408' data are only useful as a

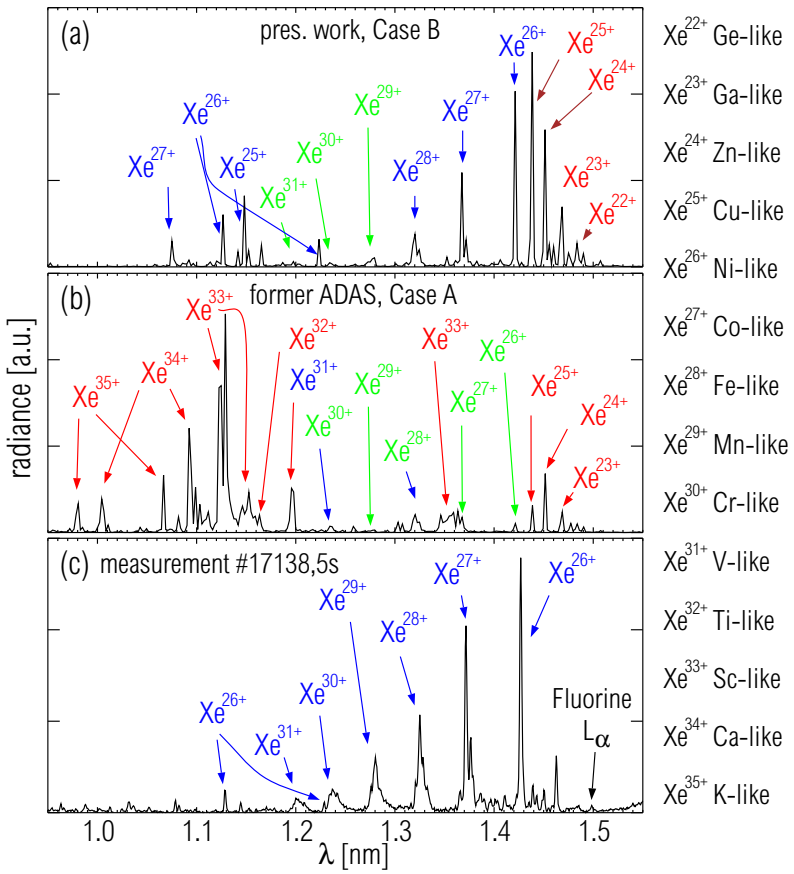

Figure 5.11: *(a)* Modeled xenon spectra using the ionization and recombination data '408+408, Case B' of the present work. Emissions which are remarkably weak in comparison to the rest of the spectrum are labeled by green ionization states and emissions which are too strong relatively to the rest of the spectrum are labeled red. *(b)* Modeled xenon spectra using the ionization and recombination data '408+408, Case A', which existed in the ADAS database. *(c)* Measured spectra from the discharge #17138, which exhibits impurity accumulation with an electron temperature of 1.3 ± 0.3 keV in the accumulation region. The identification of the spectral features is elucidated in section 7.2.

guideline and interpretations need to consider these uncertainties.

For the other high-Z elements investigated in the course of this work a different strategy is used, as the deviations of the '408+408' data in section 5.2.1 exhibit larger shifts in T_e for W than the typical energy difference expected for a small change of the nuclear charge. The ionization potentials are presented in figure 5.12. Therefore, the modified 'CADW+408' ionization and recombination coefficients have been also used for the other high-Z elements, while their values were used for the isoelectronic ionization states and a energy correction according to the differences of the ionization potentials was applied. In general, a simple energy scaling is not correct, due to the non-linear behavior of electronic states in isoelectronic sequences. However, as is

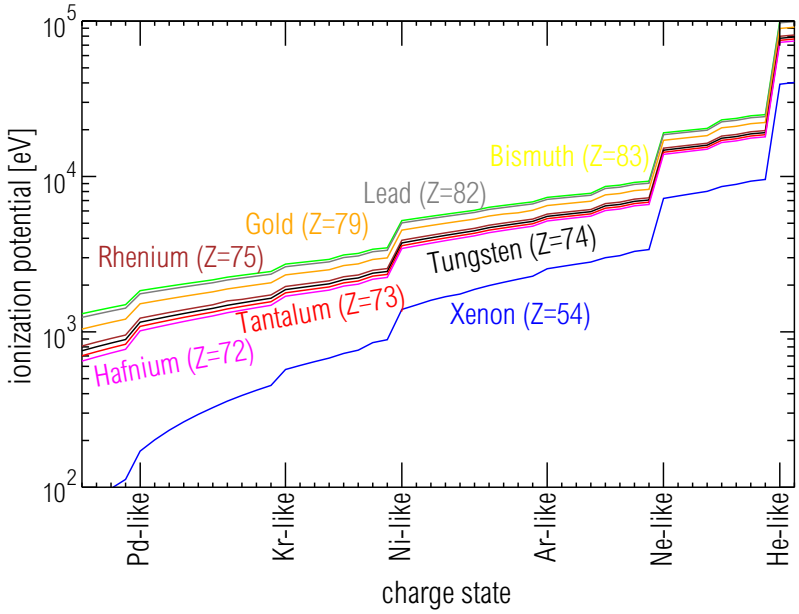

Figure 5.12: Ionization potentials for the investigated elements are being taken from [36], which features only baseline quality. As only relative differences are considered, deviations similar to those found in section 2.3.1 for tungsten, are of low importance. While the xenon ionization potentials are considerably different, the potentials of the other elements are within a narrow interval for a certain isoelectronic state.

shown in the following chapter the dominant features of the impurity spectra do not change drastically except of being shifted in wavelength. This fact justifies the scaling approach.

Chapter 6

Spectral Features of Tungsten

In this chapter, the spectral features of tungsten are presented according to the wavelength ranges in which they appear and spectral lines are identified if possible. Locating the features in wavelength is a basic requirement to do further analysis of the tungsten emissions. The features are compared to code calculations for benchmarking the calculated atomic data and to qualify them for further use. Adding up the radiances of all spectral features allows for obtaining the power radiated by tungsten, which is of central interest for fusion research and is investigated in chapter 8. As the contribution of continuum radiation and weak undetected spectral lines is difficult to estimate, the code calculations are a suitable tool to obtain these experimentally unaccounted contributions. In section 8.1.3, the diagnostic of single ionization states by analyzing corresponding spectral features or lines is described. To allow for these analyses the features and lines in the spectrum need to be known. The focus is put on tungsten, as it is of largest relevance and the analyses could be performed in great detail due to tungsten being an intrinsic impurity in ASDEX Upgrade.

6.1 Visible Spectral Range

The tungsten spectrum in the visible range exhibits many, relatively weak spectral lines. Few spectral lines in the visible spectral range are of interest for the diagnostic of fusion plasmas, as the near-neutral ionization states are abundant in the edge region of the fusion plasma only. Due to the strongly ionizing surrounding and the steep gradients in electron temperature and density, the emitted photons are proportional to the influx of impurity ions. An explanation of this fact, which is exploited by the so called S/XB-method to measure the influx of impurities, is given in [84]. A detailed investigation [85] of the tungsten spectrum at $n_e = 7{\cdot}10^{17}\,\mathrm{m}^{-3}$ and T_e=10 eV exhibited the tungsten line at 400.8 nm ($^7\mathrm{S}_3 - {}^7\mathrm{P}^o_4$) to be the strongest spectral line in the range

350 – 540 nm and best suited to obtain influx measurements in a fusion plasma. Earlier investigations of [86–88] are in agreement with these findings. The S/XB-value, i.e. the ionized tungsten atoms per emitted photon at 400.8 nm was measured as a function of electron temperature (s. figure 6.1) by [85] at the Plasma Simulator (PSI) in Berlin and was confirmed under reactor conditions by measurements on injected $W(CO)_6$ at ASDEX Upgrade [89].

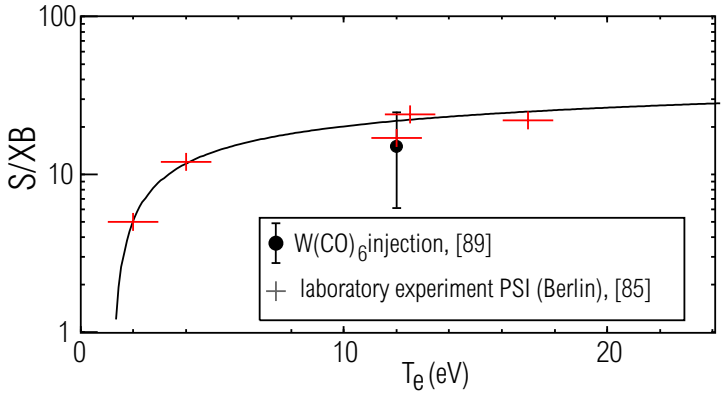

Figure 6.1: Measured S/XB values of the neutral tungsten line at 400.8 nm, including measurements from PSI in Berlin [85](red crosses) and ASDEX Upgrade [89] (black dot and error bars).

6.2 VUV spectral range

6.2.1 Spectral range 4 – 7 nm

For tungsten, the spectral range 4–7 nm has attracted much attention since here a bright emission band is situated. The emission band is formed by a large number of spectral lines and originates mainly from Ag-like W^{27+} to Y-like W^{35+} tungsten ions. This feature was already observed at the ORMAK [90] and PLT [91] tokamaks in the 1970s. A more recent study of the tungsten impurity spectrum at the ASDEX Upgrade tokamak [39] reported that for electron temperatures above 2 keV, many spectral lines appear in the spectrum which superimpose the quasicontinuum emission band. The lines represent transitions in the higher charged tungsten ions (up to Cu-like W^{45+}) and were identified in [39] by means of predicted wavelengths using the HULLAC package [28–31]. Measurements of the radiation from tungsten ions were performed at the Berlin [92] and the Lawrence Livermore National Laboratory [93] EBITs. In [92] spectra were recorded for more than 20 different ions ranging from J-like W^{21+} to Cu-like W^{45+}, while in [93] the narrower range from Rb-like W^{37+} to Cu-like W^{45+} was covered. The experimental wavelengths were compared with the results from HULLAC

calculations, and a general conclusion is that the measured lines appear at somewhat longer wavelengths than predicted (0.05-0.1 nm, depending on the transition).

In the present work, the emission characteristic of the quasicontinuum band for different electron temperature is documented and compared to the EBIT spectra of [92]. For identifying isolated spectral lines, focus is put on using experimental data, while only the number of dominant spectral lines in the considered wavelength range is taken from theory. The precise predictions on wavelengths and line intensities are used in a subsequent step. The theoretical spectra were produced by the ADAS suite [16] employing the Cowan code [14] which uses the plane-wave Born (PWB) approximation. The calculations are further processed by a collisional-radiative model and are interpreted with an ionization balance taken from [39] in the tokamak case. GRASP [24] calculations were performed to obtain corrections for the wavelengths, however the more elaborate calculations on electron impact cross sections were not targeted by GRASP calculations. Figure 6.2 shows several EBIT spectra for varying electron beam energy, while three tokamak spectra for different electron temperature $T_{e,acc}$ in the accumulation region are featured. The quasicontinuum at 5 nm is of large importance concerning the total power radiated by tungsten at electron temperatures between 1 and 2 keV. EBIT investigations [92] showed, that for the excitation with a monoenergetic electron beam the observed structure is much narrower than that emitted in a tokamak discharge, but still consists of several unresolved spectral lines forming a band. Furthermore, these investigations demonstrated that the important transitions are of the type $4p^6 4d^n$-$4p^6 4d^{n-1} 4f$ and $4p^6 4d^n$-$4p^5 4d^{n+1}$, while configuration interaction plays a crucial role [92]. It was observed that this band shifts in wavelength as a function of ion state, which links the broader spectral feature measured in a tokamak to the larger diversity of ion states which are present simultaneously. This is documented here in detail by comparing EBIT spectra with ASDEX Upgrade measurements in figure 6.2.

The vertical lines in figure 6.2 are introduced to guide the eye marking the peak maximum of individual lines. Many features in the tokamak spectra between 4.9 nm and 5.4 nm appear to be isolated spectral lines, however, EBIT findings [92] and the larger line width suggest that they consist of a few lines emitted from the same ion state. For the first time in a tokamak, it could be documented that the quasicontinuum at lower wavelengths (4.9 nm) is emitted at lower electron temperatures, just above 1 keV, while the part at the longer wavelengths (5.4 nm) is emitted at electron temperatures of up to 2.1 keV (s. gray arrow in figure 6.2). The corresponding emissions in the EBIT spectra are also highlighted with a grey arrow in figure 6.2 and are visible at 4.9 nm up to 5.4 nm for beam energies of 0.87 keV up to 1.79 keV, respectively. In [92] the emitting ion states have been identified to be Ag-like W^{27+} to Y-like W^{35+}. There,

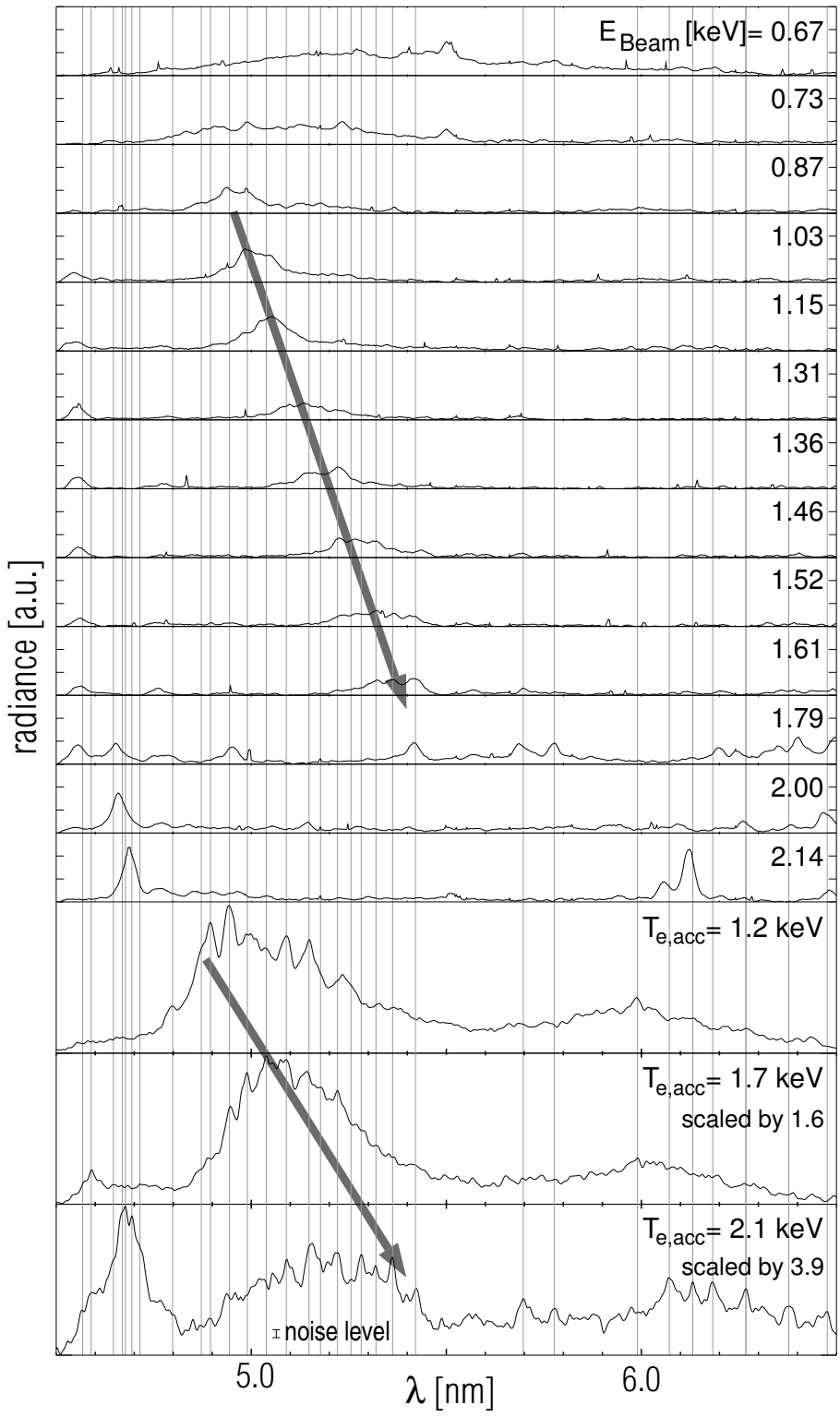

Figure 6.2: EBIT spectra for several electron beam energies compared with tokamak spectra from ASDEX Upgrade discharge #19436 with impurity accumulation. Vertical lines are drawn to guide the eye. For better display, the tokamak spectra for $T_{e,acc}$=2.1 keV (t = 6.53 s) and $T_{e,acc}$=1.7 keV (t = 6.60 s) are scaled relatively to the spectrum for $T_{e,acc}$=1.2 keV (t = 7.00 s) by factors 3.9 and 1.6, respectively. EBIT spectra are not scaled relative to each other to give an impression of the relative strength of emissions which are superimposed in the tokamak spectra.

the atomic calculations show, that high electron densities (above $\approx 1 \cdot 10^{20}\,\mathrm{m}^{-3}$) lead to a distribution of intensity on many spectral lines for each ion state, which makes the spectral feature appear broader. This effect may occur for the tokamak plasmas investigated which have densities of $\approx 8 \cdot 10^{19}\,\mathrm{m}^{-3}$. However, this effect is obscured by the simultaneous emissions of neighboring ions which is the primary reason for the broad appearance of the quasicontinuum. Several ion states between the Ag-like W^{27+} to Y-like W^{35+} coexist even for the case of impurity accumulation as is indicated by the ionization balance discussed in chapter 5. Their emission form a broad, distinct feature in the spectrum.

When looking at the tokamak spectra for $T_{e,acc} = 1.2\,\mathrm{keV}$ and 1.7 keV, a local maximum of the emission is visible at about 6.0 nm. A corresponding emission for relevant electron energies is not found in the EBIT spectra. This possibly could also be an effect of the different electron density, as is discussed above.

For electron temperatures above $\approx$2 keV single spectral lines superimpose the quasicontinuum. These lines show up in the EBIT spectra for electron energies above $\approx$2 keV. Each spectral line in the EBIT spectra was fitted with a Gaussian line profile (FWHM $\approx 0.025\,\mathrm{nm}$). The fitted amplitudes for several lines around 6.1 nm are plotted versus beam energy in figure 6.3(a). A spectrum from an ASDEX Upgrade discharge for the corresponding spectral range is shown in figure 6.3(b). By plotting the line intensity versus beam energy, identification of the emitting charge state is possible. As the energy of the ionizing electron beam is known a comparison with the ionization potentials gives the maximum ion charge attainable with a certain beam energy. The ionization potentials which are marked in figure 6.3(a) by vertical lines were calculated by GRASP.

A unique identification based on purely experimental findings is not possible for all lines. For instance, line-like feature '4' in figure 6.3(b) consists of a pair emitted by Ga-like W^{43+} and Ge-like W^{42+}. Figure 6.3(a) suggests that line blending takes place since the intensity increases already at beam energies high enough only for Ge-like W^{42+}. Conversely, when increasing the beam energy further, the line intensity decays similar to the intensities of spectral line '3', which is emitted by Ga-like W^{43+}. A confirmation of this observation is given by the fact that ADAS calculations predict two Ga-like W^{43+} and one Ge-like W^{42+} spectral lines at this wavelength range. In fact, the pair of lines can be resolved when looking in second order of the spectral lines at $\approx 12.24\,\mathrm{nm}$ and $\approx 12.26\,\mathrm{nm}$ (s. figure 6.8(b)). The accounting of lines in a wavelength range by comparison to the theoretical data does not rely on high accuracy of predicted wavelengths and intensities. However, this procedure is not successful for charge states with several weak lines close to the detection limit, i.e. Y-like W^{35+} – Kr-like W^{38+}. Ten spectral lines in the range 4 –7 nm could be identified and are summarized in table

6.1. The identification agrees with the earlier findings in [39, 92, 93] and is also affirmed by the behavior of the spectral lines, when emitted by a plasma which is cooling down. The last column in table 6.1 is indicating the method used to identify the line. 'E' indicates that the energy dependence of the line intensities in EBIT spectra was used, while transitions labeled with 'T' result from the analysis of the temporal behavior (s. section 5.1 and 6.2.2), i.e. dependence on electron temperature, of spectral lines emitted by tokamak plasmas.

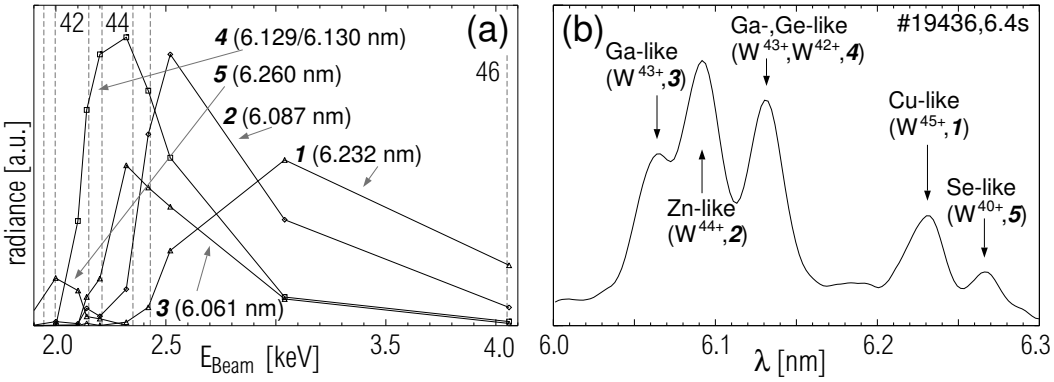

Figure 6.3: *(a)* Fitted line intensities from EBIT spectra versus electron beam energy. Numbers in front of the wavelengths correspond to the line labeling in part (b) of the figure. The vertical, dashed lines indicate the ionization potentials of Se-like W^{40+} to Ni-like W^{46+},; *(b)* Spectrum from ASDEX Upgrade.

Two observations around 4.7 nm are reported in the following which, however, do not yield identifications of individual lines. Firstly, the tokamak (s. figure 6.4) and EBIT spectra feature a structure at the short wavelength wing of the Ge-like W^{42+} line formed by lines from lower lying ion states down to about Rb-like W^{+37}. The lines are ordered such that lower charged ion states emit lines at shorter wavelengths as can be seen by comparing the spectra for decreasing $T_{e,acc}$ (s. figure 6.4). The lowermost spectrum in figure 6.4 exhibits that already at an electron temperature of $T_{e,acc} \approx 2.1$ keV the lowest emitting charge state for this feature is reached, while for the EBIT spectra this is the case for beam energies of ≈ 2.0 keV. Secondly, for even lower electron energies, the emissions in the tokamak can not be correlated to the EBIT spectra as will be described in the following. In the case of the tokamak spectra at $T_{e,acc}$=1.8 keV, many small lines form a structured background from 4.55 nm to 4.8 nm, on which the above described spectral feature is superimposed. Adjacent to the short wavelength edge of this feature, weak lines form a quasicontinuous background down to 4.4 nm. In the EBIT spectra, lines at 4.53 nm are visible for electron energies in the range 0.97–1.79 keV (s. figure 6.2), which are too weak to explain the tokamak emissions. In the tokamak no lines are observed for electron temperatures below

1.8 keV. Additionally, not only the energy range of the lines does not correlate, but also there is a larger number of lines visible in the tokamak than in the EBIT spectra. This difference may occur due to the difference in electron density between the EBIT ($\approx 1 \cdot 10^{18}\,\mathrm{m}^{-3}$) and the tokamak plasma ($\approx 8 \cdot 10^{19}\,\mathrm{m}^{-3}$). The theoretical investigation in [92] suggests the occurrence of many more lines in the tokamak case due to the higher density, however, an identification is not possible here due to the vast number of lines and the theoretical uncertainties. In figure 6.4 some spectral lines are marked with vertical lines to guide the eye.

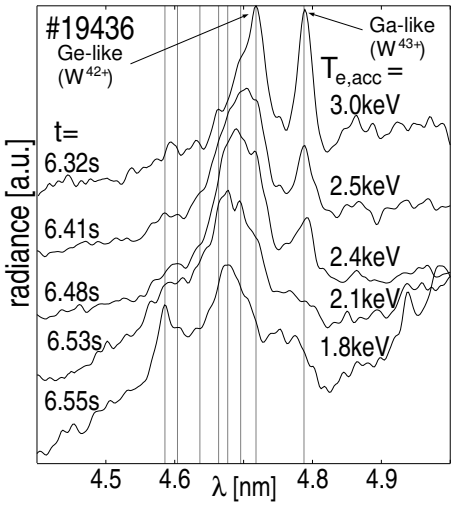

Figure 6.4: Spectra from ASDEX Upgrade showing the feature at 4.7 nm. The spectra taken at different times correspond to different electron temperatures in the accumulation region ($T_{e,acc}$) and are shifted vertically for clarity.

A closer view on the modeled spectra is presented in the following, as the code calculations of ADAS are in the focus of the present work. In figure 6.5 the modeled spectra at the spectral range 4 – 6.5 nm are presented for different electron temperatures. While figure 6.5(a) and 6.5(b) correspond to discharge phases with impurity accumulation the spectrum in figure 6.5(c) is taken from discharge #19115, which exhibits a flat tungsten concentration profile. The modeled spectra agree moderately well to the corresponding measured spectra. The differences arise in wavelength and intensity, but the main features (i.e. the dominant, isolated spectral lines, their distribution in the spectrum and their relation to the quasicontinuum) of the measured spectra can be identified in the model. In figure 6.5(c), the quasicontinuum seems to be overestimated with respect to the spectral lines as was already documented in figure 5.8. Also the quasicontinuum seems to exhibit a slightly different shape, as if the ionization states above Tc-like W^{31+} are under-represented in the ionization balance or the emissivity of the spectral lines is calculated too weak. The ionization balance was

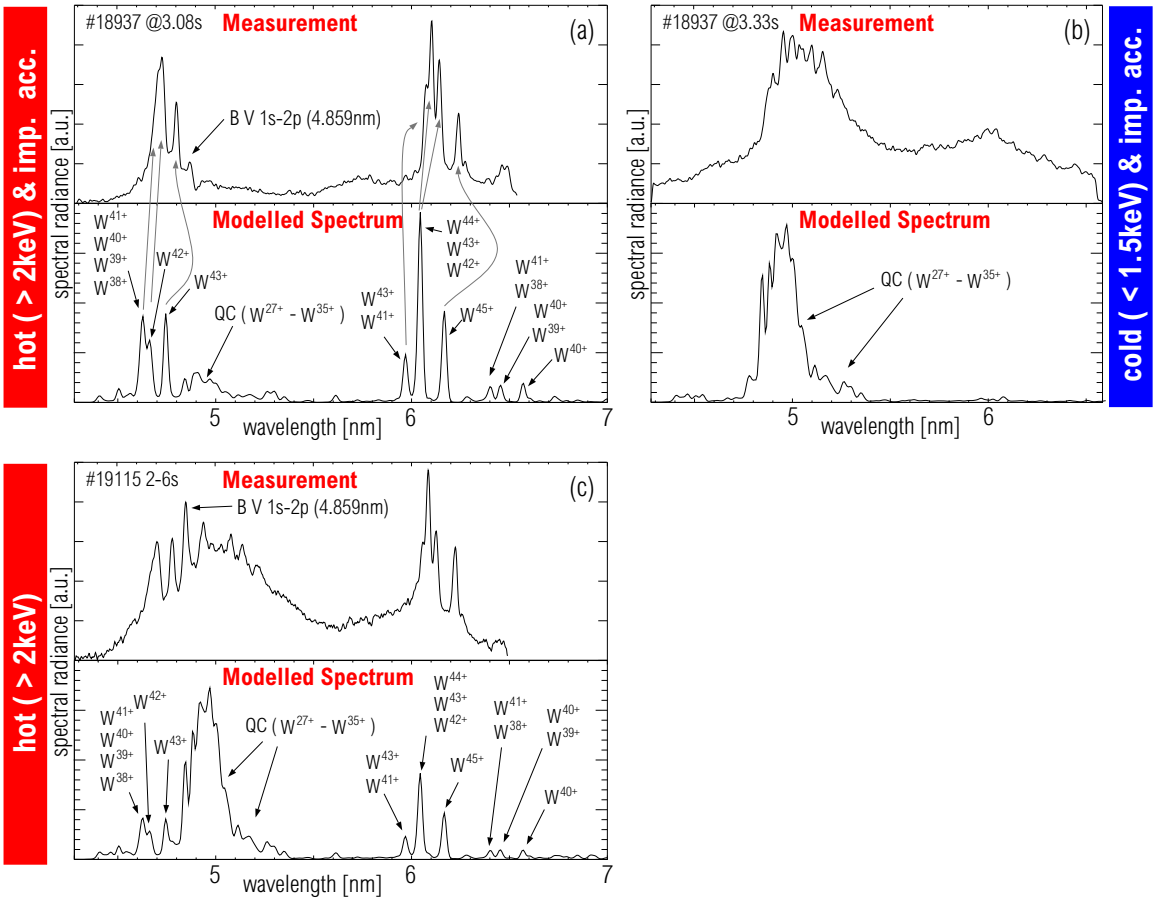

Figure 6.5: *(a)* Measured and modeled spectra for an impurity accumulation phase, in which the accumulation region exhibited a temperature of $\approx 3\,keV$. The radiation profile is peaked in the center by a factor of about 25, therefore, the quasicontinuum (QC) is strongly suppressed in comparison to the other emissions in the spectrum. The spectral lines start to emerge in the spectrum for temperatures above 2 keV. The modeled spectra were obtained using ADAS data. *(b)* as (a) but for electron temperatures below 1.5 keV *(c)* Measured and modeled spectra for discharge #19115 with an approximately flat tungsten concentration and a central electron temperature of $\approx 3.6\,keV$.

already optimized in chapter 5 and therefore, the presented discrepancy can not be resolved by further adjustment of the equilibrium. In chapter 8, also the total radiated power of this wavelength range is compared to the predicted power and agreement is found within the uncertainties. It may be noted, that the level of disagreement is comparable to that, which is found between the spectra and the HULLAC predictions in [92]. For these, also deviations in wavelengths and intensity are found, which are of similar size as the discrepancies which can be identified in figure 6.5. In [92] it was reported, that HULLAC data managed to reproduce the quasicontinuous emissions of the ionization states Rh-like W^{29+} to Y-like W^{35+}, but a systematic deviation towards lower wavelengths is observed in the HULLAC predictions (s. figure 6.6). In the presently obtained ADAS data, also the quasicontinuous structures are visible and

similar deviations, but slightly smaller, as for the HULLAC data are observed (s. figure 6.6). It may be noted, that in [92] the emissions around 5.13 nm are attributed to Rh-like W^{29+} leaving the emissions of tungsten between 4.9 and about 5.05 nm to ion states below Rh-like W^{29+}. This does not correspond to the calculation of the ADAS code, which predicts small contributions to the quasicontinuum of Ag-like W^{27+} and negligible contributions of lower lying ionization states, while only one spectral line of Pd-like W^{28+} is predicted at 4.845 nm. In [94–96] strong lines of Ag-like W^{27+}, Pd-like W^{28+} and Rh-like W^{29+} were identified at 4.9403 nm, 4.8948 nm and 4.9785 nm, respectively. This suggests, that the evaluated data points from [92] which are presented in figure 6.6 are at too long wavelengths for Rh-like W^{29+} to about Tc-like W^{31+}. In [92] it is pointed out that using an empirical rule the correlation between emissions and ionization state became possible, even though line blending is also occurring in the EBIT spectra. Additionally, the ionization potentials of Rh-like W^{29+} and charge states above differ by relatively small energies from that of the lower lying ionization states, which makes a discrimination of emission more difficult. These uncertainties may lead to the observed discrepancies.

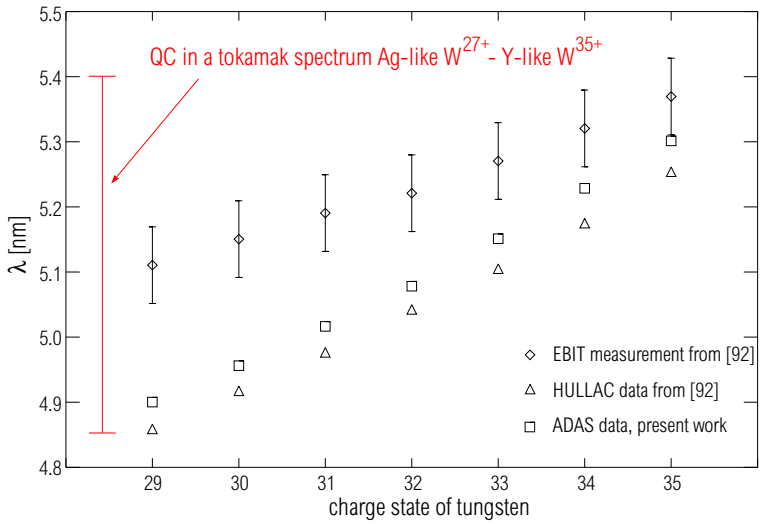

Figure 6.6: Wavelengths of the quasicontinuous emissions around 5 nm from individual ionization states of tungsten. The presented wavelengths are the mean of the emissions weighted by their intensity. Diamonds and triangles indicate the measured and calculated data from [92] originating from the Berlin EBIT and HULLAC, respectively. Squares originate from the ADAS data of the present work.

6.2.2 Spectral range 12 – 14 nm

The spectral range between 7–12 nm is omitted here as only a few, weak tungsten lines can be detected in this range. In [39] lines have been identified in the spectral range 12 –14 nm, however, the identifications of the present work exhibit clear differences. In this range we identify the charge states by analyzing the evolution of the spectral lines in a tokamak discharge as indicated in section 5.1.

In discharge #18938 impurity accumulation is observed beginning at about 2.0 s after plasma startup. While the accumulation volume stays constant in size, its temperature starts to drop and undergoes the evolution featured in figure 6.7 (b) . The temperature dependence results from a complex interplay of heating and cooling processes, but for the following analysis these details are not important since the temperature is known from measurements. The impurity accumulation remains unaffected during the change in temperature, as can be judged from the time traces of bolometer channels which behave similarly as in discharge #19436 (s. figure 5.1). Outside the accumulation region the impurity concentrations are negligibly low and the emissions from that region are not visible in the spectra. Similar to the bolometer signal which is dominated by the radiation from the accumulation region, the spectra also show emissions which preferentially originate from there. These circumstances allow the assignment of an electron temperature to the emissions with an uncertainty of about $\Delta T_e = \pm 200\,\mathrm{eV}$. At this point the analysis can be done as indicated in the section 5.1. For the phase with impurity accumulation, the temporal behavior of unknown lines is compared with that of spectral lines which have been identified unambiguously in section 6.2.1. Figure 6.7 (a) shows the time traces of the fitted amplitudes in discharge #18938 corresponding to the reference lines at 6.232 nm (Cu-like W^{45+}), 6.093 nm (Zn-like W^{44+}), 6.063 nm (Ga-like W^{43+}), 4.718 nm (Ge-like W^{42+}), and 6.268 nm (Se-like W^{40+}). Unfortunately, the fit for the spectral line at 4.718 nm is influenced by the neighboring As-like W^{41+} spectral line. Therefore, the time trace shown is a mixture of both time traces for Ge-like W^{42+} and As-like W^{41+}. The time traces have been normalized to the value of the first maximum. For As-like W^{41+}, there is no reference line from the above identification in the range 4 –7 nm. In figure 6.7(b) the temperature variation inside the accumulation region is plotted, which is responsible for the time evolution of ion abundances and corresponding spectral line intensities. In figure 6.7 (c) the time dependence for a sample of 5 spectral lines around 13 nm is traced. A distinct feature in the time traces for different ion states is the rise in the intensity from $t = 2.2\,\mathrm{s}$ to $t = 2.6\,\mathrm{s}$. It is shifted in time for different charge states. For the ion states with charges higher than W^{40+} the line intensities decrease after $t = 2.4\,\mathrm{s}$ and show two minima ($t = 2.65\,\mathrm{s}$ and $t = 2.73\,\mathrm{s}$). For the ion states below W^{41+}, the line intensities do not decrease as a further drop in temperature would be necessary for that. With this method six spectral lines at 12.720 nm

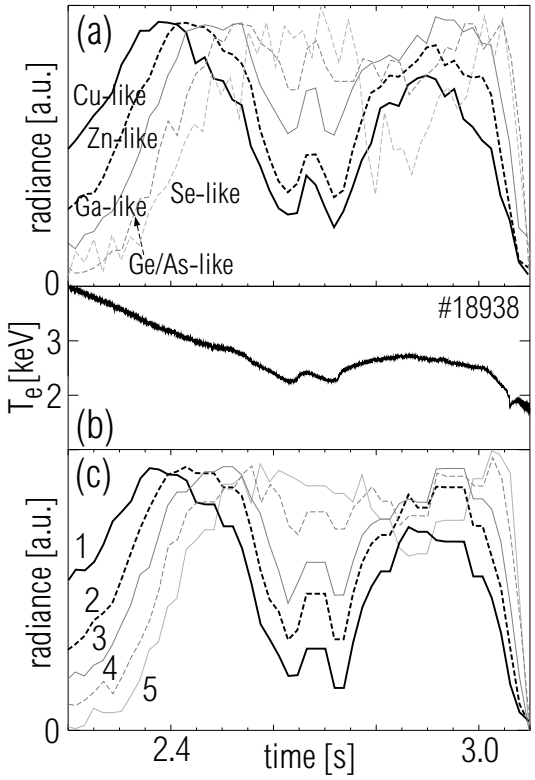

Figure 6.7: *(a)* Time traces for amplitudes of reference spectral lines in the range 4–7 nm which have been assigned in section 6.2.1 for discharge #18938; *(b)* Electron temperature inside the accumulation region at ρ_{pol}=0.15; *(c)* Time traces for intensities for a sample of 5 lines around 13 nm for which following assignment was obtained: line 1 (12.720 nm): Cu-like W^{45+}, line 2 (13.287 nm): Zn-like W^{44+}, line 3 (12.639 nm): Ga-like W^{43+}, line 4 (12.945 nm): Ge-like W^{42+}, line 5 (13.121 nm): As/Se-like $W^{41+/40+}$.

(Cu-like W^{45+}), 13.287 nm (Zn-like W^{44+}), 12.824 nm (Ga-like W^{43+}), 12.639 nm (Ga-like W^{43+}), 13.534 nm (Ga-like W^{43+}) and 12.945 nm (Ge-like W^{42+}) could be identified. For 6 additional lines, i.e. 12.912 nm (Ge/As-like $W^{42+/41+}$), 13.475 nm (Ga/Ge-like $W^{43+/42+}$), 13.121 nm (As/Se-like $W^{41+/40+}$), 13.896 nm (As/Se-like $W^{41+/40+}$), 12.864 nm (Se/Br-like $W^{40+/39+}$) and 13.487 nm (Se/Br-like $W^{40+/39+}$), the emitting charge state could be restricted to two charge states as their time traces run in between the reference time traces. To assign these spectral lines to a single charge state the modeled spectrum from figure 6.8(a) was used. Figure 6.8(b) shows the spectrum with the above assigned lines. The present assignment of lines differs from that performed in [39] (cf. figure 6.8(c)) where only the wavelength and intensity predictions were used to identify the emitting charge state.

The new line identification (cf. figure 6.8(b) and table 6.1) is supported by two facts. Firstly, the wavelength calibration has been improved and differs by about 0.05 nm from the previous values. This discrepancy lies well inside the error bars (0.1 nm) of

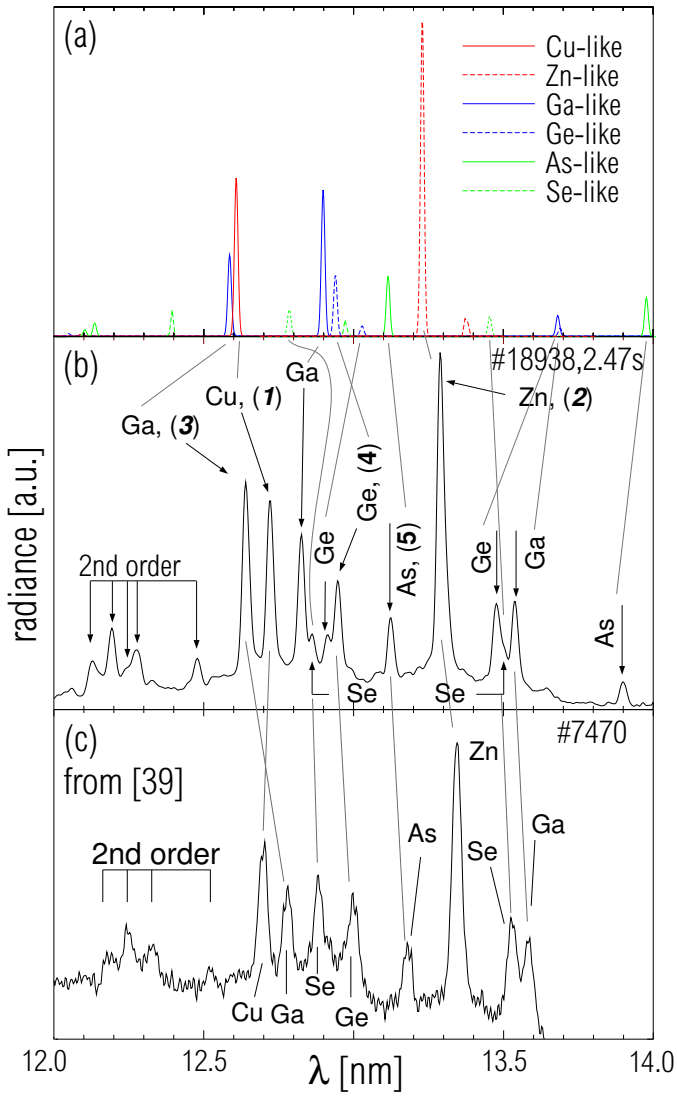

Figure 6.8: *(a)* Synthetic spectrum from ADAS (Cowan/PWB) with wavelengths adjusted according to the calculations using the GRASP code. The ion balance corresponds to corona equilibrium derived from adjusted ([39]) ADPAK data; *(b)* Tokamak spectrum with the line identification of the present work. Numbers in brackets correspond to labels in figure 6.7(c); *(c)* Tokamak spectrum and identification taken from [39]

the calibration used in [39]. Secondly, the errors in the calculated wavelengths from [39] are larger in the 12 –14 nm spectral region compared with those in the 4–7 nm range. For Cu-like W^{45+} and Zn-like W^{44+} the uncertainties of the HULLAC calculations are in the range of 0.1 nm, while for Ga-like W^{43+} to Se-like W^{40+} the errors are around 0.2 nm.

When discussing the uncertainties in the theoretical predictions it should be mentioned that the ADAS calculations typically deviate in this wavelength range by 0.25 nm and show the largest deviations of 0.5 nm for one Ga-like W^{43+} line. To

improve the calculated wavelengths of the spectral lines the energy levels have been evaluated independently by the relativistic structure code GRASP [24], since GRASP features the solution of the Dirac equation in contrast to the Hartree-Slater algorithm of the Cowan code which treats relativistic effects perturbatively. This procedure enabled improved identification of the transitions within an ion state. Typical wavelength uncertainties of the GRASP calculations are between 0.1 nm and 0.2 nm. The emissivities shown in figure 6.8 originate from ADAS.

Ion	transition	λ_{calc} (nm)	λ_{tok}	λ_{EBIT}, [92]	λ_{EBIT}, [93]	meth.
W^{45+}	$4s\ ^2S_{1/2} - 4p\ ^2P_{3/2}$	6.217	6.232	6.232	6.23355(19)	E/T
(Cu–like)	$4s\ ^2S_{1/2} - 4p\ ^2P_{1/2}$	12.609	12.720	12.701		T
W^{44+}	$4s^2\ ^1S_0 - 4s4p\ ^1P_1$	6.073	6.093	6.087	6.09310(17)	E/T
(Zn–like)	$4s^2\ ^1S_0 - 4s4p\ ^3P_1$	13.230	13.287	13.275		T
W^{43+}	$4s^24p\ ^2P_{1/2} - 4s^24d\ ^2D_{3/2}$	4.760	4.791	4.769	4.79029(24)	E/T
(Ga–like)	$4s^24p\ ^2P_{1/2} - 4s4p^2\ ^2P_{1/2}$	6.020	6.063	6.061	6.06157(42)	E/T
	$4s^24p\ ^2P_{1/2} - 4s4p^2\ ^2D_{3/2}$	6.119	6.135	6.129	6.13341(21)	E/T
	$4s^24p\ ^2P_{1/2} - 4s4p^2\ ^4P_{1/2}$	12.899	12.824			T
	$4s^24p\ ^2P_{1/2} - 4s^24p\ ^2P_{3/2}$	12.587	12.639			T
	$4s^24p\ ^2P_{3/2} - 4s4p^2\ ^2D_{5/2}$	13.682	13.534			T
W^{42+}	$4s^24p^2\ ^3P_0 - 4s4p^3\ ^3D_1$	6.115	6.123	6.130	6.13039(60)	E/T
(Ge–like)	$4s^24p^2\ ^3P_0 - 4s^24p^2\ ^1D_2$	12.940	12.945			T
	$4s^24p^2\ ^3P_0 - 4s^24p4d\ ^3D_1$	4.685	4.718	4.697	4.71905(28)	E/T
	$4s^24p^2$ J=1 – $4s4p^3$ J=2	13.029	12.912			T
	$A = 1.1 \cdot 10^{10}\,s^{-1}$					
	$4s^24p^2$ J=2 – $4s4p^3$ J=2	13.690	13.475			T
	$A = 9.0 \cdot 10^{9}\,s^{-1}$					
W^{41+}	$4s^24p^3$ J=3/2 – $4s4p^4$ J=5/2	6.482	6.481	6.482	6.48883(47)	E/T
(As–like)	$A = 2.8 \cdot 10^{11}\,s^{-1}$					
	$4s^24p^3$ J=3/2 – $4s^24p^3$ J=5/2	13.106	13.121			T
	$A = 2.5 \cdot 10^{5}\,s^{-1}$					
	$4s^24p^3$ J=3/2 – $4s^24p^3$ J=3/2	13.968	13.896			T
	$A = 6.0 \cdot 10^{4}\,s^{-1}$					
W^{40+}	$4s^24p^4\ ^3P_2 - 4s4p^5\ ^3P_2$	6.243	6.268	6.260	6.26885(38)	E/T
(Se–like)	$4s^24p^4\ ^3P_2 - 4s^24p^4\ ^1D_2$	12.786	12.864			T
	$4s^24p^4\ ^3P_2 - 4s^24p^4\ ^3P_1$	13.455	13.487			T
W^{39+}	$4s^24p^5$ J=3/2 – $4s^24p^44d$ J=5/2	6.403	6.457	6.474	6.46606(155)	E/T
(Br–like)	$A = 6.0 \cdot 10^{11}\,s^{-1}$					

Table 6.1: Identified transitions with the levels taken from atomic data calculations of ADAS; theoretical wavelengths have been taken from GRASP. Corresponding lines in the codes have been identified via their total angular momenta and Einstein coefficients, while the LS-coupled terms are attributed corresponding to a major contribution to the actual state. If no unique identification is possible only the J values and the corresponding transition probability is given. The experimental uncertainty in wavelength for the tokamak and the EBIT spectra [92] is ± 0.005 nm. EBIT wavelengths in the wavelength range around 13 nm originate from an wavelength survey at few electron beam energies. Method 'E' uses the beam energy dependence of the line intensity taken from EBIT spectra. Method 'T' uses the temporal evolution in an ASDEX Upgrade discharge.

6.2.3 Spectral range 2 – 3.5 nm

This spectral range is of low importance, when considering the total radiated power, as only relatively weak emissions are found at ASDEX Upgrade. Quasicontinuous emissions were observed here from the charge states between Sn-like W^{24+} to Tc-like W^{32+}, while spectral lines of charge states above Ni-like tungsten are observed for electron temperatures well above 4 keV. The wavelength calibration is obtained *in situ* via the H-like spectral lines of carbon at 3.373 nm and 2.847 nm and the He-like oxygen lines at 2.160 nm and 2.210 nm resulting in an uncertainty of 0.005 nm for the wavelength calibration. In figure 6.9 three spectra are presented for impurity accumulation phases with electron temperatures from 1.1 –0.65 keV. These emissions have already been reported and analyzed in [97, 98], while their behavior versus electron temperature is documented in the present work. In figure 6.9 also the theoretical predictions of ADAS (intensity and wavelength) for each ionization state is presented, which originate from transitions between the configurations $4d^{10}4f^{n}$ and $4d^{9}4f^{n}5p^{1}$ / $4f^{n-1}5g^{1}$ for ionization states below Ag-like W^{27+} (inclusive) and between $4d^{n}$ and $4d^{n-1}5p^{1}$ for the ionization states above. For the ionization states Rh-like W^{29+} to Tc-like W^{31+} also contributions from $4d^{n}$ to $4d^{n-1}5s^{1}$ are predicted between 2.9 and 3.5 nm. The wavelength dependence of the predictions exhibits that the emissions of higher charged ionization states are occurring at smaller wavelengths. The identification according to the same wavelengths is not rigid, but the obvious structures at 2.63 nm, 2.72 nm, 2.82 nm, 2.95 nm, 3.1 nm and 3.24 nm can be attributed due to the predictions and their behavior for decreasing electron temperature to the ionization state groups $W^{32+/31+/30+}$, $W^{31+/30+/28+}$, $W^{30+/29+/28+/27+}$, $W^{28+/26+}$, $W^{28+/26+/25+}$ and $W^{26+/24+}$, respectively (s. figure 6.9, lower part). For T_e=0.65 keV, the intensity of Pd-like W^{28+} to Mo-like W^{32+} emissions are much too weak compared to those at T_e=1.1 keV, when the ionization balance in figure 5.9 is used as a guideline. This hints towards discrepancies of the ionization balance for ionization states below Pd-like W^{28+}. The fractional abundance of the ionization states around In-like W^{25+} are considerably strong for 0.65 keV, but it is not clear, if they have reached their maximum or whether their fractional abundance would still increase for a further decrease in electron temperature. Even though some evidence is found for discrepancies in the ionization balance an adjustment of the recombination rates was not attempted, because many degrees of freedom exist. For these ionization states, the shape of the fractional abundance curve versus electron temperature is not available, which would allow for nearly arbitrary manipulation, which does not yield further information. For the investigation in the next subsection, the clear evidence of the large abundances of the ionization states below Pd-like W^{28+} at electron temperatures between 0.65 and 1.1 keV will be of importance.

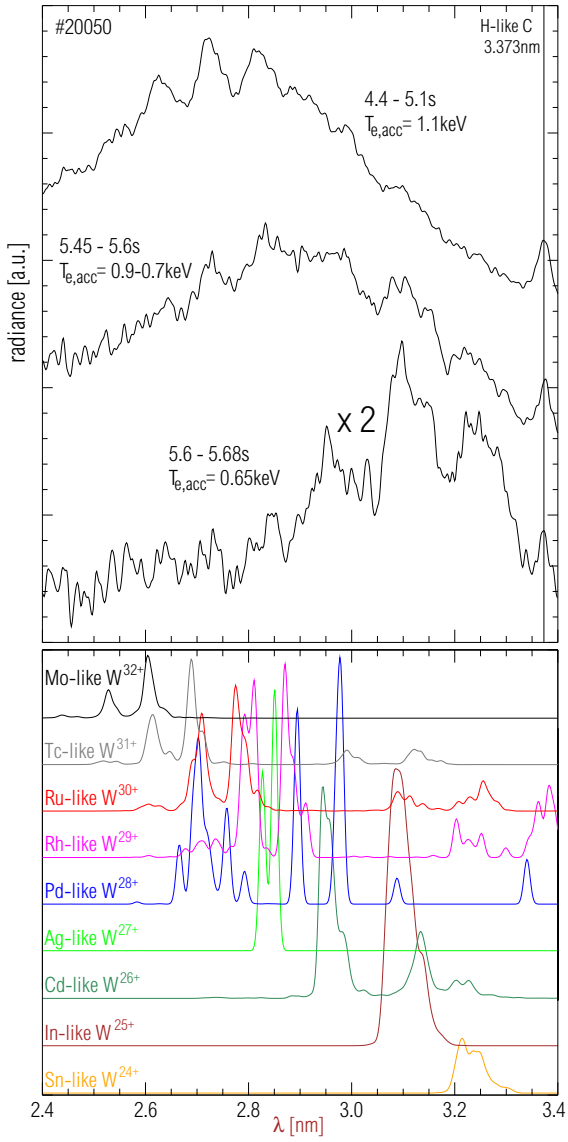

Figure 6.9: Spectral feature emitted from a region of the plasma with electron temperatures between 1.1 and 0.65 keV. The emissions originate mainly from Sn-like W^{24+} to Mo-like W^{32+} tungsten according to the dependence on electron temperature and the predicted emissions (ADAS was used for intensity and wavelength), which are presented in the lower part of the figure.

At electron temperatures above 4 keV emissions of ionization states above Ni-like W^{46+} get apparent in the range 2–3.5 nm. In figure 6.10, a spectrum for T_e=5 keV with weak impurity accumulation (peaking factor of impurities about 5–10) is presented. However, a clear identification of lines is not possible as line blending occurs and the presented signal to noise ratio can only be reached, when the spectra are averaged from 2.7–3.4 s. Therefore, the dependence of the intensity of the spectral lines on electron temperature, which is dropping after 3.4 s, is not known. In the lower part of figure 6.10, predictions of the ADAS calculations for the transition between

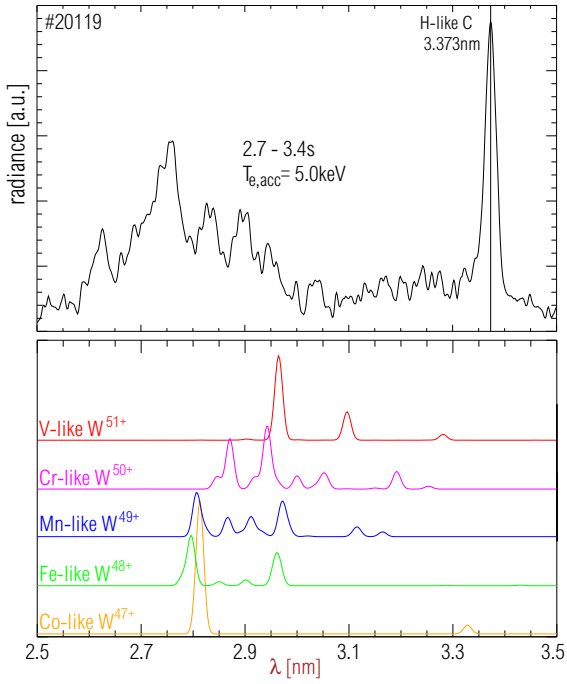

Figure 6.10: Spectral feature emitted from a region of the plasma with electron temperatures of 5 keV. The emissions originate mainly from Co-like W^{47+} to Cr-like W^{50+} tungsten according to the ionization balance of figure 5.9 and the predicted emissions (ADAS was used for intensity and wavelength), some of which are presented in the lower part of the figure.

$3p^6 3d^n$ and $3p^5 3d^{(n+1)}$ are presented. The wavelengths of the predicted spectral lines exhibit a shift of about 0.06 nm towards larger wavelengths, while GRASP calculations result in the wavelengths which are too short by only about 0.01 nm for the ionization states of Co-like W^{47+} to Mn-like W^{49+}. The corrections obtained from the GRASP calculations were not applied for figure 6.10, because for the other ion states featured the available GRASP version could not calculate the transitions of interest due to the larger complexity caused by the increasing number of missing electrons in the 3d-shell. A part of the feature around 2.755 nm can be attributed to the predicted Co-like W^{47+} and Fe-like W^{48+}, which is in agreement to the findings in [99], where these spectral lines were measured at 2.7668 nm and 2.7520 nm. It may be noted, that the feature at 2.63 nm is not understood by the predictions and the detailed correspondence of observed spectral lines and predicted emissions is obscured by line blending and the uncertainties of the predictions.

6.2.4 Spectral range 14 – 30 nm

This spectral range is used in fusion plasmas to diagnose impurities in the mid-Z to low-Z range. It has been reported from JET [18], TEXTOR [100] that in this spectral

range tungsten laser ablations led to a broad feature between 10 and 30 nm, which overlays the spectrum. At TEXTOR, the rise of the emissions after the laser ablation happened within the first two milliseconds [100]. Within that time the injected tungsten ions could have reached locations in the plasma with $T_e \leq 500\,eV$, as simulations with STRAHL suggest [100]. The analysis using STRAHL at ASDEX Upgrade points to a similar result. Figure 6.11 features the analysis on a tungsten laser ablation into a plasma with central electron temperature of 2.1 keV. The first spectrum (cf. figure 6.11(a)) after the laser blow-off (LBO) exhibits already the maximum of the emissions integrated from 16 – 22 nm. As saturation occurs for part of the spectrum the first two spectra were extrapolated in the range, where saturation occurs. For discharges with higher electron temperatures, the emissions do not saturate even for the first spectrum after the laser ablation, because the emitting ionization states are shifted further to the edge and the emitting plasma shell is thinner. For better analysis of the evolution of the radiance of the feature, discharge #18727 was nevertheless chosen. The analysis

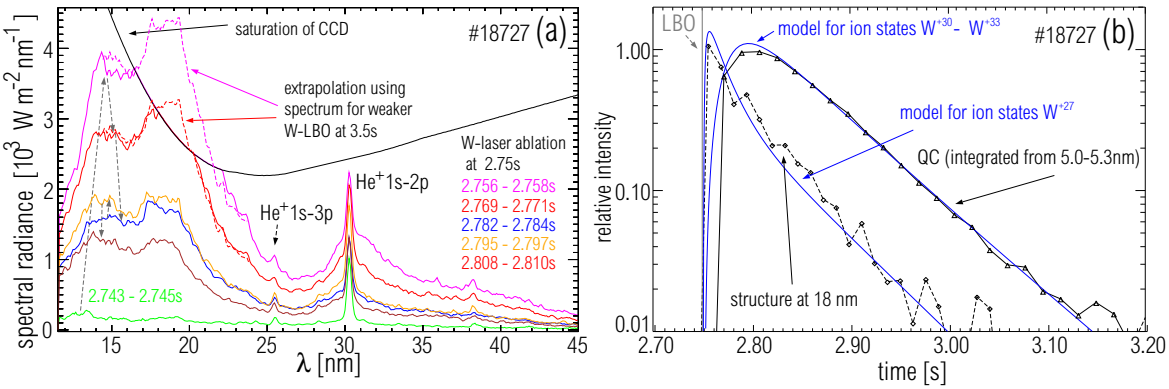

Figure 6.11: *(a)* Spectra before and after a laser ablation of tungsten featuring a broad structure around 18 nm. The first two spectra have been extrapolated using spectra of laser ablations involving less tungsten, due to a partial saturation of the measurements. *(b)*Measured evolution of the emissivities after a laser ablation. The presented traces (black using additionally symbols) correspond to the signal integrated in the interval 16 – 22 nm (structure at 18 nm) and the interval 5.0 –5.3 nm (central part of the quasicontinuum). The blue traces denote the integral of the charge state densities along the LOS for the stated charge states for the modeled plasma. Modeled behavior was obtained by STRAHL.

does not give a definite answer on the emitting ionization state of the structure around 18 nm, as it is not clear if the normalization of the measured time trace within the first 10 ms is correct, or whether emissions are not seen due to the CCD being readout at that time. However, Ag-like W^{+27} is an upper border for the emitting ionization states. Two observations allow to obtain more detailed information. The first is, that the feature exhibits a large radiance for discharge #18727, while for hotter discharges the radiance for similar LBO is smaller by about factor of 5. The second is, that

in discharge #18727 the decay of the radiance is observed, which runs in parallel to the central tungsten concentration obtained from the radiance of the quasicontinuum. The latter is only detectable, if recombination into the emitting ionization states takes place at a large enough volume before the ions are neutralized at the wall or at in the edge region with steep gradients in electron densities and temperatures. For discharges hotter than #18727 the radiance of the feature is only considerable until a few milliseconds after the LBO, and the radiance of the feature then drops drastically exhibiting no signs of recombination into the ionization states of interest. Both observations lead to the conclusion that for #18727 the emitting ion states are inside the radius of steep edge gradients, while for hotter discharges these ion states are in the steep gradient region of the plasma at $\rho_{pol} \approx 0.97$. For the analysis of the LBO in #18727 this implies that Xe-like W^{20+} is the lowest ionization state which could contribute significantly to the observed structure, while the above analysis revealed Ag-like tungsten as an upper border of emitting ion states. It may be noted that the emissions, which appear dominant in the spectrum are for discharges without LBO hardly visible, because for a continuous tungsten source from the first wall which would give similar tungsten densities at the plasma edge as during the laser blow-off, the tungsten densities at the core of the plasma would exceed critical levels. This is found for certain impurity accumulation discharges, where remarkably low central temperatures in the range and below 1 keV are observed. There, similar structures as during the laser ablation are visible in the SPRED spectrum. Figure 6.12(a) depicts the electron temperature of the impurity accumulation region in discharge #20050. Part (b) gives the integral of the measured intensity in the SPRED spectrum between 15 and 19 nm, while part (c) presents two spectra at 4.004 s and 4.329 s in the discharge. The structure around 17 nm, which is observed at 4.329 s originates from ionization states between Ag-like W^{27+} and Sn-like W^{24+}, which is revealed by the comparison to the emissions featured in figure 6.9, and is therefore also part of the structure, which is observed during a W laser blow-off (LBO). Possibly, the smoother appearance of the feature during a LBO is caused by the additional emissions of the ionization states Sn-like W^{24+}– Xe-like W^{20+}. The structure presented in figure 6.12(c) is accompanied by emissions between 28 and 30 nm, while the emissions around 35 nm are the second order reflections of the structure at 17.5 nm. The emissions could not be reproduced by the code calculations. This is due to the increasing number of electrons in the 4f-shell for ionization states below W^{27+} making the calculations very time consuming and limiting in the number and complexity of configurations used in the multiconfigurational expansion. For the ionization states Ag-like W^{27+} to Sn-like W^{24+}, the transitions $4f^{(n-1)}5p^1$ to $4f^{(n-1)}5s^1$, with n being the number of f-electrons of the ground state, exhibit many transitions in the wavelength range 13 –25 nm, however, only for Ag-like W^{27+} and Cd-like W^{26+}

the collisional radiative modeling results in line strengths, that could be attributed to the observed emissions. An estimation of the experimental emissivities of the total structure ranging from 12 nm to 25 nm for the LBO in discharge #18727 reveals that this structure considerably contributes to the total radiated power of tungsten below electron temperatures of 1 keV (s. chapter 8). It may be noted, that for ionization

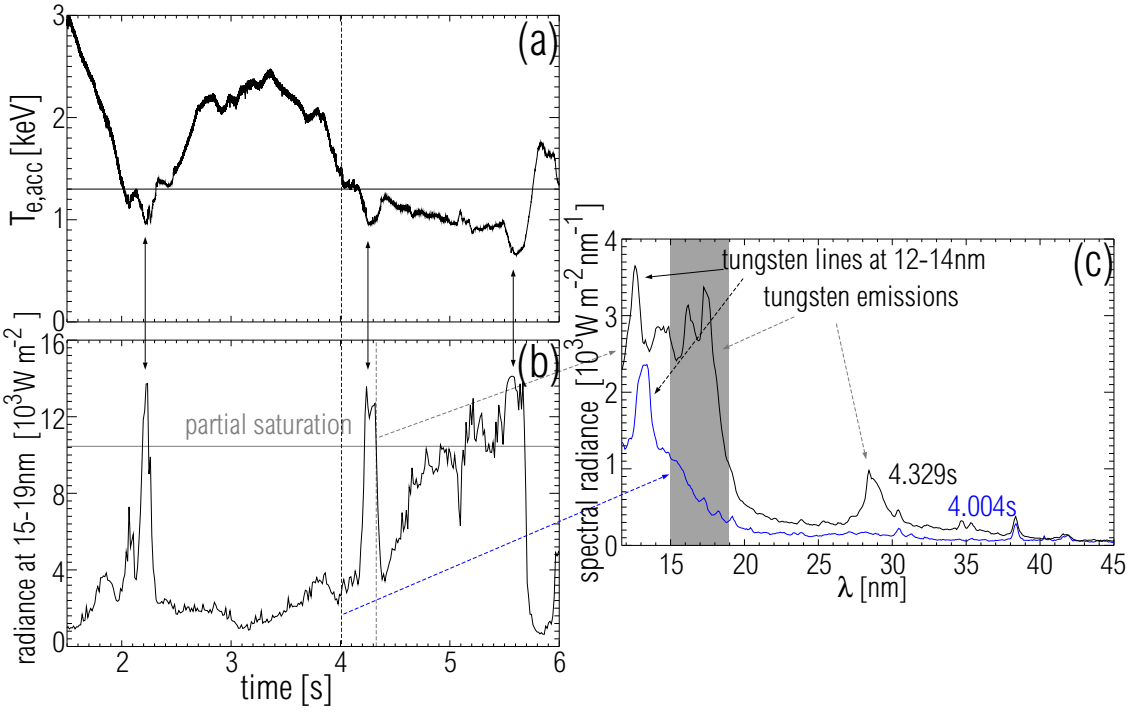

Figure 6.12: *(a)* Electron temperature derived from electron cyclotron emissions in the center of discharge #20050 during impurity accumulation. *(b)* Emissions in the SPRED spectrum integrated from 15 –19 nm. The emissions partly saturate at about 2.2 s and 4.25 s and fully saturate at about 5.6 s. A clear correlation with electron temperature is observed. *(c)* Spectra measured at 4.004 s and 4.329 s illustrating the typical appearance of the emissions of ion states below Pd-like W^{28+}. The structure at 29 nm is also emitted by these tungsten ions, while the double peak around 35 nm is the second order emissions of the structure at 17.5 nm.

states below Ba-like W^{18+} emissions with considerable emissivities are predicted from transitions of the sort $4f^{(n_1)}5s^25p^{n_2}$ to $4f^{(n_1-1)}5s^25p^{n_2}5d^1$ or $4f^{(n_1)}5s^25p^{n_2-1}5d^1$ and of the sort $4f^{(n_1-1)}5s^{n_2}5p^1$ to $4f^{(n_1-1)}5s^{n_2}5d^1$, where n_1 and n_2 are the number of electrons in the actual orbital for the ground state. These ionization states do not play a significant role in the spectra from ASDEX Upgrade, as their abundance is located in a too small volume at the edge of the plasma ($T_e \leq 300$ eV). These ionization states may contribute some emissivity to the spectra observed at TEXTOR, where the suitable electron temperatures exist in a larger plasma volume.

6.3 Soft X-ray spectral range

6.3.1 Spectral range 0.4 – 0.8 nm

Spectral lines in this range have been investigated before, the lines being emitted from laser produced plasmas ([101–105]) and from fusion plasmas at ASDEX Upgrade [13, 106, 107]. The measured spectra are compared to theoretical predictions to identify the spectral lines, a method, which is successful in this spectral region as the predicted wavelengths and emissivities agree sufficiently well with the measurement. Recently, a effort was launched at the Berlin EBIT to survey the emissions in the soft X-ray range for identifying the charge states of spectral lines experimentally. First results of these investigations (s. [13]) agree with the earlier findings. In the present work, the focus is put on the comparison of measured to predicted spectra, as the soft X-ray emissions play an important role for the radiative losses at electron temperatures between 2 and 5 keV, i.e. for Se-like W^{40+} to about Mn-like W^{49+}. In figure 6.13, the measured spectrum of tungsten (a) and the predictions of the ADAS calculations (b) along with the predictions of the HULLAC code (c) are presented. The coarse distribution of emissivity in the spectrum agrees considerably well between the spectra, which is an important prerequisite, when signals from soft X-ray cameras (SXR-cameras) are interpreted. As described in section 3.1.2 the SXR-cameras integrate the power of photons, which are energetic enough to be transmitted by a beryllium filter and at the same time have low enough energy to be absorbed by the detector. As the ADAS data give the distribution of radiation reasonably well it is possible to weight the predicted emissions with the detector efficiencies (s. figure 3.2) of the SXR-cameras, which then can be used as a quantitative diagnostic for tungsten. This may not be straight forward, because other impurities and Bremsstrahlung are also contributing to the signal of the SXR-cameras, however, it is possible to combine the information of many LOS and several SXR-cameras using different thicknesses of beryllium filters such that the contributions of the different impurity species can be disentangled. A prerequisite for this is the knowledge of the radiative characteristics of the relevant impurities.

The emissivity of the predicted spectral lines have been used to optimize the ionization balance in chapter 5. Considering single spectral lines, the discrepancies are varying and are of the order of about factor 2 for both atomic code predictions. These discrepancies seem to be of similar size for both codes, even though the plane-wave Born-approximation is using a less accurate physical model. The tungsten concentration is a free parameter in the model spectra and was adjusted for both spectra independently, such that the total emissivity of the spectral lines agrees with the measured value. The obtained concentration varies only slightly and is for the ADAS data

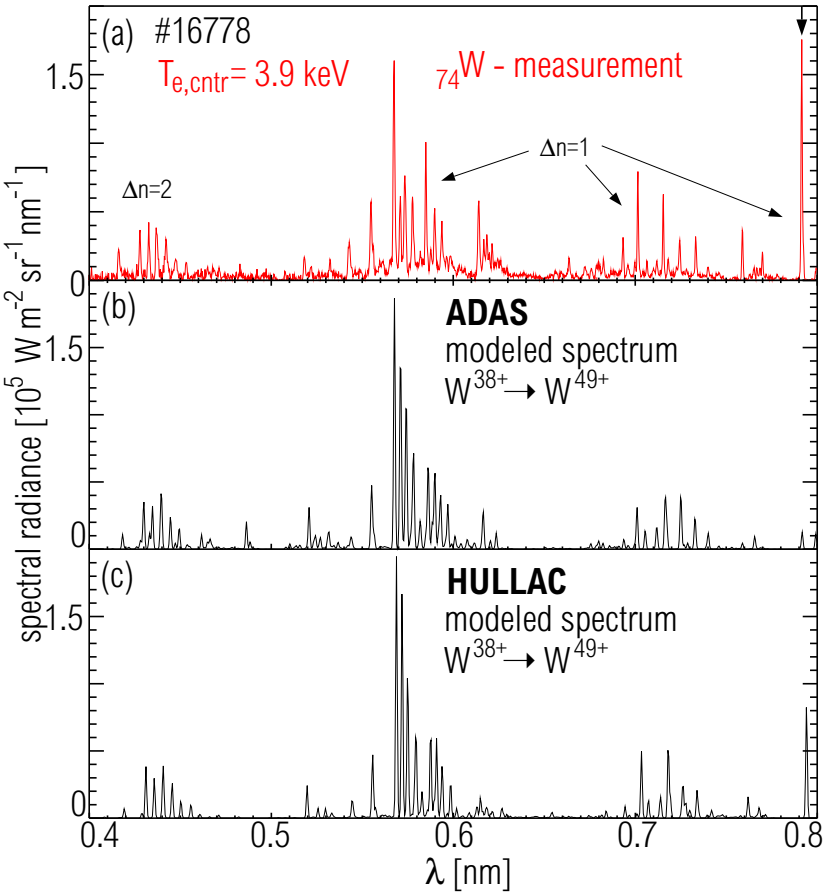

Figure 6.13: *(a)* Spectrum for discharge #16778 measured by the Bragg scanning crystal spectrometer. The tungsten concentration is approximately flat and the central $T_e \approx 3\,\mathrm{keV}$ *(b)* Modeled spectrum using the modified 'CADW+408' ionization balance and FPECs of the present work obtained by the Cowan code.*(c)* Modeled spectrum using the modified 'CADW+408' ionization balance and PECs, which were obtained by HULLAC in [30] and used in [13, 106, 107] to model the tungsten spectrum.

$2.0 \pm 0.2 \cdot 10^{-4}$ and the HULLAC data $1.9 \pm 0.2 \cdot 10^{-4}$. The uncertainties are estimated and originate from the determination of the line integrals in the measured spectrum. The largest discrepancy of a single spectral line between the ADAS spectrum and the measured spectrum is the electric quadrupole transition at 0.793 nm, which is marked in figure 6.13(a) by the small vertical arrow. ADAS predicts the spectral line too weak by about a factor of 10 while the HULLAC data are predicting the line too weak by a factor of 2. From [108, 109] it is known, that about 30 % of the line intensity originates from inner shell ionization of Cu-like W^{45+}, which results in an excited Ni-like W^{46+} in the upper state (configuration $3d^9 4s^1$) of the considered transition. This state has third lowest energy in Ni-like tungsten and virtually only decays into the ground state with an A-value of $\approx 6 \cdot 10^9\,\mathrm{s}^{-1}$. As innershell ionization is not accounted for by the

ADAS code, part of the discrepancy between the predictions is understood, however, a difference of about factor of 4 remains, which is unresolved. The excitation rates from the ground state have been compared using the predictions of HULLAC [30, 108, 109], RATIP [110] and the ADAS code. This is pointing towards similar results of all codes. Therefore, the discrepancy must originate from an other populating process, possibly from a decaying state with higher energy than the state of interest.

Considering the rough structure of the spectrum, the largest contribution is made by Δn=1 transitions, since the central structure situated just below 0.6 nm is made up from transitions of the sort $3d^n$ to $3d^{(n-1)}4f^1$. A much weaker structure is measured around 0.43 nm originating from Δn=2 transitions, while also small contributions from Δn=1 transitions of the sort $3p^6 3d^n$ to $3p^5 3d^n 4f^1$ are predicted in this structure. For detailed identifications, confer to [13, 106, 107].

Chapter 7

Spectral Features of Other High-Z Elements

This chapter is devoted to the investigations on other high-Z elements, which have been performed to benchmark the atomic data for tokamak conditions. Other sources for the spectra of highly ionized high-Z elements are less accurately diagnosed and/or exhibit a very different plasma surrounding, where recombination dominates like for laser-produced plasmas. This leads to line-rich spectra which are different to the electron collision dominated spectra of a tokamak. More details on this discussion are given in section 5.1. In the case of xenon, the results are of interest for a future fusion device, in which xenon might be used for diagnostic or cooling purposes.

7.1 Investigations on Isoelectronic Sequences

The investigations on tungsten were accompanied by analyses on other high-Z elements to investigate the atomic data in more detail. In this section, measurements of the spectral features of the elements hafnium ($_{72}$Hf), tantalum ($_{73}$Ta), rhenium ($_{75}$Re), gold ($_{79}$Au), lead ($_{82}$Pb) and bismuth ($_{83}$Bi) are presented and compared to corresponding modeled spectra.

7.1.1 VUV Wavelength Range

The main feature of all high-Z elements in the VUV range is the quasicontinuum, which has a very similar structure for all investigated elements. Investigations on W, Au and Pb have been performed earlier at the TEXT tokamak [98] and are confirmed by the present work, which includes several more elements. This is featured in figure 7.1, where, in the left column, measured spectra (black) after laser ablations are

presented along with modeled spectra (blue) of the respective impurity. In the right column the temporal evolutions of the laser blow-off (LBO) injections are depicted. For Au and Bi, the injection was accompanied by impurity accumulation, which is increasing the concentration and the decay time of the impurity density drastically, such that the concentrations in the accumulation region are well above $1 \cdot 10^{-4}$ and a decay time cannot be determined. For the laser blow-offs without impurity accumulation, central concentrations of a few 10^{-5} and decay times of the order of 100 ms are observed. On the right column of figure 7.1, the horizontal lines are indicating the time points of LBOs and of the spectra in the left column. The broken vertical lines indicate spectral lines of H-like C^{5+} (3.373 nm), He-like C^{4+} (4.027 nm), H-like B^{4+} (4.859 nm) and He-like B^{3+} (6.031 nm and 6.109 nm), which have been used for *in situ* wavelength calibration. As the ion abundances in the model are just shifted in electron temperature with respect to the ion abundances of tungsten (cf. section 5.3), only small differences arise in the weighting of Ag-like to Y-like ions for the different elements, because the integration along the LOS of the spectrometer is obscuring the radial position of the emitting ions. In the model calculations, the main feature, i.e. the large maximum, of the quasicontinuum is pronounced, while the smaller local maximum of the emissions , which is situated in the measured spectra about 1 nm at longer wavelengths is not reproduced in the model. Additionally, the modeled emissions for the main feature expand over a narrower wavelength range and are shifted to lower wavelengths by 0.1 –0.2 nm in comparison to the measured spectra. For the modeled spectra, the impurity concentration was adjusted such, that the predicted total radiance corresponds to that in the main peak of the quasicontinuum of the measurement. As both, the modeled spectra and the measured emissions for all elements, are very similar to the corresponding spectra of tungsten the findings for tungsten seem to be applicable for all other investigated elements. It may be noted in figure 7.1, that small differences in the shape of the quasicontinuum are noticeable, which probably arise from differences in the actual dynamic of the plasma following the laser ablation. For example, the main feature of the tungsten quasicontinuum seems to form a smooth maximum at about 5.1 nm, while the quasicontinuum of Re exhibits a less peaked appearance with single spectral lines being visible at the wavelength range 4.65 –5.05 nm. This, however, is not specific to Re, as the quasicontinuum of tungsten often exhibits such an appearance during other discharges like #18937 and #19115 (cf. figure 6.5). An exception of the described experimental behavior is observed for Bi, where the main feature of the quasicontinuum is remarkably broad and an additional local maximum occurs around 4.4 nm at 3.65 s, which is unaccounted for. Impurity accumulation at about 2.1 keV could pronounce the emissions of ionization states below Ag-like Bi^{36+}, enhancing the emissions of ion states, which have not been investigated

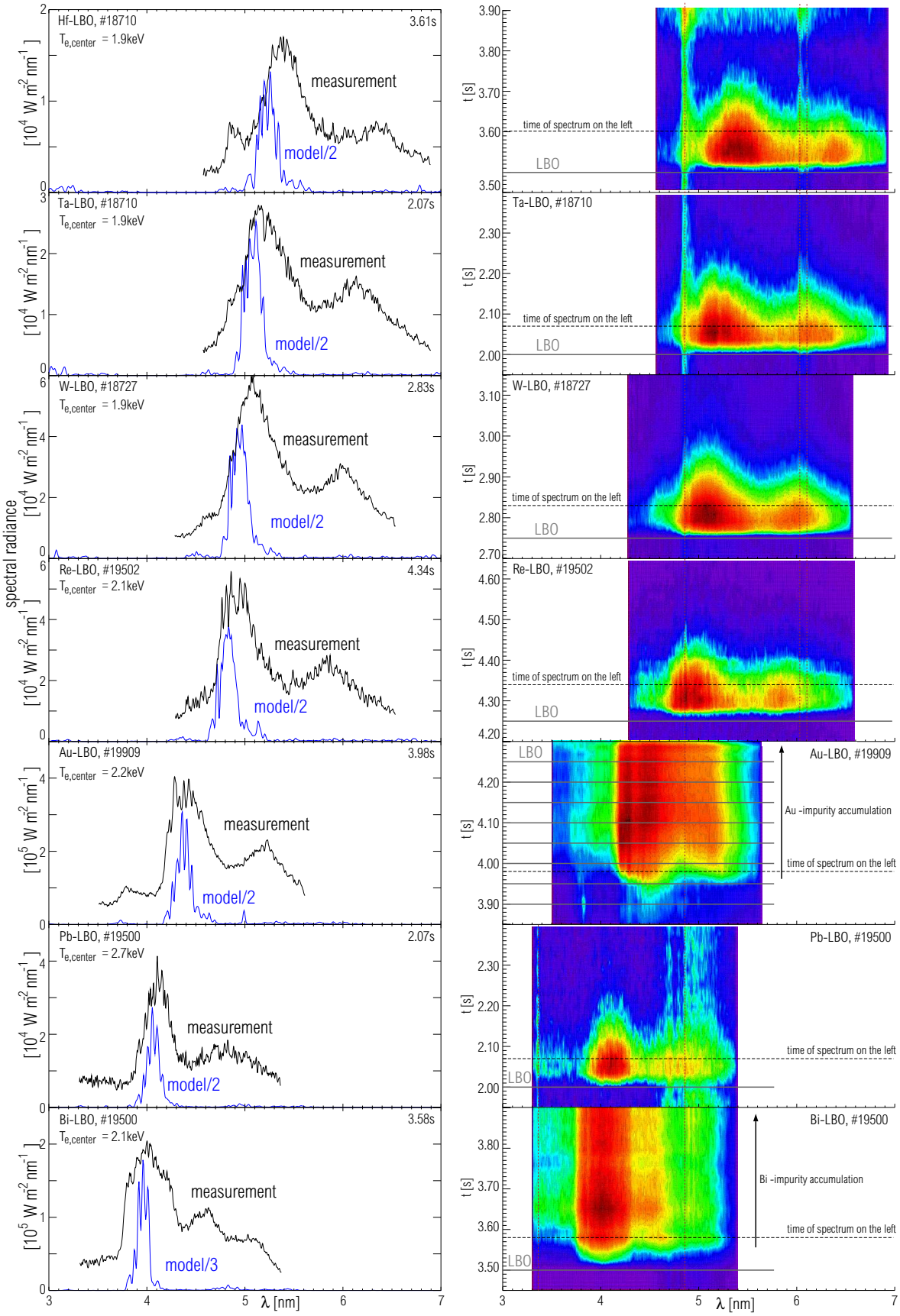

Figure 7.1: Left column: Model results and measurements of the quasicontinuum emitted by the elements $_{72}$Hf, $_{73}$Ta, $_{74}$W, $_{75}$Re, $_{79}$Au, $_{82}$Pb and $_{83}$Bi. Right column: Evolution after the impurity injections, where blue color depicts lowest spectral radiance and red the highest in the spectrum.

for bismuth in detail. Consequently, no explanation for the described envelope of the Bi quasicontinuum can be presented. In figure 7.2, the intensity weighted mean of the main maximum of the quasicontinuum is presented, along with the wavelengths of the corresponding emissions of Ru-like ions of each element. The Ru-like ions (for tungsten: W30+) are thought to exhibit emissions at a central part of the quasicontinua. The predicted wavelengths are following the measured values for increasing nuclear charge, summarizing the detailed picture of figure 7.1. For comparison, two curves are

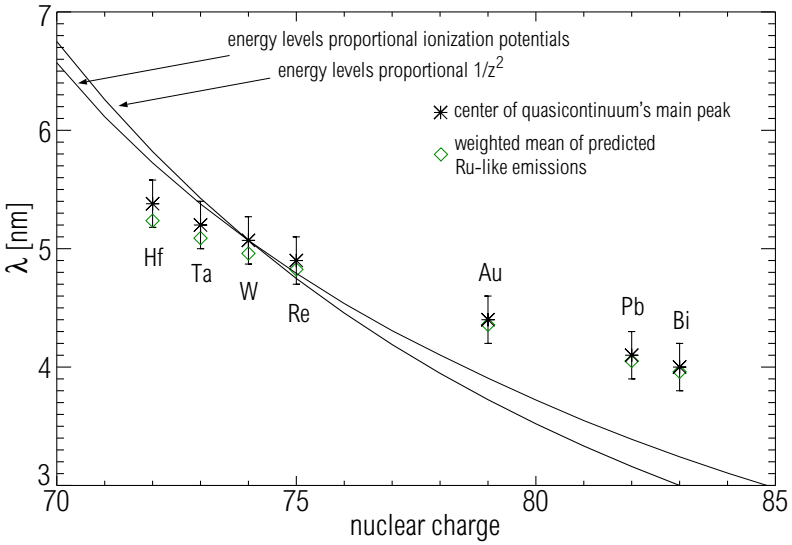

Figure 7.2: The wavelength dependence of the main feature of the quasicontinua emitted by the investigated elements $_{72}$Hf, $_{73}$Ta, $_{74}$W, $_{75}$Re, $_{79}$Au, $_{82}$Pb and $_{83}$Bi. The thin curve denotes the behavior of the wavelength shift, if level energies of the ion would be proportional to the ionization energy taken from [36], while the bold curve results from the assumption that the level energies are proportional to $1/z^2$. Both curves were normalized to the measurement for tungsten.

added. The bold curve corresponds to the hydrogenic approximation, that the transition energies are $\propto 1/z^2$, where z equals the charge of the emitting ion and the thin curve assumes that the transition energies are proportional to the ionization potentials (taken from [36]) of the emitting ion. As the transitions are $\Delta n = 0$ transitions to the ground state, deviations between the detailed model/measured data and both curves are easily understood by the strong contribution of the electron-electron interaction within the shell.

For the investigated elements except for Pb and Bi, isolated spectral lines (cf. section 6.2.1 and 6.2.2 for the corresponding tungsten lines) were observed in the wavelength range of the quasicontinuum and between 10 –15 nm, if the electron temperatures exceeded ≈ 2 keV. For elements with higher nuclear charge this threshold shifts towards higher electron temperatures, such that for Pb and Bi no sufficiently large abundance of the ionization states was available for temperatures at about 3 keV. For discharges

with central electron temperatures above 3 keV, the ablations of Pb and Bi were less effective, because the transport coefficients in the plasma discharge are enhanced by the increased heating power, which resulted in too low Pb and Bi concentrations such that no analysis could be performed. Additionally, due to the small radial range where the corresponding ion states of Pb and Bi exist the LOS integration was lower even at similar concentrations as for the other impurities. For the elements Hf, Ta, Re and Au, the detailed knowledge of the tungsten spectrum and comparisons to GRASP calculations, helped to identify the spectral lines, which are summarized in table 7.1 along with the wavelengths taken from experiment, GRASP calculations and values from literature.

Moving the focus now to the feature, which has been observed at larger wavelengths, i.e. for tungsten around 18 nm, the emissions are visible for all injected impurities, and shifted to lower wavelengths for higher nuclear charge (s. figure 7.3). For the Pb and Bi spectra, it is not clear if the total structure is visible in the spectra, as the lower wavelength part of the emissions might appear at too low wavelengths and can not be monitored by the SPRED spectrometer. In figure 7.4 the wavelengths of the rectangular structure, which is part of the full feature and indicated by small arrows is chosen to perform a comparison between the emissions of the different elements. The arrows indicating the structure have been placed at the positions in figure 7.4, after the comparisons of several LBOs and considering the time evolution of the LBO. This structure is chosen, because for Hf, Ta, W, Re and Au this is a distinct feature. Unfortunately, the structure is hardly recognizable for Pb and Bi, but as anyhow the full features for Pb and Bi are relatively narrow, the attribution of wavelengths involves about the same absolute uncertainties as for the other elements. The wavelengths are presented for the investigated elements in figure 7.4. Similar as in figure 7.2 the two solid curves give the approximations for the cases, that the transition energies scale like $1/z^2$ (bold) using the Cd-like ion charge or that the energies scale like the ionization energies of the Cd-like ions. The Cd-like ions were used, because the investigations on tungsten (s. section 6.2.4) indicated, that Cd-like W^{26+} is considerably contributing to the structure. The measured decrease of the wavelengths for increasing nuclear charge is reproduced qualitatively by the scalings. The structure of the emissions in figure 7.3 are more dispersed for elements with lower atomic number. Part of this effect may be understood by hydrogenic effects. The dashed curves in figure 7.4 are used to extrapolate the long and short wavelength edge of the tungsten feature to the other elements using the ionization potentials of Ag-like ions (short wavelengths) and the Xe-like ions (long wavelengths). These choices are based on the findings for tungsten (s. section 6.2.4). Qualitatively, the observation that the emission feature is narrower for elements with higher nuclear charge, can be understood by this simple scalings

Ion	transition	λ_{calc} (nm)	λ_{tok} (nm)	λ_{lit} (nm)
Hf^{43+}	$4s\ ^2S_{1/2} - 4p\ ^2P_{3/2}$	6.858	6.860	
(Cu–like)	$4s\ ^2S_{1/2} - 4p\ ^2P_{1/2}$	13.277	13.375	
Hf^{42+}	$4s^2\ ^1S_0 - 4s4p\ ^1P_1$	6.683	6.696	6.7015 [111]
(Zn–like)	$4s^2\ ^1S_0 - 4s4p\ ^3P_1$	13.959	14.002	14.0048 [111]
Hf^{41+}	$4s^24p\ ^2P_{1/2} - 4s^24d\ ^2D_{3/2}$	5.174	5.212	
(Ga–like)	$4s^24p\ ^2P_{1/2} - 4s4p^2\ ^2P_{1/2}$	6.620	6.653	
	$4s^24p\ ^2P_{1/2} - 4s4p^2\ ^2D_{3/2}$	6.745	6.732	
Hf^{40+}	$4s^24p^2\ ^3P_0 - 4s^24p4d\ ^3D_1$	5.092	5.132	
(Ge–like)				
Ta^{44+}	$4s\ ^2S_{1/2} - 4p\ ^2P_{3/2}$	6.529	6.530	6.5502 [112], 6.5427 [113]
(Cu–like)	$4s\ ^2S_{1/2} - 4p\ ^2P_{1/2}$	12.937	13.044	13.020 [113]
Ta^{43+}	$4s^2\ ^1S_0 - 4s4p\ ^1P_1$	6.371	6.388	6.395 [114], 6.3869 [111]
(Zn–like)	$4s^2\ ^1S_0 - 4s4p\ ^3P_1$	13.587	13.645	
Ta^{42+}	$4s^24p\ ^2P_{1/2} - 4s4p^2\ ^2D_{3/2}$	6.424	6.430	
(Ga–like)	$4s^24p\ ^2P_{1/2} - 4s4p^2\ ^4P_{1/2}$	13.537	13.593	
Ta^{41+}	$4s^24p^2\ ^3P_0 - 4s^24p^2\ ^1D_2$	13.928	13.928	
(Ge–like)				
Re^{46+}	$4s\ ^2S_{1/2} - 4p\ ^2P_{3/2}$	5.921	5.937	5.9325 [99]
(Cu–like)	$4s\ ^2S_{1/2} - 4p\ ^2P_{1/2}$	12.295	12.406	
Re^{45+}	$4s^2\ ^1S_0 - 4s4p\ ^1P_1$	5.790	5.811	5.8038 [99], 5.8071 [111]
(Zn–like)	$4s^2\ ^1S_0 - 4s4p\ ^3P_1$	12.887	12.952	
Re^{44+}	$4s^24p\ ^2P_{1/2} - 4s^24d\ ^2D_{3/2}$	4.567	4.593	
(Ga–like)	$4s^24p\ ^2P_{1/2} - 4s4p^2\ ^2P_{1/2}$	5.742	5.785	
	$4s^24p\ ^2P_{1/2} - 4s4p^2\ ^2D_{3/2}$	5.830	5.846	
	$4s^24p\ ^2P_{1/2} - 4s4p^2\ ^4P_{1/2}$	12.551	12.486	
	$4s^24p\ ^2P_{1/2} - 4s^24p\ ^2P_{3/2}$	11.716	11.743	
Re^{43+}	$4s^24p^2\ ^3P_0 - 4s^24p4d\ ^3D_1$	4.496	4.524	
(Ge–like)	$4s^24p^2\ ^3P_0 - 4s^24p^2\ ^1D_2$	12.034	12.035	
Au^{50+}	$4s\ ^2S_{1/2} - 4p\ ^2P_{3/2}$	4.877	4.895	4.8928 [115]
(Cu–like)	$4s\ ^2S_{1/2} - 4p\ ^2P_{1/2}$	11.146	11.169	11.2485 [115]
Au^{49+}	$4s^2\ ^1S_0 - 4s4p\ ^1P_1$	4.788	4.794	4.8063 [111], 4.8046 [115]
(Zn–like)	$4s^2\ ^1S_0 - 4s4p\ ^3P_1$	11.642	11.687	
Au^{48+}	$4s^24p\ ^2P_{1/2} - 4s^24d\ ^2D_{3/2}$	3.882	4.593	
(Ga–like)	$4s^24p\ ^2P_{1/2} - 4s4p^2\ ^2D_{3/2}$	4.812	4.825	
	$4s^24p\ ^2P_{1/2} - 4s4p^2\ ^4P_{1/2}$	11.300	11.192	
Au^{47+}	$4s^24p^2\ ^3P_0 - 4s^24p4d\ ^3D_1$	3.816	3.827	
(Ge–like)				

Table 7.1: Identified transitions with the levels taken from atomic data calculations of ADAS; theoretical wavelengths have been taken from GRASP. Corresponding lines in the codes have been identified via their total angular momenta and Einstein coefficients. The experimental uncertainty in wavelength for the tokamak spectra is ± 0.005 nm the uncertainties of the wavelengths from [111, 114] and [99, 112, 113, 115] are quoted to be ± 0.002 nm and ± 0.0015 nm, respectively. Several, additional spectral lines, which are emitted by the injected impurity, are visible in the spectra, but could not be identified.

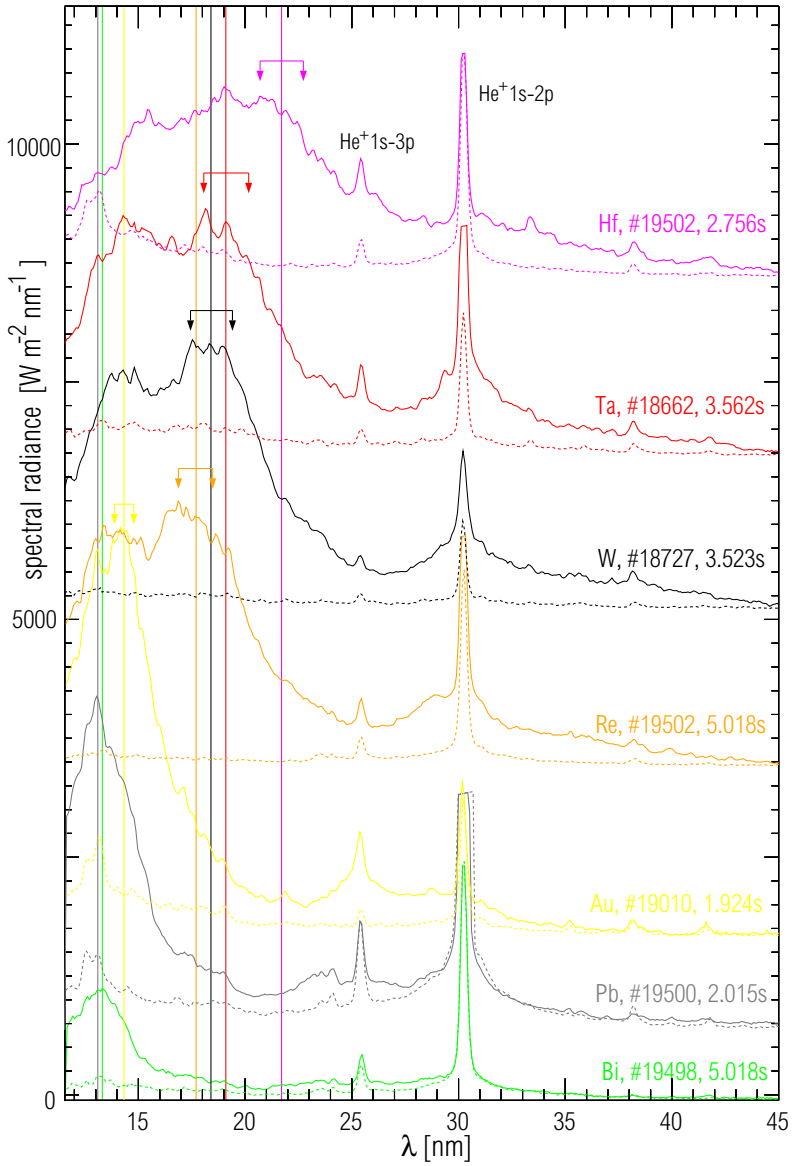

Figure 7.3: Spectral signatures of $_{72}$Hf, $_{73}$Ta, $_{74}$W, $_{75}$Re, $_{79}$Au, $_{82}$Pb and $_{83}$Bi following a LBO. An arbitrary offset is added to the spectra of each element for better display. Dashed spectra correspond to a timepoint directly before the LBO. The different absolute size of the emissions are caused by the different amount of the injected impurity, which might vary for each element due to the efficiency of the impurity injection by laser ablation.

as the two dashed curves converge for the higher charged ions in the isoelectronic sequence.

7.1.2 Soft X-ray Wavelength Range

Isoelectronic investigations have been performed also in the soft X-ray range. As the Bragg scanning crystal spectrometer needs about 1.5 s to perform a scan over

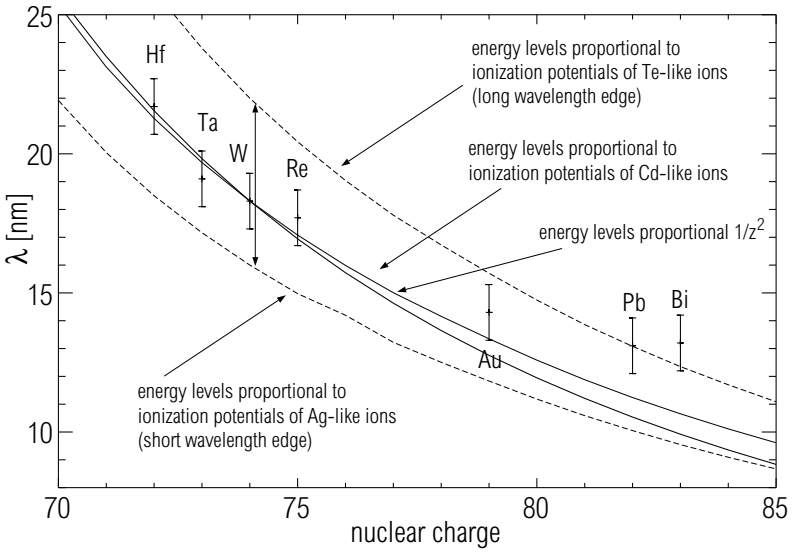

Figure 7.4: Wavelength dependence of the spectral feature emitted from 10 –25 nm by the investigated elements Hf, Ta, W, Re, Au, Pb and Bi. The thin, solid curve denotes the relative behavior of the wavelength shift, if level energies of the ion would be proportional to the ionization energy taken from [36], while the bold curve results from the assumption that the level energies are proportional to $1/z^2$. The thin, dashed curves depict the extrapolated short and long wavelength edge of the feature using the tungsten wavelengths and the scaling based on ionization potentials of Ag-like ions (short wavelengths) and Te-like ions (long wavelengths).

the presented wavelength ranges, a steady state plasma operation is needed with a constant impurity influx. The impurity concentration reaches an equilibrium within a few hundreds of milliseconds, after laser ablations with a repetition frequency of 20 Hz are performed. These "quasicontinuous" conditions are monitored for the presented spectra by the total radiated power and the VUV spectra. The constant impurity density for a full spectrum is fulfilled within a factor of 2. As the soft X-ray spectra are emitted by ionization states above the Kr-like state no spectra could be obtained for Pb and Bi, due to the low fractional abundances of the ionization states of interest. The signal could not be increased high enough by increasing the amount of impurities, before the total radiated power of the impurity affected plasma operation.

The spectra of Hf, Ta, Re and Au are presented in the figures 7.5, 7.6, 7.7 and 7.8, respectively. The structures, which have been measured, have been observed earlier from laser-produced plasmas [101, 103–105, 116, 117] and from exploded wire plasmas (Au, W) [118]. An independent identification of spectral lines is obtained here and the results are summarized in tables 7.2, 7.3 and 7.4. The most clear lines have been identified, while in several cases (marked with '*') two or more lines from the same charge state coincide at the same wavelength and the line which is predicted strongest is denoted. In the case of Hf and Ta, the plasmas in which the measurements have

been performed were very clean, such that no tungsten emissions which would blend the spectra are visible. The emissions of all four investigated elements are similar to the tungsten emissions but shifted in wavelength. The Δn=2 emissions are hardly visible for Hf, Ta and Au, as the impurity concentration during that phase was lower by about factor 2 than for the rest of the spectrum. Still, the main feature of the spectrum is well visible within each spectrum. In the case of Hf and Ta, the measured spectra are compared to modeled spectra using the modified 'CADW+408' ionization balance (s. chapter 5), FPECs from ADAS and PECs from HULLAC [119]. The HULLAC results exhibit only small differences to the ADAS modeling. Consistently to the results for tungsten, also the electric quadrupole line at 0.8545 nm (Hf) and 0.822 nm (Ta) (s. small vertical arrow in figure 7.5(a) and 7.6(a)) is underestimated by both codes.

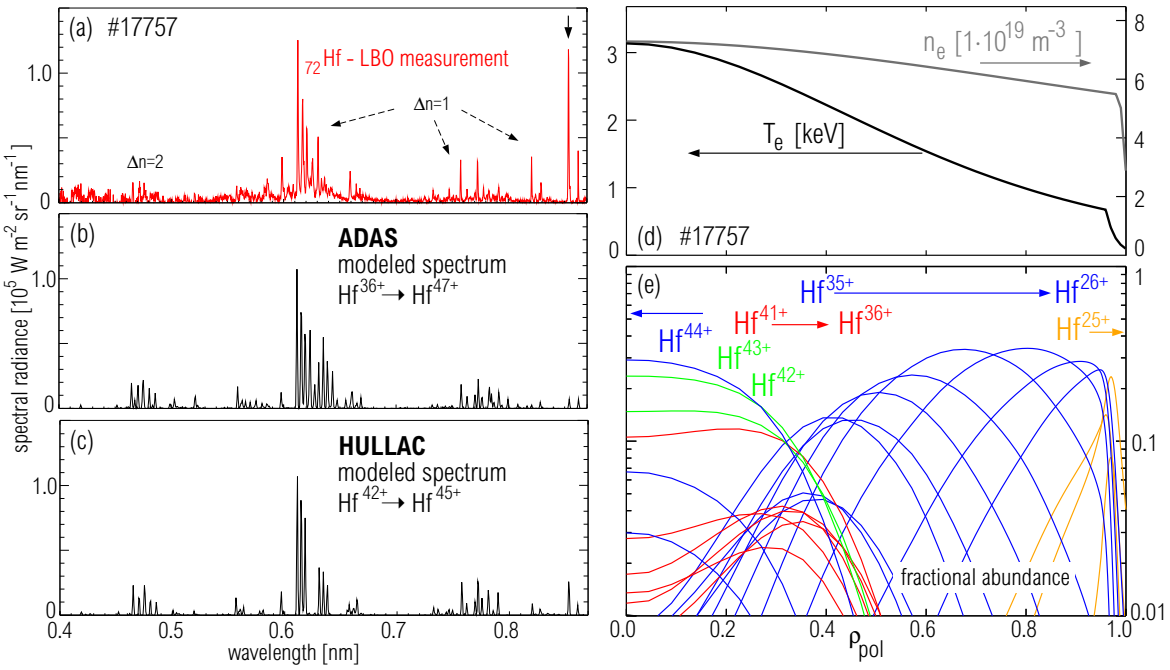

Figure 7.5: *(a)* Spectrum of $_{72}$Hf obtained in discharge #17757 and measured by the Bragg scanning crystal spectrometer. *(b)* Modeled spectrum using the modified 'CADW+408' ionization balance and FPECs of the present work obtained by the Cowan code. *(c)* Modeled spectrum using the modified 'CADW+408' ionization balance and PECs, which were supplied by [119]. *(d)* Measured electron temperature and density profiles, which have been used to model the spectrum of part (b) of the figure. *(e)* Fractional abundances of Hf ions using the above explained (s. chapter 5) color code to indicate the outermost subshell.

For Re and Au the impurity spectra are blended by tungsten emissions, which was abundant as an intrinsic impurity in the plasma. For this reason, a pure tungsten spectrum is featured in figures 7.7 and 7.8 along with the spectra obtained for the

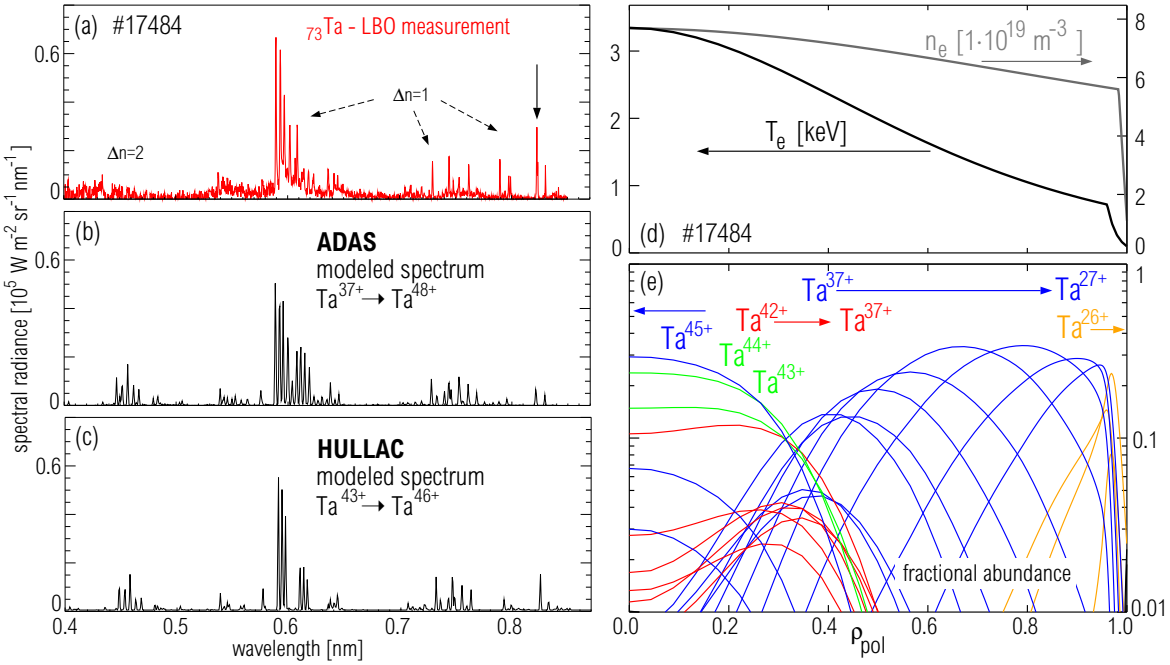

Figure 7.6: Same as figure 7.5 but for Ta-LBO.

injected impurities Re and Au. As no HULLAC data are at hand for these impurities only the comparison to the ADAS data is featured in figures 7.7(c) and 7.8(c). The picture, however remains the same, as the emissions are described relatively well by the ADAS data. For Re, the discrepancy of the electric quadrupole line is again visible, while for Au the spectra could not be obtained up to the wavelength of that line.

On the right of the figures 7.5– 7.8 the electron temperature and density profiles of the plasma are depicted, along with the resulting fractional abundances of each impurity ion state for a continuous impurity source at the edge. While the electron temperatures and densities are fits to measured data, the abundances result from a STRAHL modeling using the ionization data for the elements, which has been obtained (s. chapter 5) by scaling the tungsten data (modified 'CADW+408'). The obtained ionization and recombination rates are apparently not far from the experimental behavior.

7.2 Spectral Features of Xenon $_{54}$Xe

The emissions of xenon are of interest, because it might be used in a reactor for cooling the plasma, or as impurity on which plasma diagnostic is performed. The spectra of highly ionized xenon were investigated in fusion experiments [120–123], from laser-imploded targets [124, 125], by exciting gas jets [126] and in EBITs [127–130]. Many details of the spectra have been observed earlier. In this work, the focus is put not

Ion	transition	λ_{calc} (nm)	λ_{tok} (nm)	blending
Hf^{46+}	$3p^6 3d^8$ J=4– $3p^6 3p^7 4f^1$ J=5	0.587	0.5849 (ADAS)	*
(Fe–like)	A= $3.7 \cdot 10^{14}\,s^{-1}$ (ADAS)			
Hf^{45+}	$3p^6 3d^9$ J=5/2 – $3p^6 3d^8 4f^1$ J=7/2	0.5995	0.5979 (ADAS)	*
(Co–like)	A= $3.7 \cdot 10^{14}\,s^{-1}$ (ADAS)			
Hf^{44+}	$3p^6 3d^{10}\ ^1S_0$ – $3p^6 3d^9 5f^1\ ^1P_1$	0.466	0.4650 (ADAS)	
(Ni–like)	$3p^6 3d^{10}\ ^1S_0$ – $3p^5 3d^{10} 4f^1\ ^1D_2$	0.521	0.5213 (ADAS)	
	$3p^6 3d^{10}\ ^1S_0$ – $3p^5 3d^{10} 4d^1\ ^1P_1$	0.559	0.5591 (ADAS)	
	$3p^6 3d^{10}\ ^1S_0$ – $3p^6 3d^9 4f^1\ ^1P_1$	0.6135	0.6129 (GRASP)	
	$3p^6 3d^{10}\ ^1S_0$ – $3p^6 3d^9 4f^1\ ^3D_1$	0.6315	0.6326 (GRASP)	
	$3p^6 3d^{10}\ ^1S_0$ – $3p^5 3d^{10} 4s^1\ ^1P_1$	0.660	0.6608 (ADAS)	
	$3p^6 3d^{10}\ ^1S_0$ – $3p^6 3d^9 4p^1\ ^1P_1$	0.758	0.7605 (GRASP)	
	$3p^6 3d^{10}\ ^1S_0$ – $3p^6 3d^9 4p^1\ ^3D_1$	0.7735	0.7753 (GRASP)	
	$3p^6 3d^{10}\ ^1S_0$ – $3p^6 3d^9 4s^1\ ^3D_2$	0.8215	0.8239 (GRASP)	
	$3p^6 3d^{10}\ ^1S_0$ – $3p^6 3d^9 4s^1\ ^1D_2$	0.8545	0.8566 (GRASP)	
Hf^{43+}	$3d^{10} 4s^1\ ^2S_{1/2}$ – $3d^9 4s^1 4f^1\ ^2P_{3/2}$	0.618	0.6156 (ADAS)	*
(Cu–like)	$3d^{10} 4s^1$ J=1/2 – $3d^9 4s^1 4f^1$ J=3/2	0.6345	0.6352 (ADAS)	*
	A= $1.0 \cdot 10^{14}\,s^{-1}$ (ADAS)			
	$3p^6 3d^{10} 4s^1\ ^2S_{1/2}$ – $3p^5 3d^{10} 4s^2\ ^2P_{3/2}$	0.6655	0.6651 (ADAS)	
	$3d^{10} 4s^1\ ^2S_{1/2}$ – $3d^9 4s^1 4p^1\ ^2P_{3/2}$	0.764	0.7629 (ADAS)	
	$3d^{10} 4s^1\ ^2S_{1/2}$ – $3d^9 4s^1 4p^1\ ^2P_{1/2}$	0.771	0.7698 (ADAS)	*
	$3d^{10} 4s^1\ ^2S_{1/2}$ – $3d^9 4s^1 4p^1\ ^4D_{1/2}$	0.7835	0.7824 (ADAS)	*
	$3d^{10} 4s^1\ ^2S_{1/2}$ – $3d^9 4s^2\ ^2D_{3/2}$	0.830	0.8280 (ADAS)	
	$3d^{10} 4s^1\ ^2S_{1/2}$ – $3d^9 4s^2\ ^2D_{5/2}$	0.863	0.8621 (ADAS)	
Hf^{42+}	$3d^{10} 4s^2\ ^1S_0$ – $3d^9 4s^2 4f^1\ ^1P_1$	0.6215	0.6197 (GRASP)	
(Zn–like)	$3d^{10} 4s^2\ ^1S_0$ – $3d^9 4s^2 4f^1\ ^3D_1$	0.637	0.6395 (GRASP)	
	$3d^{10} 4s^2\ ^1S_0$ – $3d^9 4s^2 4p^1\ ^1P_1$	0.779	0.7783 (GRASP)	
	$3d^{10} 4s^2\ ^1S_0$ – $3d^9 4s^2 4p^1\ ^3D_1$	0.792	0.7928 (GRASP)	
Hf^{41+}	$3d^{10} 4s^2 4p^1$ J=1/2 – $3d^9 4s^2 4p^1 4f^1$ J=3/2	0.624	0.6237 (ADAS)	*
(Ga–like)	A= $3.5 \cdot 10^{14}\,s^{-1}$ (ADAS)			
Hf^{40+}	$3d^{10} 4s^2 4p^2$ J=0 – $3d^9 4s^2 4p^2 4f^1$ J=1	0.6265	0.6277 (ADAS)	
(Ge–like)	A= $3.1 \cdot 10^{14}\,s^{-1}$ (ADAS)			

Table 7.2: Identified transitions of Hf with the levels taken from atomic data calculations of ADAS; theoretical wavelengths have been taken from GRASP. Corresponding lines in the codes have been identified via their total angular momenta and Einstein coefficients. The experimental uncertainty in wavelength for the tokamak spectra is ± 0.001 nm. Several, additional spectral lines, which are emitted by the injected impurity, are visible in the spectra, but could not be identified. In cases, where two or more lines of the same charge state coincide in wavelength (marked with '* = blending') the line which is predicted to be strongest is denoted.

Ion	transition	λ_{calc} (nm)	λ_{tok} (nm)	blending
Ta^{46+}	$3p^6 3d^9$ J=5/2 – $3p^6 3d^8 4f^1$ J=7/2	0.577	0.5760 (ADAS)	*
(Co–like)	A= $3.9 \cdot 10^{14}\,s^{-1}$ (ADAS)			
Ta^{45+}	$3p^6 3d^{10}\ ^1S_0$ – $3p^5 3d^{10} 4d^1\ ^1P_1$	0.5375	0.5396 (ADAS)	
(Ni–like)	$3p^6 3d^{10}\ ^1S_0$ – $3p^6 3d^9 4f^1\ ^1P_1$	0.589	0.5902 (GRASP)	
	$3p^6 3d^{10}\ ^1S_0$ – $3p^6 3d^9 4f^1\ ^3D_1$	0.608	0.6094 (GRASP)	
	$3p^6 3d^{10}\ ^1S_0$ – $3p^5 3d^{10} 4s^1\ ^1P_1$	0.636	0.6381 (ADAS)	
	$3p^6 3d^{10}\ ^1S_0$ – $3p^6 3d^9 4p^1\ ^1P_1$	0.729	0.7312 (GRASP)	
	$3p^6 3d^{10}\ ^1S_0$ – $3p^6 3d^9 4p^1\ ^3D_1$	0.7435	0.7460 (GRASP)	
	$3p^6 3d^{10}\ ^1S_0$ – $3p^6 3d^9 4s^1\ ^3D_2$	0.789	0.7922 (GRASP)	
	$3p^6 3d^{10}\ ^1S_0$ – $3p^6 3d^9 4s^1\ ^1D_2$	0.822	0.8245 (GRASP)	
Ta^{44+}	$3d^{10} 4s^1\ ^2S_{1/2}$ – $3d^9 4s^1 4f^1\ ^2P_{3/2}$	0.593	0.5927 (ADAS)	*
(Cu–like)	$3d^{10} 4s^1$ J=1/2 – $3d^9 4s^1 4f^1$ J=3/2	0.612	0.6121 (ADAS)	*
	A= $1.2 \cdot 10^{14}\,s^{-1}$ (ADAS)			
	$3p^6 3d^{10} 4s^1\ ^2S_{1/2}$ – $3p^5 3d^{10} 4s^2\ ^2P_{3/2}$	0.641	0.6422 (ADAS)	
	$3d^{10} 4s^1\ ^2S_{1/2}$ – $3d^9 4s^1 4p^1\ ^2P_{3/2}$	0.734	0.7334 (ADAS)	
	$3d^{10} 4s^1\ ^2S_{1/2}$ – $3d^9 4s^1 4p^1\ ^2P_{1/2}$	0.7405	0.7399 (ADAS)	*
	$3d^{10} 4s^1\ ^2S_{1/2}$ – $3d^9 4s^1 4p^1\ ^4D_{1/2}$	0.7525	0.7528 (ADAS)	*
	$3d^{10} 4s^1\ ^2S_{1/2}$ – $3d^9 4s^2\ ^2D_{5/2}$	0.8295	0.8298 (ADAS)	
Ta^{43+}	$3d^{10} 4s^2\ ^1S_0$ – $3d^9 4s^2 4f^1\ ^1P_1$	0.5965	0.5967 (GRASP)	
(Zn–like)	$3d^{10} 4s^2\ ^1S_0$ – $3d^9 4s^2 4f^1\ ^3D_1$	0.614	0.6160 (GRASP)	
	$3p^6 3d^{10} 4s^1 4p^1\ ^1P_1$ – $3p^5 3d^{10} 4s^2 4p^1\ ^1S_0$	0.644	0.6457 (ADAS)	
	$3d^{10} 4s^2\ ^1S_0$ – $3d^9 4s^2 4p^1\ ^1P_1$	0.7475	0.7480 (GRASP)	
	$3d^{10} 4s^2\ ^1S_0$ – $3d^9 4s^2 4p^1\ ^3D_1$	0.761	0.7626 (GRASP)	
Ta^{42+}	$3d^{10} 4s^2 4p^1$ J=1/2 – $3d^9 4s^2 4p^1 4f^1$ J=3/2	0.602	0.6004 (ADAS)	*
(Ga–like)	A= $3.9 \cdot 10^{14}\,s^{-1}$ (ADAS)			
	$3d^{10} 4s^2 4p^1$ J=1/2 – $3d^9 4s^2 4p^1 4f^1$ J=3/2	0.618	6.196 (ADAS)	*
(Ga–like)	A= $1.1 \cdot 10^{14}\,s^{-1}$ (ADAS)			

Table 7.3: Same as table 7.2, but for Ta

Ion	transition	λ_{calc} (nm)	λ_{tok} (nm)	blending
Re^{48+}	$3p^6 3d^9$ J=5/2 – $3p^6 3d^8 4f^1$ J=7/2	0.537	0.5357 (ADAS)	*
(Co–like)	A= $4.4 \cdot 10^{14}\,s^{-1}$ (ADAS)			
Re^{47+}	$3p^6 3d^{10}\ ^1S_0$ – $3p^6 3d^9 5f^1\ ^1P_1$	0.415	0.4141 (ADAS)	
(Ni–like)	$3p^6 3d^{10}$ J=0 – $3p^6 3d^9 5f^1$ J=1	0.424	0.4238 (ADAS)	
	A= $1.2 \cdot 10^{14}\,s^{-1}$ (ADAS)			
	$3p^6 3d^{10}\ ^1S_0$ – $3p^6 3d^9 4f^1\ ^1P_1$	0.548	0.5484 (GRASP)	
	$3p^6 3d^{10}\ ^1S_0$ – $3p^6 3d^9 4p^1\ ^1P_1$	0.676	0.6774 (GRASP)	
	$3p^6 3d^{10}\ ^1S_0$ – $3p^6 3d^9 4p^1\ ^3D_1$	0.691	0.6924 (GRASP)	
	$3p^6 3d^{10}\ ^1S_0$ – $3p^6 3d^9 4s^1\ ^3D_2$	0.733	0.7342 (GRASP)	
	$3p^6 3d^{10}\ ^1S_0$ – $3p^6 3d^9 4s^1\ ^1D_2$	0.7635	0.7660 (GRASP)	
Re^{46+}	$3d^{10}4s^1\ ^2S_{1/2}$ – $3d^9 4s^1 4f^1\ ^2P_{3/2}$	0.551	0.5505 (ADAS)	*
(Cu–like)	$3d^{10}4s^1\ ^2S_{1/2}$ – $3d^9 4s^1 4p^1\ ^2P_{3/2}$	0.681	0.6788 (ADAS)	
	$3d^{10}4s^1\ ^2S_{1/2}$ – $3d^9 4s^1 4p^1\ ^2P_{1/2}$	0.687	0.6849 (ADAS)	*
	$3d^{10}4s^1\ ^2S_{1/2}$ – $3d^9 4s^1 4p^1\ ^4D_{1/2}$	0.6995	0.6983 (ADAS)	*
	$3d^{10}4s^1\ ^2S_{1/2}$ – $3d^9 4s^2\ ^2D_{5/2}$	0.7715	0.7704 (ADAS)	
Re^{45+}	$3d^{10}4s^2\ ^1S_0$ – $3d^9 4s^2 4f^1\ ^1P_1$	0.554	0.5543 (GRASP)	
(Zn–like)	$3d^{10}4s^2\ ^1S_0$ – $3d^9 4s^2 4p^1\ ^1P_1$	0.694	0.6926 (GRASP)	
	$3d^{10}4s^2\ ^1S_0$ – $3d^9 4s^2 4p^1\ ^3D_1$	0.7025	0.7073 (GRASP)	
Au^{52+}	$3p^6 3d^9$ J=5/2 – $3p^6 3d^8 4f^1$ J=7/2	0.468	0.4667 (ADAS)	*
(Co–like)	A= $5.6 \cdot 10^{14}\,s^{-1}$ (ADAS)			
Au^{51+}	$3p^6 3d^{10}$ J=0 – $3p^5 3d^{10} 4d^1$ J=1	0.4445	0.4414 (ADAS)	
(Ni–like)	A= $1.4 \cdot 10^{14}\,s^{-1}$ (ADAS)			
	$3p^6 3d^{10}\ ^1S_0$ – $3p^6 3d^9 4f^1\ ^1P_1$	0.481	0.4771 (GRASP)	
	$3p^6 3d^{10}\ ^1S_0$ – $3p^6 3d^9 4f^1\ ^3D_1$	0.4965	0.4941 (GRASP)	
Au^{50+}	$3d^{10}4s^1\ ^2S_{1/2}$ – $3d^9 4s^1 4f^1\ ^2P_{3/2}$	0.484	0.4786 (ADAS)	*
(Cu–like)	$3d^{10}4s^1$ J=1/2 – $3d^9 4s^1 4f^1$ J=3/2	0.500	0.4959 (ADAS)	*
	A= $2.2 \cdot 10^{14}\,s^{-1}$ (ADAS)			
Au^{49+}	$3d^{10}4s^2\ ^1S_0$ – $3d^9 4s^2 4f^1\ ^1P_1$	0.487	0.4819 (GRASP)	
(Zn–like)	$3d^{10}4s^2\ ^1S_0$ – $3d^9 4s^2 4f^1\ ^3D_1$	0.5055	0.4990 (GRASP)	
Au^{48+}	$3d^{10}4s^2 4p^1$ J=1/2 – $3d^9 4s^2 4p^1 4f^1$ J=3/2	0.490	0.4842 (ADAS)	*
(Ga–like)	A= $5.7 \cdot 10^{14}\,s^{-1}$ (ADAS)			

Table 7.4: Same as table 7.2, but for Re and Au.

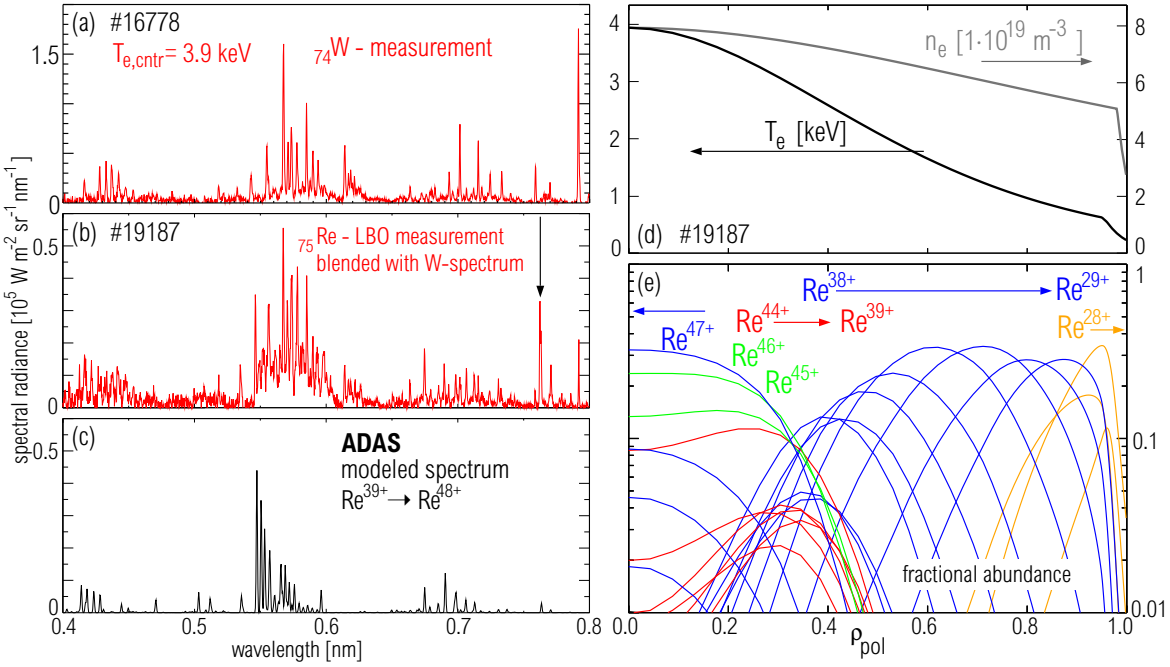

Figure 7.7: *(a)* Spectrum for discharge #16778 measured by the Bragg scanning crystal spectrometer. The tungsten concentration is approximately flat and the central $T_e \approx 3\,\mathrm{keV}$ *(b)* Spectrum of $_{75}$Re obtained in discharge #19187 and measured by the Bragg scanning crystal spectrometer. Unfortunately, the Re spectrum is blended by tungsten emissions, which may be identified via comparison to part (a) of the figure. *(c)* Modeled spectrum using the modified 'CADW+408' ionization balance and FPECs of the present work obtained by the Cowan code. *(d),(e)* Same as figure 7.5 but for Re-LBO.

on the identification of lines, but whether the atomic code manages to reproduce the most intense features, which translates directly to the accuracy of the cooling factor (s. section 8.2).

An intense feature is emitted in the VUV at about 11 nm (s. figure 7.9). It was investigated in detail by [120, 121] and most recently by [130] using the Berlin EBIT [17]. The latter reference was used to label the spectral lines in figure 7.9(a) and to find the corresponding spectral lines for model and measurement. The modeled spectrum exhibits large discrepancies, which may partly originate from the flawed ionization balance. Especially the spectral lines of Ga-like Xe^{23+}, Zn-like Xe^{24+} and Cu-like Xe^{25+} are modeled too strong in comparison to the rest of the spectrum. In section 5.3 it has been already pointed out, that the fractional abundances of these two ionization states are overestimated by the ADAS based ion balance. Only a small influence is attributed to the fact that the left half of the spectrum (s. dashed vertical line in figure 7.9) has been measured during a different discharge than the right half. By a comparison of radiated power and plasma parameters it has been ensured that the phases from which the measurements originate are nearly identical.

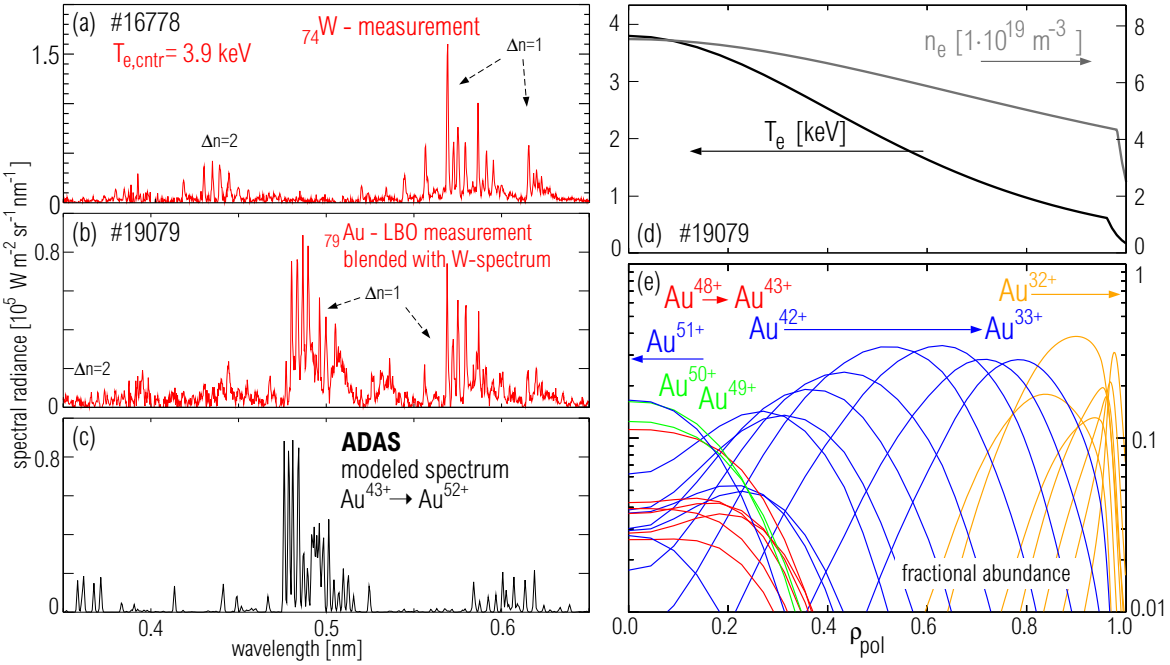

Figure 7.8: *(a)* Same as figure 7.7 but for Au-LBO.

The unresolved structure below 11 nm is not matched in detail by the model. Several spectral lines of Rb-like Xe^{17+} to Ge-like Xe^{22+} are predicted at these wavelengths, however the contributions of Rb-like Xe^{17+} to Br-like Xe^{19+} are very weak in the model, even though in experiment the spectral lines are dominant. Probably, also here the ionization balance plays a crucial role, but no further evidence is available. A xenon concentration of $3.3{\cdot}10^{-5}$ was used to obtain the modeled spectrum. The concentration was chosen to match the emissivity of the spectral lines in the measured spectrum. Unfortunately, the spectral lines are superimposed on an uneven background, which originates either from continuum radiation or from many, densely grouped spectral lines, which are not reproduced by the model calculations. However, this imposes larger uncertainties on the matching of the intensities than for other spectral features, which have been investigated by similar means in the course of the present work.

The agreement is much better for the feature just above 1 nm (figure 7.10), which has been already used to investigate the ionization balance in section 5.3. The discrepancies caused by the overestimation of the ionization states Zn-like Xe^{24+} and Cu-like Xe^{25+} are not visible, because the modeled spectrum contains only the emissions of Ni-like Xe^{26+} to Ar-like Xe^{36+}, which are in good agreement to the measurement. Here, the xenon concentration was adjusted to $1.0 \cdot 10^{-4}$ to match the summed radiance of the measured spectrum. The VUV (figure 7.9) and the soft X-ray spectrum (figure 7.10) originate from the same discharge phase, but the concentration differs by a factor

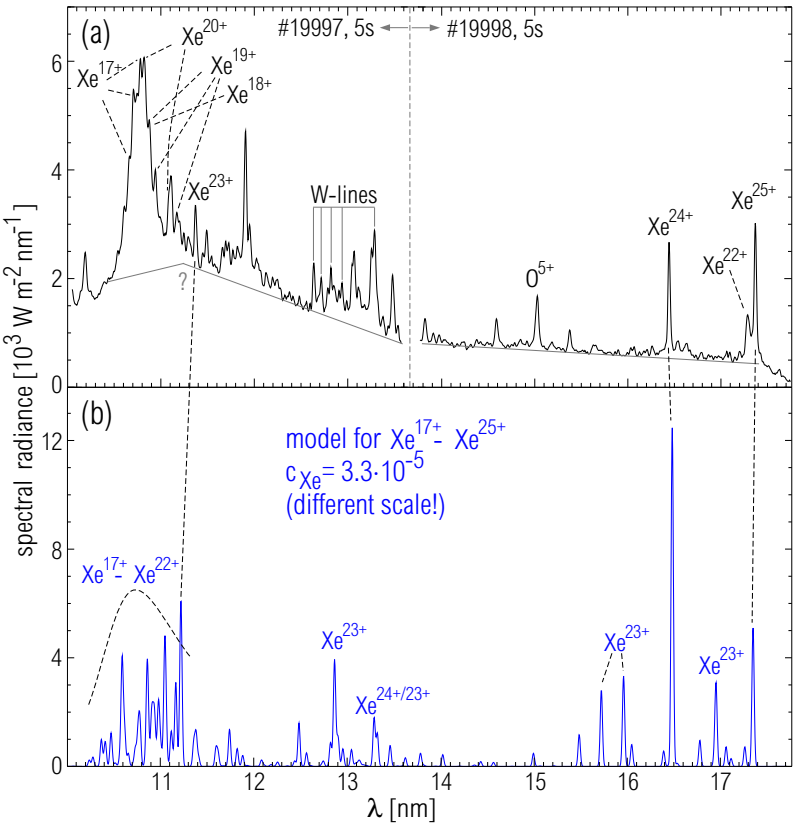

Figure 7.9: *(a)* Measured spectra from two identical discharge phases. Spectral lines are labeled according to the findings of [130]. A tentative background subtraction is indicated, however, the origin of the uneven background is unknown and therefore uncertainties exist. *(b)* Modeled spectrum using the emissions from Rb-like Xe^{17+} to Cu-like Xe^{25+}. The xenon concentration was adjusted to $3.3 \cdot 10^{-5}$ to match the summed emissivity of lines that are observed in model and experiment.

three. A comparison to the total radiation (s. chapter 8) exhibits that the result from the soft X-ray spectrum is close to the result of this more established analysis to evaluate xenon concentrations. Possibly, the analysis of the VUV spectrum is connected to larger uncertainties due to the discussed discrepancies, but also the calibration of the VUV spectrometer from 10 – 18 nm is extrapolated (s. section 3.5.2) and might exhibit uncertainties of that magnitude. This part of the soft X-ray spectrum of xenon was already investigated in [123, 126, 129].

A weak feature has been observed (s. figure 7.11) for central electron temperature above 3.5 keV. This spectral feature is emitted by ion states which are more highly charged than Ar-like Xe^{36+} and are of the type $2p^6 3s^2 3p^n$ – $2p^5 3s^2 3p^n 3d^1$ (for $Xe^{36+} - Xe^{41+}$) and $2p^6 3s^n$ – $2p^5 3s^n 3d^1$ / $2p^5 3s^n 3p^1$ (for $Xe^{42+} - Xe^{43+}$) and $2p^n$ – $2p^{n-1} 3d^1$ / $2p^{n-1} 3p^1$ (for Xe^{44+} and higher charged ions). The modeled spectrum does not fully correspond to the measurements, however, there is no doubt that the observed feature is emitted by the ionization states presented in figure 7.11. The cor-

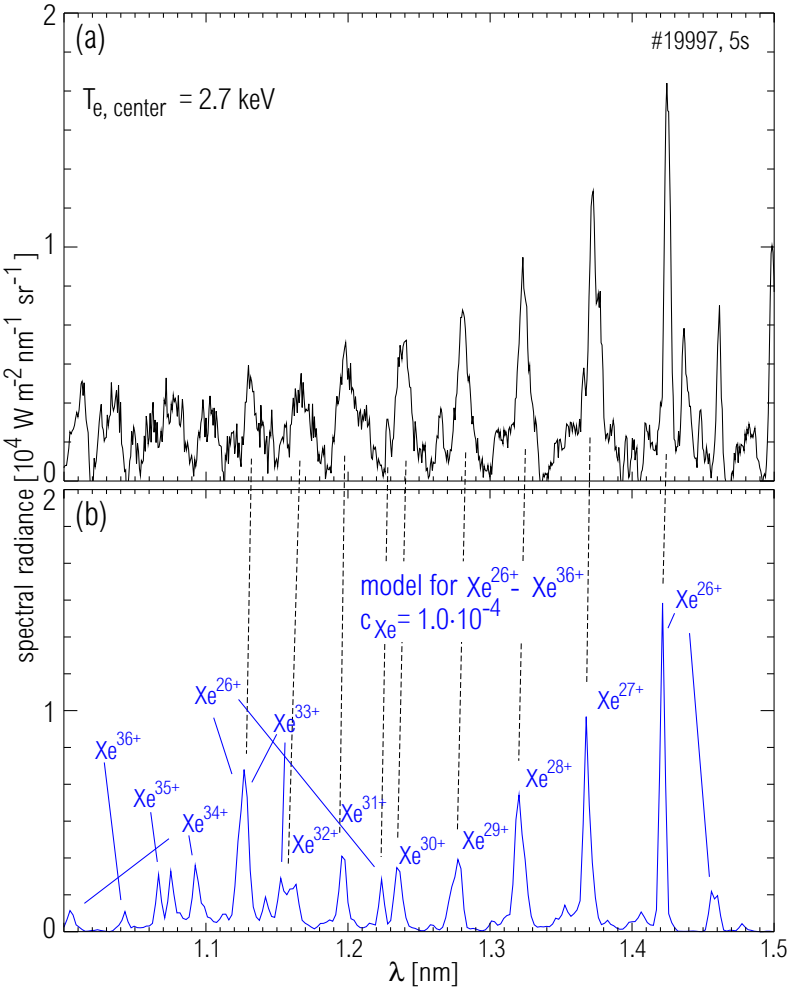

Figure 7.10: *(a)* Measured xenon spectra originating from the same discharge phase as the spectra in figure 7.9. *(b)* Modeled spectrum using the emissions from Ni-like Xe^{26+} to Ar-like Xe^{36+}. The xenon concentration was adjusted to $1.0 \cdot 10^{-4}$ to match the summed emissivity of lines that are observed in model and experiment.

respondence of modeled to measured spectra, which is indicated by the dashed vertical lines is tentatively only, but the xenon concentration obtained from the matching of intensities is $1.4 \cdot 10^{-4}$, while the value derived from the radiated power equals $1.2 \cdot 10^{-4}$. Both values involve uncertainties of about 50 % and therefore, agree within the accuracy of the values. It may be pointed out that in [127–129] only ionization states above Na-like Xe^{43+} have been investigated, while the strongest contributions in the modeled spectrum of figure 7.11 originate from Cl-like Xe^{37+} to Na-like Xe^{43+}. This is due to the low fractional abundance of the ionization states above Na-like Xe^{43+} in the plasma, but also when looking just at the PECs for all mentioned ion states strong spectral lines are emitted by Cl-like Xe^{37+} to Na-like Xe^{43+}. This feature is the only spectral signature, which was obtained in ASDEX Upgrade from these highly

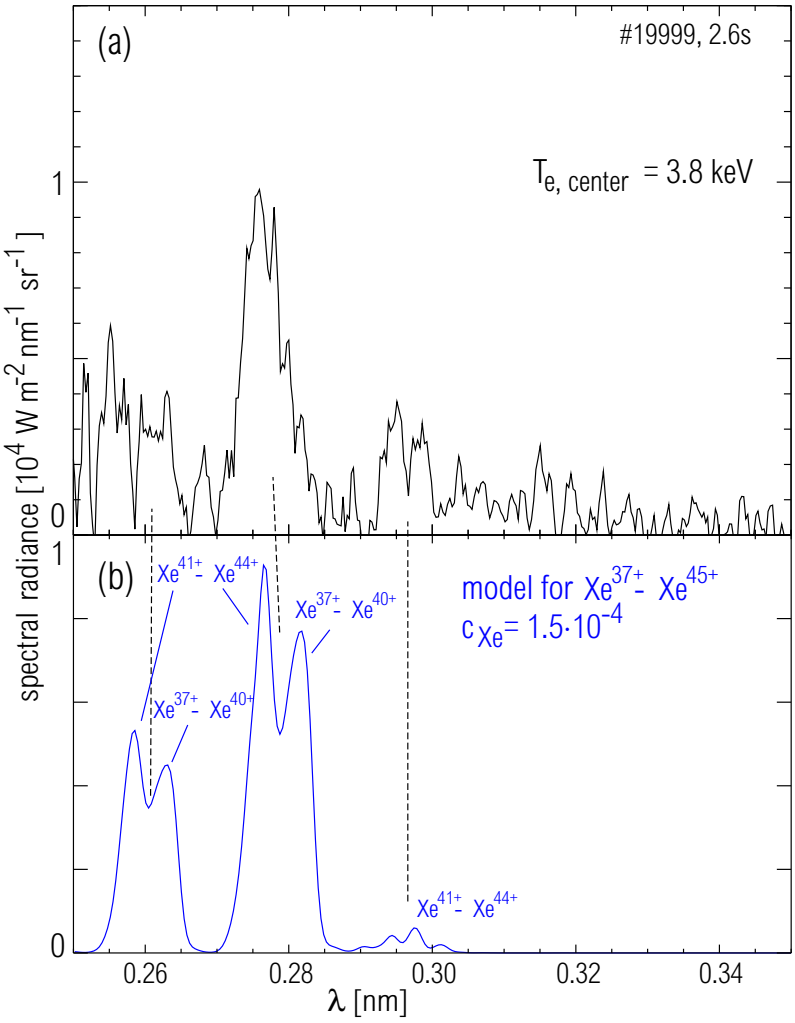

Figure 7.11: *(a)* Measured xenon spectra originating from a plasma with central electron temperature of 3.8 keV. *(b)* Modeled spectrum using the emissions from Cl-like Xe^{37+} to F-like Xe^{45+}. The xenon concentration was adjusted to $1.4 \cdot 10^{-4}$ to match the summed emissivity of lines that are observed in model and experiment.

charged ion states. Following the isoelectronic sequence to tungsten, similar emissions are predicted at about 0.14 nm, which could be a possibility to diagnose up to Ne-like W^{64+} in the central region of a fusion reactor (s. chapter 9).

Chapter 8

Investigations on the Cooling Factor

While the spectral details have been investigated in chapter 6 the total radiated power of tungsten and its neighbor elements is investigated in this chapter. For a fusion plasma this a quantity of strong interest, as reabsorption of impurity radiation is negligible and virtually all radiated power is lost from the plasma volume giving rise to cooling of the plasma. Therefore, the coefficient, which describes the efficiency of an element with nuclear charge Z to cause radiated power density P_Z ($[P_Z] = \mathrm{Wm}^{-3}$) in a plasma , is called cooling factor. The cooling factor L_Z multiplied by electron density n_e and the impurity density n_Z gives the radiated power density as a function of electron temperature and density (s. equation 8.1).

$$P_Z = L_Z(T_e, n_e) n_Z n_e \tag{8.1}$$

Even though L_Z is slightly dependent on n_e, for applications in fusion devices this dependence can hardly be noticed at all. Therefore, effects due to variations in n_e are neglected in the following. L_Z is evaluated in the present work by different means and with different underlying ionization balances. A direct measurement of the cooling factor is difficult for high-Z elements, because the radiated power needs to be measured at the same time with electron density and impurity density. The latter quantity is difficult to obtain with a higher accuracy than about factor of 3. One possibility is the measurement of the change in effective charge Z_{eff} (definition s. equation 8.2, where n_k is the density and z_k the charge of the ion state k) of the plasma following a laser ablation, for which the ΔP_Z and n_e are well measurable.

$$Z_{eff} = \frac{\sum_k^{all\ ions} n_k z_k^2}{n_e} \tag{8.2}$$

The cooling factor of high-Z elements is comparably high, such that stable plasma operation is only possible up to a concentration of few 10^{-4}. The change in the

effective charge ΔZ_{eff} of the plasma for such a concentration is at the detection limit for ΔZ_{eff} of about 0.2. Another possibility to evaluate L_Z is to precisely quantify the injected amount of impurity and compare it to P_Z. For laser ablation this holds uncertainties larger than a factor of 5 as the efficiency for an ablated tungsten ion to enter the main plasma is unknown and can be estimated only with the mentioned uncertainty. A remedy would be pellet injection of manteled tungsten (or other high-Z element) pellets such that a well defined number of impurity atoms is entering the main plasma. Again the amount of high-Z material in such a pellet needs to be below $\approx 1 \cdot 10^{17}$ particles, i.e. about $30\mu g$, to prevent major disturbances of the plasma. The production and injection of such pellets is technically challenging and was not performed in the course of this work.

8.1 Investigations on Tungsten

8.1.1 Calculated Cooling Factor

The cooling factor for tungsten vs. electron temperature is evaluated for a density of $6 \cdot 10^{19}\,\mathrm{m}^{-3}$, but it is practically unaltered for the full density regime which is accessible for tokamak operation. The cooling factors resulting from different evaluations, which are described in the following, are featured in figure 8.1. The cooling factors with the most credibility is represented by the red curve. Above 700 eV, i.e. for ion states with charge above Cd-like W^{26+} the level resolved calculations could be performed in elaborate detail and the collisional-radiative model was used to evaluate PECs for the spectral lines covering the whole spectrum. For each T_e, the emission of spectral lines is integrated to a cooling factor $L_{z,line}$ for the each charge state z. For the charge states below W^{26+}, the Cowan code calculations got too extensive as the number of transitions in the level resolved scheme reached a critical level due to an open f-shell. So, the investigations could not be conducted to a satisfying degree and the use of a collisional-radiative model (s. green curve in figure 8.1) using incomplete information on the ion state could lead to large uncertainties. Therefore, the power densities of line radiation for these ionization states have been evaluated as indicated by the scheme in section 2.3.6 (s. red curve below 700 eV in figure 8.1). Still, the possibly incomplete calculations on ion structure and electron impact cross sections yield uncertainties, which are difficult to quantify and finally also lead to a cooling factor with less credibility below 700 eV. The continuum radiation and the line radiation following dielectronic recombination, which both is contained in the curves described above, is represented by $L_{z,cont.}$ and is obtained as indicated in section 2.3.5 for each ion charge z. These contributions are represented by the gray, bold curve in

figure 8.1. L_Z is obtained at each T_e by $L_Z = \sum_{i=0}^{Z} f_i(L_{i,line} + L_{i,cont.})$, where f_i is the fractional abundance of charge state i. As in chapter 5 the recombination rate has been adjusted to fit the experimentally obtained fractional abundances, $L_{z,cont.}$ needs also to be adjusted for these ionization states. However, as the adjustments were made *ad hoc* this altered continuum and dielectronic radiation (s. grey, thin curve in figure 8.1) is only used for the red, thin curve in figure 8.1, while the other curves use the original $L_{z,cont.}$ (s. grey curve in figure 8.1). The contribution of continuum radiation and radiation following dielectronic recombination to the cooling factor only is important for ionization states above Kr-like W^{38+}. The evaluation only takes a

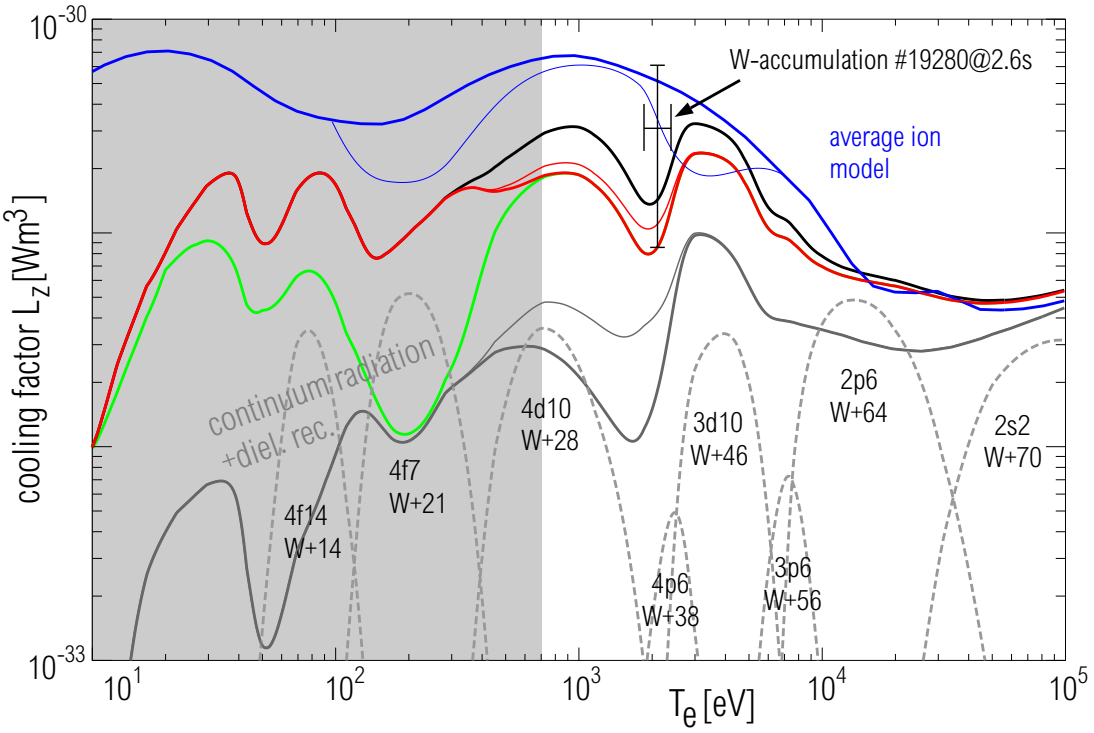

Figure 8.1: Cooling factors of tungsten based on the modified 'CADW+408' ionization balance using different evaluation schemes. Below 700 eV the uncertainties are larger due to the fragmentary calculation possibilities. Red (bold): above Cd-like W^{26+}, level resolved results with collisional-radiative model, below Cd-like W^{26+} corona model; Red (thin): the corrections on the recombination data (s. chapter 5) have been also used to enhance $L_{z,cont}$, Green: all ion states from level resolved results with collisional-radiative model, Black: like red curve, but for ion states above Cd-like W^{26+} an additional correction factor was applied to approximate the weak contributions from higher principal quantum numbers; Blue (bold): Cooling factor derived from the average ion model (Combination of cooling factors from [25, 26]); Blue (thin): Original cooling factor derived from the average ion model (from [25]); Grey,solid (bold): Contribution of the continuum radiation and radiation following dielectronic recombination, i.e.$\sum_{i=0}^{Z} f_i L_{i,cont.}$; Grey,solid (thin): Contribution of the continuum radiation and radiation following dielectronic recombination, using the adjustment factors of section 5.2.2 also for the radiation following recombination; Grey,dashed: $f_z \cdot 1 \cdot 10^{-31}\,\mathrm{W\,m^3}$ for a few ionization states.

limited number of transitions into account and naturally only Δn=0, 1 and sometimes Δn=2 are considered to limit the size of the calculation. However, contributions from higher quantum numbers increase the cooling factor represented by the red line. These contributions are roughly estimated by the assumption, that the cross sections of electron-impact excitation into upper quantum numbers n are $\propto 1/n^3$. With this assumption a correction factor is obtained for each ionization state, which scales the calculated cooling factor to a virtually complete cooling factor (black curve in figure 8.1). This curve, however, is not considered superior to the red curve, because the absence of configurations in the original atomic calculations underlying the red curve influences the results of the calculation and this influence is thought to be of similar size as the applied correction according to the scaling of cross sections. The black curve therefore, could be interpreted as the typical uncertainty of the red curve due to the unconsidered configurations. For comparison to earlier results, the cooling factor from [26] is presented (blue, bold curve), which is an enhancement of the data from [25] (blue, thin curve). It is remarkable, that the older data [25] seem to agree better to the data of the present work, since the bulk of the cooling factors above 2.5 keV is similar, while the structure exhibits differences. The shell structure in the red curve is more pronounced than in both data sets of [25, 26], as the average ion model smoothes out effects of single ionization states.

A direct test of the cooling factor could be performed during a temporary impurity accumulation event during discharge #19280. As the most intense change in impurity profile is occurring in the center of the discharge and a tungsten concentration of about $3 \cdot 10^{-4}$ is reached. A change of 0.4 in the Z_{eff} profile is observed, which is obtained by the deconvolution of many lines of sight and can be attributed to the tungsten accumulation. The error bars for the cooling factor are mainly due to the uncertainties of the Z_{eff} deconvolution, while the uncertainty in electron temperature is given by the spatial variation of electron temperature in the accumulation region. The error bar towards smaller L_z is especially large, as a curvature restriction for the deconvolution of the Z_{eff} profile restricts ΔZ_{eff} to 0.4, while without restrictions of curvature ΔZ_{eff} could be as large as 1. The data point lies closest to the curve of [25], however, all presented cooling factor are inside the uncertainties of the measurement. The measured data point lies precisely at an electron temperature where the red, bold curve exhibits a drastic drop (at T_e=2 keV) of the cooling factor. There is no experimental evidence for such a drop, even though several phases with impurity accumulation, in which the central electron temperature swept over 2 keV, were analyzed and no systematic drop in radiated power was observed. For these analyses, it has been assumed that the tungsten concentration inside the accumulation region is changing linearly with time, an assumption which is not rigidly true, but at least some structure of the total radiation

should have become visible at 2 keV, especially as turbulent transport is suppressed largely for impurity accumulation. A possible effect which would mitigate the drop of the cooling factor at 2 keV could be the underestimation of continuum radiation, as the spectra covering the total spectral range suggest that there really is less intensity in spectral lines at 2 keV. The corrections indicated by the red, thin curve point in that direction, however, the presented corrections are too small. Below, an investigation is presented on the impact of the different ionization balances on the cooling factor. As the ionization balance around 2 keV exhibits only small uncertainties, this effect is considered unimportant for the discussed issue. Nevertheless, the comparison is presented to demonstrate the effects of different ionization balances on the cooling factor also for other electron temperature ranges.

The differences between the data from [26] and the presently obtained curves are large, i.e. up to factor of 5, in the range $1-2$ keV, but decrease to less than about 50 % for temperatures above 4 keV and nearly vanish for temperatures above 10 keV. So, for future fusion devices, which aim for temperatures above 10 keV the different predictions are in agreement with each other. This fact strengthens the confidence in the predicted upper limit for the tungsten concentration allowing for reactor relevant plasma operation (s. chapter 9). Independent of the discussed uncertainties, it must be noted that the detailed investigations on the spectral features (s. chapter 6), which revealed good correspondence of the most intense spectral features and the model, put the new cooling factor in favour. The absolute intensity of spectral features will be compared to the radiated power in section 8.1.2, to check if the relative contribution of the spectral feature to the cooling factor is correctly calculated.

In chapter 5 different ionization balances were presented. In the following, the question is elucidated, how large the impact of the ionization balance is. Even though the modified 'CADW+408' data are best describing the measurements, as presented in chapter 5, the use of the other ionization balances is considered to document the possible deviations for elements which do not have higher quality data available. In principle, the impact of the ionization balance on the cooling factor should only be visible at large gradients, because if two neighboring ionization states do exhibit similar L_zs it does not matter for the cooling factor which of the two ionization states is more abundant. In figure 8.2, the cooling factor is derived following the scheme of the red, bold curve in figure 8.1, which used the ionization balance labeled modified 'CADW+408' (thick solid in figure 8.2). The other curves differ only by the used ionization balance, which are 'CADW+408' (thin solid), '408+408' (long dashed) and modified ADPAK data from [39] (short dashed). The bulk of the cooling factor is hardly changed, but the structure, which is caused by certain groups of ionization states are shifted and deformed. The local minimum at 2 keV is shifted to lower electron temperatures reach-

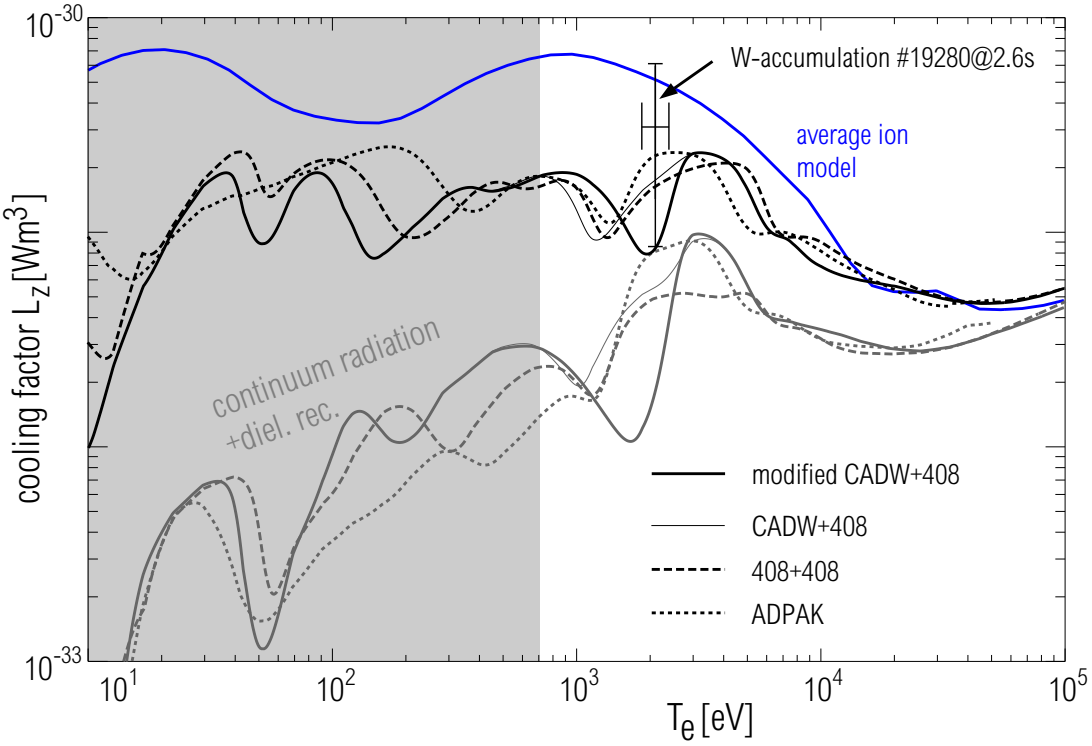

Figure 8.2: Cooling factors derived by following the scheme of the red line in figure 8.1 but for different ion balances: modified 'CADW+408' (thick solid, identical to red line in figure 8.1), 'CADW+408' (thin solid), '408+408' (long dashed) and modified ADPAK data from [39] (short dashed). The continuum radiation is given accordingly by the grey lines. The blue line corresponds to the data from [26]. The measured data point is described in the text.

ing 1.2 keV for the unmodified 'CADW+408'. The broad maximum around 3.5 keV is shifted towards higher electron temperatures for the '408+408' data, while for the 'ADPAK' data the shift is towards lower electron temperatures. For electron temperatures, where a minimum of one curve coincides with a maximum of another curve differences between the curves of up to a factor 3 occur, i.e. at 1.1 keV, 2, keV and 4.5 keV. It must be noted, that in the electron temperature range between 1 keV and about 5 keV the ionization balance of the solid line exhibits the best agreement with the detailed measurements (s. chapter 5). Therefore, the cooling factor, which exhibits the drop at 1.9 keV electron temperature (solid line), must be considered as the best available cooling factor for that temperature range. Similarly as for the curves in figure 8.2, larger discrepancies of all black curves exist below 2 keV (about factor of 5) in comparison to the blue curve from [26]. The deviations strongly decrease for temperatures above 10 keV.

8.1.2 Contribution of Spectral Emissions to the Cooling Factor

The focus is put here on the contributions from 3 spectral features. The quasicontinuum at 5 nm with importance for the total radiation in the electron temperature range 0.7– 1.6 keV, the feature at 0.6 nm with importance for the total radiation in the range 2.0– 5.0 keV and the spectral feature at 18 nm which is significant for the total radiation at electron temperatures below about 1 keV. For the first two features, the code calculations result in predictions, which are suitable to describe the main characteristic of the feature and which contribute considerably to the cooling factor. The third feature is not predicted and therefore, it is missing in the calculated cooling factors presented in section 8.1.1. For the LBO in discharge #18727, the comparison of the calculated to measured spectrum at 5 nm (s. figure 7.1) leads to a tungsten concentration of $5.3 \cdot 10^{-5}$. An analysis of the total radiation caused by the LBO yields the results $2.7 \cdot 10^{-5}$ and $9.9 \cdot 10^{-5}$ for using the cooling factor at 1.4 keV from [26] or the one of the present work, respectively. The analysis of the spectrum corresponds within a factor of 2 to the results using the radiated power. As the uncertainties of the absolute calibration of the spectrometer and the deconvolution of the radiation power density are of similar size, no significant discrepancy between the different evaluations is apparent. The uncertainties are considerably smaller for the soft X-ray spectrometer. Here, a continuous tungsten contamination is examined using the spectrum of discharge #16778 (s. figure 6.13). The tungsten concentration derived from comparison of spectrum and model is $2 \cdot 10^{-4}$. Interpreting the radiated power, the results are $9 \cdot 10^{-5}$ and $1.5 \cdot 10^{-4}$ using the cooling factor at 3 keV from [26] or the one of the present work, respectively. The discrepancy between the spectral interpretation and the interpretation of the radiated power using data of the present work is only 25 %, a discrepancy, which lies within the uncertainties of the experimental data. At an electron temperature of 3 keV, this emphasizes the completeness of the code calculations and underlines credibility of the cooling factor. As pointed out in section 8.1.1, the situation is less encouraging for the cooling factor below 700 eV. Not only the calculation detail is unsatisfactory, but also emissions are documented in the spectrum around 18 nm which are not reproduced by the code calculations (s. section 6.2.4). A rough estimation uses the assumption based on the STRAHL simulation presented in figure 6.11, that at the radial position where the emissions take place a tungsten concentration of up to $3 \cdot 10^{-4}$ is reached a few milliseconds after the LBO, where the thickness of the emitting layer is about 40 cm on the LOS integrated path. This estimation results in a contribution of the observed structure around 18 nm to the cooling factor of $1 \cdot 10^{-31} \mathrm{Wm}^3$, which is comparable to the calculated cooling factor

(s. figure 8.1). As the cooling factor is neglecting these emissions around 18 nm the cooling factor below 700 eV needs to be considered as preliminary. An improvement of the calculations can be expected, when a configuration averaged code is reliably integrated into the ADAS scheme. Such a code would treat the ionization states less accurate than the level resolved scheme used for the actual work, but for the ionization states below Cd-like W^{26+} no restriction due to calculation complexity would occur and the calculation results would be more reliable.

The relative intensity in the different wavelength ranges is not only a benchmark of the theoretical data, but is useful itself, when the absolute signal of the soft X-ray diagnostic is interpreted as an impurity diagnostic. The sensitivity versus wavelength of this diagnostic is depending on the Be-filter thickness and the thickness of the detecting diodes (s. figure 3.2). The Be-filter cuts off all emissions above a certain wavelength, while the thickness of the detecting layer of the diodes gives rise to a decreasing detection probability below a certain wavelength. With the atomic data calculated in the course of this work, it is now possible to give not only an cooling factor for the total radiation, but it is also possible to calculate the fraction of the total radiation which is detected by such a wavelength sensitive diagnostic. In figure 8.3, the three filtered cooling factors are presented that correspond to the three sensitivity curves presented in figure 3.2. For comparison, one measured data point (W-LBO in discharge #14777) and an upper limit for a measured data point (W-LBO in discharge #18727) are plotted. For the latter no signal on the soft X-ray camera was visible and the upper limit was derived using its sensitivity. These measurements originate from a camera with 100 μm Be-filter and a 300 μm thick active layer of the detecting diodes. The measured data have been obtained by comparing the radiated power measured by the bolometer to the measured soft X-ray signal and then multiplying the unfiltered cooling factor by the ratio of the signals. It was assumed that the sensitivity of the diodes is not influenced by the preceding neutron irradiation for discharge #14777, as the diodes have been exchanged before discharge #14049, and that for discharge #18727 the sensitivity has declined by a factor of 3 (for #17833 a factor of 2.6 has been determined in section 3.5.1). The presented uncertainties originate from the deconvolution of bolometer and soft X-ray signals. The deconvolution was necessary, because the comparison was performed in the plasma center at the presented electron temperatures. The agreement is satisfying which underlines the agreement of code calculations and measurements on the coarse distribution of emissions within the spectral ranges. The diagnostic of tungsten using soft X-ray cameras is superior to using the radiated power, because typically the detectable emissivity for this diagnostic is monotonically increasing towards the plasma center. This fact leads to smaller uncertainties for the deconvolution of the radial distribution of emissivity

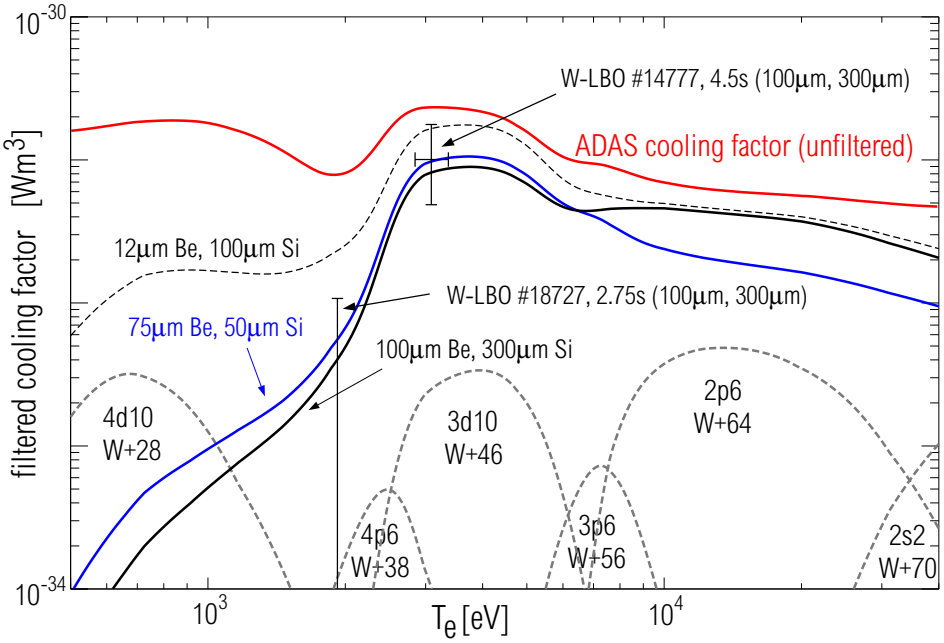

Figure 8.3: Cooling factors which are folded by different sensitivity curves of soft X-ray cameras (s. figure 3.2). The sensitivities correspond to a beryllium thickness of 12 (thin, black, dashed), 75 (blue), and 100 μm (black) for detecting diodes with an active layer thickness of 300, 50 and 300 μm, respectively. For comparison the unfiltered cooling factor (also ADAS) is presented (red). The grey, dashed curves give $f_z \cdot 1 \cdot 10^{-31}\,\mathrm{W\,m^3}$ for a few ionization states.

using the signals of many LOS. On the other hand, the sensitivity of the soft X-ray diagnostic needs to be known precisely, including the deterioration in sensitivity due to neutron irradiation. The bolometer does not suffer from such effects and it also gives information from plasma regions with temperatures below 2 keV. Therefore, the bolometer data are used instead of the soft X-ray intensities in the present work.

8.1.3 Tungsten-Diagnostic

The comparison of spectral emissions to the total radiation, which was performed in section 8.1.2 to investigate the accuracy of atomic data, has been used already before the present work to quantify the tungsten concentrations in ASDEX Upgrade [13, 39]. This was done without the use of spectral information from atomic data, but by relating the the line intensity of the Ni-like W^{46+} line at 0.793 nm (Johann spectrometer) and the intensity of the quasicontinuum to the total power radiated by tungsten. This relation has been obtained in special calibration discharges with LBO, where the change in line intensity was compared to the change of the bolometer signal for radiated power. Via the cooling factor of [25, 26] the tungsten concentration could be evaluated. The analysis also needs to consider the measured electron densities and

the fractional abundance of Ni-like W^{46+} along the spectrometer LOS. The latter has been evaluated using the ionization balance resulting from the modified ADPAK data [39] at the measured electron temperatures along the plasma radius [13, 39]. The emissions give information on the tungsten concentration only at the plasma radius, where they are emitted, i.e. the Ni-like state from 2 keV to 5 keV and the quasicontinuum from 0.8 – 1.6 keV electron temperature. Therefore, if the central temperatures of the plasma is close to or below $\approx$2 keV the abundance of Ni-like W^{46+} is so small that signal close to the detection limit corresponds to huge central tungsten concentration. An error in the assumed fractional abundance translates directly into an error in tungsten concentration, and for electron temperatures around 2 keV this means that huge uncertainties on the measured tungsten concentration exist. When comparing ionization balance for the 'ADPAK' data to that of the modified 'CADW+408' data (s. figure 5.3) the tungsten concentrations evaluated at temperatures around 2 keV would differ by a factor of 25. For this reason, the evaluation of tungsten concentration using the Ni-like W^{46+} line has been restricted to plasmas above 2 keV and with the new ionization recombination data a huge improvement for the tungsten concentration at temperatures close to 2 keV is expected. To tackle the region of 2 keV with smaller uncertainties, the evaluation of spectral lines in the VUV has been automated and all spectral lines in the VUV, which have been presented in chapter 5 and 6 are routinely analyzed. A reliable evaluation is possible down to central plasma temperatures of 1.8 keV. This is only a moderate extension of the analysis region due to the dense grouping of the As-like W^{40+} to Ni-like W^{46+} ionization states (s. figure 5.6), but the gap without tungsten diagnostic between 1.6 keV and 2 keV is considerably decreased. The temperature dependent analysis of the quasicontinuum is less critically influenced by the improved data.

8.2 Cooling Factors for Other High-Z Elements

Similar as for tungsten, the cooling factors for the other investigated elements have been derived (s. figure 8.4). The ionization data originates from scaling the tungsten data along isoelectronic sequences, except for xenon where the data were evaluated by the ADAS codes (s. section 2.3 and 5.3). The values for $L_{z,line}$ and $L_{z,cont}$ have been evaluated for all elements by the level resolved calculations (s. section 2.3). No corrections, such as indicated for W were applied. The cooling factors for all elements except Xe exhibit a very similar shape, which is shifted according to the shift of the ionization and recombination data. For Bi no revision of the data from [25] is available like for W [26]. The Bi curve of the present work compares to that from [25], similarly as the W curves do (thin blue curve in figure 8.1 corresponds to the original curve

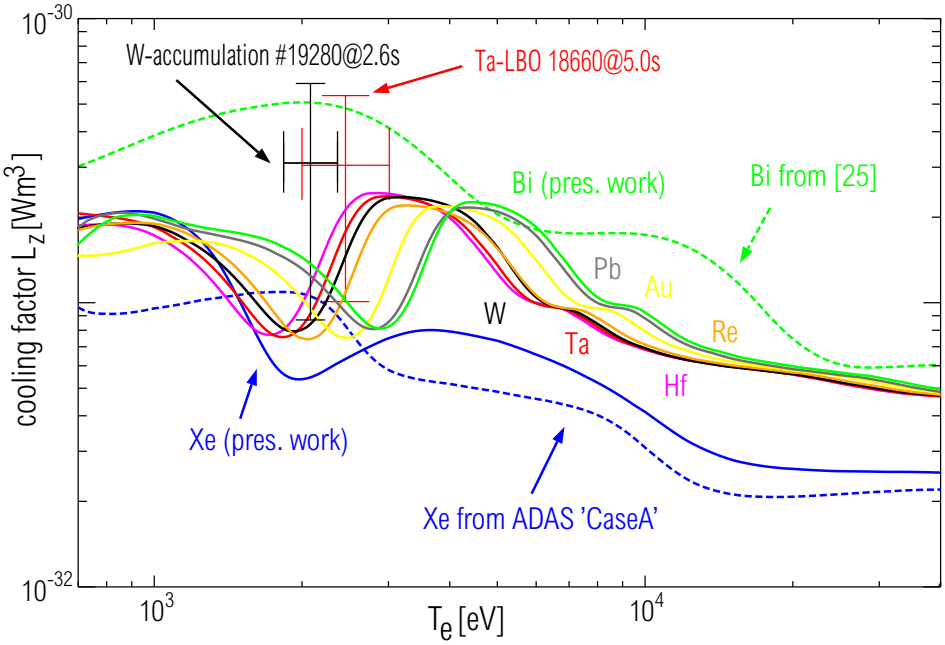

Figure 8.4: Cooling factors derived for all investigated elements. The radiation for each ion state has been derived from the level resolved ADAS calculations, while the ionization data are described in section 5.3. For comparison the earlier cooling factors of Xe (from earlier ADAS 'Case A') and Bi [25] are also presented.

from [25]). The Bi curve from [25] is up to a factor 5 larger than the curve of the present work below 4 keV electron temperature, while the two curves converge above 20 keV. In [25] the data for Ta and Au are also given, but the differences between them and the present work are qualitatively very similar to the presented differences for W and Bi. Two measured data points are presented, one originating from W (s. section 8.1.1) and the other corresponds to a LBO of Ta, for which the Z_{eff} was compared to the total radiated power. For both data points the uncertainties of the measurement are large and agree with the available predictions.

For Xe, the curve is considerably lower. The curve of the present work has a different shape than the curve from the earlier 'Case A' ADAS data. These differences are due to the different ionization data, but also the data on radiation differ between the two data sets. Nevertheless, the differences between the two curves are within a factor of two at the presented electron temperature range.

The contribution of spectral emissions to the cooling factor is investigated in the following. The measured spectral features in the VUV and soft X-ray were compared to the code calculations which resulted in the impurity concentration. These results are then compared to the interpretation of the radiated power using the ADAS cooling factor and the cooling factor from the average ion model (AIM, [25]). In the VUV the

spectral emissions are difficult to interpret and it is found that the results of such an comparison of spectral emissions to the total radiation is strongly dependent on the actual dynamics of a single LBO. One difficulty is, that when considering the LBO presented in figure 7.1 impurity accumulation occurs for Au and Bi, which makes the analysis strongly dependent on the accuracy of the ionization balance. A second uncertainty which is often observed for analyses on LBO is the fact, that the radiated power overshoots in the first 100 ms after a LBO, as the ionization balance and the populations of the ions have not yet reached an equilibrium. For W the analysis could be reliably performed (s. section 8.1.2), because the experience on many W-LBO helped to average over these uncertainties and to get more data 150 ms after the LBO where reliable conditions exist. The dynamical evolution of the impurity concentrations after the LBO is less important for more central ionization states in the plasma. These are investigated by comparison of the soft X-ray emissions to the radiated power. In figure 8.5, the analyses are presented. For Hf and Ta, the evaluation of the impurity concentrations from the spectral emissions are too high compared to the total radiated power. As this is a test of whether the spectral ADAS data agree

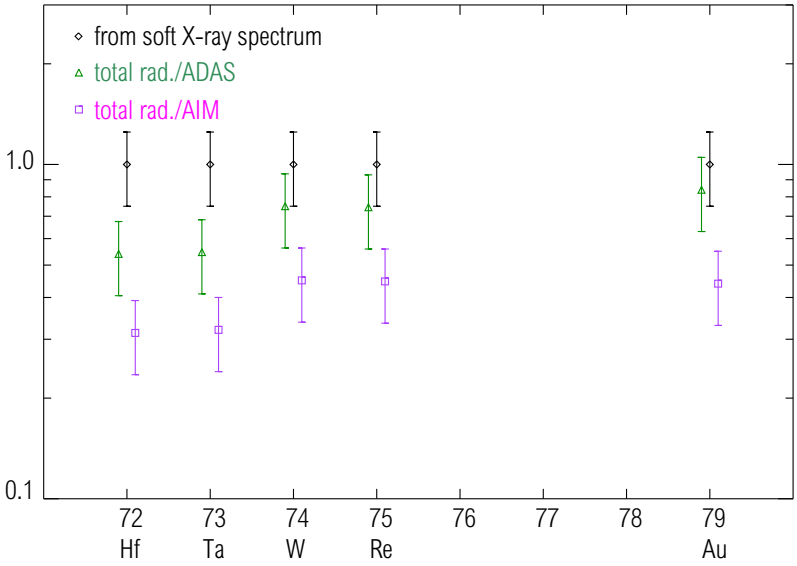

Figure 8.5: Relative comparison of the concentrations resulting from the evaluation of the spectral soft X-ray emissions (black), the interpretation of the radiated power with ADAS data (green) and with data from the average ion model (AIM,[25]) (magenta)

with the ADAS cooling factor the main focus is put on the agreement of these data points. For Hf and Ta, disagreement is found, while for W, Re and Au the data are consistent. It cannot be excluded that the error bars may be chosen too small, as several different origins of uncertainties were added using Gaussian error propagation, which assumes statistical cancellation of errors. Already 10 % larger uncertainties

would lead to an overlap of the error bars of the measurements for Hf and Ta. The good agreement for W, Re and Au underlines the accuracy of the cooling factor for the electron temperature above $\approx 2\,\mathrm{keV}$. The values of the AIM lie consistently below the concentrations derived from the spectra using ADAS data.

Chapter 9

Implications for Other/Future Fusion Devices

The question for the implications on other or future fusion devices has two interpretations. On the one hand there is the question whether the present work implies a different limit on the tolerable tungsten concentration in a fusion device. On the other hand the question needs to be answered, how tungsten can be diagnosed in the plasmas of future devices.

For answering the first question, it needs to be pointed out that the predictions on the tolerable tungsten concentrations in a fusion reactor are based on a 0-dimensional model, which only takes the central region of a reactor into account. For this region, where fusion will take place in 'burning' devices, the criteria for a self-sustained fusion reaction (ignition) is not altered by the present work, as the newly obtained cooling factor is equal to the cooling factor from [25] for the relevant electron temperatures. For electron temperatures below $\approx 10\,\mathrm{keV}$, the cooling factor of the present work is smaller than that of [25]. No clear predictions are available, how radiated power at this non-central plasma regions is affecting the performance of the fusion plasma and it is already known today that radiation at this plasma region is needed to dissipate the power flux towards the plasma walls.

Considering the second question, i.e the diagnostic of tungsten in future devices, it is obvious that investigations at ASDEX Upgrade deal with plasma parameters (up to about $T_e = 5.5\,\mathrm{keV}$) which are relevant at the outer quarter of the plasma of a fusion reactor only. For ITER (s. appendix B.3), central electron temperatures of $15\,\mathrm{keV}$ (in advanced discharges up to $\approx 30\,\mathrm{keV}$) are envisaged, which is also a reasonable temperature range for a reactor. This means, that for the core region, where the largest fraction of the fusion reactions takes place, and for the large plasma volume up to ρ_{pol}=0.7 the diagnostic for tungsten is still unexplored. In figure 9.1, the predictions

of the actual code calculations for ITER are presented along with the predictions for plasmas in ASDEX Upgrade and JET (s. appendix B.2) plasmas. The spectra were obtained by simulating a horizontal spectrometer LOS at the midplane. The ASDEX

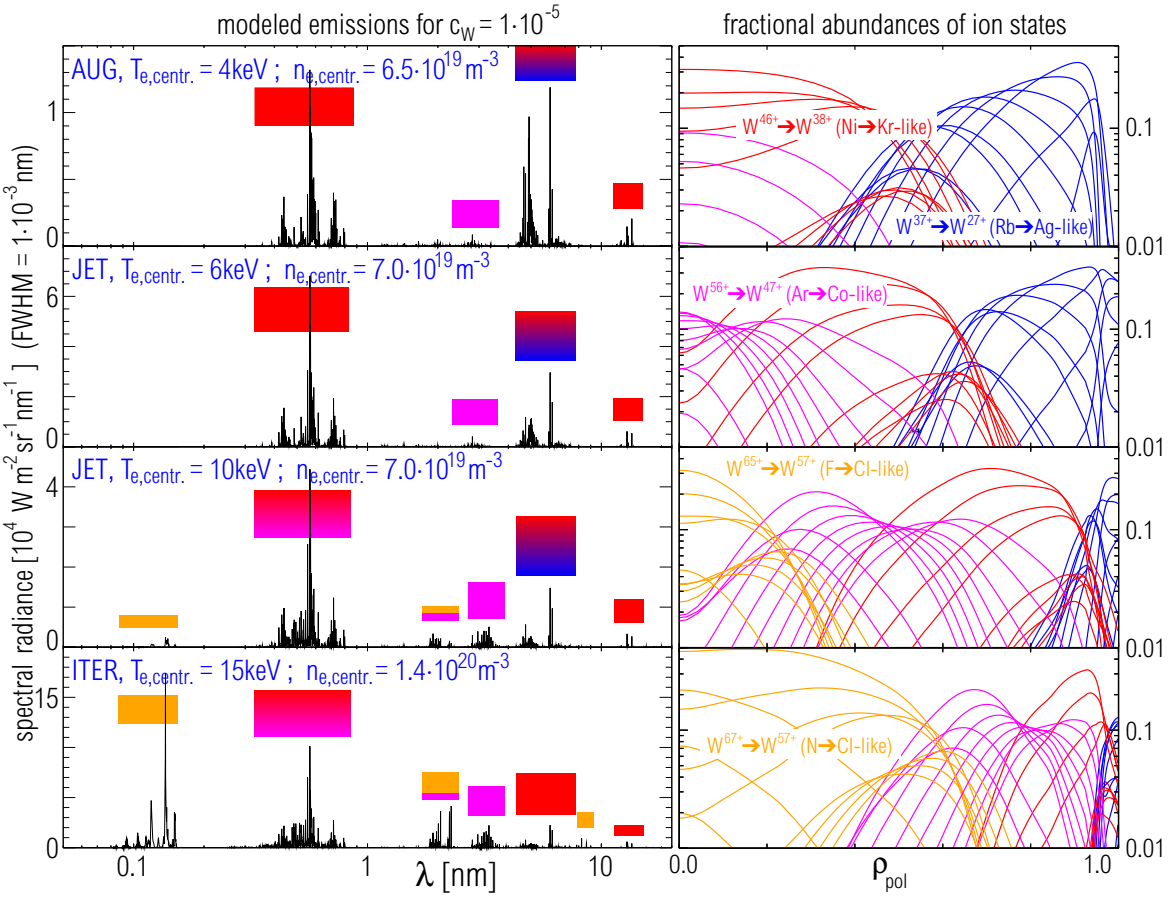

Figure 9.1: *Left column:* Comparison of predictions for tungsten spectra from ASDEX Upgrade, JET and ITER. A spectrometer LOS which runs horizontally through the midplane was assumed. The central plasma parameters are given in each spectrum. The W-concentration was assumed to be $1 \cdot 10^{-5}$ for all plasmas. All spectral lines have been convolved with an Gaussian line profile ($\mathrm{FWHM} = 1 \cdot 10^{-3}$ nm). *Right column:* Fractional abundances of the ion states of W along the normalized plasma radius ρ_{pol}. The color code corresponds to the colored boxes above the spectral lines in the left column which are emitted by the respective ion states. Note: The color code does not correspond to the colors used for displaying ion balances in earlier chapters.

Upgrade spectra are presented for reference only. Following the color code in figure 9.1 (colored box above an emission corresponds to the color of emitting ion states in the right column), the most intense emissions of central ion states, i.e. about N-like W^{67+} to Cl-like W^{57+}, in ITER are emitted between 0.08 nm and 0.15 nm and originate from transitions between the configurations $2p^n - 2p^{n-1}3d^1/2p^{n-1}3s^1$ or $2p^6 3s^n - 2p^5 3s^n 3d^1$ or $2p^6 3s^2 3p^n - 2p^5 3s^2 3p^n 3d^1$ (depending on the emitting ion state). Ne-like W^{64+} to Cl-like W^{57+} exhibit emissions around 2 nm, while Na-like W^{63+} to Si-like W^{60+} emit

spectral lines around 8 nm. The choice of the 'central' ionization states is to some extend tentative, as there exist uncertainties in the ion balance and the definition of plasma center is somewhat arbitrary. The spectral region around 3 nm exhibits many spectral lines of the Ar-like W^{56+} to Co-like W^{47+}, which represent tungsten in the plasma from about mid-radius to the $\rho_{pol} \approx 0.9$. Ni-like W^{46+} to about Ag-like W^{27+} can be used as an tungsten diagnostic for the outer quarter of the plasma. It may be noted that the absolute intensities of most spectral features, except those emitted by the ion states at the plasma edge where steep gradients exist, increase with the density and the size of the plasma. Therefore, the signal will naturally be larger in JET and ITER even for the same electron densities compared to ASDEX Upgrade and the detection of tungsten will be consequently more sensitive in these devices. To investigate the emissions of tungsten at higher electron temperatures, experimental proposals for the JET campaign in 2005/2006 are launched, which plan to inject tungsten via laser ablation into JET plasmas which exhibit up to 10 keV electron temperature. For lower electron temperatures not many new lines are expected to be visible in the spectra (s. spectrum for JET at 6 keV central electron temperature in figure 9.1). In the campaign from 2009 on tungsten surfaces are planned in the divertor of JET and more detailed investigations will be feasible. It may be possible to investigate the most important spectral lines for diagnosing the ITER standard plasma. Still, it has to be kept in mind that for the advanced ITER discharges which exhibit up to 30 keV, even higher ion states (up to Li-like W^{71+}, or even He-like W^{72+}) will occur in the plasma center at considerable fractional abundances. Independent of tokamak investigations the spectral lines of these ionization states can investigated in today's EBIT devices, which easily can investigate ions with ionization potentials up to 150 keV [131], while Li-like W^{71+} exhibits an ionization potential of only 19.7 keV. Additionally, the atomic data for elements with less electrons are easier to evaluate in more detail and the predictions will be more accurate. The detailed investigations on the spectrum of tungsten will also improve the diagnostic of tungsten using soft X-ray cameras which integrate the radiated power over a certain wavelength interval.

Chapter 10

Summary

In the present work investigations on the spectra of highly ionized tungsten have been performed with the aim to better understand the spectra, to benchmark new theoretical tools, to produce predictive atomic data using these tools, to improve the diagnostic capabilities in present experiments and to project the diagnostic capabilities for high-Z elements in future fusion devices like ITER or a fusion reactor. The work on tungsten has been complemented by investigations on other high-Z elements to further benchmark the predictions of the used atomic codes and in the case of xenon to improve the diagnostic capabilities on xenon, which might be used as a diagnostic impurity or for cooling purposes in ITER or a fusion reactor.

Preparations for these investigations have been performed by calibrating the spectrometer systems at ASDEX Upgrade, which cover the full spectral range from 0.1 nm to 100 nm. In parallel, experiences with a newly implemented code package of the ADAS project had been gathered. The code package was adjusted and optimized in several parts to fit the requirements of the elaborate calculations. The Cowan code is part of this code package and performs structure calculations for the investigated ions. The ion structure gives rise to wavelengths of spectral lines and contains the wavefunctions, which are used in a second step for the more elaborate calculations on electron impact cross sections. The ion structure and the excitation rates are then processed by an ADAS internal collisional radiative model, which yields line emissivities as a function of plasma parameters. For many spectral lines, the wavelengths have been corrected by an independent evaluation of the ion structure using the fully relativistic code GRASP, but without influencing the line intensities, as the wavefunctions, which enter the electron impact calculations, have not been adjusted. Finally, a large set of data of all ionization states of tungsten is made available by the present work, which is evaluated for the ionization states from about Xe-like W^{20+} up to about Cr-like W^{50+} by confronting the results to experimental data. Not only spectral lines have

been calculated by the atomic code, but also ionization and recombination rates were evaluated according to scaling formulas that use details of the atomic structure. The agreement of the latter data to experimental results was found to be unsatisfying, but the use of ionization rates which have been made available by other ADAS coworkers using configuration average distorted wave calculations resulted in an ionization balance for tungsten, which exhibited much better agreement for the ionization states of Se-like W^{40+} up to Ni-like W^{46+}. Additional adjustments have been applied *ad hoc* to the recombination rates of the ion states Pd-like W^{28+} to Zn-like W^{44+} to satisfy the electron temperature resolved experimental data on the fractional abundance of ionization states and to satisfy the relative weight of each ion state in the line of sight integral. The effect of impurity accumulation, which was observed during several discharges enabled these investigations. Ionization data for the neighboring elements Hf, Ta, Re, Au, Pb and Bi were obtained by scaling the ionization and recombination rates of tungsten according to the energy difference of the ionization potentials for isoelectronic states. For xenon, new ionization and recombination data were obtained using the scaling formulas implemented in ADAS, but these data also disagreed noticeably.

As the ionization and recombination rates have been made available it was possible to model the measured spectra by simulating the view of the spectrometer through the plasma regions with various plasma parameters. Good agreement with the measured spectra is found for electron temperatures above 1 keV and for ionization states above Cd-like W^{26+}. Spectral features have been identified and investigated especially between 0.4 nm and 40 nm. Most important is the feature at 5 nm, which is a major contribution to the radiated power. This feature, called 'tungsten quasicontinuum', was elucidated by comparing the tokamak spectra to spectra from the Berlin EBIT. The correspondence is documented not only for the Ag-like W^{27+} to Y-like W^{35+}, but also the spectral lines emitted by Br-like W^{39+} to Cu-like W^{45+} are observed in both measurements. Even though the EBIT and tokamak measurements are largely in agreement, it must be pointed out that some features exist which are clearly different. In the tokamak a weak maximum of the emission envelope is visible at 6 nm, which is not seen in the EBIT spectrum. Furthermore, several spectral lines from 4.4 nm – 4.8 nm are observed in the tokamak, which do not have a correspondence in the EBIT spectra. One possible reason is the higher density in the tokamak which might lead to the enhancement of spectral lines. For other strong spectral lines emitted from 4 – 7 nm, identifications have been confirmed by a new method using the dependence of spectral line on the electron temperature of the plasma. A quasi-local measurement of emissivities versus electron temperatures has been possible due to the phenomena of impurity accumulation which helped to circumvent the problems connected to the line of sight integrated measurements for non-accumulating, standard discharges. The line

identification of spectral lines from 12 – 14 nm was possible by this technique leading to twelve newly assigned spectral lines, while four have been observed for the first time. The predictions of the ADAS code are not accurate in the VUV range. Predicted lines can only be attributed to the lines of the spectrum using experimental data in addition. The width of the predicted quasicontinuum is not in agreement with the measurement, while the reason for this is unclear. However, the predicted emissivity in the spectral range seems to be close to the measured value as comparisons to the total radiation exhibit agreement within a factor of about 2. In the spectral range from 2 – 3.5 nm weak spectral lines of Mo-like W^{32+} to Sn-like W^{24+} have been observed which allow to prove the existence of these ionization states at the corresponding electron temperature. Connected to this, it was possible to demonstrate experimentally that emissions from 13 –25 nm are emitted by ionization states between Ag-like W^{27+} to about Xe-like W^{20+}. On the one hand these emissions were dominant in the spectrum during impurity accumulation with central electron temperatures below 1 keV, when also corresponding emissions at the spectral range 2 – 3.5 nm have been visible. On the other hand the analysis of the evolution of several laser blow-offs exhibited, that the above mentioned ion states are the emitting states. These emissions could not be compared to the theoretical predictions, because no consistent set of emissions is calculated by the very elaborate calculations for these ion states. Here, a limitation of the level-resolved code calculations becomes apparent, because for an open f-shell the number of levels easily exceed 5000, which is not flexible enough to perform detailed investigations. In the same spectral range from 2 – 3.5 nm at electron temperatures of about 5 keV, emissions of Co-like W^{47+} to Cr-like W^{50+} have been documented. For these, disagreements between predicted and measured wavelengths and line blending did not allow to separately identify the emitting ion states.

While not all spectral lines could be reproduced by the code calculations the most intense spectral features which are emitted above 1 keV have been reproduced. Especially the emissions in the soft X-ray range from 0.4 nm–0.8 nm are modeled with rather high precision and comparisons to the distorted wave code HULLAC exhibit only small differences between the codes, even though HULLAC's physical model is considered more accurate than the plane wave Born approximation used in the Cowan code. However, few predicted spectral lines do exhibit discrepancies to experiment of up to about factor of 10. An example for this is the strongest line in the range, i.e. an electric quadrupole transition between the configurations $3d^{10}$ and $3d^9 4s^1$. Comparisons to other calculations of HULLAC, RATIP and GRASP on the corresponding transition probability did not explain the differences. Also, a comparison between HULLAC, RATIP and the ADAS results for the electron impact excitation to the upper level of this state did not reveal the reason for the discrepancy. Possibly an

additional, populating process is neglected in the collisional radiative modeling, which figures important for this transition. Nevertheless, the distribution of radiation versus wavelength agrees to a large extend which is promising for interpreting the data of the soft X-ray diagnostic, because it measures the integral of radiation from a certain wavelength region in the soft X-ray range.

To benchmark the atomic codes further, the spectra of Hf, Ta, Re, Au, Pb and Bi have been analyzed. Unlike tungsten which is an intrinsic impurity in ASDEX Upgrade, these impurities have been injected into the plasma by laser blow-off. The investigations in the VUV region of the plasma exhibited that all injected impurities emit an intense quasicontinuous structure between 3 nm and 7 nm similar to that of tungsten, but shifted in wavelength. Bismuth is emitting the main peak of this structure at 4 nm and with decreasing atomic number the feature is shifted to longer wavelengths until for hafnium the feature is emitted at 5.4 nm. The atomic data reproduce this shift in wavelength, while for each element the agreement of the predicted emission envelope of the structure is of similar quality as that for tungsten. This underlines that like for tungsten Ag-like to about Y-like ion states are responsible for the emissions. Furthermore, the emissions between 13 nm and 30 nm are investigated for all mentioned elements. For higher atomic number the feature, which has been observed for tungsten around 18 nm, is shifted to shorter wavelengths and the emission envelope gets narrower. This can partly be understood by a simple $1/z^2$-scaling model, however, like for tungsten the emissions cannot be reproduced by the code calculations. In the range 3.5 nm to 15 nm, isolated spectral lines are observed and attributed to Ge-like to Cu-like ion states. These emissions correspond to spectral lines, which have been investigated already for tungsten. The observations have been possible only for gold and the elements with lower atomic number, because the isoelectronic states for lead and bismuth are more highly charged and exhibit too low abundances to be detected. For the same reason, the soft X-ray spectra of these elements have been investigated for Hf, Ta, W, Re and Au only. The spectra compare well to the model calculations. Like for tungsten, the coarse distribution of radiation is in good agreement and only few spectral lines exhibit discrepancies larger than a factor of 2. For all investigated elements the electric quadrupole line between the configurations $3d^{10}$ and $3d^9 4s^1$ of the Ni-like state exhibit large discrepancies to the model calculations, which remain unresolved. The fact that this discrepancy exists for all investigated elements demonstrates the robustness of its reason, which is not a peculiarity of tungsten only. Finally, also the spectra of xenon are compared to the model calculations. The comparison of the VUV emissions of xenon between 10 nm and 18 nm exhibit poor agreement. The emissions originate from ion states below Cu-like Xe^{25+} and the influence of a flawed ionization balance is obvious. The emissions of Cu-like Xe^{25+}, Zn-like Xe^{24+}

and Ga-like Xe^{23+} are overestimated, while Rb-like Xe^{17+} to Br-like Xe^{19+} are strongly underestimated. The rough structure of the spectrum, i.e. distribution of spectral lines versus wavelength, can be identified in the calculation. Much better is the agreement for the emissions just above 1 nm, which originate mainly from Ni-like Xe^{26+} to Ar-like Xe^{36+}. The measured structure is nicely reproduced by the model. Additionally, a structure at 0.29 nm has been observed, which is emitted by Cl-like Xe^{37+} to about Na-like Xe^{43+} and corresponding predictions of the atomic code are identified.

Following the above identifications of details in the spectra, also the overall power loss of a plasma due to a high-Z impurity, given by the cooling factor, is investigated. The cooling factor is containing all the calculated atomic data. Several variants of the evaluation of the cooling factor have been discussed, which differ slightly and allow to estimate the typical uncertainty of the obtained cooling factor. It is evaluated by using the ionization data from configuration averaged distorted wave calculations and the recombination data from the present ADAS calculations. The line radiation is taken from the present, level-resolved calculations of ADAS including the Cowan code, while the continuum radiation and radiation due to dielectronic recombination is obtained from scaling formulae using the ion structure from the present ADAS calculations. The cooling factor agrees above 10 keV electron temperature with the earlier cooling factor obtained via the average ion model. Below 10 keV the cooling factor of the present work is up to a factor of 5 (at 1.9 keV) lower than the earlier data. Below about 700 eV electron temperature the credibility of the cooling factor is decreasing, as here the calculations could not be performed to a satisfying degree. Considerable emissions are found for these electron temperatures in the spectrum, for which the code calculations do not account for. It is proposed that configuration averaged calculations are reliably implemented into the ADAS environment, for doing flexible calculations on the ion states with charge below Cd-like W^{26+}. Even though these calculations do not exhibit the details of level-resolved calculations the reliability of the results would be much higher. Data for these lowly charged ions are of importance for modeling the plasma edge, which is vital for the performance of a future reactor. Especially, the effects of tungsten in comparison to carbon are of interest, because large experience for carbon is available.

When looking at the implications for future devices the changed cooling factor of tungsten does not imply a change of the tolerable tungsten concentration in a future device, because the cooling factor is unchanged in the plasma region, where the criteria for ignition need to be considered. Global predictions which consider the influence of tungsten radiation at the plasma edge on fusion performance do not exist. The present work does give new information on the possible diagnostic of tungsten in ITER or a reactor up to the hot plasma center. Spectral lines around 0.14 nm, around 2 nm and

around 8 nm are the main candidates to diagnose the central tungsten concentrations in these future devices. It is suggested that these emissions need to be investigated experimentally at JET or at EBIT devices, to obtain also experimental data on them.

In summary, the work in this thesis presents an overview of the emissions of several high-Z elements in the VUV and also in the soft X-ray region. It also confronts the best available ionization and recombination data for tungsten with measurements, which exhibit detailed resolution in electron temperature due to the exploitation of peculiar transport effects in the plasma. The resulting ion balance, which is empirically adjusted to the measurements contains relative and absolute information, which can be used as a benchmark for future reassessed theoretical data on ionization and recombination rates. Although the ionization and recombination rates of the present work exhibit some disagreement, the data are of higher quality than any data before. The diagnostic of tungsten in ASDEX Upgrade benefits from the improved data and it is also a valuable basis to predict the ion abundances in ITER or a fusion reactor. The experimental spectra which are obtained and used in this work are provided for eight elements and it is remarkable that the code calculations do manage to predict nearly for all measured spectra corresponding emissions. Increasing agreement of code calculations and measurements is found for increasing charge states and higher electron temperatures. In detail, strong emissions around 18 nm, corresponding to Ag-like W^{27+} and lower charge states and emissions around 6 nm corresponding to Y-like W^{35+} and lower charge states are not at all found in the calculations, while the most intense emissions in the VUV of Ag-like W^{27+} to Y-like W^{35+} are reproduced by the calculations and emissions of Kr-like W^{38+} to Fe-like W^{48+} are remarkably well matched by the predictions. The robustness of these findings is confirmed by the investigations on neighboring high-Z elements. Additionally, investigations on xenon, which might be injected into future fusion devices for diagnostic or cooling purposes, were performed and again better agreement between measurements and predictions were found for electron temperatures above 1 keV and charge states above about Ni-like Xe^{26+}. For all investigated elements, the existing discrepancies between measurements and code calculations can be used to understand the connected atomic physics and finally the obtained spectra also will help to benchmark future improved calculation methods, which will be available due to larger computer capacities or more efficient approximations. Although a detailed analysis revealed some discrepancies, the calculated data basis is widely qualified to describe the distribution of radiated power in the spectrum of each investigated high-Z element. This is the key interest of the fusion research community and therefore, the bottom line on the newly obtained data is that there is room for improvement of the atomic data, but they are already very valuable for the interpretation of impurity radiation from fusion experiments.

Appendix A

Magnetic Confinement Fusion (MCF)

In the concept of MCF, magnetic fields hinder the transport of charged particles perpendicular to the magnetic field lines, as particles gyrate around them following the influence of the Lorentz force. Transport losses parallel to the magnetic field can be best suppressed, when the field line structure is bent to a torus. In this configuration, the centrifugal force is acting on the moving particles and at the same time the particles experience a radially inhomogeneous magnetic field. Both effects leads to drift $\mathrm{v}_{\nabla B \times B}$ dependent on the charge q_e of the particle with mass m (equation A.1) proportional to ∇B×B, which in turn causes a vertical electric field. $v_\parallel$ and $v_\perp$ denote the velocity components of a plasma particle, parallel and perpendicular to the magnetic field line, respectively.

$$\vec{v}_{\nabla B \times B} = \frac{m}{q_e B^3}(v_\parallel^2 + \frac{1}{2}v_\perp^2)\vec{B} \times \nabla \vec{B} \tag{A.1}$$

The resulting E×B force leads to a radial particle drift $\mathrm{v}_{E \times B}$ (equation A.2) and the plasma particles are lost within milliseconds (figure A.1).

$$\vec{v}_{E \times B} = \frac{\vec{E} \times \vec{B}}{B^2} \tag{A.2}$$

Adding helicity to the magnetic field line geometry solves this problem as the initial drift, that is proportional to ∇B×B, is on average zero. Ions (electrons) that move along a helical field line and tend to drift upwards (downwards) drift towards the center of the plasma when below (above) the center, while they move away from the center when above (below) it. Such a magnetic field can be produced by overlaying the toroidal field (direction of Φ in fig A.2) with a poloidal field component (direction of Θ in fig A.2). This can be produced by special shaping of the magnetic field coils, like a stellarator, or by an electric current through the plasma in toroidal direction, i.e. a

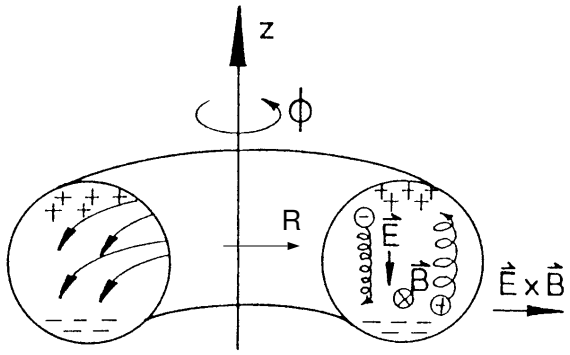

Figure A.1: Sketch of charge distributions and $E \times B$ drift for a purely toroidal magnetic field

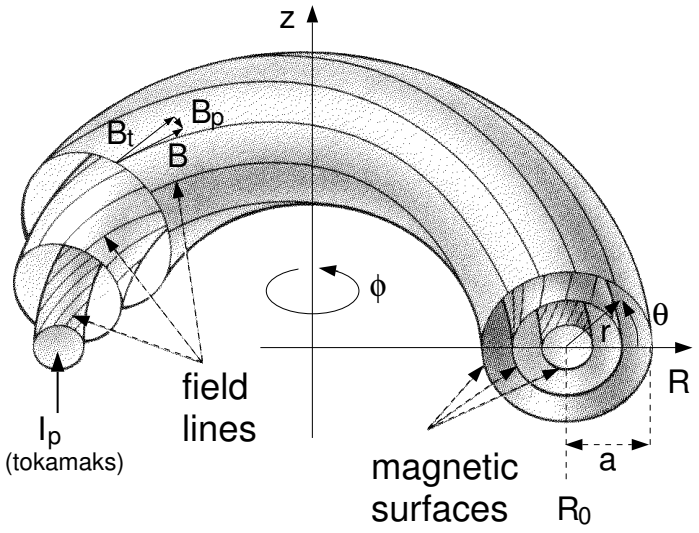

Figure A.2: Magnetic surfaces are defined by helical field lines, i.e. field lines with a poloidal field component B_p on top of a toroidal field B_t

tokamak. In figure A.3, the plasma and the field coils of the stellarator Wendelstein-7X [133] are presented, which is recently constructed in Greifswald and will be the largest fusion experiment in Germany.

In the following the focus is put on tokamaks. An extensive overview on tokamaks and corresponding physics can be reviewed in [132], here only the basics are introduced. The characteristic of a tokamak is the plasma current, which creates the necessary poloidal magnetic field overlaying the externally produced toroidal magnetic field forming a helical field structure. Often the so called safety factor q, i.e. the number of toroidal rotations per one poloidal rotation of a field line, is used to characterize the magnetic field structure. Most tokamaks are operated for magneto-hydrodynamical

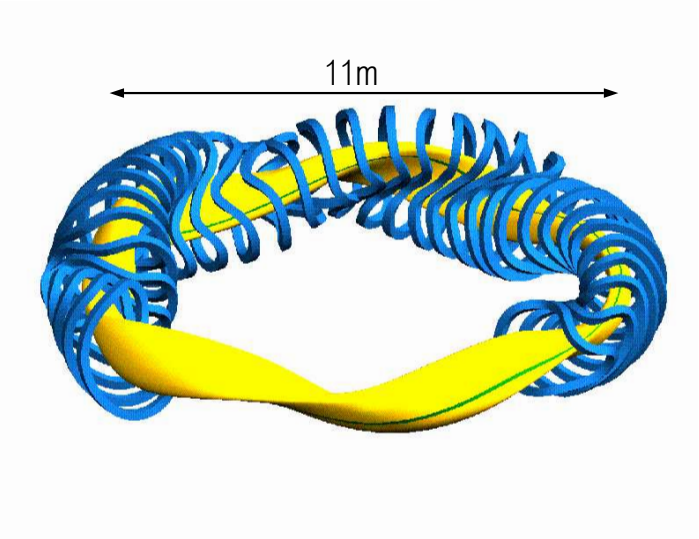

Figure A.3: Schematic view of a Wendelstein-7X plasma and its superconducting magnetic field coils.

stability with a q at the plasma boundary of $q_{edge} \approx 3$–5. It can be approximated by

$$q_{edge} = 5\frac{a^2 B_t}{R_0 I_p}(1 + \epsilon^2 c_\beta) \tag{A.3}$$

where a is the minor radius, R_0 the large radius of the plasma, I_p the plasma current and B_t the toroidal magnetic field. The term in parenthesis is about 1.1 and corresponds to corrections due to finite aspect ratio $\epsilon = a/R_0$ and and effects of the current profile (represented by the factor c_β). The field lines span magnetic surfaces that have the topology of a torus surface. Due to the fact that magnetic field lines do not intersect, the magnetic surfaces form a nested set of tori surfaces (figure A.2). The safety factor for different magnetic surfaces varies, depending on the currents that flow through their cross sections. The describe magnetic field structure also exists at the edge of the plasma, but here the magnetic field lines intersect with the first wall of the plasma vessel. Therefore, the plasma is divided into the confined part, where the magnetic field lines are closed and the scrape-off layer (SOL), where the magnetic field lines intersect with the vessel material. The last closed flux surface is the outermost flux surface, which does not intersect the first wall. For the confined part of the fusion plasma, the transport of particles and heat parallel to the magnetic field lines is so large, that the plasma pressure can be considered constant on a magnetic surface. Often magnetic coordinates are used, which correspond to the flux tube geometry. In this thesis, ρ_{pol} is used several times, which is the plasma radius normalized via the poloidal magnetic field dependence (s. equation A.4, where r is the radius towards larger R at the equatorial plane ($\Theta = 0$) and Ψ is the poloidal magnetic flux; $\Psi_{separatrix}$ corresponds to the poloidal flux at the last closed flux surface, while Ψ_{axis}

is the poloidal flux at the magnetic axis.). ρ_{pol} is between 0 and 1 in the confined plasma region while values above 1 are also well defined and correspond to the SOL of the plasma.

$$\rho_{pol}(r) = \sqrt{\frac{\Psi(r) - \Psi_{axis}}{\Psi_{separatrix} - \Psi_{axis}}} \tag{A.4}$$

For producing the plasma current, the transformer principle is used where the plasma is playing the role of the secondary coil (s. figure A.4). While the magnetic flux through the central solenoid is changed a toroidal electric field is induced in the plasma, which keeps up the plasma current. Due to the large conductivity and cross section of the fusion plasma, a loop voltage in the order of a Volt is enough to maintain a current of several MA. Even though this mechanism is producing plasma current very efficiently other means to drive current are investigated, because the magnetic flux swing of the central solenoid is limited. Operation times in the order of hours are feasible in this way for a reactor, but stepping towards a steady-state operation is envisaged in the frame work of so called 'advanced scenarios'. These use current drive by external means, i.e. special application of heating methods, and exploit intrinsic current drive effects, e.g. the so called 'bootstrap current' to prolong the maximum discharge duration.

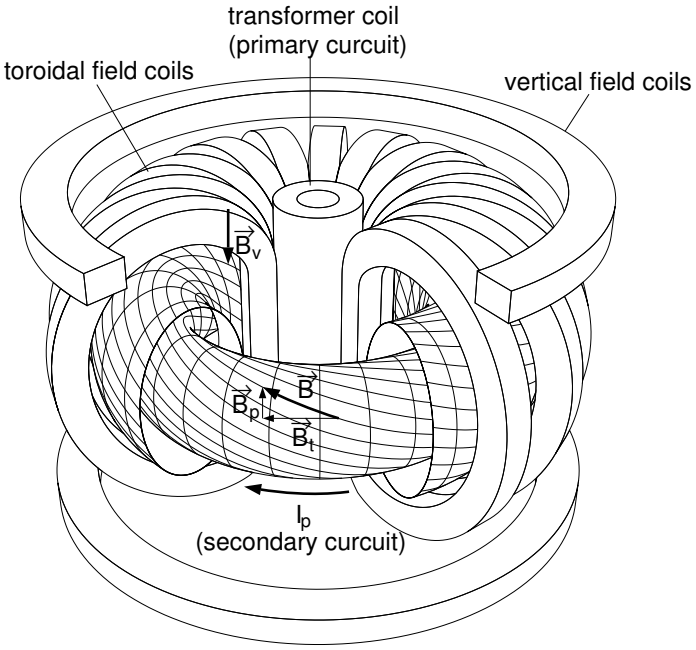

Figure A.4: Scheme of a tokamak showing the transformer principle including the vertical field coils ($\vec{B}_v$) that give stability to the plasma current

The plasma is heated by three different methods. Ohmic heating is the intrinsic method, because the plasma current is always present. However, the conductivity of the plasma is $\propto \mathrm{T}^{3/2}$ and therefore, the heating efficiency is decreasing for higher

temperatures such that temperatures above 2 keV are difficult to reach. Additional heating schemes are necessary to reach temperatures relevant for fusion. One possibility is the injection of fast neutral fuel atoms with energies of about 100 keV to 1 MeV, that are ionized and confined in the core of the plasma and then transfer their energy to the plasma by collisions. The other option is heating by radio frequency which is able to transfer energy by various resonance mechanisms on ions or electrons. In a future reactor most plasma heating will be intrinsically supplied by energetic the helium nuclei which are a product of the fusion reaction (cf. equation 1.1).

A main focus of today's research lies on the plasma-wall interaction. In principle two possibilities exist, how the plasma volume can be limited. The first possibility is using a material limiter (cf. figure A.5) which defines the plasma volume due to the magnetic field lines. An improvement to this configuration was found by introducing a divertor (cf. figure A.5) via additional magnetic coils. The plasma-wall interaction is separated from the actual main plasma due to a special shaping of the magnetic field lines. Instead of the plasma-wall interaction taking place directly at the plasma edge the interaction is shifted via the magnetic configuration to the divertor, where lower electron temperatures exist due to a local built up of plasma density. As a result the impurity concentrations are drastically lower and plasma performance is improved by using a divertor. Additionally, the so called H-mode (high confinement) regime is accessible which exhibits better confinement (about factor 2) due to an edge transport barrier that is formed above a threshold for auxiliary heating. All reactor relevant predictions (e.g., cf. appendix B.3 and B.4) rely on this regime. The next step fusion

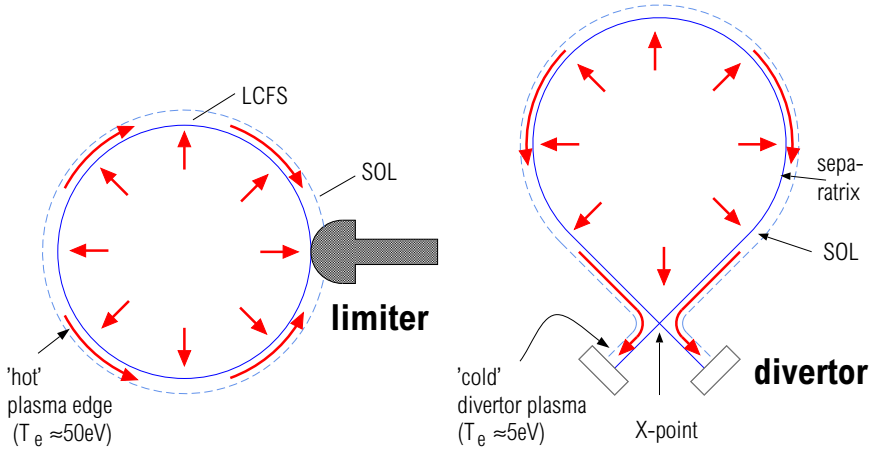

Figure A.5: Schematic view of limiter (left) and divertor (right) principle showing the large distance of the first-wall to the main plasma for the divertor concept.

device ITER (s. appendix B.3) is a tokamak.

Appendix B

Fusion Experiments/Reactors

B.1 ASDEX Upgrade

ASDEX Upgrade (Axial Symmetric Divertor EXperiment), the largest German fusion experiment, is located in Garching. The mid-sized tokamak went into operation in 1990 [135]. The plasma geometry of ASDEX Upgrade is nearly identical to that

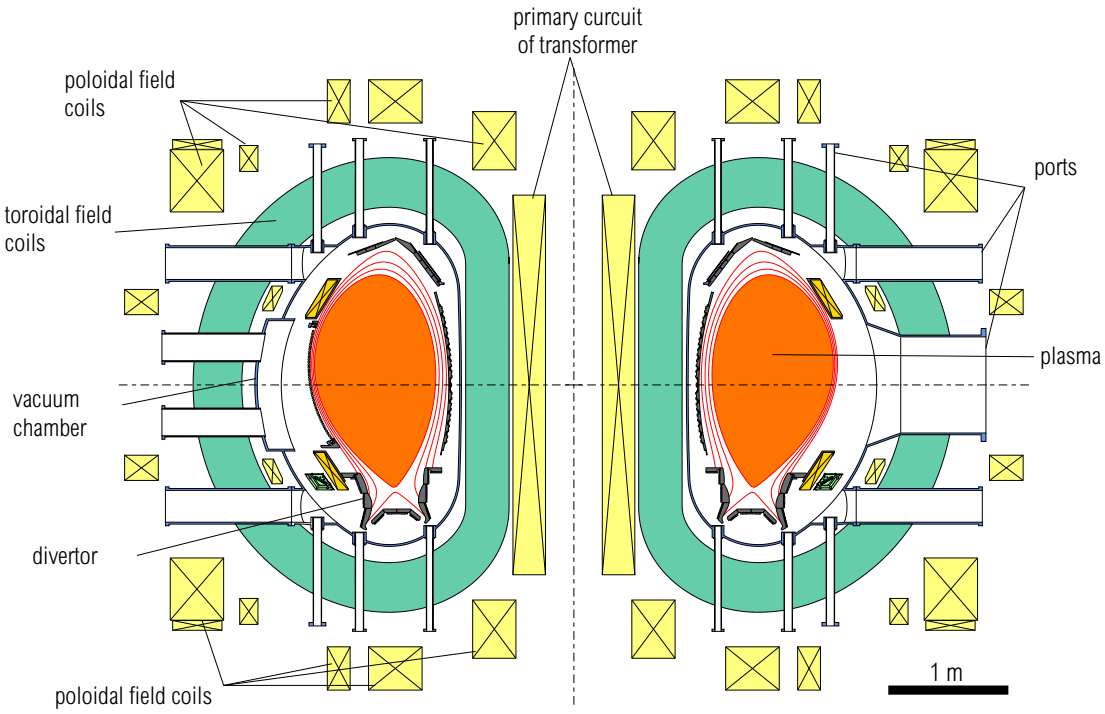

Figure B.1: Cross-section of ASDEX Upgrade

of ITER. Generally, at ASDEX Upgrade the crucial issues in fusion research under reactor-like conditions are investigated. In particular, the plasma density and wall loads are adapted to reactor relevant conditions. The standard operation is using the

Max. Auxiliary Heating	P_{aux}	$\leq 28\,MW$
Max. Neutral Beam Heating	P_{NI}	$20\,MW$
Max. ICR Heating	P_{ICRH}	$6\,MW$
Max. ECR Beam Heating	P_{ECRH}	$2\,MW$
Large Plasma Radius	R_0	$1.65\,m$
Small Plasma Radius	a	$0.5\,m$
Plasma Height	b	$0.8\,m$
Plasma Elongation	κ=b/a	1.7
Plasma Current	I_p	$\leq 1.4\,MA$
Toroidal Magnetic Field R_0	B_t	$\leq 3.2\,T$
Flat-top Pulse Length	T_p	$10\,s$
Plasma Volume	V_p	$14\,m^3$
Plasma Surface	S_p	$40\,m^2$

Table B.1: Parameter of ASDEX Upgrade

lower, closed divertor (one X-point), where powerful pumps are available. Alternatively, operation is also possible using the open, upper divertor or using both divertors simultaneously (double-null). The lower divertor is up to now still made from graphite, while since 2003 the upper divertor is made from tungsten coated tiles. The tungsten programme [60, 61, 82, 136–142] is a large activity that is pursued since 1996. Some details and references are given in chapter 3.4.

The similarity of the plasma shape to the plasma shape of ITER (cf. chap. B.3) makes ASDEX Upgrade ideal for performance analysis that can act as benchmarks for extrapolations to ITER's plasma operation. Especially, the powerful heating (28 MW for $14\,m^{-3}$) allows for reactor relevant investigations on advanced scenarios [143] that may be suited to operate a tokamak not in pulses but steady-state. Recent results obtained at ASDEX Upgrade can be reviewed in [144–146]. In table B.1 some main parameters of ASDEX Upgrade are listed. Figure B.1 shows the cross section of ASDEX Upgrade featuring the important magnetic field coils and an example plasma. A webpage is available [147]

B.2 JET

JET (Joint European Torus) is world-wide the largest tokamak, today. It went into operation 1983 and used at the beginning just limiter configuration. In 1993 a first divertor has been implemented. JET established the world-record in fusion power 16 MW during 1997's DT-experiments. Reference [148] details JET from 1973 –1999.

Max. Auxiliary Heating	P_{aux}	$\leq 40\,MW$
Power multiplication (DT in 1991/1997)	$Q=P_{fus}/P_{aux}$	≤ 0.64
Large Plasma Radius	R_0	$2.96\,m$
Small Plasma Radius	a	$1.25\,m$
Plasma Height	b	$2.1\,m$
Plasma Elongation	κ=b/a	1.68
Plasma Current	I_p	$\leq 4.8\,MA$
Toroidal Magnetic Field R_0	B_t	$\leq 3.45\,T$
Flat-top Pulse Length	T_p	$20\,s$
Plasma Volume	V_p	$\approx 100\,m^3$
Plasma Surface	S_p	$\approx 160\,m^2$

Table B.2: Parameters of JET

The aim of JET now is to support the design and extrapolations towards ITER (cf. appendix B.3) and to study physics and engineering issues that are relevant for a future reactor. Recent results of JET can be reviewed in [149]. Its parameters and a 3d-outline are featured in table B.2 and figure B.2, respectively. A webpage is available [150].

B.3 ITER

ITER is the next step fusion device, for which detailed construction plans and physics predictions already exist [151–155]. An alternative version of ITER that was planned to reach ignition has been redesigned in order to reduce the costs. Its main objective is the demonstration that a fusion reactor is feasible not only from the physics point of view, but also under technical and economical boundary conditions. ITER will be the largest fusion experiment of the world (cf. table B.3). For the first time a fusion plasma will be heated mostly by the α-particles that emerge from DT-fusion reactions, while only about 10 % of the heating is provided externally. Plasma operation will explore regimes for steady-state operation, where plasma current is externally driven. Key technologies for a reactor will be tested. A webpage is available [154].

In this context also the experience of ITER with its plasma facing components will be a milestone on the way to a reactor. Figure B.3 is featuring the material mix as it is envisaged for the ITER first wall. However, a change of the plans is still possible, while also a change of the first wall after start up of the device is discussed. A challenge for ITER arises due to the fact, that many boundary conditions need to be met for the first time in one device. Namely, the mitigation of wall loads, operation with low impurity

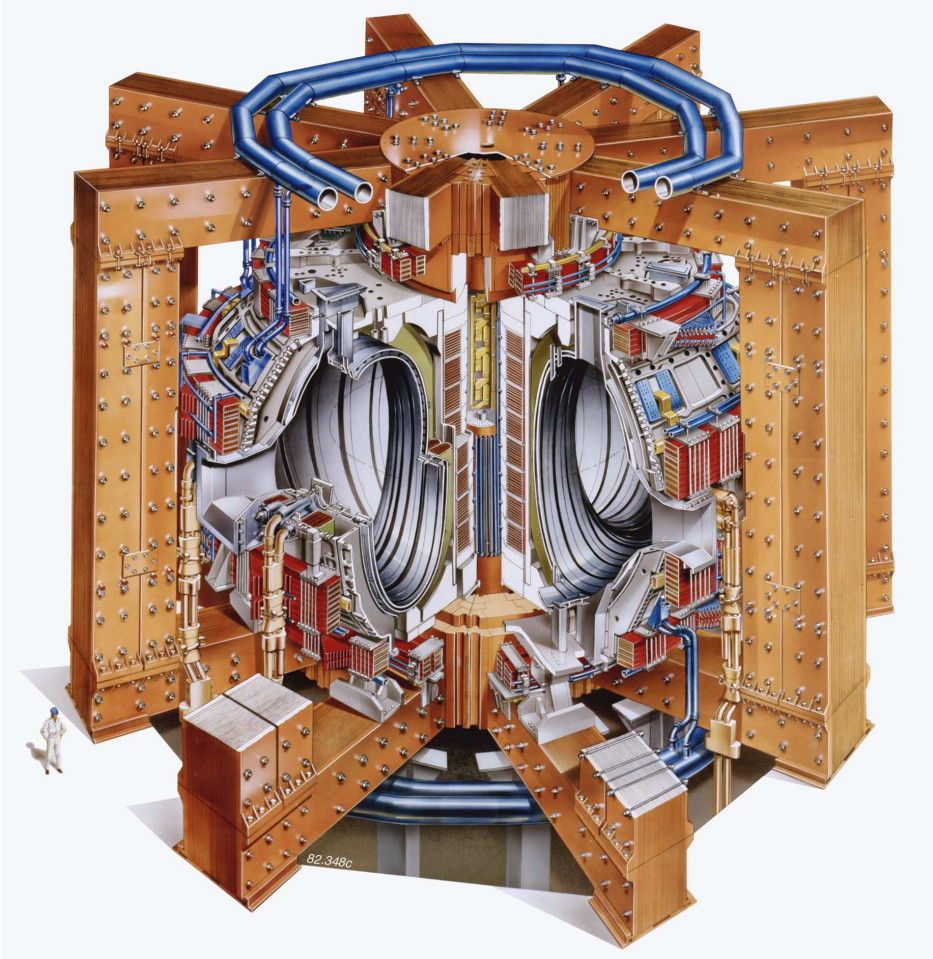

Figure B.2: 3d-scheme of JET

content and erosion of armour material, good plasma performance, compatibility with tritium fuel, remote handling and use of large superconducting coils are some of the upcoming issues that will be integrated.

B.4 DEMO

DEMO is going to be the prototype of a fusion reactor. Up to now it is not decided whether this device is a tokamak or a stellarator [156]. However, an extrapolation to a reactor is done by several groups [157–159], which use the most advanced experiments as benchmarks. The resulting designs imply a development towards even larger dimensions, stronger magnetic fields and higher particle fluxes than in ITER. Tungsten is used in all designs as first-wall material in the divertor, while the design in [159] foresees the use of tungsten coated low-activation steel also in the main chamber. The design of [158] implements beryllium as PFMs in the main chamber, which according

Fusion Power	P_{fus}	500 MW (700 MW)
Max. Auxiliary Heating	P_{aux}	73 MW (100 MW)
Envisaged Power multiplication	$Q=P_{fus}/P_{aux}$	≥ 10
Large Plasma Radius	R_0	6.2 m
Small Plasma Radius	a	2.0 m
Plasma Height	b	3.6 m
Plasma Elongation	κ=b/a	1.8
Plasma Current	I_p	15 MA (17.4 MA)
Toroidal Magnetic Field R_0	B_t	5.3 T
Flat-top Pulse Length	T_p	≥ 400 s
Plasma Volume	V_p	837 m^3
Plasma Surface	S_p	678 m^2

Table B.3: Parameters of ITER

to [2] seems not to be a favorable choice. Reference [157] plans a first-wall in the main chamber made from ferritic steel, a material for which more experience is needed to come to a conclusion. However, several observations in today's tokamaks [160–162] suggest that the mid-Z materials like iron enter the plasma easily while they also account for strong radiation losses. Better predictions for DEMO will be possible after results from ITER operation enter into the extrapolations. Today's predictions put tungsten in favor for becoming an important first-wall material in DEMO.

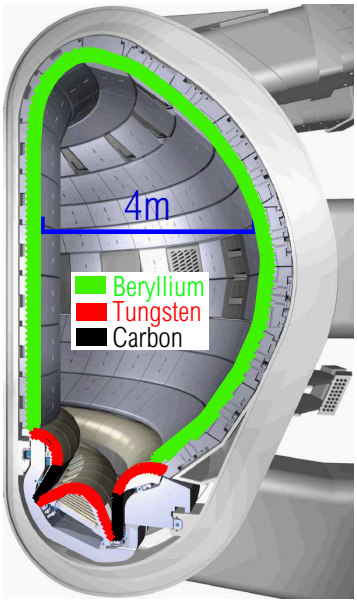

Figure B.3: ITER cross section showing actual plans for plasma facing components

Bibliography

[1] K. Heinloth, *Die Energiefrage*, Vieweg & Sohn Verlagsgesellschaft, Braunschweig, 2nd edition, 2003.

[2] H. Bolt, V. Barabash, G. Federici, J. Linke, J. Loarte, A. Roth, et al., Journal of Nuclear Materials **307-311**, 43–52 (2002).

[3] G. Janeschitz, ITER JCT, and ITER HTs, Journal of Nuclear Materials **290 – 293**, 1 – 11 (2001).

[4] P. Andrew, D. Brennan, J. Coad, J. Ehrenberg, M. Gadeberg, et al., Journal of Nuclear Materials **266-269**, 153 (1999).

[5] M. Mayer, V. Philipps, P. Wienhold, H. G. Esser, J. von Seggern, et al., Journal of Nuclear Materials **290–293**, 381–388 (2001).

[6] V. Rohde, H. Maier, K. Krieger, R. Neu, J. Perchermeier, et al., Journal of Nuclear Materials **290–293**, 317–320 (2001).

[7] C. Skinner, E. Amarescu, G. Ascione, W. Blanchard, C. Barnes, et al., J. Nucl. Mat. **241-243**, 214–226 (1997).

[8] G. Federici, R. Anderl, P. Andrew, J. Brooks, R. Causey, et al., Journal of Nuclear Materials **266-269**, 14–29 (1999).

[9] G. Federici, P. Andrew, P. Barabaschi, J. Brooks, R. Dörner, et al., Journal of Nuclear Materials **313–316**, 11–22 (2003).

[10] G. Federici, J. Brooks, D. Coster, G. Janeschitz, A. Kukuskhin, et al., Journal of Nuclear Materials **290-293**, 260–265 (2001).

[11] V. Arunasalam, C. Barnes, K. Bol, K. Brau, N. Bretz, et al., Recent Results from the PLT tokamak, in *Proc. 8th Conf. EPS, Prague 1977*, volume 2, pages 17–28, Geneva, 1978, EPS.

[12] R. Neu, R. Dux, A. Kallenbach, T. Pütterich, M. Balden, et al., Nuclear Fusion **45**(3), 209–218 (2005).

[13] R. Neu, Tungsten as a Plasma Facing Material in Fusion Devices, Rep. IPP 10/25, Max-Planck-Institut für Plasmaphysik, Garching, 2003.

[14] R. D. Cowan, *The Theory of Atomic Structure and Spectra (Los Alamos Series in Basic and Applied Sciences)*, University of California Press, California, 1981.

[15] ADAS Homepage, 'http://adas.phys.strath.ac.uk/'.

[16] H. P. Summers, Atomic data and analysis structure users manual, JET-IR 06 (Abingdon: JET Joint Undertaking) (1994).

[17] C. Biedermann, T. Fuchs, G. Fußmann, and R. Radtke, in: Trapping of Highly Charged Ions: Fundamentals and application (2001), NOVA Science Publishers.

[18] M. O'Mullane, H. Summers, A. Whiteford, R. Barnsley, I. Coffey, et al., Review of Scientific Instruments **74**, 2080–2083 (2003).

[19] E. Merzbacher, *Quantum Mechanics*, Wiley, New York, NY, Third edition, 1998.

[20] M. Mizushima, *Quantum Mechanics of Atomic Spectra and Atomic Structure*, W. A. Benjamin, New York,NY, 1970.

[21] P. A. M. Dirac, Proceedings of the Royal Society **A117**, 610 – 612 (1928).

[22] P. A. M. Dirac, Proceedings of the Royal Society **A118**, 351 – 361 (1928).

[23] P. A. M. Dirac, *Principles of Quantum Mechanics*, Oxford University Press, Fourth edition, 1982.

[24] I. P. Grant, C. T. Johnson, F. A. Parpia, and E. P. Plummer, Comput. Phys. Commun. **55**, 425–456 (1989).

[25] D. Post, R. Jensen, C. Tarter, W. Grasberger, and W. Lokke, At. Data Nucl. Data Tables **20**, 397–439 (1977).

[26] D. Post, J. Abdallah, R. Clark, and N. Putvinskaya, Phys. Plasmas **2**, 2328 – 2336 (1995).

[27] D. Post, Private communication, 2001.

[28] A. Bar-Shalom and M. Klapisch, Comp. Phys. Commun. **50**, 375–393 (1988).

[29] A. Bar-Shalom, M. Klapisch, and J. Oreg, Phys. Rev. A **38**, 1773 (1988).

[30] K. Fournier, At. Data Nucl. Data Tables **68**, 1 – 48 (1998).

[31] M. Klapisch, J. Schwob, B. Fraenkel, and J. Oreg, J. Opt. Soc. Am. **67**, 148 (1977).

[32] S. Fritzsche, Journal of Electron Spectroscopy and Related Phenomena **114–116**, 1155–1164 (2001).

[33] S. Fritzsche, Physica Scripta **T100**, 37–46 (2002).

[34] P. G. Burke and K. A. Berrington, *Atomic and molecular processes - an R-matrix approach*, Institute of Physics Publishing, Bristol, 1993.

[35] A. D. Whiteford, On the spectral emission of impurity species for diagnostic application to magnetically confined fusion plasmas, Technical report, University of Strathclyde, Sept. 2004, Doctoral thesis, September 04.

[36] T. Carlson, C. Nestor, N. Wassermann, and J. McDowell, Atomic Data **2**, 63 (1970).

[37] W. Lotz, Z. Phys. D **216**, 241 (1968).

[38] A. Burgess and M. Chidichimo, Mon. Not. R. astr. Soc. **203**, 1269 – 1280 (1983).

[39] K. Asmussen, K. B. Fournier, J. M. Laming, R. Neu, J. F. Seely, et al., Nuclear Fusion **38**(7), 967–986 (1998).

[40] S. D. Loch, Private communication, 2004.

[41] S. D. Loch, M. S. Pindzola, C. P. Ballance, D. C. Griffin, D. M. Mitnik, et al., Phys. Rev. A **66**, 052708 (2002).

[42] A. Burgess, Astrophysical Journal **141**, 1588 – 1590 (1965).

[43] N. R. Badnell, M. G. O'Mullane, H. P. Summers, Z. Altun, M. A. Bautista, et al., Astronomy and Astrophysics **406**, 1151–1165 (Aug. 2003).

[44] M. Bessenrodt-Weberpals, J. C. Fuchs, M. Sokoll, and ASDEX Upgrade Team, Soft X-ray Diagnostics for ASDEX Upgrade, Technical Report 1/290, IPP, Garching, Germany, Aug. 1995.

[45] R. Fonck, A. Ramsey, and R. Yelle, Applied Optics **21** (1982).

[46] Proscan GmbH, D-86836 Lagerlechfeld, more informations under 'http://www.proscan.de'.

[47] R. Dux, Private communication, 2005.

[48] McPherson, Inc. - 7A Stuart Road, Chelmsford, MA 01824 USA, more informations under 'http://www.mcphersoninc.com'.

[49] E. Unger, Untersuchungen zur Absolutkalibration eines Grazing-Incidence-Spektrometers für Verunreinigungstransport an einem Fusionsexperiment, Technical Report III/187, IPP, Garching, Germany, 1992.

[50] D. McKenzie, P. Landecker, and J. Underwood, Space Science Instrumentation **2**, 125 – 139 (1976).

[51] A. Oed, Nucl. Instr. Meth. **A263**, 351 – 359 (1988).

[52] D. Bolshukhin, R. Neu, D. Schlögl, R. Dux, and ASDEX Upgrade Team, Review of Scientific Instruments **72**(11), 4115–4124 (2001).

[53] H. H. Johann, Zeitschschrift für Physik **69**, 185–206 (1931).

[54] T. Johansson, Zeitschrift für Physik **82**, 507–528 (1933).

[55] B. Endras, Aufbau und Test einer Pulshöhen-Analyse-Diagnostik für den Tokamak ASDEX Upgrade, Technical report, Diploma thesis, Universität Augsburg, 1997.

[56] J. Friichtenicht, Review of Scientific Instruments **45**, 51 (1974).

[57] E. Marmar, J. Cecchi, and S. Cohen, Review of Scientific Instruments **46**, 1149 – 1154 (1975).

[58] S. Mattoo, L. Wirtz, A. Pospieszczyk, and B. Schweer, Nucl. Instr. Meth. B **124**, 579–590 (1997).

[59] R. Neu, K. Asmussen, S. Deschka, A. Thoma, M. Bessenrodt-Weberpals, et al., Journal of Nuclear Materials **241–243**, 678–683 (1997).

[60] R. Neu, K. Asmussen, K. Krieger, A. Thoma, H.-S. Bosch, et al., Plasma Physics and Controlled Fusion **38**, A165–A179 (1996).

[61] K. Krieger, H. Maier, R. Neu, and ASDEX Upgrade Team, Journal of Nuclear Materials **266–269**, 207–216 (1999).

[62] K. Asmussen, R. Neu, R. Dux, W. Engelhardt, K. Fournier, et al., Investigations of Tungsten in the Central Plasma of ASDEX Upgrade, in *Europhysics Conference Abstracts (Proc. of the 24th EPS Conference on Controlled Fusion and Plasma Physics, Berchtesgaden, 1997)*, edited by M. Schittenhelm, R. Bartiromo, and F. Wagner, volume 21A, part IV, pages 1393–1396, Petit-Lancy, 1997, EPS.

[63] R. Neu, R. Dux, A. Geier, O. Gruber, A. Kallenbach, et al., Fusion Engineering and Design **65**(3), 367–374 (2003).

[64] M. Mayer, V. Rohde, T. Pütterich, P. Coad, P. Wienhold, et al., Physica Scripta **T111**, 55–61 (2004).

[65] T. Pütterich, R. Dux, J. Gafert, A. Kallenbach, R. Neu, et al., Plasma Physics and Controlled Fusion **45**(10), 1873–1892 (2003).

[66] V. Rohde, R. Dux, M. Mayer, R. Neu, T. Pütterich, et al., Physica Scripta **T111**, 49–54 (2004).

[67] S. Stepanov, Computer code for simulating dynamical x-ray diffraction from strained crystals, multilayers, and superlattices, 'http://sergey.gmca.aps.anl.gov/gid_sl.html'.

[68] B. L. Henke, E. M. Gullikson, and J. C. Davis, At. Data and Nucl. Data **54**, 181–342 (1993).

[69] C. Fuchs, Kalibrierung von Detektoren zur Plasmadiagnostik im weichen Röntgenbereich, Technical Report 1/292, IPP, Garching, Germany, Nov. 1995, Diploma thesis TU Munich, 1995.

[70] A. Mück, Private communication, 2003.

[71] A. Gude, Private communication, 2000.

[72] R. Dux, Impurity Transport in Tokamak Plasmas, Rep. IPP 10/27, Max-Planck-Institut für Plasmaphysik, Garching, 2004.

[73] R. Dux, Fusion Science and Technology **44**(3), 708–715 (2003).

[74] A. Boscolo, L. Placentino, and L. Poletto, Pure Appl. Opt. **7(4)**, L43 – L47 (1998).

[75] J. A. R. Samson, *Techniques of Vacuum Ultraviolet Spectroscopy*, John Wiley & Sons, Inc., New York, 1967.

[76] K. Behringer, 'Description of the impurity transport code STRAHL', JET-R(87)08, JET Joint Undertaking, Culham (1987).

[77] R. Dux, STRAHL Manual, www.aug.ipp.mpg.de/~Ralph.Dux/strahl.ps.

[78] S. de Peña Hempel, Untersuchungen zum Transport leichter Verunreinigungen an ASDEX Upgrade, Technical Report 10/8, IPP, Garching, Germany, July 1997, Doctoral thesis TU Munich, June 97.

[79] S. de Peña Hempel, R. Dux, A. Kallenbach, H. Meister, and ASDEX Upgrade Team, Low-Z-Impurity Transport Coefficients at ASDEX Upgrade, in *Europhysics Conference Abstracts (Proc. of the 24th EPS Conference on Controlled Fusion and Plasma Physics, Berchtesgaden, 1997)*, edited by M. Schittenhelm, R. Bartiromo, and F. Wagner, volume 21A, part IV, pages 1401–1404, Petit-Lancy, 1997, EPS.

[80] R. Dux, A. Peeters, A. Gude, A. Kallenbach, R. Neu, et al., Measurement of Impurity Transport Coefficients in the Confined Plasma of ASDEX Upgrade, in *Proc. of the 18th IAEA Conference Fusion Energy (CD-Rom), Sorrento, Italy, October 2000*, volume IAEA-CSP-8/C, pages IAEA–CN–77/EXP5/32, Vienna, 2001, IAEA.

[81] R. Dux, A. G. Peeters, A. Gude, A. Kallenbach, R. Neu, et al., Nuclear Fusion **39**(11), 1509–1522 (1999).

[82] R. Neu, R. Dux, A. Geier, H. Greuner, K. Krieger, et al., Journal of Nuclear Materials **313–316**, 116–126 (2003).

[83] R. Dux, A. Herrmann, A. Kallenbach, R. Neu, J. Neuhauser, et al., Journal of Nuclear Materials **337-339**, 852–856 (2005).

[84] K. Behringer, H. P. Summers, B. Denne, M. Forrest, and M. Stamp, Plasma Physics and Controlled Fusion **31**, 2059–2099 (1989).

[85] J. Steinbrink, U. Wenzel, W. Bohmeyer, G. Fußmann, and PSI Team, Sputtered Tungsten Atoms Investigated in a Linear Plasma Generator, in *Europhysics Conference Abstracts (Proc. of the 24th EPS Conference on Controlled Fusion and Plasma Physics, Berchtesgaden, 1997)*, volume 21A, pages 1809–1812, Geneva, 1997, EPS.

[86] D. Laun and C. H. Corliss, J. Res. NBS A **72**, 609–755 (1968).

[87] H. Obarius and M. Kock, J. Phys. B **15**, 527 – 533 (1982).

[88] B. Michelt, Spektroskopische Messung der Oszillatorenstärke und Besitzungsdichten angeregter Wolframzustände in einem WF_6 dotierten Argonbogen, Technical report, Diploma Thesis, Universität Bochum, 1992.

[89] A. Geier, H. Maier, R. Neu, K. Krieger, and ASDEX Upgrade Team, Plasma Physics and Controlled Fusion **44**(10), 2091–2100 (2002).

[90] R. Isler, R. Neidigh, and R. Cowan, Phys. Lett. **A63**, 295 (1977).

[91] E. Hinnov and M. Mattioli, Phys. Lett. **A66**, 109 (1978).

[92] R. Radtke, C. Biedermann, J.-L. Schwob, P. Mandelbaum, and R. Doron, Phys. Rev. A **64**, 012720 (2001).

[93] S. B. Utter, P. Beiersdorfer, and E. Träbert, Can. J. Phys. **80**, 1503–1515 (2002).

[94] J. Sugar, V. Kaufman, and W. Rowan, J. Opt. Soc. Am. **B10**, 1321 (1993).

[95] J. Sugar, V. Kaufman, and W. Rowan, J. Opt. Soc. Am. **B10**, 1977 (1993).

[96] J. Sugar, V. Kaufman, and W. Rowan, J. Opt. Soc. Am. **B10**, 799 (1993).

[97] E. Hinnov, K. Bol, D. Dimock, R. Hawryluk, D. Johnson, et al., Nuclear Fusion **18**, 1305 (1978).

[98] M. Finkenthal, L. Huang, S. Lippmann, H. Moos, P. Mandelbaum, et al., Phys. Lett. A **127**, 255 (1988).

[99] J. Seely, C. Brown, and W. Behring, J. Opt. Soc. Am. **B6**(1), 3 – 6 (1989).

[100] W. Biel, Private communication, 2004.

[101] A. Zigler, H. Zmora, N. Spector, M. Klapisch, J. Schwob, et al., J. Opt. Soc. Am. **70**(1), 129 – 132 (1980).

[102] M. Klapisch, A. Bar-Shalom, P. Mandelbaum, J. Schwob, A. Zigler, et al., Physics Letters **79A**, 67 – 70 (1980).

[103] P. Mandelbaum, M. Klapisch, A. Bar-Shalom, J. Schwob, and A. Zigler, Physica Scripta **27**, 39 – 53 (1983).

[104] A. Zigler, M. Klapisch, and P. Mandelbaum, Phys. Lett. A **117**(1), 31 – 35 (1986).

[105] N. Tragin, J.-P. Geindre, P. Monier, J.-C. Gauthier, C. Chenais-Popovics, et al., Physica Scripta **37**, 72 – 82 (1988).

[106] R. Neu, K. B. Fournier, D. Bolshukhin, and R. Dux, Physica Scripta **T92**, 307–310 (2001).

[107] R. Neu, K. B. Fournier, D. Schlögl, and J. Rice, J. Phys. B: At. Mol. Opt. Phys. **30**, 5057–5067 (1997).

[108] K. Fournier, R. Neu, D. Bolshukhin, A. Geier, and the ASDEX Upgrade Team, Soft X-ray emission spectra from highly charged tungsten ions as a quantitative diagnostic of fusion plasmas, in *Bulletin of the American Physical Society*, volume 46, page 267, 2001.

[109] K. Fournier, private communication (2001).

[110] S. Fritzsche, Private communication, 2005.

[111] C. Brown, J. Seely, D. Kania, B. Hammel, C. Back, et al., Atomic Data and Nuclear Data Tables **58**, 203 (1994).

[112] J. Reader and G. Luther, Physica Scripta **24**, 723 (1981).

[113] D. R. Kania, B. J. MacGowan, C. J. Kaene, C. M. Brown, J. O. Ekberg, et al., J. Opt. Soc. Am. B **7**, 1993 (1990).

[114] J. Reader and G. Luther, Phys. Rev. Lett. **45**, 1980 (1980).

[115] J. F. Seely, J. O. Ekberg, C. M. Brown, U. Feldman, W. E. Behring, et al., Physical Review Letters **57**, 2924–2926 (1986).

[116] P. Audebert, J.-C. Gauthier, J.-P. Geindre, C. Chenais-Popovics, C. Bauche-Arnoult, et al., Phys. Rev. A **32**(1), 409 – 411 (1985).

[117] M. Busquet, Z. Jiang, C. Côté, J. Kieffer, M. Klapisch, et al., Physical Review E **61**(1), 801 – 808 (2000).

[118] P. Burkhalter, C. Dozier, and D. Nagel, Phys. Rev. A **15**(2), 700 – 717 (1977).

[119] K. B. Fournier, Private communication, 2004.

[120] C. Breton, C. DeMichelis, W. Hecq, M. Mattioli, J. Ramette, et al., Physica Scripta **37**, 33–37 (1988).

[121] H. Hacker, R. Burhenn, K. Kondo, M. Anton, D. Assmus, et al., Applied Physics B **73**, 59–64 (2001).

[122] E. Hinnov, Phys. Rev. A **14**(4), 1533 – 1541 (1976).

[123] J. Wyart, C. Bauche-Arnoult, E. Luc-Koenig, and TFR Group, Physica Scripta **32**, 103 – 106 (1985).

[124] C. Keane, B. Hammel, A. Osterheld, and D. Kania, Physical Review Letters **72**, 3029–3032 (1994).

[125] Y. Conturie, B. Yaakobi, U. Feldman, G. Doschek, and R. Cowan, J. Opt. Soc. Am. **71**(11), 1309 – 1314 (1981).

[126] C. Chenais-Popovics, V. Malka, J.-C. Gauthier, S. Gary, O. Peyrusse, et al., Physical Review E **65**, 046418 (2002).

[127] J. Asada, F. Currell, T. Fukami, T. Hirayama, K. Motohashi, et al., Physica Scripta **T73**, 90 – 92 (1997).

[128] T. Werner, G. Zschornack, F. Großmann, V. Ovsyannikov, and E. Ullmann, Physica Scripta **T92**, 241 – 243 (2001).

[129] I. Kink, J. Laming, J. Takás, J. Porto, J. Gillaspy, et al., Physica Scripta **T92**, 454 – 456 (2001).

[130] C. Biedermann, R. Radtke, G. Fußmann, J. Schwob, and P. Mandelbaum, Nucl. Instr. Meth. B **235**, 126–130 (2005).

[131] P. Beiersdorfer, S. Elliott, J. Crespo López-Urrutia, and K. Widmann, Nuclear Physics A **626**, 357c–364c (1997).

[132] J. Wesson, *Tokamaks*, Clarendon Press, Oxford, 2 edition, 1997.

[133] Wendelstein 7X Homepage, 'http://www.ipp.mpg.de/eng/for/projekte/w7x/for_proj_w7x.html'.

[134] LHD Homepage, 'http://www.lhd.nifs.ac.jp/en/'.

[135] W. Köppendörfer, M. Blaumoser, H. Bruhns, C. Dorn, J. Gernhardt, et al., Completion of Assembly and Start of Technical Operation of ASDEX Upgrade, in *Fusion Technology (Proc. of the 16th Symposium on Fusion Technology, London, U.K., 1990)*, edited by B. Keen, M. Huguet, and R. Hemsworth, volume 1, pages 208–212, Amsterdam, 1991, Elsevier.

[136] R. Neu, R. Dux, A. Kallenbach, C. F. Maggi, T. Pütterich, et al., Tungsten: An Option for Divertor and Main Chamber Plasma Facing Components in Future

Fusion Devices, in *Proc. of the 20th IAEA Conference Fusion Energy (CD-Rom), Vilamoura, Portugal, November 2004*, volume IAEA-CSP-25/CD, pages IAEA–CN–116/EX/10–5, Vienna, 2005, IAEA.

[137] A. Geier, K. Krieger, J. D. Elder, R. Pugno, V. Rohde, et al., Journal of Nuclear Materials **313–316**, 1216–1220 (2003).

[138] K. Krieger, K. Asmussen, R. Neu, V. Rohde, J. Roth, et al., Erosion and Transport of Tungsten in ASDEX Upgrade, in *Plasma Physics and Controlled Nuclear Fusion Research 1996*, volume 1, pages 817–823, Vienna, 1997, IAEA.

[139] R. Neu, R. Dux, A. Geier, A. Kallenbach, R. Pugno, et al., Plasma Physics and Controlled Fusion **44**(6), 811–826 (2002).

[140] R. Neu, V. Rohde, A. Geier, K. Krieger, H. Maier, et al., Journal of Nuclear Materials **290–293**, 206–210 (2001).

[141] V. Rohde, R. Neu, R. Dux, A. Geier, X. Gong, et al., Operation of ASDEX Upgrade with Tungsten Coated Walls, in *Proc. of the 19th IAEA Conference Fusion Energy (CD-Rom), Lyon, France, October 2002*, volume IAEA-CSP-19/CD, pages IAEA–CN–94/EX/D1–4, Vienna, 2003, IAEA.

[142] V. Rohde, R. Neu, K. Krieger, H. Maier, A. Geier, et al., Operation of ASDEX Upgrade with High-Z Wall Coatings, in *Proc. of the 18th IAEA Conference Fusion Energy (CD-Rom), Sorrento, Italy, October 2000*, volume IAEA-CSP-8/C, pages IAEA–CN–77/EXP4/24, Vienna, 2001, IAEA.

[143] A. Sips, J. Hobirk, and A. G. Peeters, Fusion Science and Technology **44**(3), 605–617 (2003).

[144] O. Gruber, R. Arslanbekov, C. Atanasiu, A. Bard, G. Becker, et al., Nuclear Fusion **41**(10), 1369–1389 (2001).

[145] S. Günter, C. Angioni, M. Apostoliceanu, C. Atanasiu, M. Balden, et al., Overview of ASDEX Upgrade Results, in *Proc. of the 20th IAEA Conference Fusion Energy (CD-Rom), Vilamoura, Portugal, November 2004*, volume IAEA-CSP-25/CD, pages IAEA–CN–116/OV/1–5, Vienna, 2005, IAEA.

[146] H. Zohm, Overview of ASDEX Upgrade Results, in *Proc. of the 19th IAEA Conference Fusion Energy (CD-Rom), Lyon, France, October 2002*, volume IAEA-CSP-19/CD, pages IAEA–CN–94/OV/2–1, Vienna, 2003, IAEA.

[147] ASDEX Upgrade Homepage, 'http://www.ipp.mpg.de/eng/for/projekte/asdex/for_proj_asdex.html'.

[148] J. Wesson, The Science of JET, available on the JET-Hompage at http://www.jet.efda.org/documents/wesson/wesson.html.

[149] J. Paméla, E. R. Solano, and JET EFDA Contributors, Nuclear Fusion **43**(12), 1540–1554 (2003).

[150] JET-Homepage, 'http://www.jet.efda.org'.

[151] R. Aymar, P. Barabaschi, and Y. Shimomura, Plasma Physics and Controlled Fusion **44**, 519–565 (2002).

[152] R. Aymar, V. Chuyanov, M. Huguet, Y. Shimomura, and ITER Joint Central Team and Home Teams, Nuclear Fusion **41**, 1301 – 1310 (2001).

[153] D. Campbell, Phys. Plasm. **8**, 2041 – 2049 (2000).

[154] ITER-Homepage, 'http://www.iter.org'.

[155] ITER physics basis editors, Nuclear Fusion **39**, 2137 – 2638 (1999).

[156] K. Lackner, R. Andreani, D. Campbell, M. Gasparotto, D. Maisonnier, et al., Journal of Nuclear Materials **307-311**, 10–20 (2002).

[157] S. Konishi, S. Nishio, K. Tobita, and DEMO design team, Fus. Eng. Design **63-64**, 11–17 (2002).

[158] G. Shatalov, I. Kirillov, Y. Sokolov, Y. Strebkov, N. Vasiliev, et al., Fusion Eng. Des. **56-57**, 163 – 172 (2001).

[159] R. Toschi, P. Barabaschi, D. Campbell, F. Elio, D. Maisonnier, et al., Fusion Eng. Des. **56-57**, 163 – 172 (2001).

[160] R. Dux, C. Giroud, K. Zastrow, and JET EFDA Contributors, Nuclear Fusion **44**, 260 – 264 (2004).

[161] A. Tabasso, H. Maier, J. Roth, K. Krieger, and ASDEX Upgrade Team, Journal of Nuclear Materials **290–293**, 326–330 (2001).

[162] W. West, M. Wade, C. Greenfield, E. Doyle, K. Burrell, et al., Physics of Plasmas **9**, 1970 – 1981 (2002).

At the end of my thesis I would like to thank several people, who supported me, made this work possible or contributed directly or indirectly to the success of this work. In detail, I would like to thank

- **Prof. Dr. Kurt Behringer**, who offered me the possibility to work on the thesis at the IPP.
- **Prof. Dr. Achim Wixforth** for being the second referee to this work.
- **Dr. Rudolf Neu**, for the outstanding support and supervision of my work, which would not have been possible without his personal and professional advice. I'm grateful for his ability to supply me with strategies which helped me to participate in the scientific community. His profound knowledge on plasma wall interactions never ceased to amaze me.
- **Dr. Ralph Dux**, for his support and advice, which were very useful to me. I could always count on him when help was needed.
- **Dr. Arne Kallenbach**, for his supporting optimism and help to advertise my work.
- **Dr. Roberto Pugno** for worthwhile discussions and his support.
- my room colleague **Jens Harhausen** and my colleague **Igor Radivojevic** for the interesting discussions and the positive atmosphere.
- **Mr. Manfred Hien, Mr. Jochen Fink and Mr. Rembert Seth** for the beneficial work on technical equipment and the practical support on the spectrometers, the laser blow-off manipulator and the large-area x-ray source.
- **the division E4**, for the friendly atmosphere.
- **Prof. Dr. Hugh Summers** for his strong support of my work and helpful discussions about atomic physics.
- **Dr. Allan Whiteford** for his patience answering my e-mails and for giving me crucial support on atomic physics questions and bug fixing. I'd also like to point out that I'm very grateful about the social experiences in Glasgow which were enabled by his kind invitation.
- **Dr. Martin O'Mullane** for his professional support on the code calculations and his experienced advice on atomic physics.
- **Manuel Garcia-Munoz** for the support on our challenging task as PhD representatives.

- **Dr. Reinhard Drube, Mr. Asher Flaws, Dr. Jörg Hobirk, Dr. Marc Maraschek, Dr. Hans Meister, Dr. Doris Merkl, Dr. Anja Mück, Dr. Hans Werner Müller, Ms. Eilis Quigley, Dr. Matthias Reich, Mr. Karl Sassenberg, Mrs Jasmine Schirmer, Mr. Andreas Schmid, Ms. Carolin Tröster and Ms. Laura Urso**, for many fruitful discussions and conversations during lunch, and at our Stammtisch.

- **the ASDEX Upgrade Team**, which earned the name 'team' by its uncomplicated and efficient way of working together.

- **My parents Mr. Egon und Mrs. Elfriede Pütterich** for their loving support throughout my studies and my PhD work. They have always been an important backing for my optimism.

- **My girl friend Birgit Bader** for her infinite patience and her loving support.

- **Everybody, whom I forgot to thank** and who would have deserved it.